

ALGERIAN DEMOCRATIC AND POPULAR REPUBLIC  
MINISTRY OF HIGH EDUCATION AND SCIENTIFIC RESEARCH

UNIVERSITY FRERES MENTOURI CONSTANTINE 1  
FACULTY OF SCIENCES EXACTES  
PHYSICS DEPARTMENT

Order N°:101/D3C/2018  
Series:09/phy/2018

THESIS

PRESENTED FOR LMD DOCTORAT DEGREE IN PHYSICS

SPECIALITY

Nanomaterials and Advanced Materials

THEME

---

Realization and electrical characterization of thin film heterojunction for  
photovoltaic application

---

By

***BOUTBAKH FATIMA ZOHRA***

Defended on: 09 / 10 / 2018

Jury committee:

President :	B. BOUDINE	Prof.	Univ. frères Mentouri Constantine1
Advisor :	N. ATTAF	Prof.	Univ. frères Mentouri Constantine 1
Examiners :	L.HADJERIS	Prof.	Univ. Oum El-Bouaghi
	M.ZAABAT	Prof.	Univ. Oum El-Bouaghi





بِسْمِ اللَّهِ الرَّحْمَنِ الرَّحِيمِ  
( وَقُلْ رَبِّ زِدْنِي عِلْمًا )  
[طه: 114]



---

## Acknowledgements

---

*"Be a scientist .... If you can not, be educated, if you can not, love scientists, if you can not ,do not hate them "After years of research and effort and diligence culminated by the completion of this research, First thanks to **ALLAH** for his grace and for his help to let me completing my research.*

*For most, I would like to express my sincere gratitude to my previous advisor **Mr. Mohammed Saleh Aida** professor at King Abdul-Aziz University, Saudi Arabia, for continuing support of my Ph.D research until the end, for his patience, motivation, enthusiasm, and immense knowledge and advice , thank you so much for accepting to advisor me in my PhD at the first time.*

*I would like to thank especially Mr. **Nadir ATTAF** Professor at the University of Frere Mentouri-Constantine 1. Thank you for supervising my thesis work and for supporting and encouraging me along the way.*

*I am very grateful to Mr. **B.Boudine**, professor at the University of Freres Mentouri-Constantine 1, I am sensitive to the honor he gave me by agreeing to read this manuscript and for agreeing to serve as president of the panel.*

*I would like to thank all members of the examining committee of this PhD thesis. Thanks to Mr. **L.Hadjeris** and Mr.**M.Zaabat** professors at University of Oum bouaghi for accepting the evaluation of my work.*

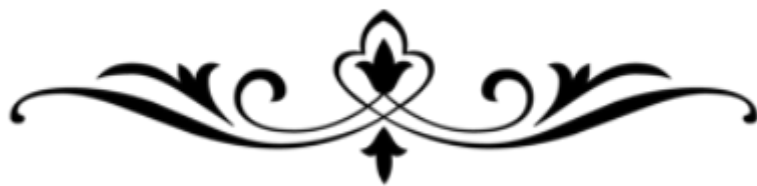
*I would like to express my gratitude to Prof. **Slivia Maria Pietralunga** professor at the Institute for Photonics and Nanotechnologies of the Italian National Research Council (IFN -CNR), Milan, Italy for here guide, kindest, trust all the times, and help for doing and finishing my characterization during my internship at POLIMI university.*

*For my **parents**, words are not enough to express my gratitude for you. Without your selfless love and endless support, I cannot be me today. Thank you for always being there*

***Finally, I would like to give heartfelt thanks to all the people (family, friends, and colleagues) for their care and help during my work!***

*Fatima*

# Contents



# Contents

FIGURES CAPTION	I
TABLES CAPTION	VI
<b>INTRODUCTION</b>	<b>i</b>

---

## CHAPTER I

### Photovoltaic energy and thin film solar cells

---

<b>I.1 PHYSICS OF PHOTOVOLTAIC</b>	<b>1</b>
I.1.1 History of photovoltaic Effect	1
I.1.2 Physics of p-n junction	2
I.1.3 Function of a solar cell	3
I.1.4 Current-Voltage characterization in the dark	4
I.1.4 .1 Ideality factor	5
I.1.4.2 Current saturation ( $I_s$ )	6
I.1.5 I-V characteristics under-illumination	6
I.1.5.1 Open circuit voltage ( $V_{oc}$ )	7
I.1.5.2 Short-circuit current ( $I_{sc}$ )	7
I.1.5.3 Fill factor (FF)	7
I.1.5.4 Photovoltaic efficiency	8
I.1.6 Losses in solar cells	9
I.1.7 Band discontinuity at hetero-junction interface	10
<b>I.2 THIN-FILM SOLAR CELLS</b>	<b>12</b>
I.2.1 History of thin film solar cells	12
I.2.2 Possible configuration for solar cell	13
I.2.3 Thin film solar cells technologies	14
I.2.3.1 Amorphous silicon (a-Si)	14
I.2.3.2 Cadmium Telluride (CdTe)	14
I.2.3.3 Cu (InGa) Se <sub>2</sub> (CIGS)	15
<b>I.3 Cu<sub>2</sub>ZnSnS<sub>4</sub> SOLAR CELLS</b>	<b>15</b>
I.3.1 Introduction	15

I.3.2 A material based on abundant and friendly elements in nature	16
I.3.3 Fundamental properties	17
I.3.3.1 Crystal structure and polymorphous	17
I.3.3.2 Secondary Phases in CZTS thin films	18
I.3.3.3. Detecting secondary phases in CZTS	19
I.3.3.4 Point defects in the CZTS	20
I.3.3.5 Electrical properties	22
I.3.3.6. Optical properties	23
I.3.4 The role of the Buffer layer in CZTS Thin Film Solar Cell	24
a. CdS buffer layer	25
b. ZnS buffer layer	24
c. ZnSe buffer layer	24
d. ZnO buffer layer	25
e. In <sub>2</sub> S <sub>3</sub> buffer layer:	25
I.3.5 Band alignments diagram of Cu <sub>2</sub> ZnSnS <sub>4</sub> /buffer device	25
I.3.6 Diffusion length of CZTS	27
I.3.7 Progression of kesterite solar cells	27

---

## CHAPTER II

### Deposition and characterization techniques

---

<b>II.1 DEPOSITION TECHNIQUES OF CZTS</b>	<b>29</b>
II.1.1 Physical Vapor Deposition	29
II.1.1.1 Evaporation	29
II.1.1.2. Sputtering technique	30
II.1.1.3 Pulsed laser Deposition	30
II.1.2 Chemical Vapor Deposition (CVD)	31
II.1.2.1 Electrodeposition	31
II.1.2.2 Sol-Gel	32
II.1.2.3 Spray pyrolysis	32
II.1.3 Thin films preparation and device fabrication	35

II.1.3.1 CZTS thin film deposition	35
<i>PART I: THE STUDIED PARAMETERS OF CZTS THIN FILMS</i>	37
1. Effect of substrate temperature	37
2. Deposition time	38
3. Copper salt concentration	38
4. Effect of zinc molarities	38
<i>PART II: CZTS DEVICE FABRICATION</i>	39
1. Effect of back contact	40
2. Effect of i-ZnO intrinsic layer	41
3. The effect of sulfurization temperature on CZTS/CdS solar cells performance	41
<b>II.2 ANALYSIS TECHNIQUES</b>	42
II.2.a Films characterization	42
II.2.a.1 X-Ray Diffraction (XRD)	42
II.2.a.2 Raman spectroscopy	43
II.2.a.3 The UV-visible spectrophotometer	44
II.2. a.4. Atomic force microscopy(AFM) and scanning electronic microscopy(SEM)	46
II.2. a.5. Hall effect measurement	46
II.2.b. Device characterization	46
II.2.b.1 Current-Voltage measurements	46
II.2.b.2. Conductance-Capacitance-frequency measurement	48

---

## CHAPTER III

### FILMS RESULTS AND DISCUSSION

---

<b>III.1 THE EFFECT OF SUBSTRATE TEMPERATURE</b>	<b>51</b>
III.1.1 structural properties	51
III.1.2 Morphological analysis	56
III.1.3 Optical properties	57
III.1.4. Electrical properties	60
<b>III.2 DEPOSITION TIME EFFECT</b>	<b>61</b>
III.2.1 Structural properties	63

III.2.2 Morphological properties	64
III.2.3 Optical properties	65
III.2.4 Electrical properties	67
<b>III.3 COPPER CONCENTRATION EFFECT</b>	<b>68</b>
III.3.1 Structural properties	68
III.3.2 Optical properties	71
III.3.3 Electrical properties	73
<b>III.4 ZINC MOLARITY EFFECT</b>	<b>75</b>
III.4.1 Structural properties	75
III.4.2 Morphological properties	78
III.4.3 Optical properties	79
III.4.4 Electrical properties	82

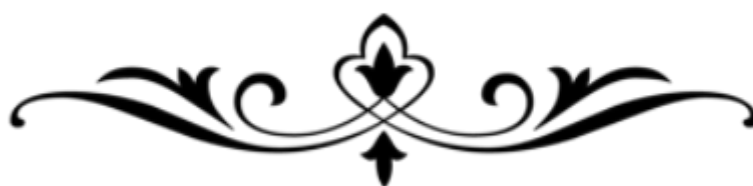
## CHAPTER IV

### Device properties, result and discussions

<b>IV.1 BACK CONTACT STUDY OF CZTS/ZNS HETEROJUNCTION</b>	<b>84</b>
IV.1.1 Films properties	84
IV.1.1.1 Structural properties	84
IV.1.1.2 Optical and electrical properties	86
IV.1.2 Device properties:	89
IV.1.2.1 Current-Voltage characterization	89
IV.1.2.2 Conductance-frequency characteristic	94
IV.1.2.2.a Conductance-frequency at room temperature(G-f)	94
IV.1.2.2.b Conductance -Frequency-Temperature (G-f-T)	97
<b>IV.2 THE EFFECT OF I-ZNO INTRINSIC LAYER AND MEASUREMENT TEMPERATURE</b>	<b>101</b>
IV.2.1 I-V characteristic in the dark at room temperature	101
IV.2.2 I-V-T characteristic in the dark	102
IV.2.3 I-V characteristic under illumination	104
<b>IV.3 EFFECT OF SULFURIZATION TEMPERATURE</b>	<b>105</b>
IV.3.1 Films properties	106

IV.3.1.1 Structural properties	106
IV.3.1.2 Morphological properties	108
IV.3.1.3. Optical properties	110
IV.3.1.4. The electrical properties	112
IV.3.2 Characteristic of the devices	113
IV.3.2.1. Current-Voltages characteristic	113
<b>Conclusion</b>	<b>119</b>
<b>REFERENCES</b>	<b>123</b>

# Figures caption



**Introduction**

- Figure 1** *Abundance on earth's crust and cost of constituent elements for CIGS, CdTe, and CZTS (Se) absorber materials for thin film solar cells* iii

**CHAPTER I**

- Figure I.1** *Formation of the depletion zone within a p-n junction* 2
- Figure I.2** *Energy band diagram of a p-n junction in thermal equilibrium* 3
- Figure I.3** *Illustration of a PV function* 3
- Figure I.4** *Absorption of different photons by a semiconductor material* 4
- Figure I.5** *I-V characterization of CZTS/ZnS hetero-junction and the equivalent circuit of an ideal diode.* 5
- Figure I.6** *Semi logarithmic scale of the current as function of applied voltage of a diode* 6
- Figure I.7** *I-V curve of CZTS based solar cells and an ideal equivalent circuit* 7
- Figure I.8** *Current-voltage characteristics showing the method for calculating FF* 8
- Figure I.9** *Real solar cell with two resistors  $R_s$  and  $R_{sh}$*  9
- Figure I.10** *p-n hetero-junction band diagram* 10
- Figure I.11** *Type I and type II hetero-junction interfaces* 11
- Figure I.12** *Band alignment of hetero-interface considering the electrostatic potentials (a): type I interface. (b): type II interface* 12
- Figure I.13** *Possible configuration of thin film solar cells* 14
- Figure I.14** *Thin films technologies* 15
- Figure I.15** *Relative abundance of the elements* 16
- Figure I.16** *Crystal structures of zinc-blende, chalcopyrite, kesterite and stannite* 17
- Figure I.17** *Ternary phase diagrams of CZTS* 19
- Figure I.18** *X-Ray Diffraction spectra of kesterite  $Cu_2ZnSnS_4$ ,  $Cu_2SnS_3$ , and ZnS showing overlap of the main peaks* 29
- Figure I.19** *Typical Raman spectrum of a  $Cu_2ZnSnS_4$  monograin powder* 21
- Figure I.20** *Inonisation level of different defect in CZTS* 22
- Figure I.21** *The band alignment of different buffers and CZTS values of the VBO, CBO, and  $E_g$  are indicated* 67
- Figure I.22** *Evolution of the conversion efficiency of thin film solar cells* 28

## CHAPTER II

<b>Figure II.1</b>	<i>Beam evaporation technique in the left and thermal evaporation in the right</i>	30
<b>Figure II.2</b>	<i>Illustration schema of pulsed laser deposition system</i>	31
<b>Figure II.3</b>	<i>Basic electrode-position system with three electrodes</i>	32
<b>Figure II.4</b>	<i>Schematic of different spray pyrolysis (sp) parameters</i>	33
<b>Figure II.5</b>	<i>Simplified schematic of spray pyrolysis system</i>	34
<b>Figure II.6</b>	<i>The variation of solution color with adding different precursors</i>	35
<b>Figure II.7</b>	<i>System used for CZTS film deposition</i>	37
<b>Figure II.8</b>	<i>Realized CZTS/ZnS Hetero-Junction</i>	40
<b>Figure II.9</b>	<i>Realized CZTS/Zn(O,S) Device</i>	41
<b>Figure II.10</b>	<i>Realized CZTS/CdS solar cells</i>	41
<b>Figure II.11</b>	<i>Illustration of the interaction between X-Rays and crystallographic planes</i>	42
<b>Figure II.12</b>	<i>Illustration of the energy-level diagram for Rayleigh scattering, stokes Raman scattering, and anti-stokes Raman scattering</i>	44
<b>Figure II.13</b>	<i>(a) and (b) graphs represent the transmittance and gap energy of CZTS</i>	45
<b>Figure II.14</b>	<i>Tektronics meter for the I-V measurement</i>	47
<b>Figure II.15</b>	<i>I-V system used for solar cells efficiency calculation (Dicle University, Diyarbakir, Turkey)</i>	48
<b>Figure II.16</b>	<i>Impedance meter used for C-G-f measurement</i>	49
<b>Figure II.17</b>	<i>Illustration of G/w and capacitance as function of pulsation of CZTS/ZnS hetero-junction</i>	50

## CHAPTER III

<b>Figure III.1</b>	<i>XRD patterns of CZTS thin films elaborated at various Ts</i>	52
<b>Figure III.2</b>	<i>Variation of strain and crystallites size as function of Ts</i>	54
<b>Figure III.3</b>	<i>(a) XRD Shifted of the preferential peak of CZTS as function of Ts.(b): shifted of peak position due to lattice strain</i>	54
<b>Figure III.4</b>	<i>Micro Raman spectra of CZTs thin films deposited with various substrate temperatures.</i>	55
<b>Figure III.5</b>	<i>Lattice strain variation with: (a) Raman shifted and (b) XRD peak position shift of CZTS fthin films as function of Ts.</i>	56
<b>Figure III.6</b>	<i>AFM image of CZTS thin film deposited at various Ts (300 390°c)</i>	57
<b>Figure III.7</b>	<i>Transmission spectra of CZTS thin film deposited at various Ts</i>	57
<b>Figure III.8</b>	<i>Absorption coefficient of CZTS films grown at various Ts</i>	58
<b>Figure III.9</b>	<i>Gap energy determination of CZTS thin films deposited at various Ts</i>	59
<b>Figure III.10</b>	<i>(a,b) Carrier concentration and mobility with the conductivity as function of substrate temperature</i>	61
<b>Figure III.11</b>	<i>XRD patters of CZTS thin film deposited at various deposition time</i>	62
<b>Figure III.12</b>	<i>The Raman spectra of CZTS elaborated at various deposition time</i>	63

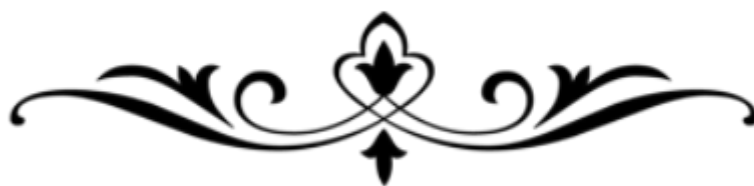
<b>Figure III.13</b>	<i>a, b, and c, SEM images of CZTS thin film deposited at 15 min ,30 min, and 45 min.</i>	64
<b>Figure III.14</b>	<i>Transmission spectra of CZTS films deposited at various deposition times</i>	65
<b>Figure III.15</b>	<i>Absorption coefficient of CZTS films deposited at various deposition time as function of lambda</i>	66
<b>Figure III.16</b>	<i>Gap energy variation as function of deposition time</i>	66
<b>Figure III.17</b>	<i>The variation of carrier concentration and mobility as function of deposition time</i>	68
<b>Figure III.18</b>	<i>XRD patterns of CZTS thin film with various copper molarity</i>	69
<b>Figure III.19</b>	<i>(a) The variation of (112) peak position in XRD pattern of CZTS films as a function of cu molarity, (b) their variation with lattice strain</i>	71
<b>Figure III.20</b>	<i>Transmittance spectra of CZTS thin with different copper concentration.</i>	72
<b>Figure III.21</b>	<i>Tauc's plot of CZTs thin film with different copper molarities</i>	72
<b>Figure III.22</b>	<i>Variation of carrier concentration and conductivity with mobility as function of copper concentration</i>	74
<b>Figure III.23</b>	<i>XRD patterns of CZTS thin films prepared under different zinc salt concentration</i>	76
<b>Figure III.24</b>	<i>(112) Peak position shifted as function of Zn concentration</i>	77
<b>Figure III.25</b>	<i>3D AFM image of CZTS Thin film deposited with various zinc salt concentration</i>	78
<b>Figure III.26</b>	<i>Crystallites size and roughness as function of zinc concentration</i>	79
<b>Figure III.27</b>	<i>Transmittance spectra of CZTS thin film with the variation of zinc salt molarity</i>	80
<b>Figure III.28</b>	<i>Tauc's plot of CZTS films elaborated with various zinc salt molarity</i>	81
<b>Figure III.29</b>	<i>Band tails width and gap energy variation as function of zinc molarity</i>	82
<b>Figure III.30</b>	<i>Conductivity and carrier concentration of CZTS film as function of zinc salt concentration</i>	83

## **CHAPTER IV**

<b>Figure IV.1</b>	<i>(a) XRD and Raman spectra of CZTS thin films</i>	84
<b>Figure IV.2</b>	<i>(a,b) XRD patterns of ZnS and FTO thin films</i>	85
<b>Figure IV.3</b>	<i>Transmittance spectra of CZTS, ZnS, and FTO thin films</i>	86
<b>Figure IV.4</b>	<i>Transmittance spectra of FTO in UV-visible-IR range</i>	87
<b>Figure IV.5</b>	<i>(a-c): <math>(\alpha h\nu)^2</math> vs <math>h\nu</math> of CZTS, ZnS and FTO thin films</i>	88
<b>Figure IV.6</b>	<i>Characterization of heterojunctions (a)-CZTS/ZnS with different back contact in the dark and at room temperature and (b) CZTS/Al,(c)-</i>	90

	<i>CZTS/Ag, (d)- CZTS/Au hetero-junctions at different measurement temperature</i>	
<b>Figure IV.7</b>	<i>Band diagram of ohmic and schottky contact of metal/Sc (p)diode</i>	92
<b>Figure IV.8</b>	<i>Ideality factor variation as function of measured temperature of CZTS/ZnS with different back contact</i>	94
<b>Figure IV.9</b>	<i>C-f variation Of CZTS/ZnS Hetero-Junction With Different Back Contact</i>	95
<b>Figure IV.10</b>	<i>G-<math>\omega</math> variation of CZTS/ZnS with different back contact</i>	96
<b>Figure IV.11</b>	<i>(a): G/<math>\omega</math> - <math>\omega</math> And (b): C-<math>\omega</math> variation of CZTS/ZnS hetero-junction with Al, Ag, And Au back contact at different temperature</i>	99
<b>Figure IV.12</b>	<i>Arhenuis plot of CZTS/ZnS hetero-Junction</i>	100
<b>Figure IV.13</b>	<i>I-V Characteristic in the dark and at room temperature of CZTS/ZnS hetero-junction (a) with ZnO and (b) without ZnO layer</i>	101
<b>Figure IV.14</b>	<i>The I-V characteristic of CZTS/ZnS/ZnO hetero-junction in the dark at different temperature</i>	102
<b>Figure IV.15</b>	<i>Saturation current as function of 1000/T</i>	103
<b>Figure IV.16</b>	<i>Semi-log plot of I-V characteristic under-illumination</i>	104
<b>Figure IV.17</b>	<i>XRD patterns of CZTS films sulfurized at different temperature</i>	106
<b>Figure IV.18</b>	<i>Crystallites size and strain as function of sulfurized temperature</i>	107
<b>Figure IV.19</b>	<i>Raman spectroscopy of CZTS at various sulfurized temperature</i>	108
<b>Figure IV.20</b>	<i>3D and 2D AFM images of CZTS deposited at various sulfurized</i>	109
<b>Figure IV.21</b>	<i>(a) lattice strain and (b) crystallite size variation with surface roughness as function of sulfurized temperature</i>	110
<b>Figure IV.22</b>	<i>Transmittance spectra of CZTS film as function of sulfurized temperature</i>	111
<b>Figure IV.23</b>	<i>Tauc's plot of CZTS thin film sulfurized at various temperature</i>	112
<b>Figure IV.24</b>	<i>Images of CZTS thin film, solar cell, and the cross section of our device.</i>	113
<b>Figure IV.25</b>	<i>Semi log plot of CZTS/CdS solar cells sulfurized at various annealing temperature</i>	114

# Tables caption



---

## TABLES CAPTION

---

### CHAPTER I

<b>Table I.1</b>	<i>Five absorber layers that have been used for thin film solar cell with highest efficiency</i>	13
<b>Table I.2</b>	<i>Crystallographic properties of CZTS</i>	20
<b>Table I.3</b>	<i>Raman Shift of CZTS material and related secondary phases</i>	21
<b>Table I.4</b>	<i>Rresistivity, mobility and carrier concentration of CZTS thin film obtained by different technique</i>	23

### CHAPTER II

<b>Table II.1</b>	<i>Highest of CZTS efficiency obtained by different methodes</i>	35
<b>Table II.2</b>	<i>Parameters used for the deposition of CZTS films with various substrate temperatures (Ts)</i>	37
<b>Table II.3</b>	<i>Experimental condition of CZTS with the variation of deposition time</i>	38
<b>Table II.4</b>	<i>Experimental condition of CZTS films with the variation of copper salt concentration</i>	39
<b>Table II.5</b>	<i>Experimental condition of CZTS with the variation of zinc salt concentration</i>	39
<b>Table II.6</b>	<i>The experimental condition for absorber layer deposition</i>	39
<b>Table II.7</b>	<i>The experimental condition for buffer layer deposition</i>	40
<b>Table II.8</b>	<i>The experimental condition for FTO layer deposition</i>	40

### CHAPTER III

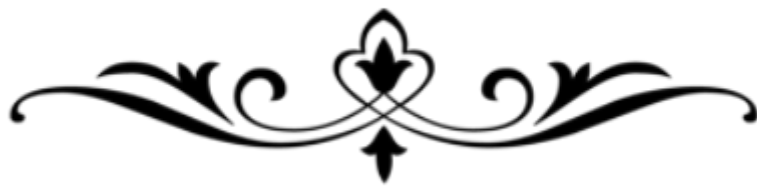
<b>Table III.1</b>	<i>FWHM, crystallite size and lattice strain of CZTS with different growth temperature</i>	53
<b>Table III.2</b>	<i>The Conductivity, carrier concentration and Hall mobility as function of growing temperature of CZTS films</i>	60
<b>Table III.3</b>	<i>Electrical parameters of CZTS thin film with different deposition time.</i>	67
<b>Table III.4</b>	<i>Crystalites size and strain of CZTS thin film as function of copper salt concentration</i>	70

<b>Table III.5</b>	<i>Carrier concentration, mobility and conductivity of CZTS thin film.</i>	74
<b>Table III.6</b>	<i>The FWHM values and grain sizes of (112) orientation of the CZTS thin films obtained at different zinc concentration</i>	78
<b>Table III.7</b>	<i>RMS values of CZTS thin films deposited with various zinc concentration</i>	79
<b>Table III.8</b>	<i>The electrical parameters of CZTS thin films at different zinc concentration</i>	82

## **CHAPTER IV**

<b>Table IV.1</b>	<i>Electrical parameters and gap energy of CZTS, ZnS, and FTO</i>	89
<b>Table IV.2</b>	<i>Electrical parameters of CZTS/ZnS hetero-junction with different back contact.</i>	91
<b>Table IV.3.a</b>	<i>Ag/CZTS diode parameters determined from I-V plots</i>	93
<b>Table IV.3.b</b>	<i>Al/CZTS diode parameters determined from I-V plots</i>	93
<b>Table IV.3.c</b>	<i>Au/CZTS diode parameters determined from I-V characteristic</i>	93
<b>Table IV.4</b>	<i>Density of state and life time of carriers of CZTS /ZnS hetero-junction with different back contact at room temperature</i>	97
<b>Table IV.5</b>	<i>Density of state, life time and energy level of CZTS/ZnS hetero-junction with different back contacts</i>	100
<b>Table IV.6</b>	<i>Electrical characterization of CZTS hetero-junction with ZnO and without ZnO.</i>	102
<b>Table IV.7</b>	<i>Electrical properties of realized devices at various measurement temperatures</i>	104
<b>Table IV.8</b>	<i>Electrical parameters of the fabricated solar cells</i>	104
<b>Table IV.9</b>	<i>FWHM, crystallites size, and strain of CZTS films sulfurized at varies temperature</i>	107
<b>Table IV.10</b>	<i>RMS values of CZTS films annealed at various temperatures</i>	110
<b>Table IV.11</b>	<i>Film thickness, band gap, carrier concentration, Hall mobility and conductivity of CZTS thin film sulfurized at different annealing temperature</i>	113
<b>Table IV.12</b>	<i>The calculated parameters of the fabricated solar cells.</i>	116
<b>Table IV.13</b>	<i>The electrical parameters of CZTS solar cells calculated by several authors.</i>	117

# Introduction



### Introduction and aim of the Work

---

Without energy billions of people stay cold and hungry. The main of this energy comes from fossil fuels which are consisted principally of carbon and hydrogen bonds such as: oil, natural gas, and coal. Because of the growing population in the world the amount of this fuel start diminishing. It may not be possible to offer the needed energy for people. As well known, these sources of energy caused the increasing emission of Carbon dioxide, sulfur dioxide emission, and greenhouses effects, the earth's air, land, and water became polluted and cause global warming as well as the enlarged of the ozone hole. The consequences of global warming consist of the change in the climate which effected on even people, animals, plants and living organisms. In 1952 four thousand people died in London because of the high concentration of pollution [1]. Recently in 2012 the World Health Organization (WHO) reported around 7 million of people died because of air pollution exposure [2]. The air pollution became the biggest environmental health risk in the world.

The solution to reduce this abasement of the climate as well as the global distortion of ecological system is to reduce the use of fossil fuels and developing the renewable energies. Especially, the solar conversion energy. In this context, research is focus on two areas. The first concerns the development of photovoltaic cells with high conversion efficiency. The second axis of research deals in the development of new processes and materials for the manufacture of low-cost photovoltaic cells. The renewable energies include the conversion of sunlight, wind, nuclear power and thermal earth heat into energy which could meet the most needs of energy in the world, the use of theses energies sources can diminish the emission of carbon to 60-80 % (Flavin and dawn; 123). The alternative renewable energy source such as geothermal, wind, hydroelectric and solar power are the extraordinary solution which donate electricity with little or no damaging effect to the environment.

Among all alternative sources of energy, solar energy is the most extensively renewable energy used recently across the world; the conversion of solar energy can be due by either thermal or photovoltaic (PV) systems. The PV panels for energy conversion were started by the discovering of photovoltaic effect by a French scientist called Becquerel in 1839, which has observed the photovoltaic effect on silicon crystal [3]. The first solar cell based on silicon were done by Ohl in 1941 using melt grown junction with an efficiency less than 1% [4], then in 1952 Kingsbury and Ohl cited a junction formed using helium ion bombardment and present an efficiency up to 1 % [5]. After that, Bell Laboratory fabricated the first crystalline

## Introduction

---

silicon solar cells in 1953, achieving 4.5% efficiency. In 1954, three American researchers, Gerald Pearson, Calvin Fuller and Daryl Chapin, discovered the use of silicon as a semiconductor and designed a silicon solar cell capable of achieving a conversion efficiency rate of 6% [7]. The efficiency based on this material increased progressively and its record reach 18 % in 1983 [8], recently an efficiency about 26.3% [9] of mono-crystalline silicon were reported which is near to their theoretical limit (33.7 %) [10].

In 2011, 87% of photovoltaic installations installed in the world consisted of mono or multi crystalline silicon. The success of this technology is limited by some factor namely, the silicon can't find in its pure state, it must extract from the silica, purified, shaped and the doped before being used, all of these operations increase the silicon cost, moreover this material have indirect band gap energy which make it not an optimal absorber for solar cells application. Therefore, the second generation of solar cells was emerged as the key to avoid the high cost production of silicon solar cells. The second generation of solar cell is called thin films solar cells technologies (TFSCs), in this technology the bulk material (silicon) is replaced by a thin film with a thickness about a micrometer, with a large choice of growth technique for different films composed the device, this allow the optimization of the solar cell stack properties for enhancing the device performances. Thin film PV is celebrated for the fabrication of low cost solar cells having a high efficiency record. In 1980, The Institute of Energy Conversion at University of Delaware develops the first thin film solar cell exceeding 10% efficiency using  $\text{Cu}_2\text{S}/\text{CdS}$  technology [11]. However, the instability due to Cu migration dictated the research of more stable materials. Thereafter, copper indium gallium diselenide (CIGS) and cadmium telluride (CdTe) have been appears as the most used and extensively studied in this solar cells generation. The recent recorded efficiency with these materials reached 20.8 and 19.6% respectively [12]. However, despite this reached efficiencies, these materials suffer from severe issues namely: selenium and cadmium toxicity and indium and gallium scarcity. Consequently, research of alternative materials composed of abundant and nontoxic elements is necessary and from there the apparition of kesterite thin films as a good alternative absorber to CIGS technology was appeared. New cells are already being developed in anticipation of the likely shortage of indium. However, replacing the cells with CIGS represents a real challenge as this absorbent is effective.

The quaternary chalcogenide compound copper zinc tin sulfide  $\text{Cu}_2\text{ZnSnS}_4$  (CZTS) has recently attracted much attention due to the fact that it is composed of earth-abundant and environmental friendly elements. Moreover, CZTS has optical and electronic properties

## Introduction

similar to that of CIGS, while having the advantage of being composed of just abundant elements (different to tellurium in CdTe and indium in CIGS technologies) and no one of their elements are toxic (unlike to cadmium in CdTe). Moreover, its basic constituents would be five times less expensive than those of the CIGS sector as seen in figure I.1. This confers to CZTS the status of a promising candidate, and a serious alternative for application as absorber layer in thin film solar cells.

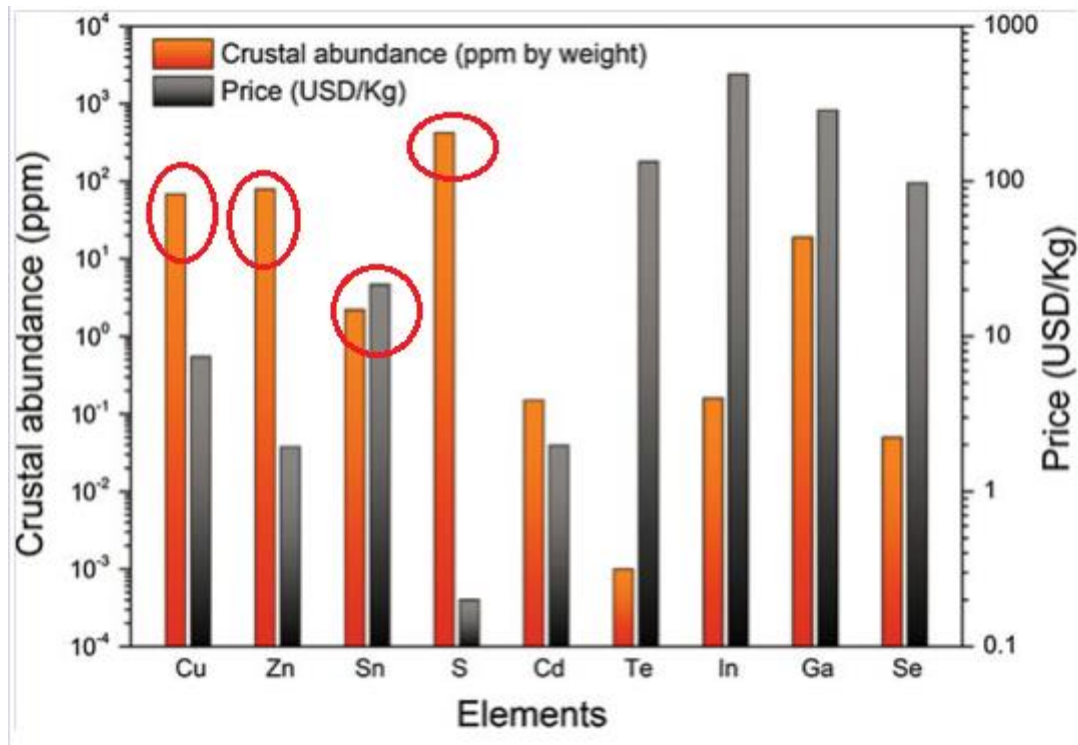


**Figure.1:** Abundance on earth's crust and cost of constituent elements for CIGS, CdTe, and CZTS (Se) absorber materials for thin film solar cells [13]

The objective of this thesis is the realization and characterization of CZTS absorber layer, CZTS/ZnS, and CZTS/CdS devices using a low cost and simple spray pyrolysis method. In the first part of this work we have tried to optimize the different deposition parameters leading to obtain high quality of CZTS active layers, which will use as absorber in the realized devices. In a second part, we have realized and characterized CZTS/ ZnS and CZTS/ CdS hetero-structures on which we have studied the effect of back contact nature and ZnO intrinsic layer on CZTS/ZnS properties and the effect of sulfurization temperature on the CZTS/CdS solar cell efficiency.

## Introduction

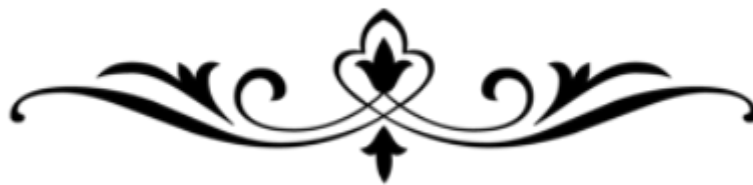
---

The thesis is organized as following:

- The first chapter is a bibliographic reminder of photovoltaic energy conversion and the different properties of CZTS material such as structural, electrical, optical properties, defects and secondary phases which can be present in kesterites system
- The second chapter is dedicated to the description of the experiments carried out during the thesis work: the deposit system, the experimental conditions used for developing the different materials and the characterization technique used for analyzing films and devices properties
- The third chapter regrouped with discussions the different results obtained by studied the effect of several experimental conditions on films properties such as: substrate temperature variation, deposition time, copper concentration, and zinc molarities effect.
- The fourth and last chapter was focused on the presentation with discussions of the obtained electrical properties of CZTS/ZnS and CZTS/CdS devices.

# Chapter I

## Photovoltaic energy and thin film solar cells



In this chapter, we will give an overview on the state of the art of photovoltaic energy, thin film solar cells history, and the different properties of kieserite's thin films and solar cells efficiency limits.

## **I.1 Physics of Photovoltaic**

Today, the sun is the most important and available source of renewable energy. Photovoltaic energy comes from the conversion of sunlight into electricity by semiconductor materials based on silicon or other material suitable for photovoltaic application such as CZTS, CIGS, CdTe, CuO, and SnS thin films. These photosensitive materials have the property of releasing their electrons under the influence of an external energy. Energy is provided by photons (components of light) that excite the electrons and release them, producing an electric current.

### **I.1.1 History of photovoltaic Effect**

In 1839, Alexander Edmond Becquerel have discovered the photovoltaic effect [3], this phenomenon allowed the conversion of light into electricity experimentally with metal electrodes and electrolytes, he discovered that the conductivity increase with the illumination. Then, in 1873, WILLOUGHBY SMITH observed the photoconductivity phenomena of selenium (Se) and in 1876 with his student WILLIAM G. ADAMS have observed that the illumination of a junction between selenium and platinum also has a photovoltaic effect, these two discoveries formed a foundation for the first selenium solar cell construction. After that, in 1883 an American called CHARLES FRITTS developed the first solar cells with an efficiency about 1 %. In 1904, EINSTEIN described the phenomenon and get the Noble Prize in 1921. Their theory were done experimentally by ROBERT MILLIKAN in 1932. Then in 1951, the first solar cell based on germanium was realized. later than, an American engineer called Charles Calvin Fuller created the first photovoltaic cell (PV) based on silicon with an important record efficiency equal to 6 %. In 1958, silicon solar panels were included on the American spacecraft Vanguard I. Hoffmann Electronics increased the efficiency to 14%. In the following 50 years, the global PV production has reached over 140 MW. The 21th century many workers were focused on the development of PV energy as well as solar panels in space, autonomous and regularly under illumination was a source of energy to power satellites.

### I.1.2 Physics of p-n junction

A p-n junction is the juxtaposition of n-type and p-type semiconductors, because of the gradient of majority carrier's concentration the holes from the p-side diffuse to the n-side and the electrons from the n-side diffuse to the p-side. This gives rise to a diffusion current across the junction. When an electron diffuses from the n-side to the p-side, an ionized donor is left behind on the n-side, which is immobile. Similarly, when a hole goes from the p-side to the n-side, an ionized acceptor is left behind in the p-side. Thus, the created zone without mobile carriers (ionized atoms) is called the space charge region (SCR) or depletion zone as seen in figure I.1. The difference of potential which formed when the two semiconductors are in contacts created an electric field  $\mathbf{E}$  which opposes the diffusion of the majority carriers. This electric field allows the migration of the holes towards the p-doped zone in the direction of and the electrons towards the doped zone n in the opposite direction to the field.

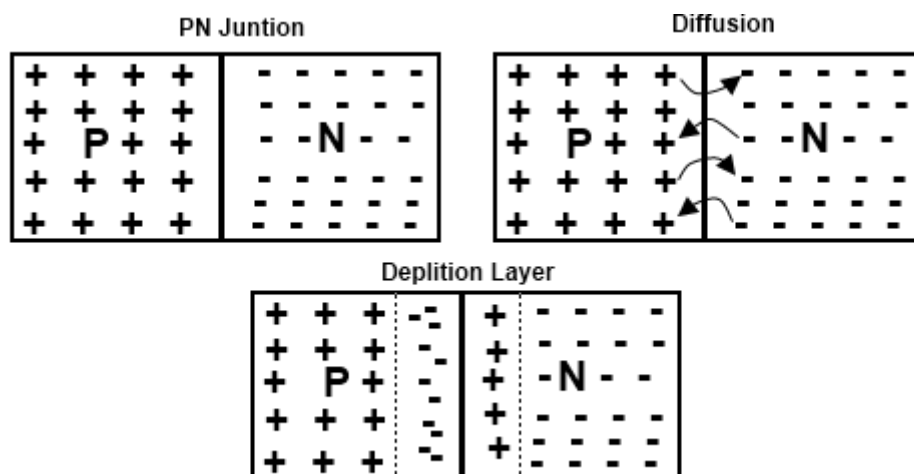


*Figure I.1. Formation of the depletion zone within a p-n junction*

The diffusion of carriers doesn't stop until the drift current balances the diffusion current, thereby reaching thermal equilibrium as indicated by an alignment of Fermi level ( $E_F$ ) which induces a curvature of the bands as well as a potential barrier  $V_D$  as seen in figure I.2.

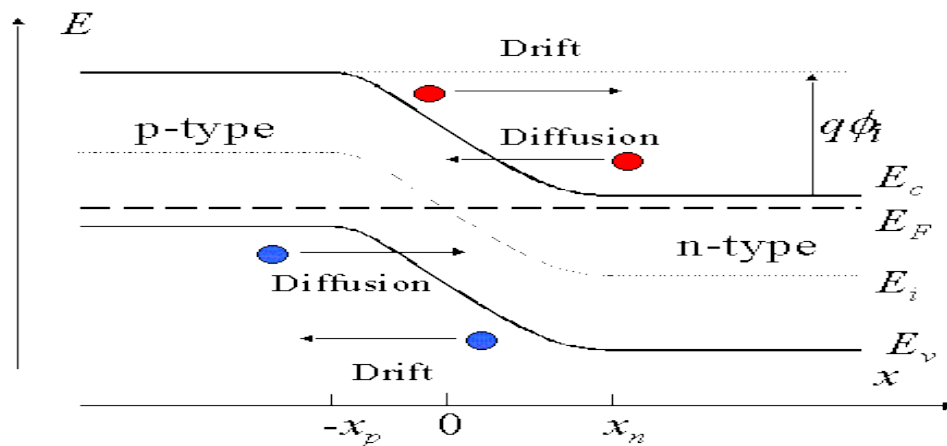


Figure I.2: Energy band diagram of a p-n junction at thermal equilibrium [4]

### I.1.3 Function of a solar cell

A solar cell is a device in their function principal it uses photovoltaic effect to convert the sun radiation into electricity when it is exposed directly to light (figure I.3).

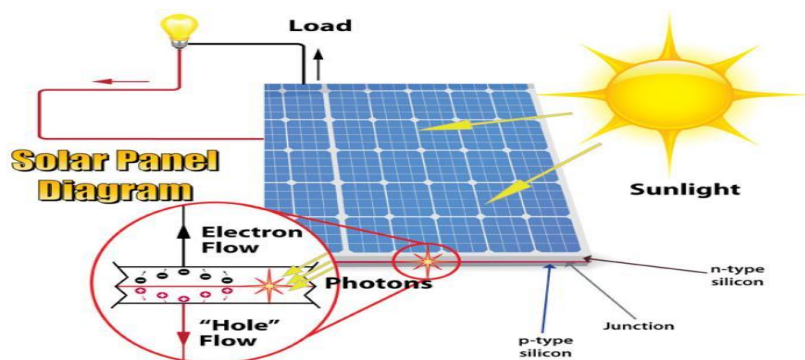


Figure I.3. Illustration of a PV function [12]

The production of electricity by PV photovoltaic system follows three mechanisms:

#### i. Absorption of photons

Solar radiation is an electromagnetic wave that can be assimilated to particles (photons) whose energy is inversely proportional to the associated wave length. The absorption of these photons is done by a semiconductor, called an absorber, having the capacity to absorb the energy ( $h\nu$ ) of the incident photons of energy greater than or lower to the energy of its gap ( $E_g$ ). The loss of energy in the absorber, known by Queisser Schottky limit is due to:

- If  $h\nu \geq E_g$ : the energy of the incident photons is enough to excite the electrons of the valence band and make them pass to the conduction band leaving a hole behind

them. The remaining energy ( $h\nu - E_g$ ) is lost by thermalization of the electron in the conduction band  $\sim 47\%$ , which has the effect of heating the material as seen

in figure I.4.

- If  $h\nu < E_g$ : the energy of the incident photons is less than the energy of the band gap ( $E_g$ ) of the material so the excited electrons can't jump the forbidden band and remain in the valence band. The transmission loss of lower photon energy  $\sim 18\%$ .

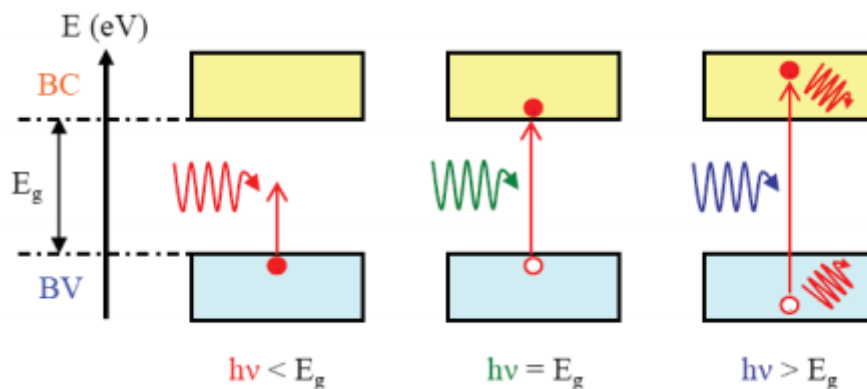


*Figure I.4. Absorption of different photons by a semiconductor material*

## ii. Separation of charges:

The separation of free charges (electrons and holes) and their extraction towards the collecting electrodes is achieved by p-n junction as described before.

## iii. Collection of porters

The electric field in the space charge region will separate the photo-generated carriers in this zone and extract them to the zone of majority carriers, where the probability of recombination is very low. The generated charges are collected and injected into an external circuit via the conductive electrodes.

### I.1.4 Current-Voltage characterization in the dark

I-V measurements in the dark are very useful for examining the properties of the metallurgical junction, the diode is a p-n junction connected to two contacts, the variation of the applied voltage across the hetero-junction creates a current varied exponentially with the voltage as shown in figure I.5. The current across the hetero-junction varies exponentially with the applied voltage and their variation can be described by the standard Schottky diode equation [13].

$$I (v) = I_s \left( \exp \left( \frac{qV}{KTn} \right) - 1 \right) \quad (I.1)$$

Where:  $I_s$ : saturation current,  $n$  is the ideality factor and  $V$  applied voltage,  $k$  is the Boltzmann constant,  $T$  is the absolute temperature,  $q$  is the elementary electronic charge.

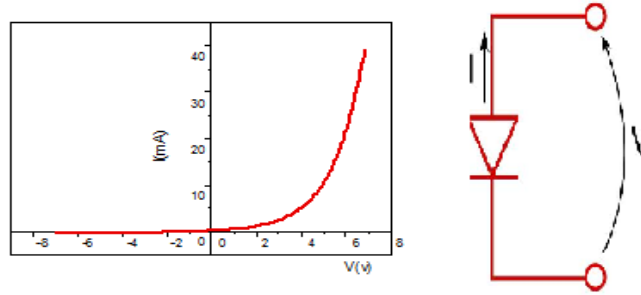


**Figure I.5:** *I-V characterization of CZTS/ZnS hetero-junction and the equivalent circuit of an ideal diode.*

The (I-V) characterization is an important tool to studied and analyzed the electrical properties of the diode by the determination of the diode parameters such as: ideality factor ( $n$ ), and saturation current ( $I_s$ ).

#### I.1.4.1 The ideality factor

The ideality factor “ $n$ ” is an important parameter of the diode which shows how close the realized diode to the ideal diode of Schottky. It is used to determine the dominate transport mechanism of the current across the hetero-junction. In the case of  $n$  equal to unity, the current is dominating by diffusion mechanism, whereas if  $n \leq 2$ , the recombination and generation in the depletion layer is the dominant one [14]. Whereas, when  $n > 6$  it has been suggested that the interface states contribute mainly in the transport [15,16]. The ideality factor ( $n$ ) was calculated from the variation of the slope of the linear portion of  $\ln(I)$ - $V$  as shown in figure I.5 and it can be expressed as the following formula:

$$n = \frac{q}{kT} \left( \frac{dV}{d(\ln I)} \right) \quad (I.2)$$

#### I.1.4.2 Current saturation ( $I_s$ )

The saturation current ( $I_s$ ) is activated by the activation energy  $E_A$  and is represent the diode leakage current in the absence of light.  $I_s$  is due to the diffusion of minority carriers in quasi

neutral region (electron in the n region and holes in p region) and refer also to the generation of free carriers in the space charge region. Saturation current and ideality factor were determined from the semi logarithmic plot of the current as function of applied voltage as seen in figure I.6.

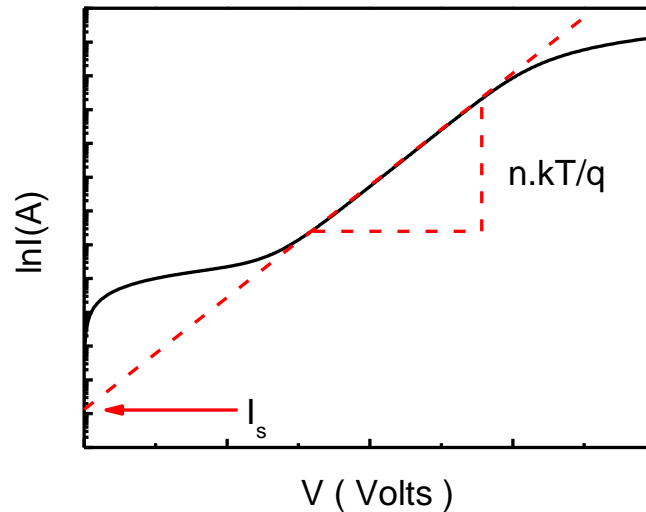


*Figure.I.6. Semi logarithmic scale of the current as function of applied voltage of a diode*

### I.1.5 I-V characteristics under-illumination

The illumination of a solar cells caused the generation of pairs electron-hole which give a rise to the photo-generated current ( $I_{ph}$ ). The generation of current can divide in two processes: firstly, the generation of pair's electrons and holes by the absorption of the coming photons, if the photon energy is greater than the band gap energy of the semiconductor. The second process is the collection of these carriers by the load or the conductive electrodes of the cell. Figure I.7 illustrate the I-V characterization of a CZTS/ZnS solar cells and the equivalent circuit of an ideal solar cell without shunt and series resistance. The photo-generated current has the effect of shifting down the I-V characteristics as seen in Figure I.7. When a cell is light irradiated the output current became as the following expression:

$$I(v) = I_s \left( \exp \left( \frac{qV}{kTn} \right) - 1 \right) - I_{ph} \quad (I.3)$$

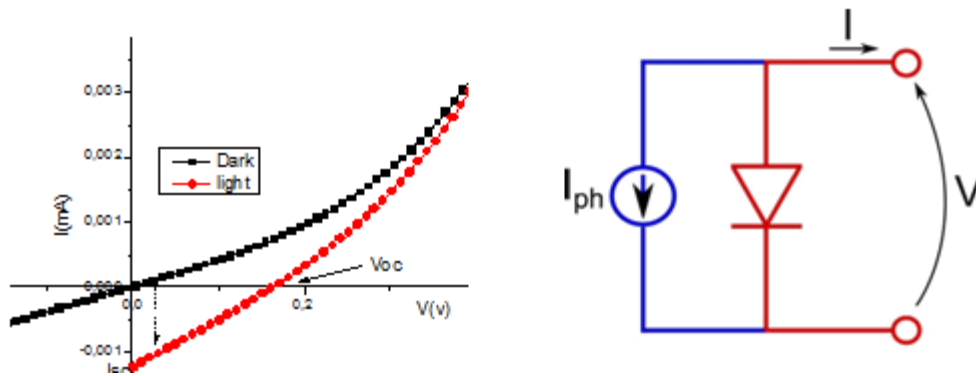


*Figure.I.7. I-V curve of CZTS based solar cells and an ideal equivalent circuit*

### I.1.5.1 Open circuit voltage ( $V_{oc}$ )

The first characteristic parameter of a PV cell is the open circuit voltage ( $V_{oc}$ ). Which represent the maximum voltage that the cell can generate when the terminals are not connected to any load (the current is equal to zero).

### I.1.5.2 Short-circuit current ( $I_{sc}$ )

The short-circuit current ( $I_{sc}$ ) is the second important characteristic parameter describing a photovoltaic cell. The  $I_{sc}$  is the maximum current which passes through the cell when the device is short-circuited. The short-circuit current is due to the generation and collection of light-generated carriers.

### I.1.5.3 Fill factor (FF)

The "Fill Factor", more commonly known by its abbreviation (FF). The fill factor is used to qualify the quality of the PV cell. The fill factor is calculated from (I.4). FF is the ratio between the maximum powers supplied by the cell to the product of  $V_{oc} \times J_{sc}$ . This report must have a value as close as possible to 1. Graphically, the FF is a measure of the "squareness" of the solar cell and is also the area of the largest rectangle which will fit in the I-V curve as seen in figure I.8.Fill factor expression in written as eq. (I.4),

$$FF = I_{mp} V_{mp} / J_{sc} V_{oc} \quad (I.4)$$

$I_{mp}$  and  $V_{mp}$  are the maximum current and voltage supplied by the cell respectively.

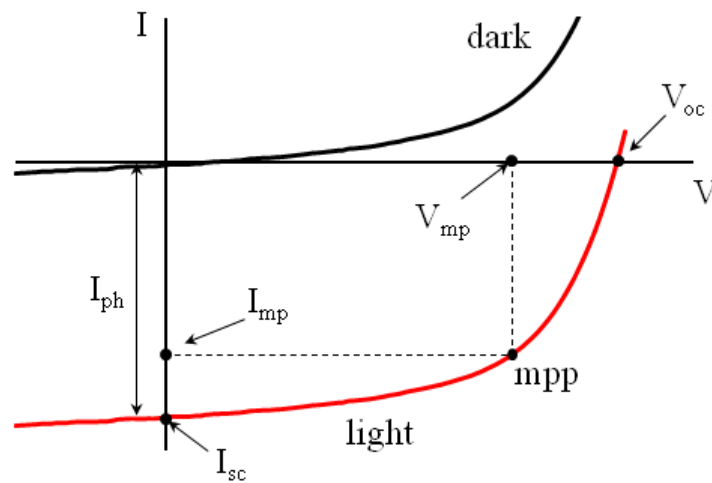


**Figure.I.8.** Current-voltage characteristics showing the method for calculating *FF*

#### I.1.5.4 Photovoltaic efficiency ( $\eta$ )

After the extraction of  $V_{oc}$ ,  $J_{sc}$ , and *FF* it is possible to determine the efficiency of the realized solar cell. This is the most important parameter. Since, it makes possible to evaluate the performance of the fabricated PV cell. The efficiency represents the relation between the generated power by the cell ( $P_{max}$ ) and the incident power ( $P_{in}$ ) of the radiation illuminating the cell. It is calculated according to the following formula:

$$\eta = P_{max}/P_{in} \quad (I.5)$$

Where :  $P_{max} = V_{oc} I_{sc} FF$  , the expression (I.6) of the efficiency became;

$$\eta = V_{oc} I_{sc} FF / P_{in} \quad (I.6)$$

#### I.1.6 Losses in solar cells

In a solar cell many reasons can cause the loss in their performance such as optical or electrical losses as described below:

1. **Optical losses:** Optical losses are due to non-absorption, thermalization, reflection, and transmission. The non-absorption happens when the energy of the incident photon is lower than the gap energy of the absorber material.
1. **Thermalization:** When the coming photon energy is greater than the gap energy of the absorber, the excess energy is dissipated as heat, this heat increases the temperature of the solar cell which increases the reverse saturation current due to the increase in carriers

concentration and diffusion length of minority carriers which caused a decrease of the open circuit voltage value ( $V_{oc}$ ) [17].

2. **Reflection loss:** The reflection is due to the blocking of the light by the top contact, reflection from the top surface and reflection from the back contact without proper absorption [18].
3. **Transmission loss:** This is due to the small thickness of cell and the low absorption coefficient of the absorber layer.
4. **Area loss:** This loss is due to metal grid design or by metal electrode coverage [19]. These type of optical losses can be reduced by using an antireflective coating (ARC) of quarter wavelength thick on the top surface.

## II. Electrical loss

1. **Collection losses:** These losses are due to surface and bulk recombination at metal or semiconductor contact and recombination in depletion region. These recombination losses mainly affect the open circuit voltage. Impurities, crystalline defects and incomplete chemical bond on semiconductor acts as traps for photo-excited carriers, and recombination on these traps cause the reduction of photocurrent. The reduction in the concentration of impurities and defects can increase the diffusion length of minority carriers and this can decrease the recombination losses in a solar cell [20].
2. **Recombination losses:** can be reduced by creating a heavily doped metallic region which acts as back contact, by chemical treatment of the materials or by using a thin layer of passivating oxides.
3. **Series resistance ( $R_s$ ):** The Photovoltaic cell is never perfect. To properly translate the behavior of a cell PV, two resistors are added on the equivalent diagram (Figure I.6).

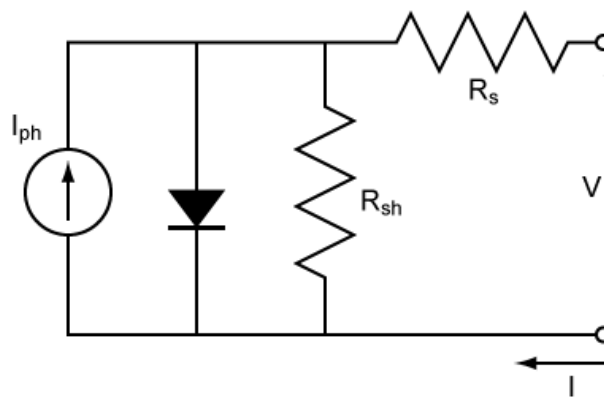


*Figure I.9. Real solar cell with the resistors  $R_s$  and  $R_{sh}$*

The first important loss in solar cells is because of the series resistance which regroups the back and front metal contacts resistances, the semiconductors bulk resistances and the interfaces resistance. To obtain a high record efficiency the series resistance must be as low as possible because of their negative effect on the photo-generated current.

#### 4. Shunt resistance (Rsh)

The second and important loss in solar cell is due to the shunt resistance (Rsh) which is due mainly to the presence of defects in the bulk of semiconductors and at interfaces. It is estimated from the reverse bias of the I-V characteristics. Shunt resistance reduces the open circuit voltage (Voc). It should be as high as possible in order to prevent losses [21] which are recognized in parallel with the diode and the generated current as seen in figure I.6.

#### I.1.7 Band discontinuity at hetero-junction interface

In a hetero-junction the two semiconductors have different band gap energies  $E_{g1}$  and  $E_{g2}$ , assuming that  $E_{g1} > E_{g2}$ . Figure I.10 shows the band diagrams of this hetero-junction, however the vacuum level is parallel to the band edges and is continuous, while because of the difference in gap energies of the two semiconductors will occur a discontinuity in conduction ( $\Delta E_c$ ) and valence band edges ( $\Delta E_v$ ). This electronic band diagrams determined from the band gap energies, and the affinity  $\chi_1$  and  $\chi_2$  of the two semiconductors [22].

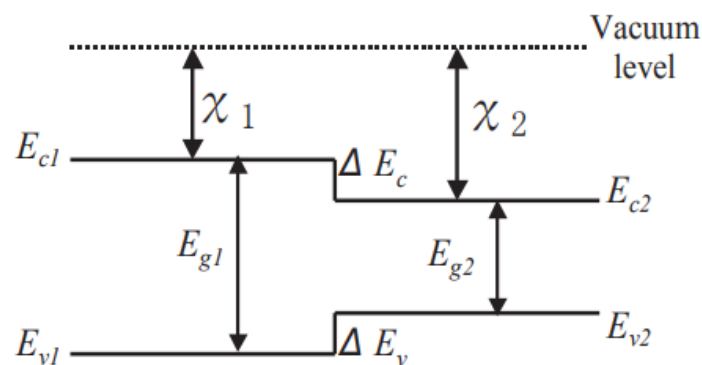


*Figure I.10. P-n hetero-junction band diagram [22]*

Because of the difference electron affinity  $\chi_1$  and  $\chi_2$  of the two materials, we can have two types of band discontinuities or hetero-junction interfaces as shown in figure I.11, we could have either type I or type II of interfaces. However, while conduction-band minimum (CBM) of material 1 is above that of material 2, and valence band maximum (VBM) of

semiconductor 1 is below that of the second, and then the band alignment is of type I. On the other hand, if the both of CBM and VBM for material 1 are below that of material 2, the band alignment is the type II.

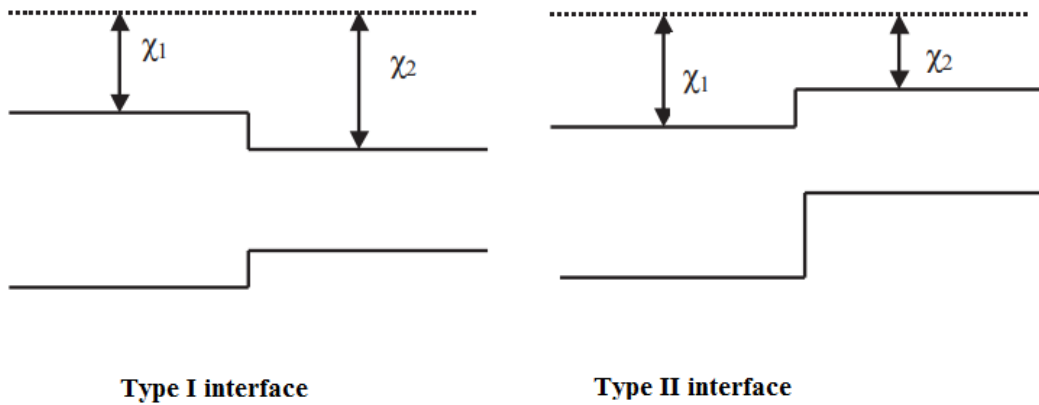


*Figure I.11. Type I and type II hetero-junction interfaces [22]*

In the equilibrium and when the voltage is applied, the band diagram will become as shown in figure I.12. A band bending is occurring in the depletion regions which reflects the formation of an electric field because of the electrostatic potential. In equilibrium the Fermi level flattens and becomes constant through the device. The vacuum level is bending also because of the electric field response. The presence of band offset between two semiconductors leads to the formation of either a spike or a cliff depending on the sign of the offset, as seen in figure 1.12. (a) and (b). If the band offset produces a cliff, the probability of the recombination of majority carriers at the interface is increased, and the flat band condition is achieved at a bias smaller than  $E_g/q$  of the absorber [22x]. Band alignment with a moderate spike is quite optimal, although the presence of a large spike decreases the flow of the minority carrier.

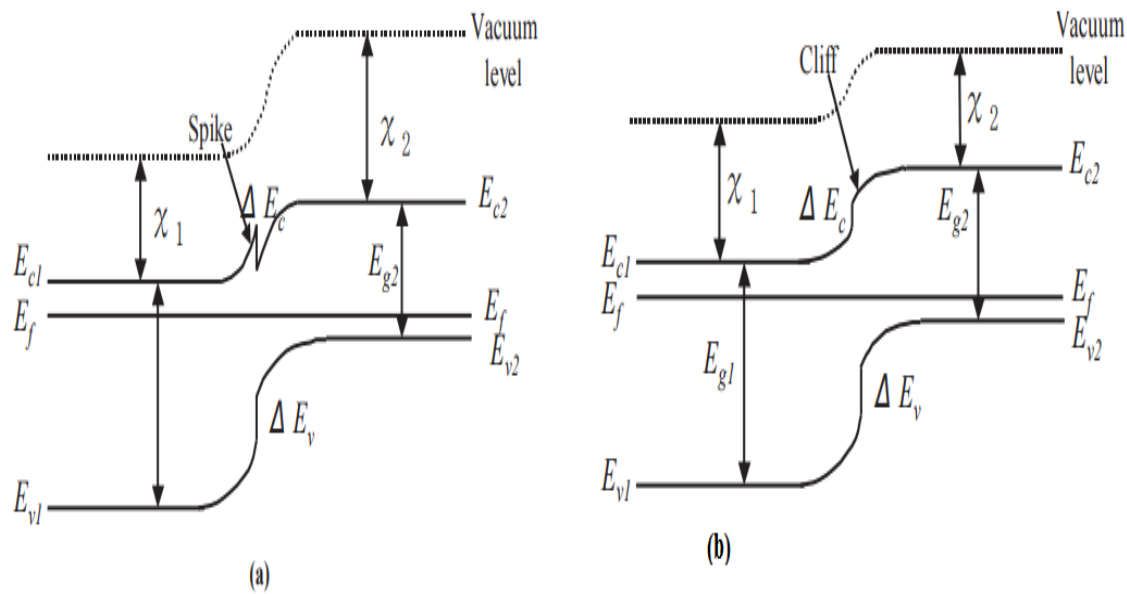


**Figure I.12.** Band alignment of hetero-interface considering the electrostatic potentials(a): type I interface. (b): type II interface [22]

## I.2 Thin-film solar cells

A thin-film solar cell (TFSc) is the name given to the second generation of solar cells, which is realized by the deposition of one or more thin layers of photovoltaic material on a substrate (glass, plastic or metal). Thin-film solar cells are commercially used in several technologies, including amorphous thin-film silicon (a-Si, TF-Si), cadmium telluride (CdTe), and copper indium gallium selenide (CIGS). In this technology of solar cells, the film thickness varies from a few of nanometers (nm) to tens of micrometers ( $\mu\text{m}$ ), different to the first generation of solar cell which uses silicon wafers with a thickness up to 200  $\mu\text{m}$ , the other drawback of silicon is their indirect band gap energy, however the probability of absorption of a photon is much lower than the semiconductor with direct band gap energy, whereas semiconductor used in thin film solar cells have direct band gap energy and characterized by a high absorption coefficient, and low cost of fabrication.

### I.2.1 History of thin film solar cells

In 1963, Cusano reported 6% efficiency polycrystalline thin-film solar cells consisting of  $\text{Cu}_{2-x}\text{Te}$ -CdTe hetero-junctions [23]. In 1969 Andirovich et al. reported a thin-film solar cell consisting of a hetero-junction between n-type CdS and p-type CdTe which was deposited on  $\text{SnO}_2$ -coated glass [24]. Even though, the efficiency of this cell was only 1% at that time. In

1974, Wagner et al. fabricated a heterojunction for photovoltaic application, it consisted of an n-type CdS window layer which was vacuum-deposited on a p-type CuInSe<sub>2</sub> single crystal. In the following year, the same group reported a solar cell which had the same hetero-structure and exhibited a high value of efficiency about 12% [25]. In 1976 Kazmerski et al. developed the first thin-film solar cell consisting of CuInSe<sub>2</sub> with an efficiency of 4–5% [26]. In 1978 Konagai et al. developed a 13.5% efficiency solar cell consisting of an n-type (Ga, Al) As/p-type GaAs hetero-junction [27]. Five types of thin-film solar cells achieved an efficiency higher than 10%, as listed in Table I.1. All of these solar cells are consisted of semiconductor thin films which are characterized by an optimal direct band gap energy. They were all invented several decades ago (except for the last one) and the first three were brought into commercial use after intensive research and development efforts. Recent progression CZTS-based thin-film solar cell technology is remarkable, despite the fact that the semiconducting properties of CZTS and its photovoltaic effect were not known of until 1988. Gunawan and coworkers at IBM Thomas J. Watson Research Center have succeeded in achieving over 10% efficiency CZT (S, Se) thin-film solar cells using solution-based processing in this decade [28-29].

<i>Absorber</i>	<i>CdTe</i>	<i>CIGSe</i>	<i>CIGS</i>	<i>GaAs</i>	<i>CZTSSe</i>
<i>E<sub>g</sub>(eV)</i>	<i>1.5</i>	<i>1.12</i>	<i>1.5</i>	<i>1.43</i>	<i>1.13</i>
<i>Efficiency(%)</i>	<i>20.4</i>	<i>20.3</i>	<i>12.9</i>	<i>28.8</i>	<i>12.6</i>
<i>Laboratory</i>	<i>First solar</i>	<i>ZSW</i>	<i>Sulfurcell,</i> <i>Shinshu U.</i>	<i>Alta Device</i>	<i>IBM Watson</i> <i>Research</i> <i>Center</i>

**Table I.1:** Five absorber layers that have been used for thin film solar cell with highest efficiency[30]

### I.2.2 Possible configuration of solar cell

A thin film solar cell has two possibilities of fabrication from top to down or down to top. the two configurations are called superstrate and substrate as seen in figure I.10. The different between them is that, in superstrate configuration the light goes through the superstrate

material before reaching the p-n junction, while in substrate configuration the light reaches the p-n junction without going through the substrate so why we can use different type of substrate, this is the advantage of the first configuration on which we can use different types of substrate.

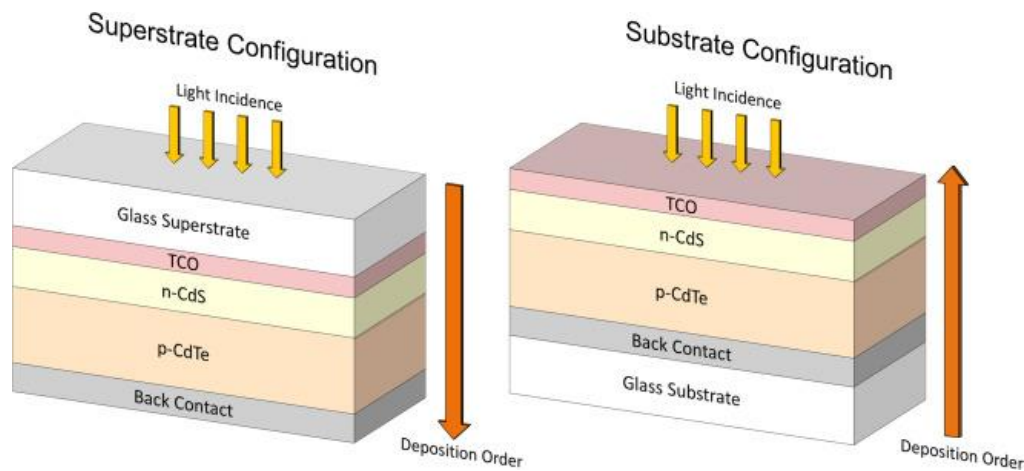


*Figure 1.13: Possible configuration of thin film solar cells*

### **I.2.3 Thin film solar cells technologies**

#### **I.2.3.1 Amorphous silicon (a-Si)**

PV cells based on amorphous silicon are the least expensive cells on the market with theoretical conversion efficiency about 25% whereas in laboratory their record efficiency reaches 10.7% at Oerlikon Solar Lab [31] with a simple junction, whereas 13.4% is achieved in a-Si:H/ $\mu$ c-Si:H/ $\mu$ c-Si:H triple-junction [32].

#### **I.2.3.2 Cadmium Telluride (CdTe)**

Cadmium telluride (CdTe) has long been used as an optimal candidate for thin-film PV applications [33], because it is a chemically stable semiconductor compound with large absorption coefficient ( $>10^4 \text{ cm}^{-2}$ ) and a direct band gap energy about 1.45 eV [34]. CdTe can be p or n type semiconductor but in solar cells it used as p type semiconductor. The first PV cell based on CdTe with a record efficiency equal 21.5% achieved in February 2015 [35]. Despite the development made in the CdTe technology by achieving cost-effective, the toxicity of cadmium which risk to the environment and humans and the scarcity of tellurium are the drawback of the use of this material in solar cell, the development of this type of thin films solar cells is limited by the searching of abundant and no toxic material.

### I.2.3.3 Cu(InGa)Se<sub>2</sub> (CIGS)

Chalcopyrite semiconductor compounds such as copper indium diselenide (CuInSe<sub>2</sub>), copper indium disulfide (CuInS<sub>2</sub>) and copper gallium indium diselenide (CuGa<sub>1-x</sub>In<sub>x</sub>Se<sub>2</sub>), have direct band gaps energies with high absorption coefficients, making them suitable material for PV application. In 1976 Kazmerski *et al.* [26], fabricated the first thin film solar cells CdS/CuInSe<sub>2</sub> with an efficiency equal to 4.5 %. After that, gallium (Ga) was incorporated in CuInSe<sub>2</sub> to make Cu(InGa)Se<sub>2</sub>. The quaternary compound Cu<sub>2</sub>InGaSe<sub>4</sub> (CIGS) is the most successful chalcopyrite absorber with a record efficiency of 20.8% [36]. CIGS thin films have been produced using different deposition methods. CIGS solar cells realized following the substrate configuration starting with the deposition of molybdenum layer as the back contact deposited on glass substrate succeeding by the deposition of the absorber p type CIGS thin films. Then the deposition of n-CdS buffer layer which formed the hetero-junction with CIGS, then, a thin ZnO intrinsic layer and finally the deposition of aluminum doped ZnO thin film as optical window in front contact. Similar to the CdTe technology, indium scarcity represents an issue in CIGS PV applications, where the high price of indium impacts cell and module costs. Figure I.14 show the configuration of the three technologies of thin film solar cells (CdTe, CIGS and, a-Si)

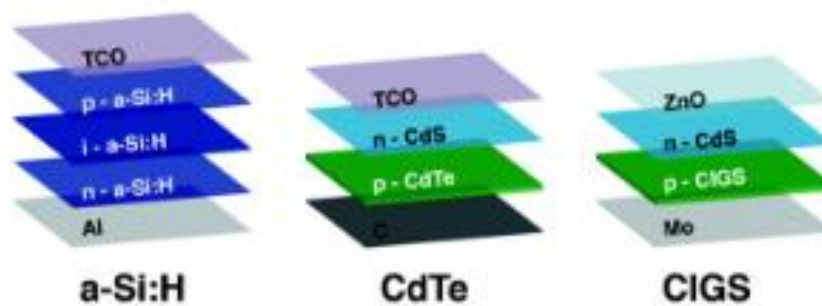


*Figure.I.14 Thin films solar cells technologies*

The high efficiency obtained by the most promise absorber material used in thin film solar cells are resumed in Table I.1

## I.3. Cu<sub>2</sub>ZnSnS<sub>4</sub> solar cells

### I.3.1. Introduction

Recently, a new material belongs to kesterite group called Cu<sub>2</sub>ZnSnS<sub>4</sub> (CZTS) has been proposed to replace CIGS and CdTe which are contain toxic and scarcity elements. The CZTS semiconductor material has a direct band gap energy. Moreover, it's absorption coefficient is

greater than  $10^4 \text{ cm}^{-1}$  [37.38], intrinsic p doped material, contain just abundant and friendly elements to the environment. The different properties of CZTS are described with details in the following paragraphs.

### I.3.2 A material based on friendly and abundant elements in nature

CZTS is a metallic chalcogenide composed of copper (Cu), zinc (Zn), tin (Sn), and sulfide (S). These elements are widely present in the earth's crust, particularly in contrast to the indium and gallium compounds that form the CIGS. The indium (In) is a rare element with an estimated abundance in the earth's crust making it a very expensive metal. Gallium (Ga) is a metal difficult to produce because it is only in the state of trace amounts in aluminum and zinc ores. Additionally, the metals composing the CZTS are between 25 and 400 times cheaper than indium and gallium. Beyond the price which represents only a small part of the cost of PV panels, these 2 elements are already widely used in the electronics industry, which could procurement for a very large scale PV industry development. However, the abundance and low prices of copper, zinc, and tin make this material very interesting for the PV conversion in the recent years. Figure I.15 illustrate the content and the world trading price of the elements used as light absorbers for thin film solar cells.

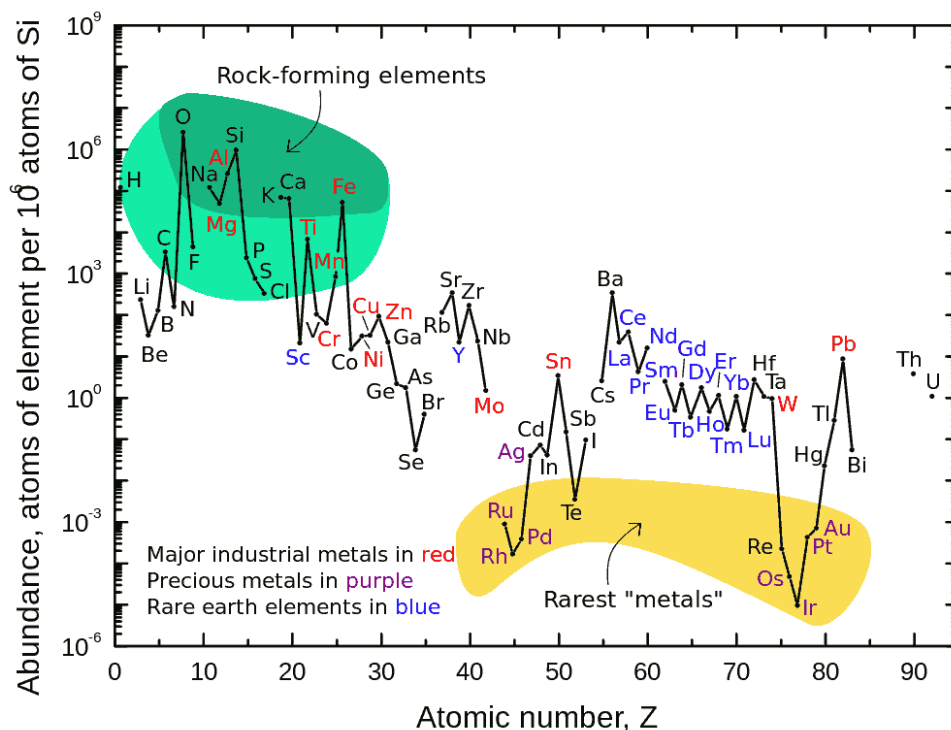
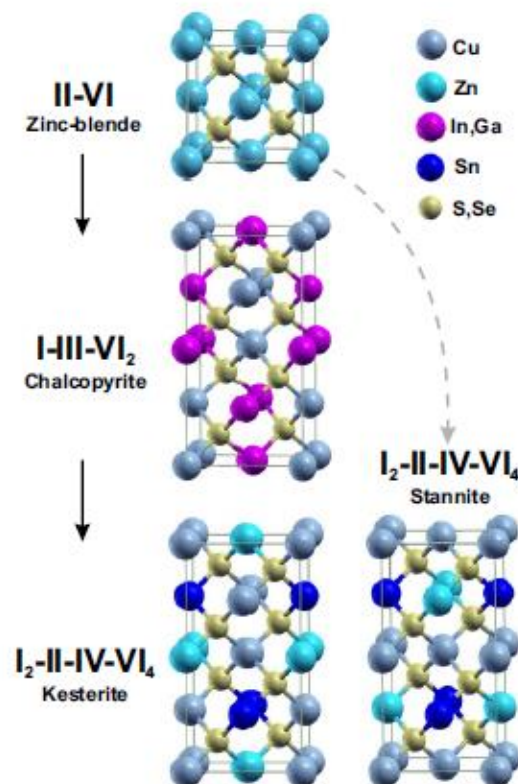


Figure I.15: Relative abundance of the elements [39].

### I.3.3 Fundamental properties

#### I.3.3.1 Crystal structure and polymorphous

The  $\text{Cu}_2\text{ZnSnS}_4$  is a quaternary compound belongs to  $\text{I}_2\text{-II-IV-VI}_4$  group, derived from II-VI compounds such as zinc-blende ( $\text{ZnS}$ ). By replacing atoms of group-II with atoms of group-I and one group-III atoms, we obtain a I-III-VI<sub>2</sub> semiconductor such as the Cu-based chalcopyrite  $\text{CuInS}_2$  (CIS). Then, two atoms of indium are replaced by an atom of zinc and a tin atom whereas the copper atoms always occupy the same positions by replacing half of the In atoms with group-II atoms such as Zn and the other half with group-IV atoms such as Sn, we can produce  $\text{Cu}_2\text{ZnSnS}_4$ . Similarly, the  $\text{Cu}_2\text{ZnSnSe}_4$  compound can be derived from  $\text{CuInSe}$ . Figure I.16 illustrates the derivation of CZTS from ZnS. This material can crystallize under either stannite [40] or kesterite structure [41]. Chen et al. [42] has reported that the energy between this two structure is equal to 3meV/atom. According to the theoretical calculations DFT showed that the kesterite phase is more stable than the stannite phase, Chen et al. [42] have reported that in kesterite structure the strain energy is lower than that of stannite. The difference between the two structure is the location of copper(Cu) and Zinc(Zn) atoms in the crystallographic structure as illustrated in figure I.16.



**Figure. I.16:** Crystal structures of zinc-blende, chalcopyrite, kesterite and stannite [45].

The both structures are tetragonal. These two structures are not differentiable by X-ray diffraction. Further, Schorr et al. [43] has experimentally confirmed the DFT results by neutron diffraction. In addition, a partial disorder of zinc and copper in the plane (001) for  $z = \frac{1}{4}$  and  $a = \frac{3}{4}$  has also been demonstrated. This phase is called disorderly kesterite. Scragg et al. have shown that the transition temperature order kesterite disorder is close to 260°C [44].

### I.3.3.2 Secondary Phases in CZTS thin films

Because of the constitution of CZTS material with the combination of four elements the probability of the formation of secondary phases is higher than in other materials. Experimentally, it's difficult to grow pure and single phase of kesterite CZTS (Se), during the synthesizing of CZTS film must take on account the composition for avoiding the formation of various binary and ternary phases including  $Zn_xS$ ,  $Cu_xS$ ,  $Sn_xS$  and  $Cu_xSnS$  which can form easily during the growth of CZTS thin films that can be refer to the complexity of this quaternary compound as seen in figure I.17. Those phases affect strongly on the CZTS thin films properties and on related devices performance. Generally,  $Cu_xS$  phase was detected in CIS alloys also as a result of Cu rich condition in the preparation of CZTS, and enhance the crystallization of the film [46], the enhancement of the crystallization was reported in co evaporated CZTS [47] but in contrary in [48], for CZTS thin film grown via sol gel and electrochemical deposition. Furthermore, a trend opposite to CIS was also reported by katagiri group [49] for CZTS grown via co-sputtered precursors in which an enhancement of the morphology of CZTS was observed with the decreasing of copper content. However, the two secondary phases Cu-S and Cu-Sn-S compound are highly conductive [50] and can create shunting path in the final cell and can lowering the band gap energy of CZTS thin films. While ZnS secondary phases have a high probability for formation under Cu-poor and Zn – rich condition and it was observed in several works [51.52]. This secondary phase was observed even in best solar cells in the literature [52]. As well as the effect of this phase may be not detrimental of the cell performance. The other secondary phase is tin sulfide SnS phase which was detected and reported by some authors [53], no negative effect on the cell performance was reported. To reach a high performance of CZTS devices the control of these secondary phases is necessary, the phase diagram of the system has shown that a single-phase CZTS material can be formed only in a very small region as seen in figure I.17.

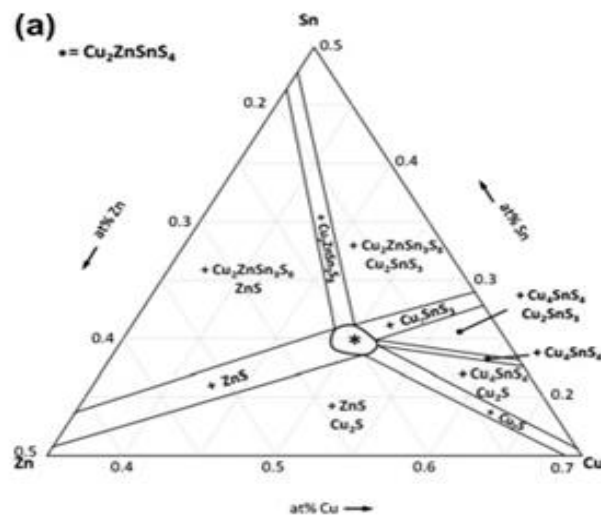


Figure I.17: Ternary phase diagrams of CZTS [54]

### I.3.3.3 Detecting secondary phases in CZTS

X-ray diffraction (XRD) and Raman Spectroscopy are generally used for detecting the different phases in CZTS sample.  $\text{Cu}_x\text{S}$  phases, as well as  $\text{Sn}_x\text{S}_y$  compounds ( $\text{SnS}$ ,  $\text{SnS}_2$  and  $\text{Sn}_2\text{S}_3$ ) can be easily identified by X-ray diffraction, showing diffraction peaks clearly different from those of CZTS. However, as shown in Figure I.18 [55],  $\text{ZnS}$  and  $\text{Cu}_x\text{SnS}_{x-1}$  (CTS) phases are difficult to be distinguished from CZTS phase.

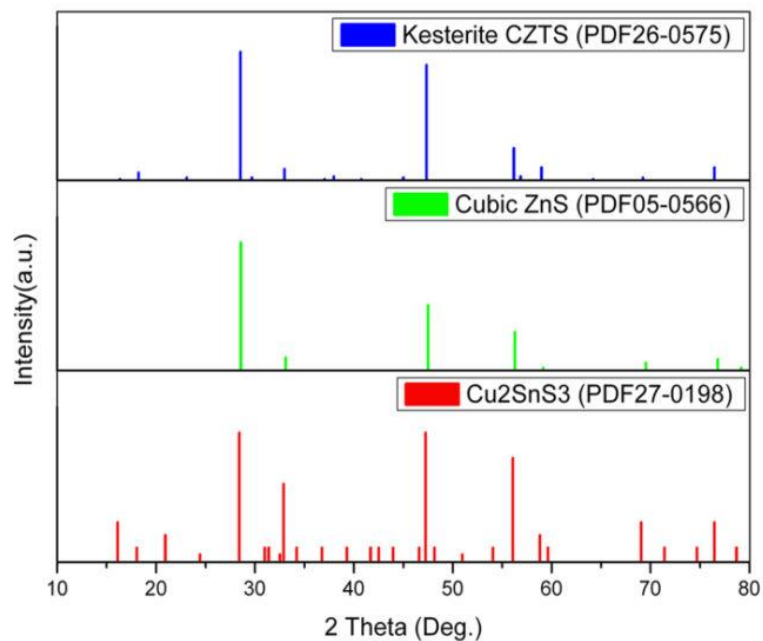


Figure I.18: X-ray diffraction spectra of kesterite  $\text{Cu}_2\text{ZnSnS}_4$ ,  $\text{Cu}_2\text{SnS}_3$ , and  $\text{ZnS}$  showing overlap of the main peaks [55].

Indeed, the most probable ZnS cubic phase shows a crystal structure very similar to CZTS. Therefore, ZnS diffraction pattern is superimposed to the CZTS one. Among CTS compounds, only the orthorhombic  $\text{Cu}_3\text{SnS}_4$  phase can be detected in CZTS samples by XRD, whereas problems similar to ZnS are found for  $\text{Cu}_2\text{SnS}_3$  compounds: because of their similar symmetry and lattice constant with CZTS, the diffraction peaks of both cubic and tetragonal  $\text{Cu}_2\text{SnS}_3$  are superimposed to those of CZTS phase [56].

The different crystallographic parameters of CZTS calculated using XRD such as interrelated distance, intensity, (h k l) plane, and peaks positions are reports in table I.4.

d(Å)	I/I <sub>0</sub> (%)	(hkl)	2θ(degree)
5.421	1	002	16.338
4.669	6	101	18.205
3.847	2	110	23.101
3.126	100	112	28.530
3.008	2	103	29.675
2.713	9	200	32.966
2.426	1	202	37.025
2.368	3	211	37.966
2.212	1	114	40.758
2.013	2	105	44.996
1.919	90	220	47.331
1.636	25	312	56.177
1.618	3	303	56.856
1.565	10	224	58.969
1.45	1	314	64.177
1.365	2	008	69.229

**Table.I.2.** crystallographic properties of CZTS [57]

Raman spectroscopy is an alternative way to detect possible secondary phases present in CZTS material. A clear Raman spectrum of a  $\text{Cu}_2\text{ZnSnS}_4$  sample (measured on a monograin powder) showing all the CZTS characteristic peaks is reported in [58] and it is shown here in Figure I.19. A list of the Raman peaks of other interest phases are reported in Table I.3.

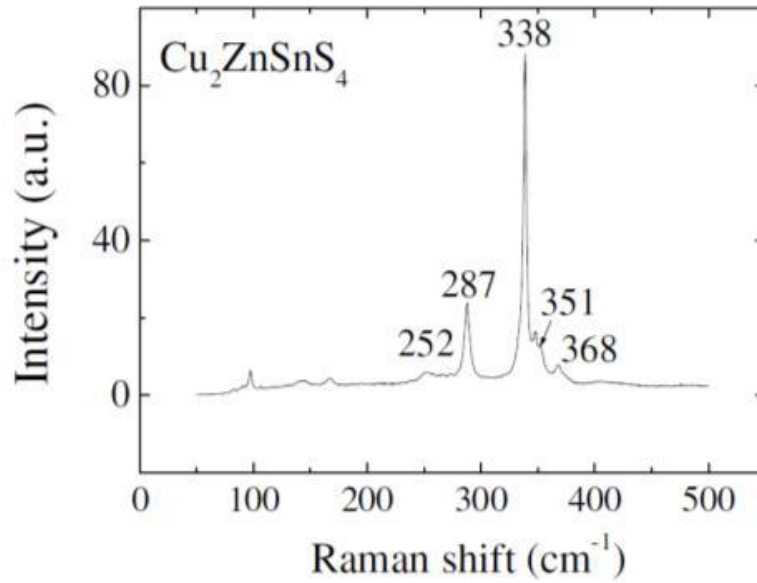


**Figure.I.19:** Typical Raman spectrum of a  $\text{Cu}_2\text{ZnSnS}_4$  monograin powder [58].

	<i>Raman Shift(cm-1)</i>	<i>Reference</i>
<i>CZTS</i>	338,287,351,368,257	[58.59]
<i>ZnS</i>	352,75	[60]
<i>Cu<sub>2</sub>SnS<sub>3</sub>(tetragonal)</i>	337,352,297	[61.62]
<i>Cu<sub>2</sub>SnS<sub>3</sub>(cubic)</i>	303,356	[61.62]
<i>Cu<sub>3</sub>SnS<sub>4</sub></i>	318,295,348	[61.62]
<i>Cu<sub>2-x</sub>S</i>	476	[59]
<i>SnS</i>	160,190,219	[63]
<i>Sn<sub>2</sub>S<sub>3</sub></i>	307	[63]
<i>SnS<sub>2</sub></i>	215,315	[63]

**Table.I.3.** Raman Shift of CZTS material and related secondary phases[58]

#### I.3.3.4 Point defects in the CZTS

The knowledge of defects in a semiconductor used as solar cell absorber material is very important for improving and controlling the efficiency of related solar cells. Density functional theory calculations can help to access potential defect states, and support the interpretation of experimental findings. In CZTS material, various intrinsic point defect can form including antisite defects ( $\text{Cu}_{\text{Zn}}$ ,  $\text{Zn}_{\text{Cu}}$ ,  $\text{Sn}_{\text{Zn}}$ ,  $\text{Zn}_{\text{Sn}}$ , and  $\text{Cu}_{\text{Sn}}$ ), vacancies ( $\text{V}_{\text{Cu}}$ ,  $\text{V}_{\text{Zn}}$ ,  $\text{V}_{\text{Sn}}$ , and  $\text{V}_{\text{S}}$ ) and interstitial defects such as ( $\text{Cu}_i$ ,  $\text{Zn}_i$ ,  $\text{S}_i$ , and  $\text{Sn}_i$ ). These defects can be acceptor or

donor, can be situated either in shallow or deeper level within the band gap energy, and act as recombination center which affected on the opt-electrical properties of the film and the performance of the device. Theoretical calculation of the formation of defect in kesterite compound where reported in [64], the value of the intrinsic defect ionization levels within the band gap energy of different defect which may appear in CZTS is reported by Chen et al. [65] are resumed in figure I.20 [55]. Further,  $V_{Cu}$  vacancy is the shallow acceptor defect, it is located just above the valence band, whereas  $Cu_{Zn}$  antisite is situated in a level with an energy formation equal to 0.12 eV with the lowest formation energy, that result was confirmed experimentally in [66,65]. Moreover, there are self-compensated defect pair complexes such as  $[Cu_{Zn}^- + Zn_{Cu}^+]$  for Cu-rich/Zn-poor growth condition and  $[V_{Cu}^- + Zn_{Cu}^+]$  for Cu-poor/Zn-rich condition in CZTS [65].

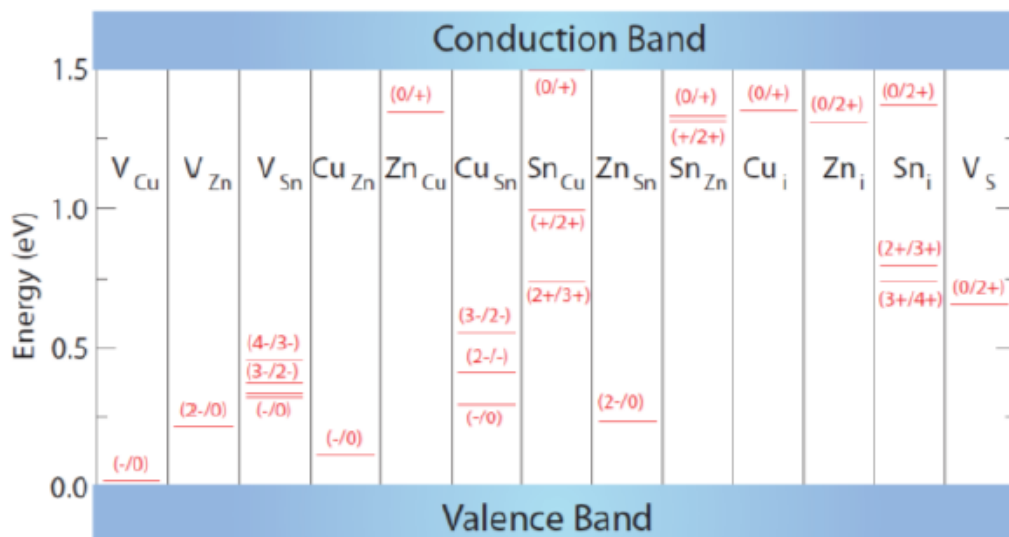


*Figure.I.20: Ionisation level of different defect in CZTS [65]*

### I.3.3.5. Electrical properties

Different to silicon which need be doped for being n or p type semiconductor, CZTS quaternary compound is a self-doped semiconductor, the p-type conductivity of CZTS is refer to the formation of acceptor defect and especially  $Cu_{Zn}$  antisite (Cu in Zn site) defect which have the lower formation energy than the other defects as we have discussed above. According to the publish data the resistivity of CZTS material varied in the range  $10^{-3}$  to  $10^{-1}$   $\Omega.cm$  as reported in case of best CZTS solar cells efficiency [67], and the hole concentration

vary between  $10^{16}$  and  $10^{18}$   $\text{cm}^{-3}$  [68-70]. The carrier's mobility varied from 0.1 to 30  $\text{cm}^2/\text{Vs}$ . Tanaka et al. [71] reported in their work that the carrier concentration increase with the formation of  $\text{Cu}_2\text{Se(S)}$  phase. That why the electrical properties of CZTS are very sensitive to the secondary phases and also by the presence of defects. Further, in [72] they reported a mobility value varied from 5 to 12  $\text{cm}^2/\text{Vs}$  for CZTS film grown by sulfurization of metallic precursors deposited by ion-beam sputtering. Also, Repins et al. [73] reported a high mobility value about 44.7  $\text{cm}^2/\text{Vs}$ , for the film deposited using reactive co-sputtering deposition of metallic precursors in  $\text{H}_2\text{S}$  atmosphere. The highest resistivity value reported for sprayed CZTS was about 200  $\Omega\cdot\text{cm}$  [74]. Fore control the values of resistivity or conductivity we have to controlled the secondary phases. Therefore, the high values of the conductivity is due to the Cu rich condition which elevate the concentration of  $\text{Cu}_{\text{Zn}}$  defect that's reported in [75], and favorite the formation of copper sulfide phase, whereas under Zn-rich condition the ZnS phase is formed as reported in our publish work [76], when the zinc concentration increase the zinc sulfide is formed and the resistivity increase, some published results for the conductivity, mobility and carrier concentration measured by hall effect are resumed in the table below.

<i>Resistivity(<math>\Omega\cdot\text{cm}</math>)</i>	<i>Hall Mobility (<math>\text{cm}^2/\text{V s}</math>)</i>	<i>hole concentration (<math>\text{cm}^{-3}</math>)</i>	<i>Refs</i>
0.15	6.3	$8.2 \cdot 10^{18}$	[77]
0.13	6	$8.2 \cdot 10^{18}$	[78]
0.13	12.6	$3.8 \cdot 10^{18}$	[79]
0.36	11.6	$4.5 \cdot 10^{17}$	[77]
5.4	30	$3.9 \cdot 10^{16}$	[70]

**Table I.4:** Resistivity, mobility and carrier concentration of CZTS thin films obtained by different techniques

### I.3.2.6 Optical properties

The electronic structure of CZTS and CZTSe and other related compounds were investigated by first principle calculations in several works [80,81]. Details of the electronic band structure of CZTS (e) can be found in [81]. The results show a direct -point energy gaps for both CZTS kesterite and stannite structures, with energy gap values of 1.56 and 1.42 eV, respectively. These values agree quite well with experimental works on CZTS single-crystals [82,83], even though other works found slightly different values (varying from 1.4 to 1.7 eV) can be found in the literature for CZTS thin films [84-85].

### I.3.4 The role of the Buffer layer in CZTS Thin Film Solar Cell

The primary function of a buffer layer in a hetero-junction is to form a junction with the absorber layer while admitting a maximum amount of light to the junction region and absorber layer [86]. In addition, this layer should have minimal absorption losses and should be capable of driving out the photogenerated carriers with minimum recombination losses and transporting the photogenerated carriers to the outer circuit with minimal electrical resistance. It should have minimal resistive loss and the band gap energy should be as high as possible and the layer should be as thin as possible to give low series resistance. It is also important that any potential ‘spike’ in the conduction band at the hetero-junction interface must be as low as possible for minority carrier transport. The requirements of a good buffer layer are cited below:

- i. The material should be n-type in order to form a p-n junction with the absorber layer.
- ii. The band gap should be wide for limited light absorption.
- iii. The process for deposition should be low cost and suitable for wide area deposition.
- iv. The process and material choice of the buffer layer should provide an alignment band conduction with that of the absorber with a conduction offset ( $\Delta E_C$ ) about 0 – 0.4.

For enhancing CZTS solar cells efficiency the buffer layer should hold the previous properties, the possible buffer layers which can formed a p-n junction with CZTS are cited below:

#### a. CdS buffer layer

Cadmium sulfide material is the commonly buffer layer used in CIGS and CdTe solar cells and it's extended to CZTS solar cell. The role of CdS buffer layer is the optimization of the band alignment between CZTS and ZnO layer, reduction of defect density at the interface and the increase of lifetime of free carriers, and the protection of absorber layer surface.

#### b. ZnS buffer layer

The ZnS-based buffer layer is one of the most popular candidates for replacing the CdS buffer layer which stayed undesirable because of the toxicity of cadmium. It can deposit by several of technique physical or chemical.

#### c. ZnSe buffer layer

The progress of the ZnSe-based buffer layer is dominated by the processes CBD and Metal Organic Vapor Phase Epitaxy (MOVPE). The CBD method was optimized at HMI (Hahn

Meitner Institut, Berlin, Germany) using the chemicals Zn-salt/ammonia/selenourea and  $\text{Cu(In,Ga)(Se,S)}_2$  absorbers from Siemens/Shell Solar. A maximum active-area efficiency of 15.7% [87] or a total area efficiency of 14.4% [88].

#### **d. ZnO buffer layer**

ZnO buffer can also be used as buffer-free cells when the ZnO window is directly deposited on CZTS by chemical or physical techniques. The problem with ZnO is the large band gap which implies a large band alignment between absorber and ZnO buffer layer which affect the device properties and performance.

#### **e. $\text{In}_2\text{S}_3$ buffer layer**

$\text{In}_2\text{S}_3$  has emerged as a promising buffer layer material, it has improved the performance of CIGS(Se) solar cells and avoid the use of CdS buffer layer which is toxic. It can be deposited using different growth methods (CBD, ALD, evaporation, and sputtering)

### **I.3.5 Band alignment diagram of $\text{Cu}_2\text{ZnSnS}_4$ /buffer hetero-structure**

One key issue for enhancing the CZTS solar cell efficiency is to find an optimal buffer layer, one of the limited reasons for the performance of CZTS solar cells is the small open circuit voltage (around 0.6 eV), probably resulting from a non-optimal conduction band alignment between the p-type CZTS absorber and the n-type buffer layer. As in chalcopyrite CIGS solar cells, in CZTS solar cells the CdS is used as the “standard” buffer layer. The conduction band alignment of CdS/CIGS is “spike-like” (as described in precedent paragraphs) with a desired band offset of 0.2–0.3 eV, which facilitates the high efficiency of a CIGS solar cell, especially for high  $V_{oc}$  [89]. However, the type of conduction band offset (CBO) is still unresolved when it comes to the case of CdS/CZTS based cells. Theoretically, the CBO of CdS/CZTS has been calculated to be negative (i.e., cliff-like), while the reported experimental values vary widely. For example, Richard et al. report a spike-like CBO of 0.41 eV [90], whereas other studies have measured cliff-like CBO values of -0.06 eV [91], -0.33 eV [92], and -0.34 eV [93]. As the band alignment has been found to be very sensitive to the interface of CdS/CZTS, the differences in the reported experimental CBO of CdS/CZTS could be due to the variation in the surface of the CZTS absorber and/or any treatment prior to the CdS buffer deposition. Further investigation is required to resolve this issue. On the other hand, if the CBO of CdS/CZTS is indeed cliff-like, it is imperative to identify alternative buffer materials which yield an optimal band alignment with CZTS (small spike-like CBO of 0.1–0.2 eV). However, very few experimental attempts have been made to measure band alignment at the interface of CdS free buffer layers and CZTS (pure sulfide). Yan et al [94]

have measured the band alignment of three buffer layers (CdS, Zn(O,S), and In<sub>2</sub>S<sub>3</sub>) with CZTS. The valence band maximum (VBM) and Valence Band Offset (VBO) are determined by X-ray Photoelectron Spectroscopy (XPS). The CBO between CdS and CZTS is confirmed to be cliff-like, whereas those at Zn (O, S)/CZTS interface and In<sub>2</sub>S<sub>3</sub>/CZTS interface are spike-like as seen in figure I.21.

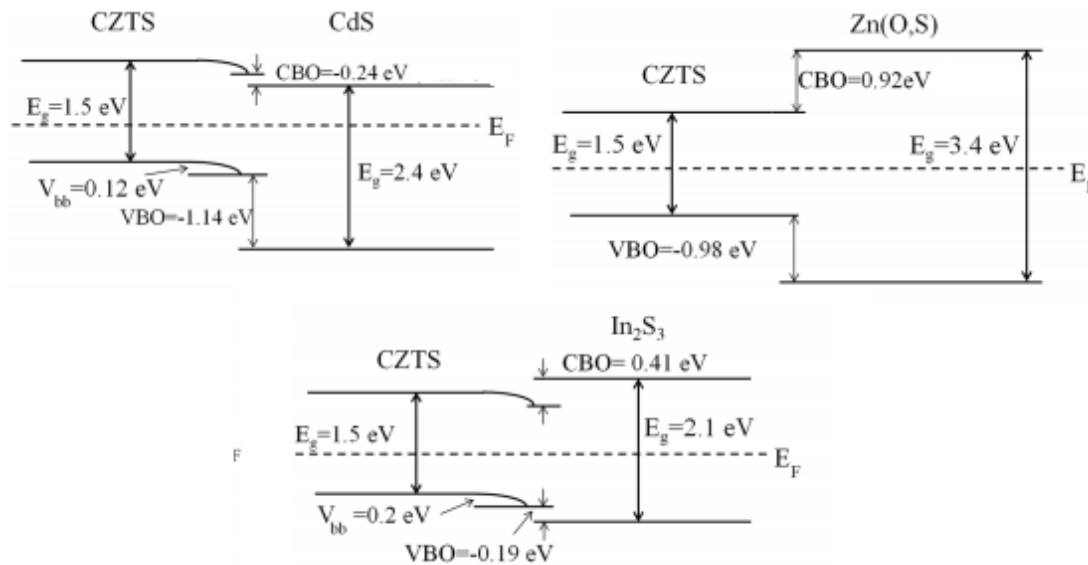


**Figure.I.21:** The band alignment of different buffers and CZTS values of the VBO, CBO, and  $E_g$  are indicated [94].

The measured device parameters show that the device with an In<sub>2</sub>S<sub>3</sub> buffer layer has higher open circuit voltage  $V_{oc}$  than that using CdS and Zn (O,S). The difference in conduction band offset (CBO) types of In<sub>2</sub>S<sub>3</sub>/CZTS and CdS/CZTS could cause the  $V_{oc}$  change. According to p-n junction band alignment simulation by Minemoto et al.[95] the convincingly small CBO spike (0–0.4 eV) prevents interface recombination, especially recombination between electrons in the conduction band of the buffer and holes in the valence band of CZTS. In contrast, the cliff-like CBO facilitates this kind of recombination, especially in the presence of interface defects and/or a high interface recombination velocity, resulting in a considerably decreased  $V_{oc}$ . Yan et al [94] find that the CBO between CZTS and Zn(O,S) and In<sub>2</sub>S<sub>3</sub> are spikes while between CZTS and CdS is a cliff, the devices were tested under illumination. The In<sub>2</sub>S<sub>3</sub> buffer layer with a CBO equal to 0.41 eV showed the best  $V_{oc}$  value (590 mV) while CdS (470 mV) and no photogenerated current for the device with Zn(O,S) buffer layer because of the large CBO (0.9 eV) which block the photo-generated carriers.

As a result a reasonable spike-like CBO enabled improvement of  $V_{oc}$  compared to a cliff-like CBO. However, may the hybridation of CdS with such Zn(O,S) or In<sub>2</sub>S<sub>3</sub> will allow to achieve an optimum spike like CBO value(0-0.3), that may enhance the  $V_{oc}$  and the performance of CZTS solar cells.

### I.3.6 Diffusion length of carriers in CZTS

Different to CIGS thin film solar cells which have a long diffusion length ( $L_d$ ) more than 1  $\mu\text{m}$  as reported in [96]. However, B.Shine et al. [4] reported a value of  $L_d=350$  nm with an efficiency around 8.4%, also the declared work on CZTSe with an efficiency equal to 12.6 % show a value of  $L_d = 750$  nm [5], whereas, Courel et al.[59] reported low minority diffusion length of sprayed CZTS which vary in the range 100–171 nm. The lifetimes of carriers and their diffusion lengths depend strongly on the morphological properties of the thin film and the crystalline quality which must be taken in account for enhancing the transport properties of free carriers. Further the long minority carrier lifetime is due to the low band gap energy as in CIGS and CZTSe and contrary to CZTS. For enhancing CZTS efficiency we must improve the different properties such as, the film morphology, the compositional homogeneity, and phase purity of the absorber should be controlled in order to increase the power conversion efficiency.

### I.3.7. Progression of kesterite solar cells

In 1988, Nakazawa et al [98] observed for the first time the photovoltaic effect on CZTS material deposited by atom beam sputtering. Where, they fabricated a CZTS hetero-junction with n type transparent cadmium-tin oxide thin film and reported an open circuit voltage value equal to 160 mV this value was improves soon by the same group to 265 mV [99]. After that, in 1997 Katagiri et al.[100] built the first pure CZTS solar cell with a *PCE* about 0.66% where CZTS absorber formed a hetero-junction with n type CdS buffer layer, Molebdenum (Mo) and ZnO:Al (AZO) are used as back and front contacts respectively. Same group in 1999, fabricated CZTS solar cells by two-step sulfurization process from electrodeposited of Cu/Sn/Zn precursors and set a new *PCE* record of 2.62% [101] which was the first reported result for two-step sulfurization with vacuum deposited precursors. New records were established when they optimized the sulfurization process (5.4% *PCE*) in 2003 [102], discovered how to etch remaining metal oxides on the surface of the absorber at the end of the annealing process (6.7% *PCE*) in 2008 [103]. By 2010, Todorov et al. reported efficiency for CZTSe devices equal to 9.6 % [104]. This record survived till for the first time

chalcogens intermixing is introduced in the alloy forming CZTSSe. Mitzi and his group at IBM reported 9.7% *PCE* CZTSSe solar cells by using a hybrid particle solution approach [59]. The CZTSSe absorber layers for these devices were deposited using two-step approach where precursors are dissolved in hydrazine and spin-coated on Mo coated glass followed by annealing [59]. In 2010 the group of Agrawal at Perdue 34 University (USA) introduced for the first time germanium in the alloy forming CZGeTSSe leading to a 8.4% *PCE* [105]. In the two years following (2011-2012), Todorov *et al.* pushed the *PCE* to 10.1% and 11.1% then still using hybrid particle-solution method [106]. Nowadays the world record efficiency for CZTSSe solar cells is at 12.6% set at IBM Watson [107] the evolution of the conversion efficiency of CZTSSe solar cells is illustrated in Figure I.22.

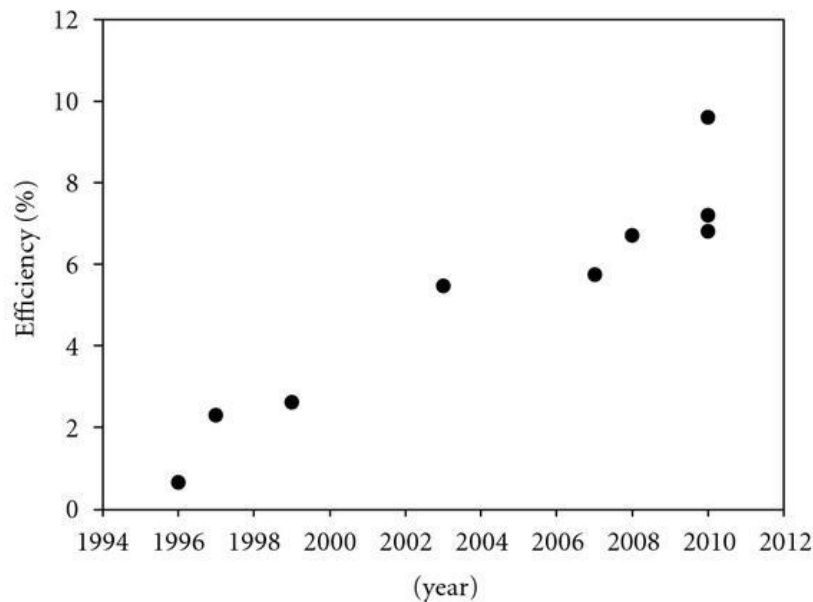
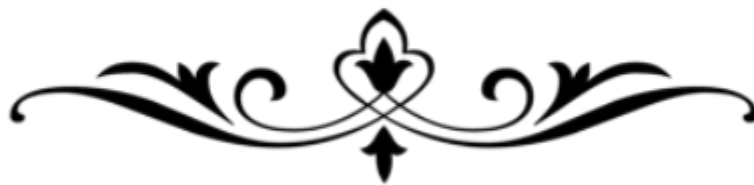


**Figure I.22:** Evolution of the conversion efficiency of thin film solar cells using CZTS as light absorber layer.

# Chapter II

## Deposition and characterization techniques



In the first part of this chapter, we will present the different deposition techniques of CZTS thin film, and specially the system used in my PhD thesis. The experimental condition used for the deposited of CZTS thin films and the stack of layers composed the device are reported. In the second part, we will cite the characterization techniques used for studding the different properties of CZTS samples and the realized devices.

---

## *II.1 Deposition techniques of CZTS*

---

CZTS (Se) thin film can be realized using different deposition methods either physical or chemical. The main goal of the use of different deposition method is for finding an economic and suitable route for deposition a good quality of the active layer, generally those techniques can be classified in two categories, vacuum which consisted on physical method and no vacuum which included chemical ones.

### **II.1.1 Physical Vapor Deposition (PVD)**

Physical deposition technique requires high vacuum and present best properties, it including: thermal evaporation, RF/DC magnetron, atom beam sputtering, hybrid sputtering, and pulsed laser deposition. This various PVD techniques are explained in details in the following paragraphs.

#### **II.1.1.1 Evaporation**

Different types of evaporation technique were used for the deposition of high quality of kesterite such as: thermal evaporation and electron beam evaporation, figureII.1 represent the schematic of the two processes. Katagiri et al. [100] has used an electron beam evaporation method to deposit a Cu/Sn/Zn stack layer sequentially on a SLG substrate at 150°C in high vacuum. The fabricated solar cell has an efficiency about 0.66% and a  $V_{oc}$ = 400mV and a short current density = 6mA/cm<sup>2</sup> which was the first CZTS solar cell, after that Friedlmeier et al. [108] have fabricated CZTS solar cell under high vacuum using thermal evaporation with 2.3% of solar efficiency. Later on, Katagiri et al.[66] have improve the efficiency by replacing the Zn precursor by ZnS layer and elevate the substrate temperature to 400°C with a variation of the absorber thickness from 0.95 to 1.63 μm, the enhancement by replacing Zn with ZnS were observed by an increase of the efficiency to 2.62 % and in 2003 it was improved to 5.45% with a  $V_{oc}$ =582mV and  $J_{sc}$ =15.5 mA/cm<sup>2</sup> using evaporation technique[102]. After that, the researches for the enhancement of CZTS efficiency continued with years and in 2012

Shin et al. [105] have reported a high record efficiency of CZTS solar cell by evaporation technique about 8.4% in 2012 and 12.6 % for CZTSSe solar cells [107].

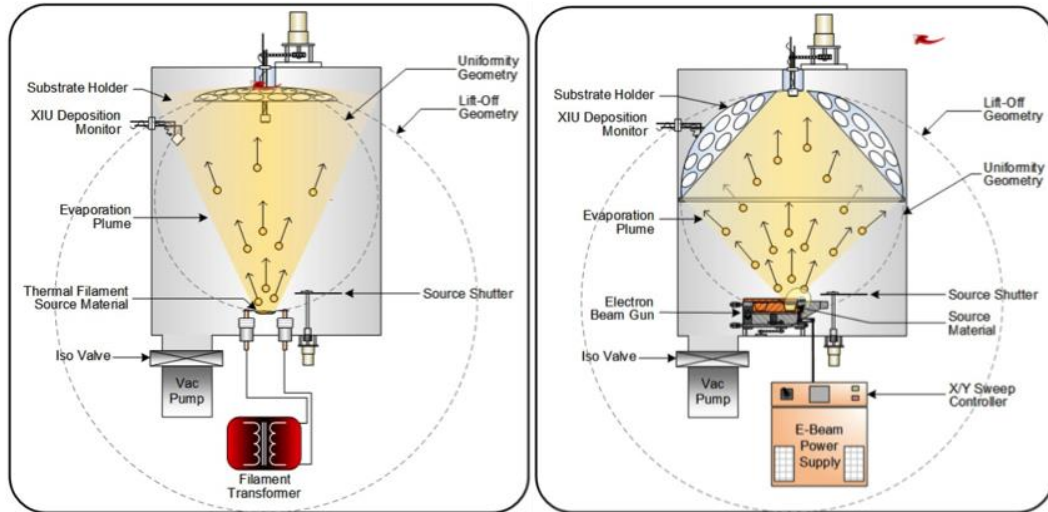


*Figure II.1. Beam evaporation technique in the left and thermal evaporation in the right [108x]*

### II.1.1.2 Sputtering technique

Another deposition technique which need high vacuum is called sputtering method, it gives high quality of absorber thin film. Sputter technique include argon beam sputtering, DC/RF magnetron, and reactive sputtering [109-112]. The first report of sputtering CZTS solar cell was by Ito and Nakazawa [98] in 1988, with a  $V_{oc}=265$  mV and  $J_{sc}=0.1$  mA/cm<sup>2</sup>. In 2003 Seol et al. [113] have prepared CZTS by RF sputtering with the use of Cu<sub>2</sub>S, ZnS, and SnS<sub>2</sub> powders as targets, whereas the hybrid sputtering was employed by Tanaka et al. [114].

### II.1.1.3 Pulsed laser Deposition

Pulsed Laser deposition (PLD) is a newer technique deposition compared to sputtering and evaporation, it gives also a high quality and crystalline thin films under high vacuum level with great reproducibility [115]. In this deposition technique, a pulsed laser beam with high power is used in a vacuum chamber to strike a material target, causing material evaporation from the surface of the target as seen in figure II.2. The evaporated material is then deposited as a thin film on a substrate, Cu<sub>2</sub>S, ZnS and SnS<sub>2</sub> powders are used as a target to deposit CZTS compound. By the use of this technique we can study various deposition parameters such as laser power, substrate temperature, duration, distance between target and substrate, and pulse rate. There are few reports concerning the deposition of CZTS thin film solar cell using this technique because of the small area of film deposited which is not enough for

commercial manufacturing which need large area of cells. In 2006, Sekiguchi et al. [116] reported the epitaxial growth of CZTS thin film on n-type oriented GaP substrate using (PLD). The first solar cells using this technique was in 2007 by Moriya et al. [117].

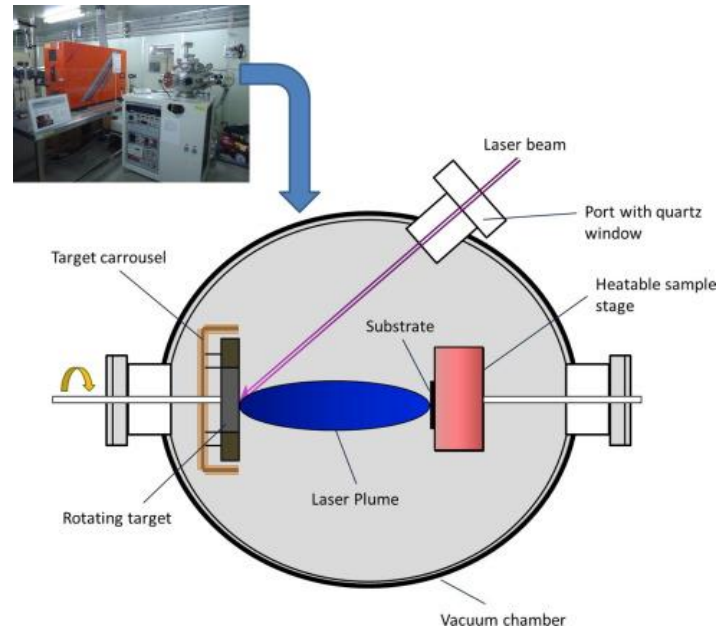


*Figure.II.2: Illustration schema of Pulsed Laser Deposition system [115]*

### II.1.2 Chemical Vapor Deposition (CVD)

Different to physical technique, this type of methods is not expensive and do not need vacuum, it suited technique for manufacture of PV system with low cost of PV module which is the core of any technology, various chemical routes were employed for the fabrication of CZTS thin films and related devices such as: electro-deposition, sol gel, spray pyrolysis, and chemical bath deposition technique.

#### II.1.2.1 Electro-deposition

Scragg et al. [118] was the first who realized CZTS solar cells by electro-deposition technique, they have used copper, tin, and Zinc chloride as precursors dissolved separately in a mixture solution containing NAOH, the deposition was at room temperature on a conductor substrate with the order of metals Cu, Sn, Zn using 3 electrodes with a platinum counter electrode and Ag/AgCl as reference electrode as seen in figure II.3. The growing films were sulfurized at 550 °C; the realized solar cell exhibit an efficiency equal to 0.8 %. In 2009, the efficiency increase to 3.4% by Ennaoui et al. [119] and 7.3% in 2012 by Ahmed et al. [120] using 3 step method: firstly, metal stacks of either Cu/Zn/Sn or Cu/Sn/Zn were

electrodeposited, then they did annealing at 210-350°C under N<sub>2</sub> gas and finally CuZn and CuSn alloys were annealed at 550-590 °C in sulfur vapor for 5 to 15 min and a single and highly crystalline film were obtained.

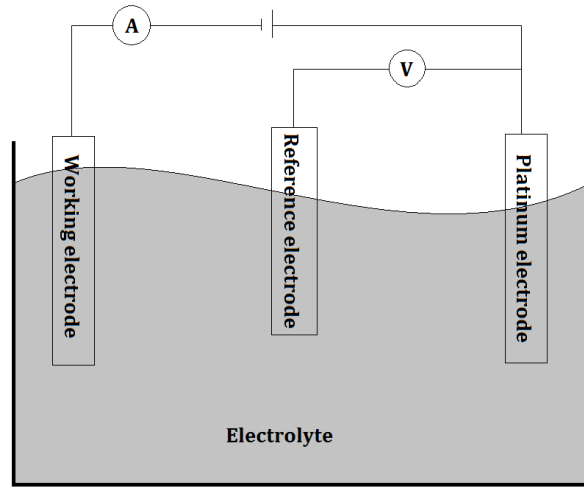


*Figure.II.3.* Basic electrode-position system with three electrodes

### II.1.2.2 Sol-Gel

The sol-gel solution was prepared by dissolving of copper(II) acetate monohydrate, zinc(II) acetate dehydrate and tin(II) chloride dehydrate in mixture solution of 2-methoxyethanol(2-metho), deionized water then, the solution was spin coated on Mo-coated soda lime glass substrate followed by drying at 300°C on a hot plate [121] the films were annealed at 500 °C in an atmosphere of N<sub>2</sub>+H<sub>2</sub>S (5%), then a buffer layer of CdS was grown on CZTS film by chemical bath deposition(CBD) ,the final solar cell has given an efficiency equal to 1.61%.Later on, the efficiency of CZTS solar cell using sol gel method was enhance by Tanaka et al.[122] and reach 2.23 % next, several works were done using this technique and the best efficiency was about 5.1 % [123].

### II.1.2.3 Spray pyrolysis

Spray pyrolysis technique including its different types (ultrasonic, pneumatic, and electrostatic) became an attractive deposition method due to its simplicity, low cost, not require high-quality of substrates, and the possibility for deposition large area which required for industry application. Spray pyrolysis was used widely for the fabrication of thin film devices such as: solar cells, antireflection coating, thermal coating, solid oxide fuel cells, sensors, and others. Various works on spray pyrolysis techniques have been published such as Moony and Radding have reported in their work the spray pyrolysis method, properties of the deposited films in relation to the conditions, specific films (particularly CdS), and device

application [124]. Tomar and Garcia have discussed the preparation and the properties of sprayed films as well as their application in solar cells, anti-reflection coatings, and gas sensors [125]. Albin and Risbud presented a review of the equipment, processing parameters, and optoelectronic materials deposited by the spray pyrolysis technique [126]. Pamplin has published a review of spraying solar cell materials as well as a bibliography of references on the spray pyrolysis technique [127]. Recently, thin metal oxide and chalcogenide films deposited by spray pyrolysis and different atomization techniques were reviewed by Patil [128]. Furthermore, the first report in sprayed CZTS was reported by Nakayama et al. [129] in 1996, spray pyrolysis became an interesting technique and it used widely for kesterite deposition, many works were reported in sprayed CZTS thin films [130-131], and several parameters were studied for eg : the effect of tin precursors were studied by Rajeshmon et al. [132] who tested  $\text{SnCl}_2$  and  $\text{SnCl}_4$  precursors and found that both tin sources give kesterite structure with the better crystallization for the film prepared using  $\text{SnCl}_2$  precursor. The advantage of spray technique is the possibility of controlled many conditions, including solution conditions and system parameters, schema below shows the different parameters which can be study using this technique.

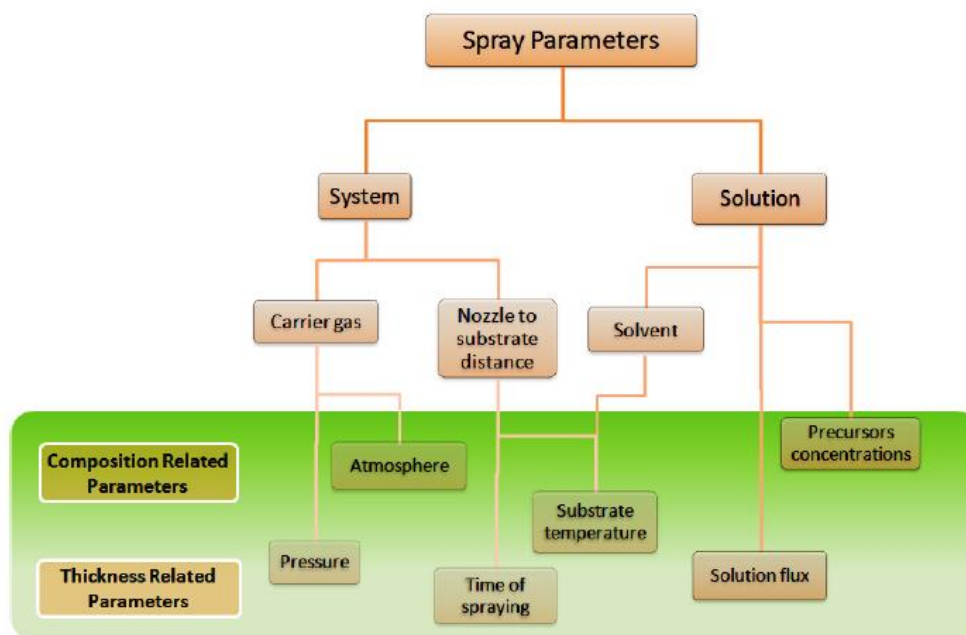


**Figure II.4** schematic of different spray pyrolysis (SP) parameters [133]

Figure II.5 shows a typical spraying system. It mainly consists of spray nozzle, precursor solution, substrate heater, temperature controller and air compressor or gas propellant. To

measure the flow of precursor solution and air, liquid and gas flow meters are used. The spray head movement is also controlled by stepper motor driven linear stages in X and Y directions.

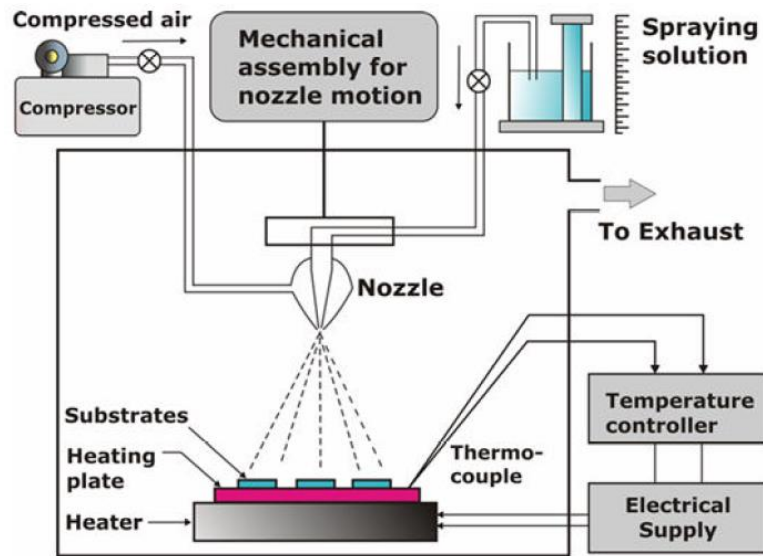


*Figure.II.5 Simplified schematic of Spray pyrolysis system*

The properties of the prepared film depend on spray rate, substrate temperature, ambient atmosphere, carrier gas, droplet size and also the cooling rate after deposition. The film thickness depends upon the distance between the spray nozzle and substrate temperature, the concentration of the precursor solution and the quantity of the solution sprayed. The film formation depends on the process of droplet landing, reaction and solvent evaporation, which are related to droplet size. An ideal deposition condition is when the droplet approaches the substrate just as the solvent is removed completely. The three principal processing steps for spray pyrolysis deposition are:

- *Atomization Procedure*
- *Aerosol Transport of Droplets*
- *Precursor Decomposition*

The high efficiency obtained using various deposition techniques (CVD and PVD) is reported in Table II.1.

<i>Method</i>	<i>Precursor</i>	<i>Efficiency(%)</i>	<i>Year</i>	<i>References</i>
<i>Evaporation</i>	<i>Cu,Zn,Sn,S</i>	<i>8.4</i>	<i>2011</i>	<i>[105]</i>
<i>sputtering</i>	<i>Cu,SnS,ZnS</i>	<i>6.77</i>	<i>2008</i>	<i>[103]</i>
<i>electrodeposition</i>	<i>Cu(II)ion,Zn(II)ion,Sn(IV)ion</i>	<i>7.3</i>	<i>2012</i>	<i>[120]</i>
<i>Sol gel</i>	<i>Cu(II),Zinc(II) acetate dehydrate,SnCl<sub>2</sub>,2H<sub>2</sub>O</i>	<i>2.23</i>	<i>2011</i>	<i>[123]</i>
<i>Pulsed Laser Deposition</i>	<i>In_house fabricated CZTS pellet</i>	<i>3.14</i>	<i>2011</i>	<i>[134]</i>
<i>Spray pyrolysis</i>	<i>Not availbale</i>	<i>1.15</i>	<i>2011</i>	<i>[135]</i>
<i>Np-based method</i>	<i>Cu(II)acetylacetonate,zinc acetate,SnCl<sub>2</sub>,2H<sub>2</sub>O,Sulfure</i>	<i>0.23</i>	<i>2009</i>	<i>[136]</i>
<i>Screen –printing</i>	<i>CZTS microparticle</i>	<i>0.49</i>	<i>2010</i>	<i>[51]</i>
<i>CBD-ion exchange</i>	<i>SnCl<sub>2</sub>,2H<sub>2</sub>O,zinc acetate dehydrate,aqueuse Cu<sup>+2</sup></i>	<i>0.16</i>	<i>2011</i>	<i>[137]</i>

**Table II.1** Highest of CZTS efficiency obtained by different methodes

### II.1.3 Thin films preparation and device fabrication

In our experimental work, firstly we have consisted to study the different parameters of the active layer which is a quaternary compound named  $\text{Cu}_2\text{ZnSnS}_4$  (CZTS). The goal of this study is to deposit and enhance the different properties of the absorber layer and their related devices using spray pyrolysis technique. CZTS thin films, hetero-junction, and solar cells have been investigated.

#### II.1.3.1 CZTS thin film deposition

The goal of the present study is the deposition of CZTS thin films by spray pyrolysis technique. Influence of different parameters related to this technique will be investigated. Experimental details of films preparation by this technique will be presented. The most important parameters have been studied namely: substrate temperatures, duration, and precursor salt molarities. Flow rate, solvent and precursor nature were fixed. The steps of deposition process are as follow:

- 1. Substrate preparation:** in this work, we have used glass as substrate. Firstly, the glass substrate was cleaned ultrasonically in acetone to remove impurities (grease or dust) present in the surface of the substrate for 10 min. Then, the glass substrates were cleaned

ultrasonically in distilled water to remove any trace of the acetone for 10 min and finally, the cleaned glass substrates are dried and became ready for the use.

- The preparation of the solution:** the preparation of the solution is not complicate it based on the mixing of four salts: copper acetate or copper chloride ( $\text{CuCl}_2, 2\text{H}_2\text{O}$ ) as source of **copper (Cu)**, Zinc acetate as source of **Zinc (Zn)**, tin chloride ( $\text{SnCl}_2, 2\text{H}_2\text{O}$ ) for **tin (Sn)**, and thiourea ( $\text{CS}(\text{NH}_2)_2$ ) as source of **sulfur (S)**, the solution was agitated through magnetron stirring until a transparent solution is obtained. The variation of solution color's with adding of precursors is illustrated in figure II.6.



*Figure II.6: The variation of solution color with adding different precursors*

**3.Thin film deposition:** After the preparation of the substrates and the solutions, we start the deposition procedure which follow several stages: In the first, we start by replacing the well cleaned substrate on a heated substrate holder at the desirable temperature, when the temperature is reached droplets of 40  $\mu\text{m}$  diameter are sprayed onto heated substrates. The of the temperature is to cause the pyrolysis activation of the chemical reaction leading to the layer formation, while the other elements volatilize after reaction. Finally, the deposition process is finish and the thin film is formed, we stop the heating and let the substrates cool down slowly above the substrate holder at room temperature to avoid the thermal shock. Then the samples will be ready for the various characterizations.

The deposition of the whole films with various deposition condition and the layers composed the realized device were done using spray pyrolysis technique (HOLMARC) as seen in figure II.7



**Figure II.7** System used for CZTS film deposition

In the following paragraphs we have summarized the deposition conditions of the different studied parameters in this thesis which can be divided into two parts: the first one is focused on the study of CZTS thin film properties, while in the second part, we have described in detail the realization of CZTS hetero-structures.

### **Part. I. The studied parameters of CZTS thin films**

#### **1. Effect of substrate temperature**

To obtain the optimal temperature for CZTS thin film deposition, we have fixed all parameters and varied the substrate temperature from 300 to 390 °C with a step of 30 °C, using distilled water as solvent (40 ml). The used parameters are summarized in table II.2

<i>precursors</i>	<i>molarities</i>	<i>Flow rate(ml/h)</i>	<i>Duration(min)</i>
$CuCl_2 \cdot 2H_2O$	0.02	10	30
$Zn[CH_3COO]_2 \cdot 2H_2O$	0.01		
$SnCl_2 \cdot 2H_2O$	0.01		
$CS(NH_2)_2$	0.12		

**Table II.2** parameters used for the deposition of CZTS films with various substrate temperatures ( $T_s$ ).

### 2. Deposition time

In this part we have studied the effect of time deposition on different properties of CZTS thin films. The deposition time was varied from 15 to 45 minute with take all other parameters fixed.

<i>precursors</i>	<i>molarities</i>	<i>Flow rate(ml/h)</i>	<i>Temperature(°C)</i>
<i>CuCl<sub>2</sub>·2H<sub>2</sub>O</i>	0.02	10	350
<i>Zn[CH<sub>3</sub>COO]<sub>2</sub>·2H<sub>2</sub>O</i>	0.01		
<i>SnCl<sub>2</sub>·2H<sub>2</sub>O</i>	0.01		
<i>CS(NH<sub>2</sub>)<sub>2</sub></i>	0.12		

*Table II.3 Experimental condition of CZTS with the variation of deposition time*

### 3. Copper salt concentration

Copper concentration was varied from 0.01 to 0.03 M with fixed the other precursors molarities and parameters.

<i>precursors</i>	<i>Molarity(M)</i>	<i>Flow rate(ml/h)</i>	<i>Temperature(°C)</i>	<i>Duration(min)</i>
<i>CuCl<sub>2</sub>·2H<sub>2</sub>O</i>	0.01-0.03	10	350	30
<i>Zn[CH<sub>3</sub>COO]<sub>2</sub>·2H<sub>2</sub>O</i>	0.01			
<i>SnCl<sub>2</sub>·2H<sub>2</sub>O</i>	0.01			
<i>CS(NH<sub>2</sub>)<sub>2</sub></i>	0.12			

*Table II.4 Experimental condition of CZTS films with the variation of copper salt concentration*

### 3. Effect of zinc molarities

In this part we have studied the effect of zinc acetate salt molarities on CZTS properties, in which zinc molarity varied from 0.01 to 0.025 M. The experimental conditions are resumed in table II.5

<i>precursors</i>	<i>molarities</i>	<i>Flow rate(ml/h)</i>	<i>Temperature(°)</i>	<i>Duration(min)</i>
$CuCl_2 \cdot 2H_2O$	0.02	10	350	30
$Zn[CH_3COO]_2 \cdot 2H_2O$	0.01-0.025			
$SnCl_2 \cdot 2H_2O$	0.01			
$CS(NH_2)_2$	0.12			

*Table II.5 Experimental condition of CZTS with the variation of zinc salt concentration*

### *Part. II : CZTS device fabrication*

#### **1. Effect of back contact**

CZTS/ZnS hetero-junction was realized from of a stack of layers such as: Fluorine doped tin oxide (FTO) which used as the front contact, ZnS as buffer layer, CZTS as the active layer, and three metals back contacts were tested: aluminum (Al), silver (Ag), and gold (Au). The experimental condition used are resumed in the previous tables and paragraphs.

**a. CZTS absorber layer:** The experimental conditions for the deposition of absorber layer are resumed in Table II.6

<i>precursors</i>	<i>molarities</i>	<i>Flow rate(ml/h)</i>	<i>Temperature(°C)</i>	<i>Duration(min)</i>
$CuCl_2 \cdot 2H_2O$	0.02	10	350	30
$Zn[CH_3COO]_2 \cdot 2H_2O$	0.01			
$SnCl_2 \cdot 2H_2O$	0.01			
$CS(NH_2)_2$	0.12			

*Table II.6 The experimental condition for absorber layer deposition*

#### **b. ZnS buffer layer**

The deposition of zinc sulfide (ZnS) buffer layer was done using spray pyrolysis technique with the experiment condition as resumed in Table II.7

<i>precursors</i>	<i>molarities</i>	<i>Flow rate(ml/h)</i>	<i>Temperature(°C)</i>	<i>Duration(min)</i>
$Zn[CH_3COO]_2 \cdot 2H_2O$	0.01	5	350	5
$CS(NH_2)_2$	0.05			

*Table II.7 The experimental condition for buffer layer deposition*

### c. Fluorine doped tin oxide

FTO thin film is used in this structure as the front contact and the deposition conditions are resumed in Table II.8

<i>precursors</i>	<i>molarities</i>	<i>Flow rate(ml/h)</i>	<i>Temperature(°C)</i>	<i>Duration(min)</i>
$NH_4F$	F/Sn=12%			
$SnCl_2 \cdot 2H_2O$	0.1	5	450	3

*Table II.8 The experimental condition for FTO layer deposition*

### d. Back contact deposition (Ag, Al, and Au)

Silver and aluminum back contact were deposited using thermal evaporation technique whereas gold were deposited using cathodique sputtering (Edward sputter coter S 150B) with a thickness about 100 nm. The final realized device is illustrated in figure II.8

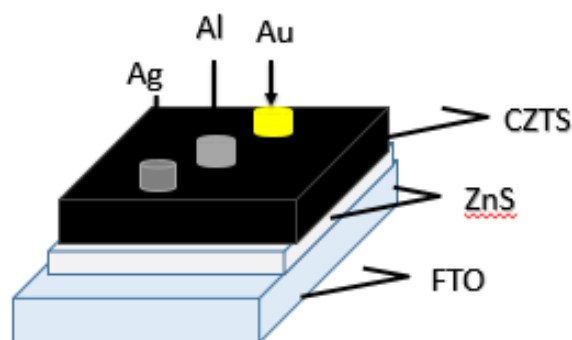


*Figure II.8. realized CZTS/ZnS hetero-junction*

## 2. Effect of i-ZnO intrinsic layer

Same conditions are used for the deposition of CZTS, ZnS, FTO and gold(Au), the difference is that in this work we have added an intrinsic layer to the fabricated device which is ZnO intrinsic layer.

\* **Deposition of zinc oxide (ZnO):** for the preparation of ZnO solution we have dissolved 0.1M of zinc acetate in 40 ml of distilled water, the solution sprayed on a heated substrate at 350 °C and the flow rate was fixed at 5ml/h for 3 minutes of time deposition. The realized hetero-structure is illustrated in figure II.9

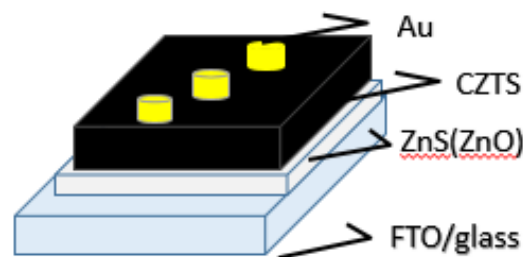


*Figure I.9: Realized CZTS/ZnS/(ZnO) device*

## 3. The effect of sulfurization temperature on CZTS/CdS solar cells performance

In this part of work, we have studied the effect of sulfurization temperature on CZTS solar cell efficiency, the fabricated solar cell is formed by the multi-junction: ZnO:Al/ZnO/CdS/CZTS/Mo as reported in figure II.10. Molybdenum coated glass were used as substrate with a thickness about 1  $\mu\text{m}$ , then the absorber layer (CZTS) was deposited on Mo coated glass using ultrasonic spray pyrolysis. Mo/CZTS was annealed at different temperatures (450, 500, and 550°C) in H<sub>2</sub>S: Ar gas (30 sccm) gas mixture atmosphere for 30 minutes. After annealing, 50 nm thickness of cadmium sulfide (CdS) layer was deposited onto CZTS using DC sputtering at 175 °C, followed by DC sputtering deposition of an intrinsic ZnO layer and ZnO:Al thin film as window layer with a thicknesses of 50 nm. Finally, the device structure was completed by silver grids deposition on the top of the cell by thermal evaporation technique.

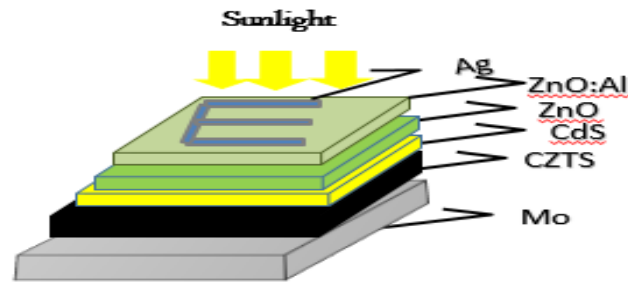


*Figure II.10 Realized CZTS/CdS solar cell*

## ***II.2 Analysis techniques***

For understand the properties of the deposited CZTS thin film, characterization at both material and device stage are obligatory. In particular, it is essential to observe the compositions and elemental distribution of CZTS absorber, since it is not often homogeneously distributed and since these elemental distributions may affect the electrical characteristics of the CZTS solar cell.

### **II.2.a Films Characterization**

#### **II.2.a.1 X-Ray Diffraction (XRD)**

X-ray diffraction is a non-destructive technique that is widely used to analyze crystal structure of materials. When an X-ray beam strikes a crystal at an angle  $\theta$  (figure II.11), constructive interferences and a peak in the intensity of reflection are observed if Bragg's law is verified and gives by the relation (II.1)

$$2d\sin(\theta) = n\lambda \quad (\text{II.1})$$

With:  $n$  is the order of diffraction,  $\lambda$  is the wavelength of the X-ray beam,  $d$  is the spacing between consecutive parallel planes, and  $\theta$  is the incident angle.

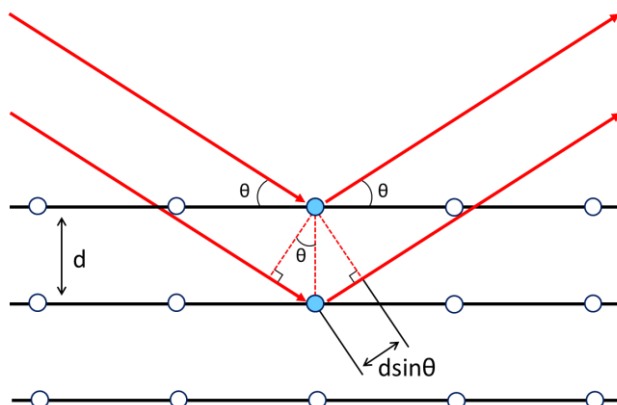


*Figure II.11: Illustration of X-rays diffraction on crystallographic planes*

Because the diffraction pattern of any given substance is unique to the atoms and structure of that substance, the angles and intensities of the diffracted X-Rays can be measured to produce a three-dimensional picture of the electron density within the substance. The compounds present within a substance can be determined by comparing its diffraction pattern to known diffraction patterns using JCPD cards (Joint Committee on Powder Diffraction Standards card). Our Measurements were made using Philips X Pert system with Cu- $\alpha$  radiation of wavelength  $\lambda = 1.5418 \text{ \AA}$ . The diffract meter reflections were taken at room temperature and the  $2\theta$  values were varied from 10 to  $80^\circ$ . The X Ray Diffraction is a useful technique which provides information on:

- The crystalline phase or phases (position of the peaks);
- The size of the crystallites and / or the internal stress (width of the peaks at mid-height);
- Orientation of the crystallites (absence or presence of reflections).

### II.2.a.2: Raman spectroscopy

Raman spectroscopy uses the Raman Effect to characterize the chemical composition and structure of materials. Raman spectroscopy is used in this work as a complementary technique for XRD to identify secondary phases in the CZTS compound and it is used to observe the vibration modes of materials. It is based on Raman scattering (inelastic scattering) of monochromatic light, usually from a laser in the visible, near-infrared, or near-ultraviolet range.

### A. Principle of Raman spectroscopy

When monochromatic radiation is incident upon a sample then this light will interact with the sample. It may be reflected, absorbed or scattered. It is the scattering of the radiation that occur which gives information about molecular structure, the scattering of the incident light has two possibilities when interact with the molecules of the material:

- If the incident radiation is being elastically diffused without change of energy in this case, we are speaking about **Rayleigh scatter**.
- If a small portion of the incident light can interact with the material. It absorbs (or gives) energy to photons incidents thus producing **Stokes (or anti-Stokes)** radiation (Figure II.12).

The variation of energy observed on the photon informs us about the energy levels of rotation and vibration of the concerned molecule. As part of the Raman spectrometry, we are interested in vibration and rotation energies, very weak compared to incident photons.

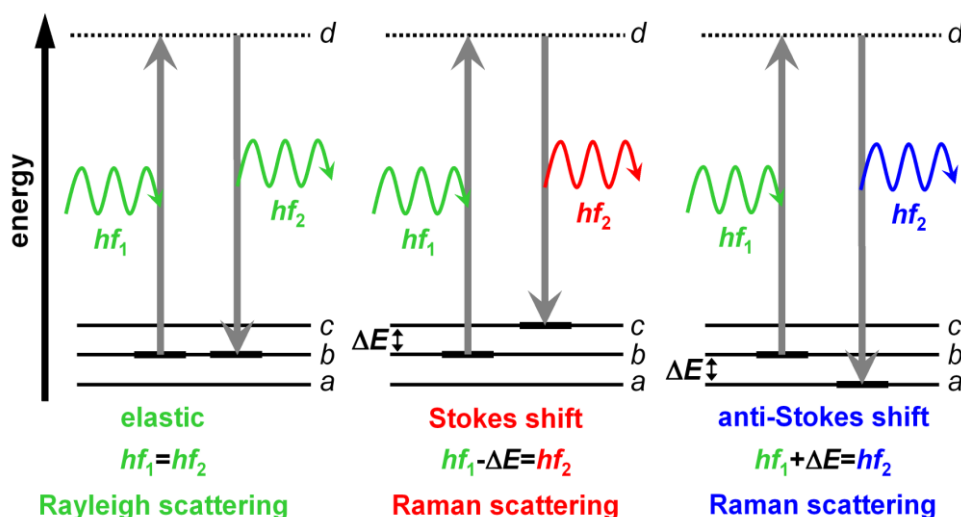


*Figure II.12: Illustration of the energy-level diagram for Rayleigh scattering, Stokes Raman scattering, and anti-Stokes Raman scattering.*

### B. Given Information by Raman spectroscopy

The information provided by Raman spectroscopy is relatively extensive:

- Identification of phases or chemical compounds.
- Characterization of materials.
- Determination of the molecular structure.
- intermolecular interactions of the studied material

### II.2.a.3 The UV-visible spectrophotometer

The optical properties of the growing thin films were analyzed by UV-Visible transmittance Spectroscopy by means of Shimadzu 3101PC double beam spectrophotometer in the 190-1000 nm wavelength range for CZTS thin films. From transmittance data various parameters were extracted such as: the optical band gap, the refractive index and the absorption coefficient was also determined from transmittance data using the giving expressions:

- The absorption coefficient ( $\alpha$ ): in the spectral region of the light's absorption, was deduced from the Beer-Lambert law using the following expression [138]:

$$\alpha = - (1 / d) \ln (100/T (\%)) \quad (\text{II.2})$$

With:  $\alpha$  is absorption coefficient ( $\text{cm}^{-2}$ ),  $d$  is the film thickness (cm), and  $T$  is the transmittance. The thickness  $d$  was estimated from Hebal optic code which simulate the transmittance spectra of the film.

The value of the forbidden band energy of the CZTS material was determined from transmittance data. Indeed, the "law" of Tauc allows to link absorption coefficient( $\alpha$ ) and bandgap energy according to the formula:

$$(\alpha h\nu) = A (h\nu - E_g)^n \quad (\text{II.3})$$

$$\text{With} \quad A = (4\pi\sigma / n c E_c) \quad (\text{II.4})$$

While  $E_g$  is the optical energy gap of the material,  $n$  is the parameter which characterizes the transition process,  $c$  is the speed of light,  $\sigma$  is the minimum metallic conductivity (extrapolated dc conductivity at  $T=\infty$ ),  $E_c$  is a measure of the width of the tail states distribution and  $n$  is the refractive index. In semiconductors there exist two types of band to band transitions (i) allowed and (ii) forbidden (forbidden transition take into account the small but finite momentum of photon these transitions are less probable). The allowed transition can occur in all values of  $k$  but forbidden transition can only occur at  $k \neq 0$ .  $n = 2$  and  $2/3$  for direct allowed and forbidden transitions respectively. In indirect semiconductor, a phonon is involved in the transition in order to conserve momentum. In the indirect transitions,  $n = 1/2$  and  $1/3$  for indirect allowed and forbidden transitions, respectively.

Thus the plot of  $(\alpha h\nu)^2$  as a function of  $h\nu$  allows determining the value of  $E_g$  to the intersection of the tangent to the curve in its linear part and the abscissa axis as shown in the figure II.13

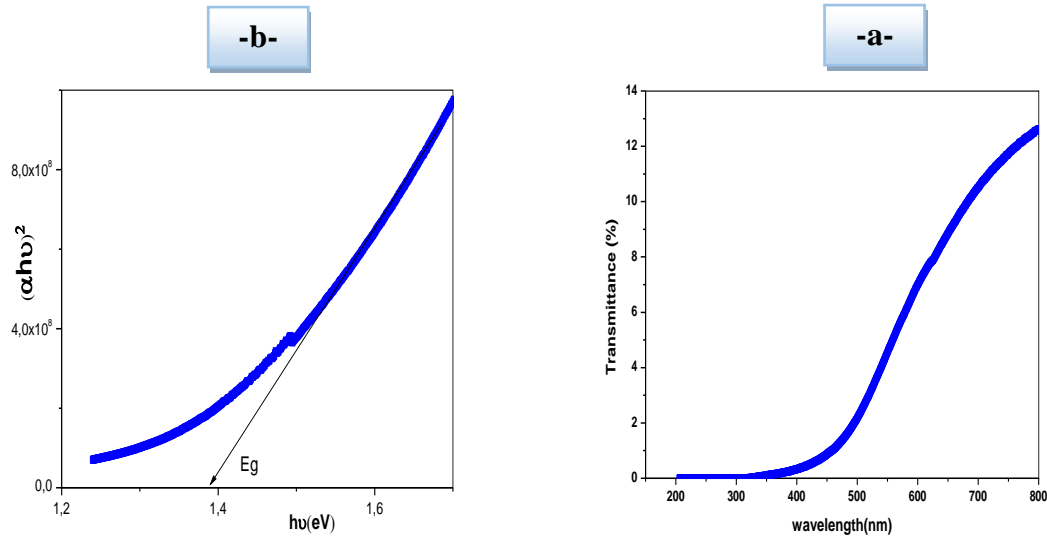


*Figure II.13 (a) and (b) graphs represent a typical transmittance and gap energy of CZTS*

#### II.2.a.4 Atomic force microscopy(AFM) and scanning electronic microscopy(SEM)

The morphological properties of CZTS thin films were studied using Atomic Force Microscopy, it provides a high resolution 3-D topographic profile of the surface. AFM was used for the measurement of film thickness, RMS roughness, and percent roughness of the films which calculated from the AFM software, Ambios. The morphology of the thin layers was observed also using scanning electron microscope (SEM). The sample is subjected to a bombardment of electrons emitted by a gun in a column maintained under vacuum. These so-called "primary" electrons are focused on the surface of the sample. The electron-matter interaction causes the emission of secondary electrons from the surface of the sample, the images presented in this thesis are secondary electron images. Their emission depth is in the order of few tens of nanometers. The yield of secondary electrons depends on the composition and topography of the surface. As the analyzed layers are fine and conductive, no prior treatment of the samples has been performed. SEM images of CZTS films and the cross section of the device, have been done at the CNST@PoliMI – IIT (IIT polimi, Italy).

#### II.2.a.5 Hall effect measurement

Hall effect phenomena was discovered in 1879 by Edwin Hall. Hall effect can be observed when a semiconductor device (eg. thin films: CZTS, ITO, FTO,) set into a magnetic field which caused by the Lorentz Force. It can be observed when the combination of a magnetic field through a sample and a current along the length of the sample creates an electrical current perpendicular to both the magnetic field and the current, which in turn creates a

transverse voltage that is perpendicular to both the magnetic field and the current. Hall effect system is generally used for determination of electrical properties of material such as: Hall voltage ( $V_h$ ), carrier mobility, carrier concentration( $n$ ), Hall coefficient ( $R_h$ ), resistivity, and the conductivity type (N or P).

### II.2.b. Device characterization

#### II.2.b.1 Current-Voltage measurements

The dark and illuminated current versus voltage (I-V) characteristics of a photovoltaic (PV) were used for the determination of the different electrical parameters of the hetero-junction and solar cells. The I-V characterization in the dark of the first hetero-junctions were done using Tektronix tracer (diodoscope) (figure II.14) whereas the power conversion of realized cells determined using a simulated solar cell at room temperature with an intensity equal to  $100 \text{ mW/cm}^2$  connected with Keithly as seen in figure II.15 (a-c).



*Figure II.14. Tektronics meter for the I-V measurement*

When a solar cell is illuminated under solar spectrum, additional electron-hole pairs are created giving rise to the so-called photogenerated current ( $I_{ph}$ ). The major parameters that characterize the performance of a solar cell as mentioned in chapter I are: the open circuit voltage ( $V_{oc}$ ), the short circuit current ( $I_{sc}$ ), power maximum ( $P_{max}$ ), the fill factor(FF), and the efficiency.

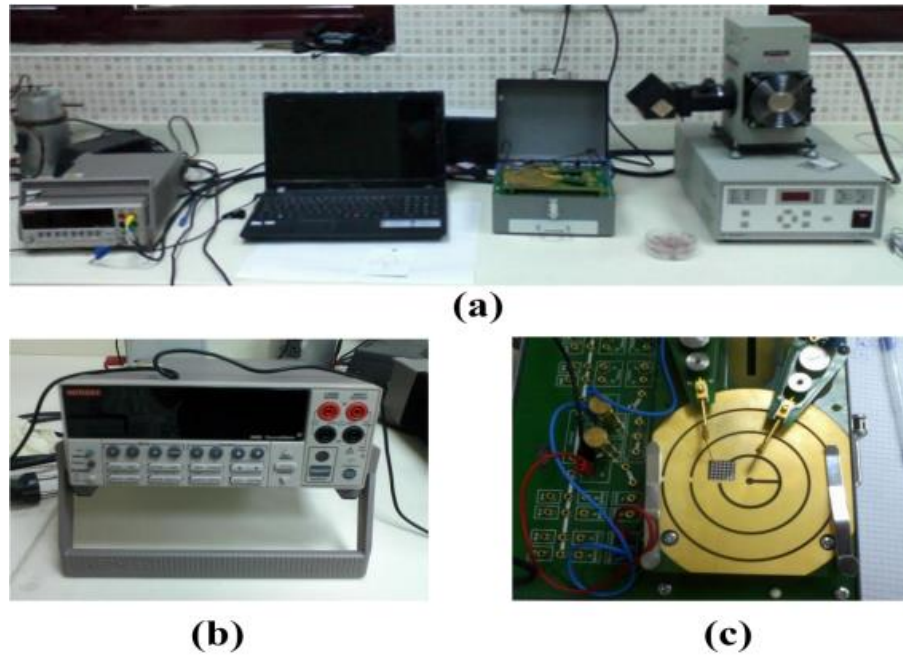


*Figure II.15. I-V system used for solar cells efficiency measurement (Dicle University, Diyarbakir, Turkey)*

### II.2.b.2 Conductance-Capacitance-frequency measurement

Among other capacitance based techniques such as capacitance-voltage and deep level transient spectroscopy. Admittance spectroscopy is commonly used to characterize majority-carrier trapping defects in PV materials and devices. The capacitance-conductance versus frequency. It is an important analysis for study the interfacial properties of devices. The admittance measurements were performed in a homemade cryostat in dark condition with temperatures ranging 298 K to 375 K, using LCR METER (type Agilent 4284A Precision Impedance Analyzer) and an Oxford ITC4 temperature controller. The samples to be tested are placed in a dark chamber connected to the LCR METER by coaxial cables (Figure II.16). The voltage of the Ac signal or their amplitude was about 0.3 V and the analyzed frequency range from 1000 KHZ to 1MHZ. This technique was already used on CZTS based hetero-structure grown by co-evaporation methods and also on CdTe and CIGS solar cells [139.140]. In this technique an AC response equivalent circuit was proposed and from the resulting model several parameters were extracted, allowing the characterization of the CZTS/CdS hetero-junction, and the Mo/MoS<sub>2</sub>/CZTS back contact interfaces. Admittance spectroscopy analyzed or show the response of a device to small Ac bias voltage and its dependence on frequency and temperature which due to the capture and emission of active defect



*Figure.II.16. Impedance meter used for C-G-f measurement*

The Admittance spectroscopy is a provable method to extract defect parameters such as activation energy capture, cross-section, and density of states. The frequency  $\omega_r$  of the resonant peak (as seen in figure II.17) is expressed by the following relation [141]:

$$\omega_{r(T)} = 2e_i(T) = A \cdot T^2 \exp(-E_a/KT) \quad (\text{II.5})$$

Where:  $\omega_r$  is the inflection frequency  $e_i$  is the emission rate of trapped charges and  $E_a$  is the activation energy.

The interface state density ( $N_{ss}$ ) can be deduced from the conductance peak by using the following relation [142]:

$$N_{ss} = \frac{(G/\omega)_{\max}}{0.402qS} \quad (\text{II.6})$$

Where  $q$  is the electronic charge and  $S$  is the diode area.

The time constant ( $\tau$ ) for electrons exchange between interface states and valence band can be calculated using the relation  $\tau = 1/\omega_r$  [143].

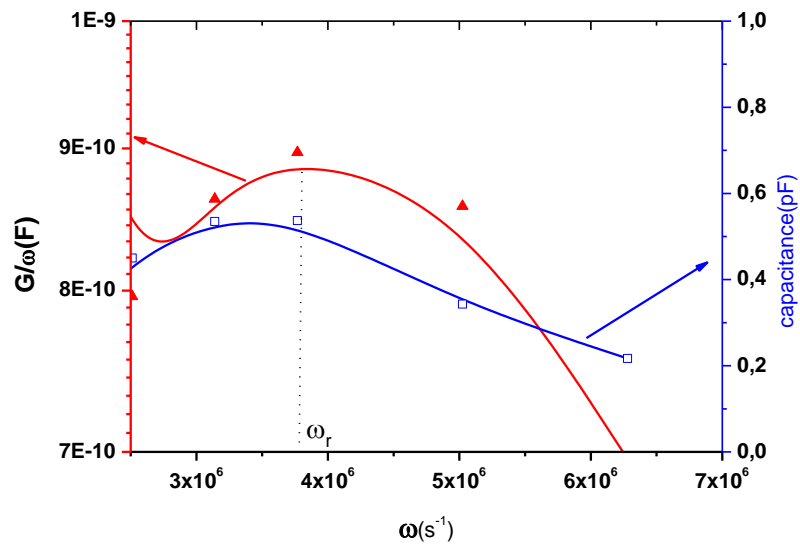
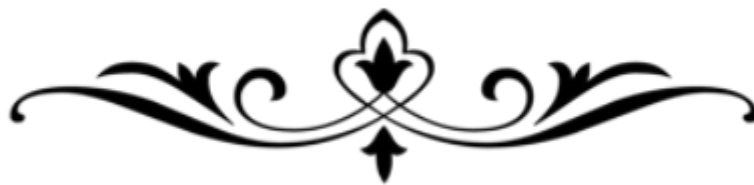


*Figure II.17. Illustration of a typical  $G/\omega$  and capacitance as function of pulsation of CZTS/ZnS hetero-junction*

# Chapter III

## CZTS Thin films results and Discussion



In this chapter, different experimental conditions were investigated. Four parameters were tested such as, substrate temperature, deposition time, copper concentration salt, and zinc molarities for finding the optimal condition to obtain high quality of CZTS thin films which are required for application in thin film solar cells. The results are presented with discussions in the following paragraphs.

---

### *III.1 The effect of substrate temperature*

---

Copper chloride ( $\text{CuCl}_2, 2\text{H}_2\text{O}$ ), zinc acetate ( $(\text{CH}_3\text{COO})_2\text{Zn} \cdot 2\text{H}_2\text{O}$ ), tin chloride ( $\text{SnCl}_2, 2\text{H}_2\text{O}$ ) and thiourea ( $\text{CS}(\text{NH}_2)_2$ ) were used as precursors of Cu, Zn, Sn and S respectively. The deposition conditions are mentioned with details in chapter II. The effect of substrate temperature was investigated, it varied from 300 to 390°C with a step of 30 °C for 30 minutes of time deposition and with a flow rate about 10 ml/h.

#### **III.1.1 structural properties**

##### **a. X Ray Diffraction**

The XRD measurements were carried out at room temperature with a diffraction angles varied between 10 to 80 degree. XRD patterns of different deposition temperature are regrouped in figure III.1. The influence of substrate ( $T_s$ ) on the films can be clearly seen and suggests that the films structural proprieties are very influenced by this parameter. The formation of kesterite CZTS with tetragonal structure was confirmed according to JCPDS (# 26-0575) cards. The peaks position were observed at  $2\theta = 28.6^\circ, 32.9^\circ, 47.5^\circ$ , and  $56.5^\circ$  corresponding to the crystal planes (112), (200), (303), and (312) respectively with a preferential orientation along (112) plane. We note that the same observation was obtained in [37,48]. The intensity of the main peak was increased with the increase of  $T_s$ . However, a similar variation was observed by M. Sun et al. [144]. As seen in figure III.1, as the temperature increase, the probability of secondary phases formation is increased. On other hand, we noted that the variation in substrate temperature leads to the appearance and the disappearance of some peaks. At lower deposited substrate temperature, we do not observe the formation of secondary phases. However, at  $T_s=330^\circ\text{C}$  we noted the appearance of ZnS phase at  $31.9^\circ$  position according to (#010677) card and no change for the other peaks. At higher substrate temperature ( $360^\circ\text{C}$ ), we remark the disappearance of ZnS phase and the appearance of  $\text{Cu}_7\text{S}_4$  phase at  $43.6^\circ$  (#720617), and CuS at  $46.5^\circ$  (#850620) which are conductive phases

with a decrease in the main peak intensity. While, the film deposited at 390 °C shows the best crystallinity of the film with a high intensity of the preferential orientation. Thereafter, we can conclude that the (112), (200), (303), (312), and (332) orientations emerge at low and high substrate temperature

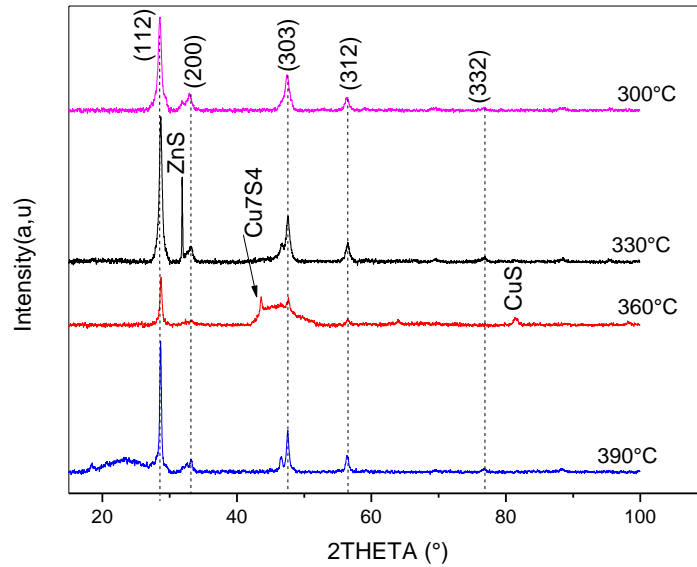


**Figure III.1:** XRD patterns of CZTS thin films deposited at various  $T_s$

The average crystallite size ( $D$ ) was calculated using Debye Scherer's formula (III.1) [145],

$$D = \frac{(K\lambda)}{\Delta(2\theta) \cdot \cos \theta} \quad (\text{III.1})$$

with:

$D$ : is the average size of crystallites.

$\lambda$ : Wavelength of X-rays.

$\Delta(2\theta) = \beta$ : the full width at half the maximum (FWHM) in radians of the X-ray diffraction peak.

$K$ : crystallite shape factor a good approximation is 0.9.

The distances are expressed in ( $\text{\AA}$ ) and the angles in radian.

Lattice strain was calculated from deformation formula, the deformation " $\epsilon$ " is linearly proportional to the strain as seen equation (III.2) [146]:

$$\sigma = C \times \epsilon \quad (\text{III.2})$$

Each component of the homogeneous deformation  $\epsilon_{ij}$  is related to the component  $\sigma_{ij}$  by the linear relation (equation III.2). Since the values of these constants are not always available in

the literature (Cij off CZTS), other approaches have been used to estimate the strain of the film, as the ratio of the deformation  $\varepsilon = \Delta d / d_0$ .

Knowing that ( $\Delta d$ ) is the offset of the inter plane with respect to its initial value ( $d_0$ ) in the case of a monocryalline. This difference is estimated from the position of the diffraction peak. The average microstrain was calculated using the following expression (eqt.III.3) [147]

$$\varepsilon = \frac{\beta \cos \theta}{4} \quad (\text{III.3})$$

The calculated values of strain ( $\varepsilon$ ), crystallites size (D) and FWHM are resumed in table III.1. As seen, when the substrate temperature increases the crystallites size increase and became larger which is an advantage for photovoltaic application, by reducing the recombination rate as well as the reduction of grain boundaries [148]. The increase of crystallites size with substrate temperature was observed also in [149-150]. It is generally accepted that the increase in substrate temperature is always accompanied by an increase in the crystallites size. However, during the growth of the films under a high substrate temperature, the species in growth have greater surface mobility which gives them the opportunity to form agglomerations of crystallites of large sizes. The diminution of crystallites size for the film grown at 330°C may be due to the presence of disorder in the film network.

<i>T<sub>s</sub></i> (°C)	<b>300</b>	<b>330</b>	<b>360</b>	<b>390</b>
<i>FWHM</i> [°2 $\theta$ .]	0.165	0.259	0.165	0.136
<i>Crystallite size</i> (nm)	51	33	54	60
<i>Strain</i> ( $\varepsilon$ )	0.0028	0.0044	0.0025	0.0020

**Table III.1:** FWHM, crystallite size and lattice strain of CZTS with different growth temperature

In figure III.2, we have illustrated the variation of strain and crystallites size with the variation of growing temperature. we can observe clearly the correlate between crystallites size and lattice strain, the increase of the last one is lead to a decrease in crystallites size, we can conclude that the crystallites size is controlled by the presence of strain in film network.

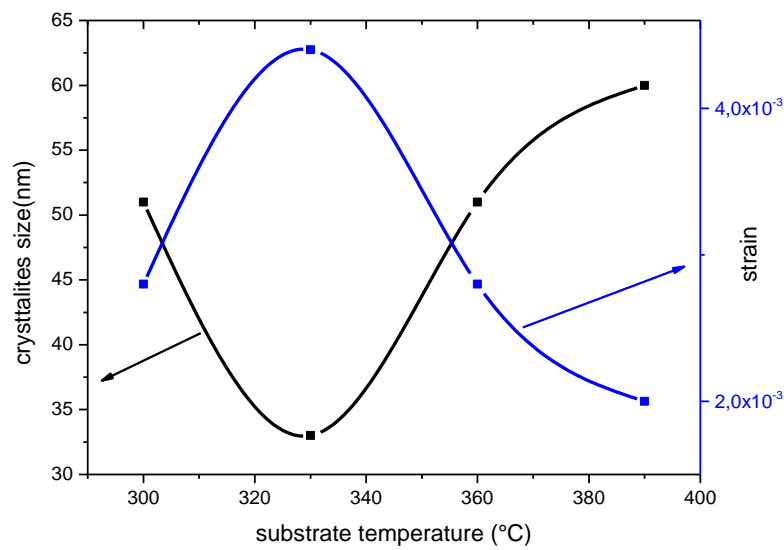


**Figure III.2:** variation of strain and crystallites size as function of substrate temperature

Figure III.3 (a, b), shows the XRD shifted of the preferential peak of CZTS thin film as function of substrate temperature and the shifted of peak position due to lattice strain. We can see evidently the shifted of the preferential peak towards the higher angles, the shifted of XRD peaks with the variation of substrate temperature was seen in various works as reported in [151], the shift is due to the variation of the intercross distance  $d$  which shifted the position of the peaks.

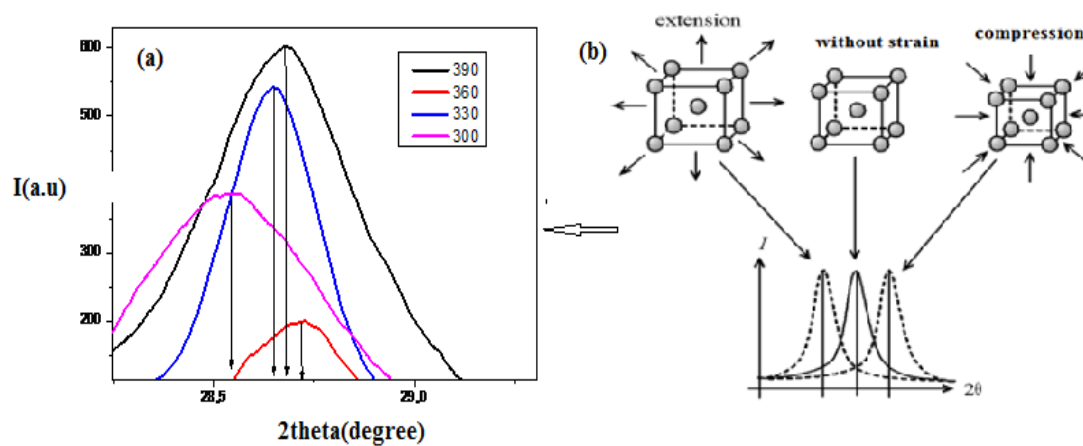


**Figure III.3:** (a) XRD shift of the preferential peak of CZTS as function of  $T_s$ . (b): Shift of the peak

***b. Raman analysis***

Figure III.4 depicted the Raman spectra of CZTS thin film elaborated at a different temperature, Raman shows the vibration mode and provide the confirmation of CZTS phase formation. Two Raman position peaks at 335 and 373  $\text{cm}^{-1}$  were observed and associated both to CZTS phase, the position of the peaks are in agreement with the reported ones cited in [58] which confirms the presence of a single phase CZTS with tetragonal structure. The Raman peak position at 473  $\text{cm}^{-1}$  is attributed to  $\text{Cu}_x\text{S}$  phase. However, an identical peak was cited by Fernandez et al. and Wang et al. [58,152]. This peak appears at a low and high temperature only whereas the films deposited at  $T_s=360$  and  $330$   $^\circ\text{C}$  show pure CZTS phase.

The insert graph in figure III.4 shows the shifted of Raman peaks as function of substrate temperature as we have seen in the case of XRD. It's evident that, as the temperature increase the shifted of the position toward high wavelength number is occurred. This shift may due to the apparition of  $\text{Cu}_x\text{S}$  film at  $300$   $^\circ\text{C}$  then it was hidden at  $330$  and  $360$   $^\circ\text{C}$ . While, this phase was appeared again at high temperature ( $390$   $^\circ\text{C}$ ).

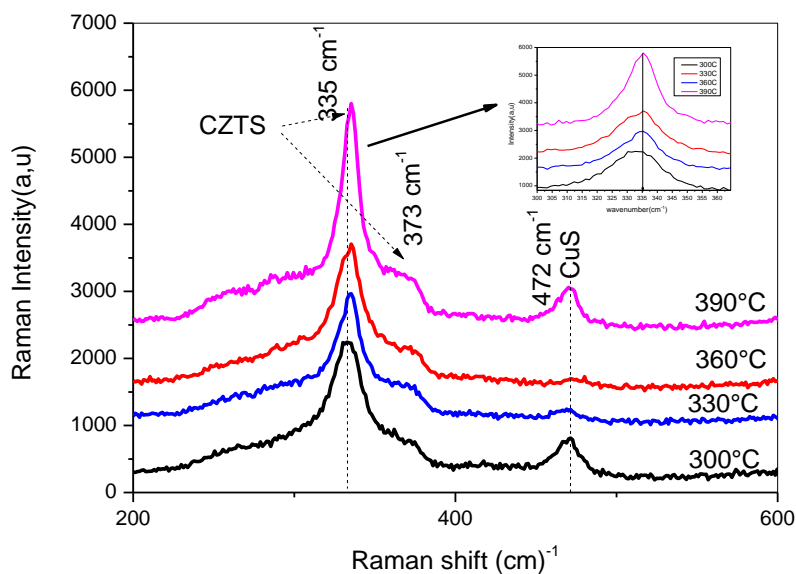


***Figure III.4:*** Micro Raman spectra of CZTS thin films deposited with various substrate temperatures.

Figure III.5 regrouped Raman and XRD shift value of the main peak with network strain as function of substrate temperature. As seen in the figure the shift of Raman and XRD have same trend, as the substrate temperature increase the shift of Raman toward the high wavelength number occurs and the shift XRD toward high angle was observed also. Nevertheless, the structural properties of CZTS thin film are affected by substrate temperature

and we can say that XRD and Raman peaks position are controlled by the presence of micro strain in film network.

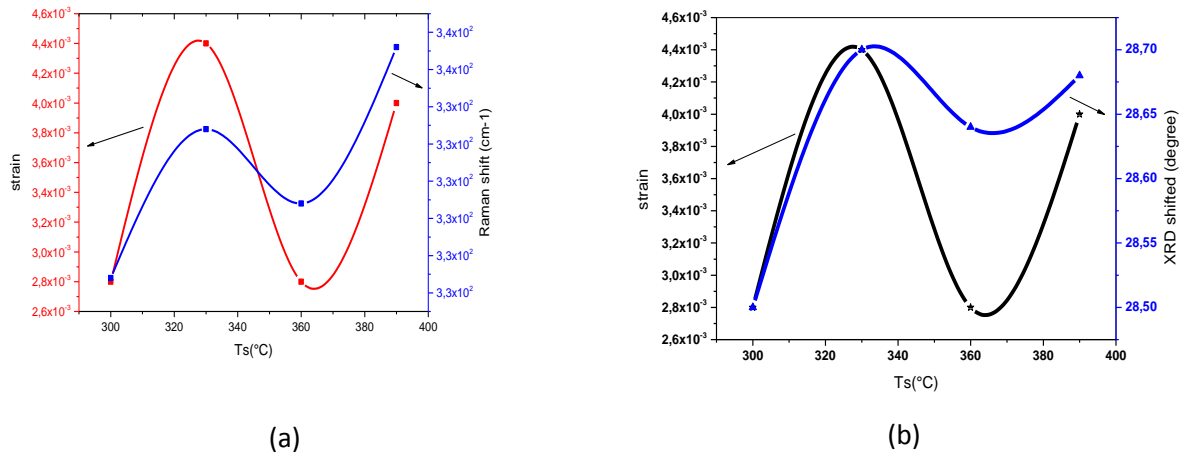


**Figure III.5:** lattice strain variation with: (a) Raman shifted and (b) XRD peak position shift of CZTS thin film as function of  $T_s$ .

### III.2. Morphological analysis

Surface morphology and roughness were carried out using Atomic Force Microscopy (AFM). The AFM images (figure III.6.a-d) show that films morphology changes with deposition temperature. The variation of the surface roughness is estimated from the 3D AFM images which are reported in figure III.6.(a-d), the size of the scanned area was  $(2 \times 2) \mu\text{m}^2$ . With increasing the growing temperature, CZTS thin films became rougher. Regardless, we can remark with the increase of substrate temperature, the surface roughness has increased with increasing the substrate temperature from 330 to 360 °C then the roughness increase by a factor of (2) for the film grown at 390 °C from 48 nm to 99 nm. The obtained results are in agreement with the results recorded by Kamoun et al [150], they reported a roughness value varied from 76 nm to 202 nm with increasing of substrate temperature. Thus, they explained the obtained results by the agglomeration at higher temperatures of the micro-crystallites observed at lower temperatures.

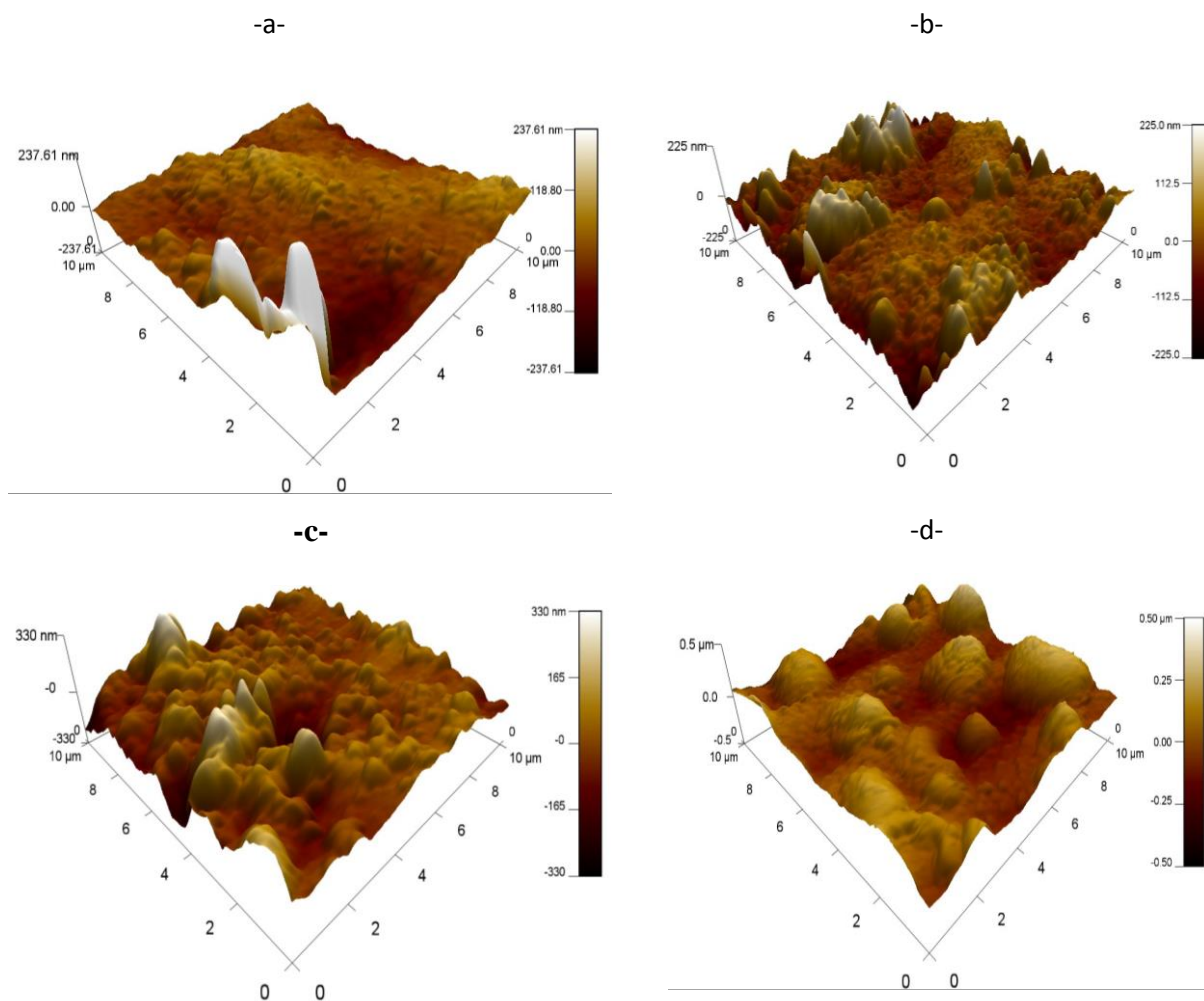


*Figure III.6: a-d, 3D AFM image of CZTS thin film deposited at various  $T_s$ (300-390°C)*

### III.3. Optical properties

#### a. Transmittance

The transmittance spectra of sprayed CZTS thin films have been measured using UV-Vis spectrometer are shown in Figure III.7.

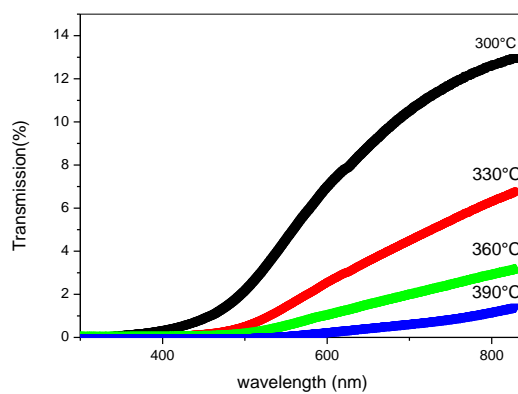


*Figure III.7: Transmittance spectra of CZTS thin film deposited at various  $T_s$*

The shape of transmission spectra of CZTS thin films deposited at various substrate temperatures is the same; we can distinguish two distinct domains of transmission according to the wavelength:

- A range of transparency located between 500 and 900 nm (visible range), the transmission decreases sharply and tends to values between 12 and 5% for the values of lambda higher than 500 nm.
- Then, the transmittance decrease rapidly and reach a value less than 1%. for the value of lambda less than 500 nm ( $\lambda < 500$  nm)
- The decrease of transmittance with the increase of growing temperature can be due to the increase of film thickness. The same variation was observed in several works [149.150]

### b. Absorption

In figure III.8 we have reported the variation of absorption coefficient ( $\alpha$ ) as function of the wavelength.

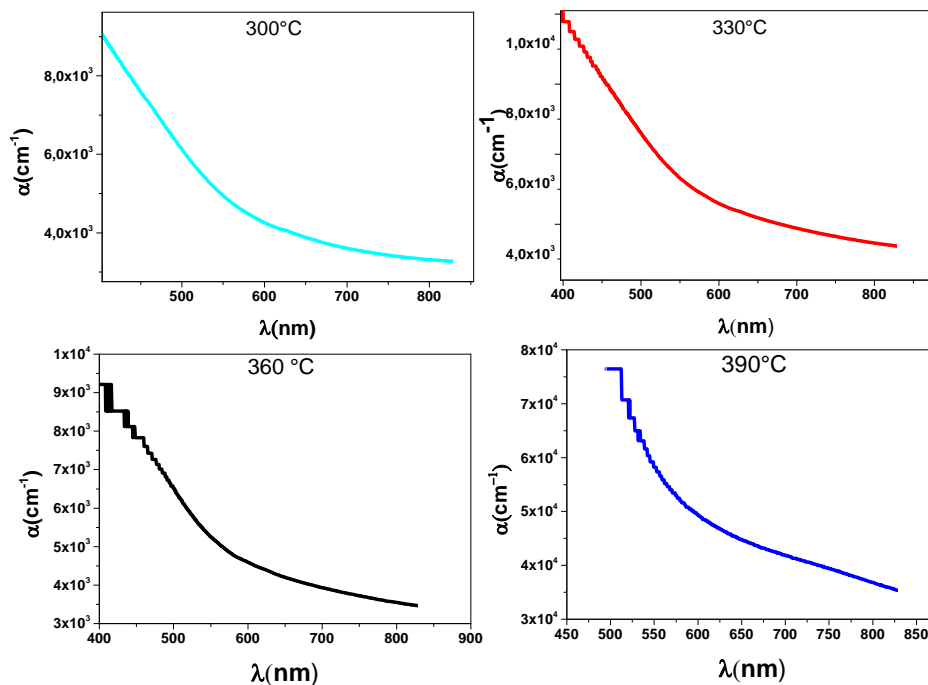


**Figure III.8:** Absorption coefficient ( $\alpha$ ) of CZTS films grown at various  $T_s$

It can be seen that all the films have relatively high absorption coefficients with a value highest than  $10^4 \text{cm}^{-1}$  in the visible range of the wavelength. The calculated absorption

coefficient is in agreement with the theoretical value and the experimental ones as reported in [37,48], which indicates the increase of the probability of the occurrence of direct transitions. It is also noted that the absorption coefficient increases with growing substrate temperature, film shows the highest absorption which can be attributed to the stoichiometry and the thickness of the elaborated film.

However, the films deposited at 390 °C show the highest absorption coefficient about  $8 \times 10^4 \text{ cm}^{-1}$ . The optimal optical proprieties of deposited CZTS films revealed that are strong candidate as a new absorber layer in thin film photovoltaic solar cells.

### c. Band gap energy

Gaps energies were deduced from transmission data by using Tauc's formula for direct band gap semiconductors (III.4) [20]:

$$(\alpha h\nu)^2 = B (E_g - h\nu) \quad (\text{III.4})$$

where  $\alpha$  is a absorption coefficient, B is a constant, h is Planck constant,  $E_g$  is the band gap energy, and  $h\nu$  is the incident photon energy.

The optical band gap ( $E_g$ ) of CZTS films is deduced from the plot of  $(\alpha h\nu)^2$  vs.  $h\nu$ , by extrapolation the straight line part of the graph ( $h\nu=0$ ) as seen in figure III.10. The direct band gap energy for CZTS thin films was determined and their variation is showing in the insert figure of figure III.9.

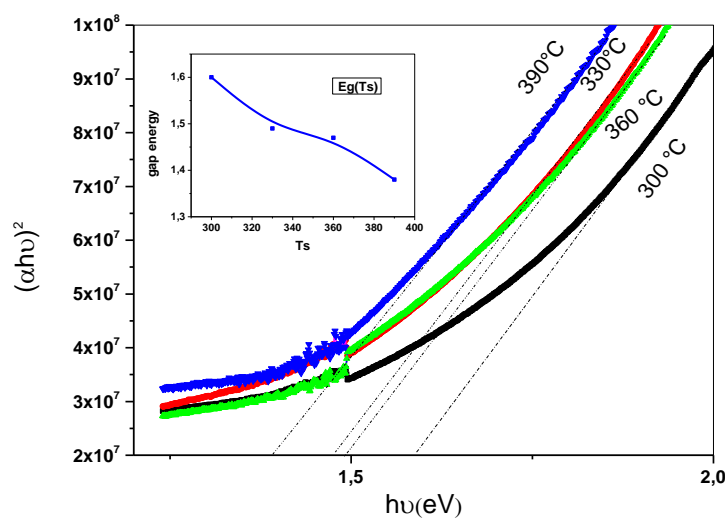


**Figure III.9:** Gap energy determination of CZTS thin film deposited at various  $T_s$

From the graph, the band gap is found to decrease from 1.6 to 1.38 eV as the substrate temperature increase that can explain by the increase of the thickness of films. However,

Kahraman et al. [153] and Touati et al. [154] had reported the same behavior of the gap energy of CZTS with the variation of deposited temperature. The extracted value of CZTS gap energy is near to the theoretical value of 1.5 eV [149] and the reported values using experimental work as cited by Sheng et al. [155]. Shined et al. [156] has reported that the change of the gap energy with the temperature can be due to a change in homogeneity and crystallinity of the films. The change in thickness is as a result of a change in particle sizes resulting in a change in band gap as cited by Lydia and Reddy [157]. The band gaps of our films are quite close to the optimum band gap energy required for a solar cell, indicating that CZTS thin film is very promising material for thin film solar cell applications.

#### III.4 Electrical properties

The electrical parameters such as: conductivity, carrier concentration, and hole mobility were measured by Hall effect in the dark and at room temperature, the whole deposited films indicate that's CZTS compound is a p-type semiconductor, the conductivity of the films was increase with the increase of deposited temperature, the value of the films conductivity is higher than  $100 (\text{cm}.\Omega)^{-1}$  and it can be due to Cu rich composition as reported by Tanaka et al.[71], whereas the carrier concentration was varied from  $10^{16}$  to  $10^{18}\text{cm}^{-3}$ , which is in agreement with reported value by Fernandez et al. [68]. Own films characterized by a high mobility compared to the cited one in [72]. The high mobility can refer to the presence of CuS and  $\text{Cu}_7\text{S}_4$  phases in the film which are characterized by a high conductivity and large crystallites size. The conductivity ( $\sigma$ ), carrier concentration( $\rho$ ), and Hall mobility ( $\mu$ ) values are regrouped in table III.2

$T_s(^{\circ}\text{C})$	$\rho/\text{cm}^3$	$\mu (\text{cm}^2/\text{vs})$	$\sigma(\text{cm}.\Omega)^{-1}$
300	$1.26 \cdot 10^{18}$	$7.8 \cdot 10^2$	$1.5 \cdot 10^2$
330	$8.85 \cdot 10^{16}$	$2.75 \cdot 10^3$	3.9
360	$2.59 \cdot 10^{16}$	$7.09 \cdot 10^2$	2.94
390	$2.35 \cdot 10^{16}$	1.57	1.8

**Table III.2:** The Conductivity, carrier concentration and Hall mobility as function of growing temperature of CZTS films

Figure III.10 reported the variation of the measured electrical parameters of CZTS thin films, as seen the carrier concentration and the conductivity follow faithfully the trend of the strain, it's clearly that the conductivity is controlled by the number of free carriers in the bulk, and both parameters decrease with the increase of  $T_s$  which can due to the apparition of secondary phases in the film, whereas the mobility increases and reaches a highest value equal to  $2.10^2 \text{ cm}^2/\text{Vs}$  then decreases with the substrate temperature until  $1.57 \text{ cm}^2/\text{Vs}$  at  $390^\circ\text{C}$ .

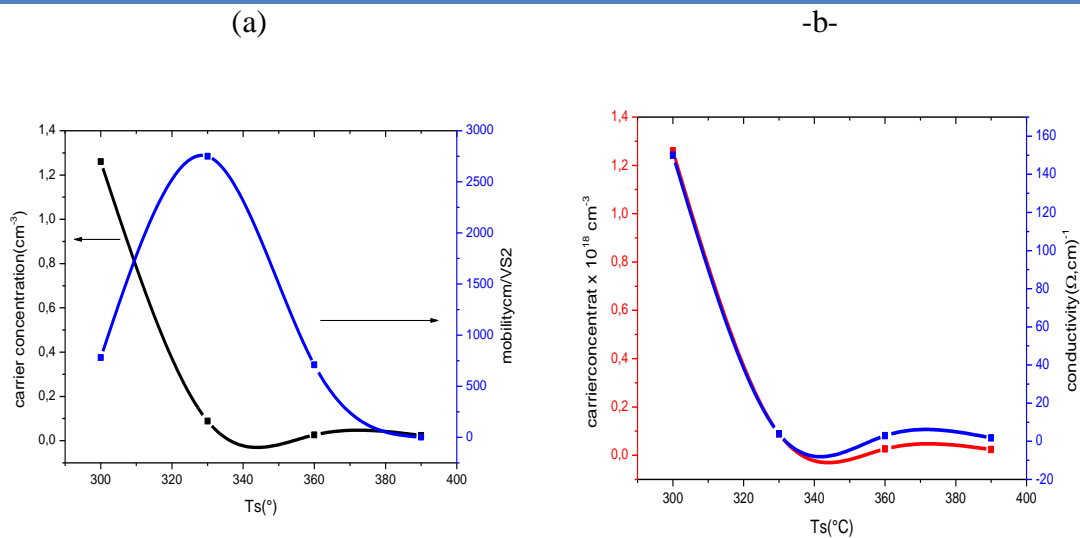


**Figure III.10:** Carrier concentration and (a) mobility : (b) the conductivity as function of substrate temperature

### III.2 Deposition time effect

The effect of deposition time on CZTS thin films properties was studied in the following paragraphs. Deposition time was varied from 15 to 45 minutes without change on the other experimental conditions.

#### III 2.1 structural properties

##### a. X Ray Diffraction

In figure III.11, XRD diffraction patterns of CZTS films elaborated with different deposition time are regrouped. We can clearly observe the reliance of the structural properties with

deposition time. The whole prepared films show a dominate peak with strong orientation along (112) plane situated at 2 theta equal to  $28.6^\circ$  and two other small peaks associated to (200) and (312) planes which are all related to kesterite CZTS films and suggested that our films are polycrystalline. The prepared films have indeed tetragonal structure according to (#26-0575) card.

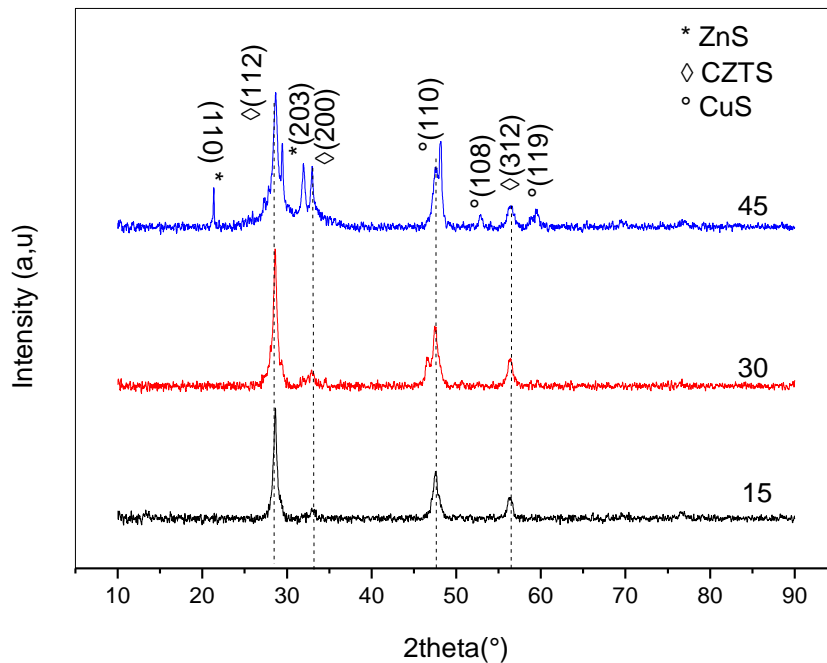


**Figure III.11:** XRD patterns of CZTS thin film deposited at various Deposition time

With further increasing deposition time, the peak related to the plane (112) became more intense. When, the deposition time increase, we observed the emergence of zinc sulfide (ZnS) phase along (203) and (110) planes according to (#010677) card which is appeared in the film growing for 45 minute, knowing that the energy formation of ZnS phase is about  $-1.9$  eV which is relatively high, that's why this phase need more time to be formed, whereas CuS secondary phases has grown along (119), (108), and (110) planes according to (PDF#850620). Therefore, CuS thin film characterized by a low formation energy as equal as to  $-0.51$  eV, CuS phase has appeared in the whole prepared films with an important intensity along (110) plane. While, the quaternary compound CZTS material has the higher formation energy with a value about  $-4.59$  eV [158], meaningful that as the constituent elements in the compounds increases their formation energy increase and as results the possibility of the formation of this phase became hard. Further, CuS secondary phases generally appears during

the growing of CZTS thin films and generally refer to Cu rich condition as reported by Tanaka et al. [71], the intensity of CuS phase along (110) plane increase with the increase of deposition time. We can conclude that the film deposited for 30 minute presented the better structural properties with lower number of secondary phases.

### b. Raman analysis

Raman spectroscopy conducted to distinguish the secondary phases which are not detected using X Ray Diffraction. Figure III.12 regrouped the Micro-Raman spectra of CZTS films coated on glass substrate for different deposition duration such as 15, 30, and 45 minutes.

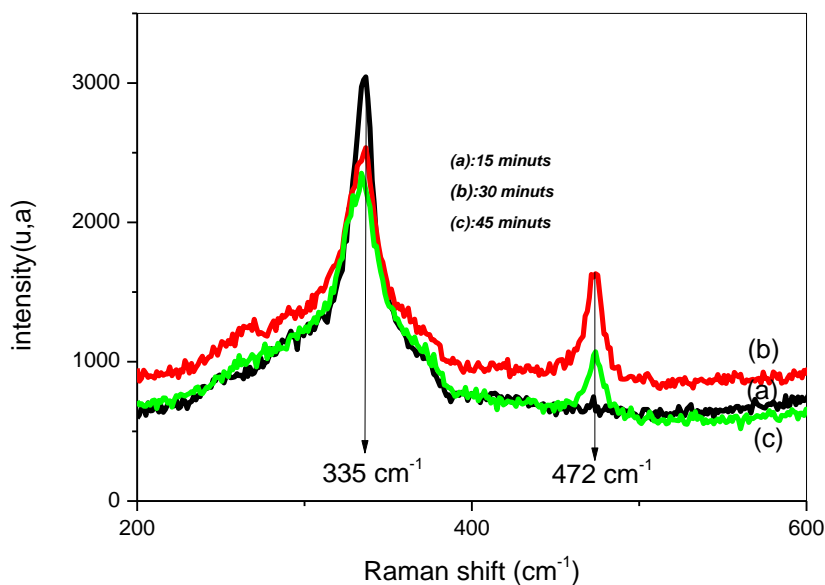


**Figure III.12:** The Raman spectra of CZTS elaborated at various deposition times.

The Raman spectrum of the whole films are characterized by a strong peak position located at  $335\text{ cm}^{-1}$  which confirmed the formation of CZTS films with tetragonal structure according to a variety of work reported in [57-58]. While, the additional peak at  $472\text{ cm}^{-1}$  is attributed to the  $\text{Cu}_2\text{S}$  binary phase, the same results were reported in [58,152]. The formation of cupric sulfide secondary phase is due to the excess of copper in the starting solution by comparison to zinc, no ternary phase such as  $\text{Cu}_2\text{SnS}_3$  ( $318\text{ cm}^{-1}$ ) which reported by Fernandes et al [61] was detected in our films. The intensity of the main peak decreases with the increases of deposition time which can due to the apparition of  $\text{Cu}_2\text{S}$  secondary phase.

### III.2.2 Morphological properties

The morphology of the films (CZTS) was analyzed by Scanning Electron Microscopy (SEM). SEM imaging makes it possible to study the morphology of the studied materials surface.

Figure III.13 shows SEM images of CZTS layers deposited on glass at various deposition times.

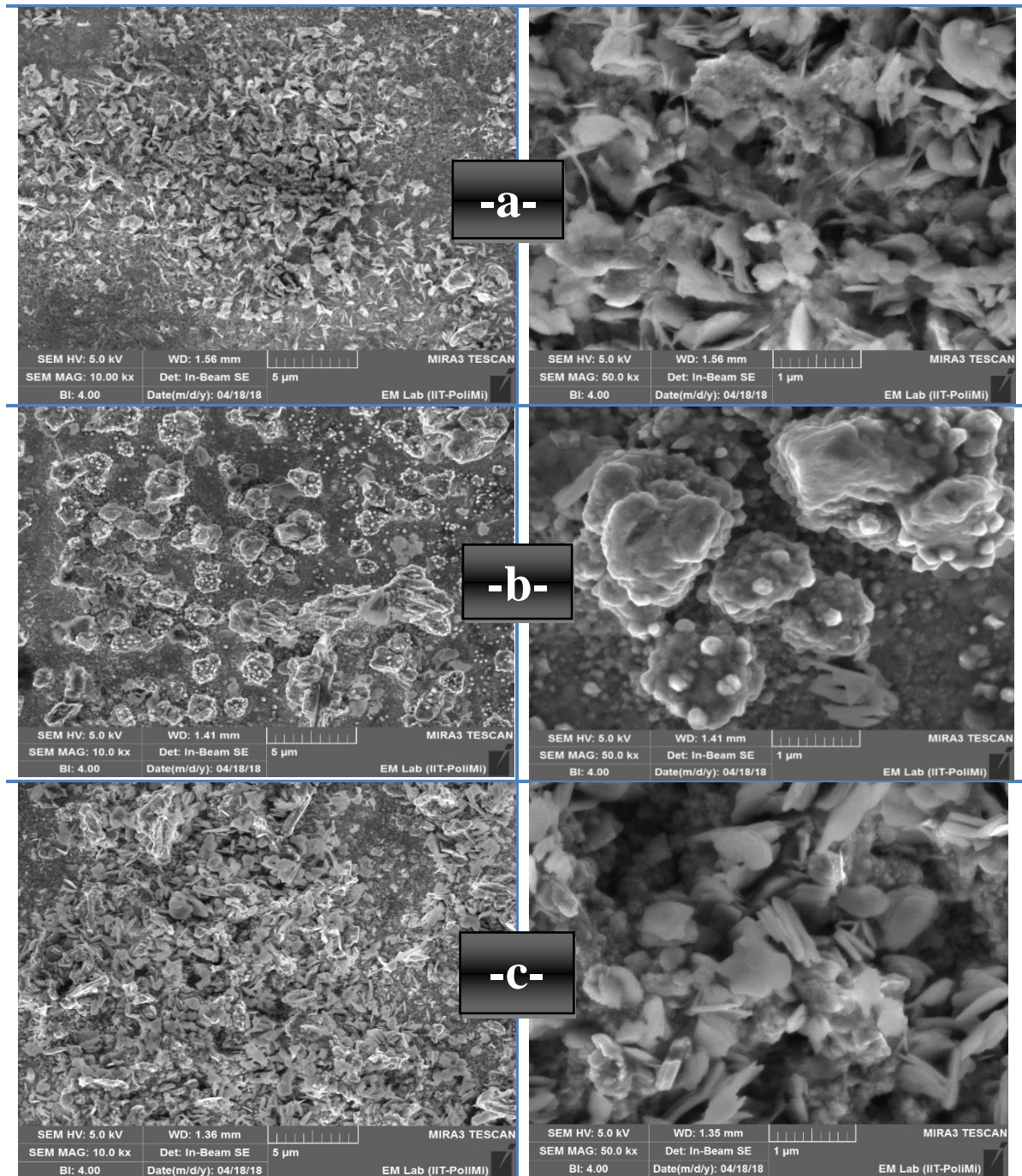


*Figure III.13: a, b, and c, SEM images of CZTS thin film deposited at 15 min, 30 min, and 45 min.*

From these images, it is obvious that the increase in the deposition time leads to a quiet change of the morphology and the structure of the films. We noticed that the surface of the layer is regular with a low roughness. It is also clear that the size of the grains is very small. According to the figure, it is clear that the films has a non-uniform distribution of

agglomerated particles with well-defined limits. We can see also the appearance of large flat grains (lamella). From this study it can be concluded that the morphology of CZTS thin film surface is highly dependent on deposition time.

### III.2.2. Optical properties

#### a. Transmittance

Figure III.14 shows the transmittance spectra of CZTS thin film deposited at various deposition time in UV-Vis range, the films transparency decrease from 80 to 10% with increasing of deposition time for the wavelength over 600 nm, then the transmittance decrease rapidly for the wavelength lower than 600 nm and reached value less than 10 % for the whole films. However, the transmission can express as  $e^{-\alpha d}$  with d is the thickness and  $\alpha$  is absorption coefficient. Hence, the decrease of transmittance values with the increase of deposition time is referring to the increase of film thickness.

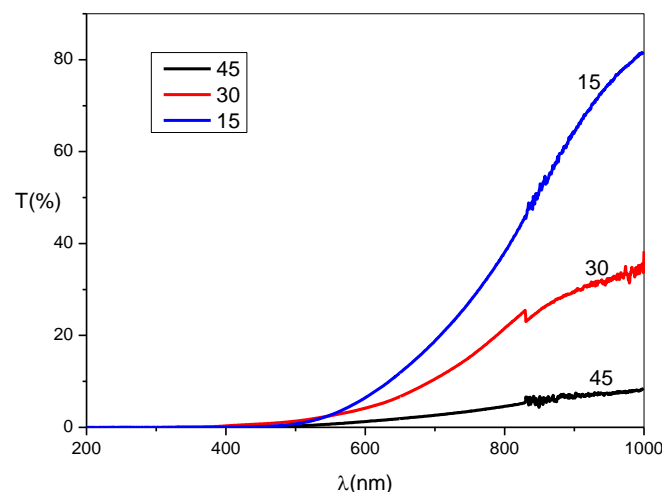


*Figure III.14 Transmittance spectra of CZTS films deposited at various deposition times*

#### b. Absorption

Figure.III.15 displays the variation of the absorption coefficient as function of wavelength, it evident from absorption spectra that CZTS material is a good absorber of light radiation for application in solar cells, thus as seen in figure III.15, the absorption coefficient of the whole deposited films is higher than  $10^4 \text{ cm}^{-1}$ . The obtained values of CZTS absorption coefficient are in agreement with the reported values by several authors [37-48]. Knowing that, an increase in deposition time allows more materials to be deposited onto substrates as well as

thicker films will be formed and as result the increase of absorption coefficient. The high absorption of our films is one of required properties for the use of this material as an absorber layer in thin film solar cells.

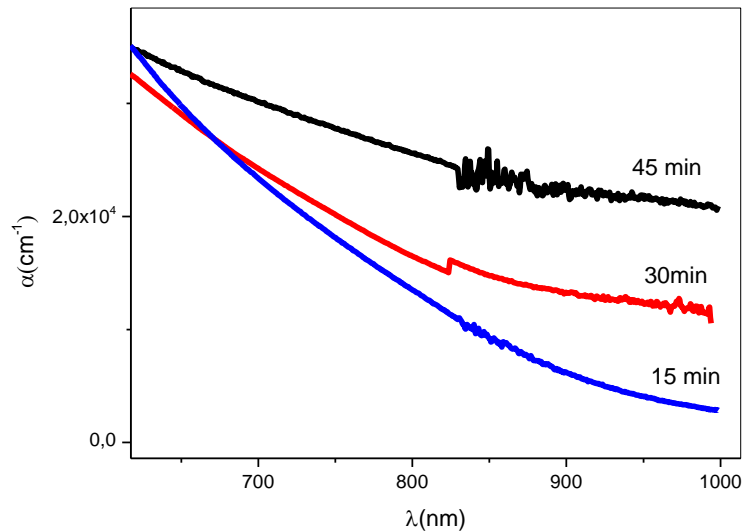


*Figure III.15: Absorption coefficient of CZTS films deposited at various deposition times as function of lambda*

### c. Band gap energy

Fig III.16. Presents the variation of  $(\alpha h\nu)^2$  as function of deposition time. As can be seen from the figure, the gap energy varied slightly with deposition time, it decreases with the increases of substrate temperature from 1.6 to 1.3 eV.

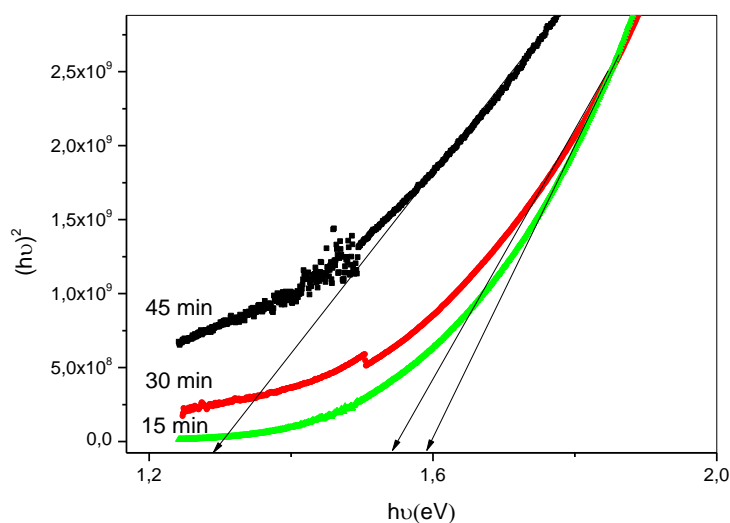


*Figure III.16 :  $(\alpha h\nu)^2$  vs.  $h\nu$  variation as function of deposition time*

The variation of the gap energy of the film is referring to variation of film composition with the increase of deposition time. The reduction of the band gap energy for the film deposited for 45 min may due to the presence of CuS secondary phase which have low band gap energy. The extrapolated optical band gap values are in suitable rang for photovoltaic application.

### III.2.3 Electrical properties

The electrical properties of CZTS thin film were studied using Hall effect in the dark and at room temperature with a current equal to 0.1  $\mu\text{A}$ . The whole samples show p-type conductivity according to positive sign of Hall coefficient. The conductivity ( $\sigma$ ), mobility ( $\mu$ ), and holes concentration ( $\rho$ ) are resumed in Table III.3, It is well known that the conductivity is related strongly to the composition of the film.

$Dt(\text{min})$	$\rho/\text{cm}^{-3}$	$\mu(\text{cm}^2/\text{vs})$	$\sigma (\text{cm}.\Omega)^{-1}$
15	$5.10^{18}$	9.18	7.3
30	$1.6 10^{18}$	$2.3 10^2$	6.4
45	$1.49 10^{18}$	$5.2 10^2$	$1.24 10^2$

**Table III.3:** Electrical parameters of CZTS thin film with different deposition time.

The  $\text{Cu}_{\text{Zn}}$  intrinsic defect is the responsible one of the p-type conductivity of kesterite which due to their lower formation energy compared to the others intrinsic defects such as  $\text{V}_{\text{Cu}}$ ,  $\text{V}_{\text{S}}$ ,  $\text{Zn}_{\text{Cu}}$ ,  $\text{Sn}_{\text{Cu}}$ , ...etc. The increase of the conductivity with deposition time can be explained by the filmcomposition variation in one hand and to the surface roughness increase in the other hand.

Fig III.17 shows the variation of both carrier concentration and mobility as function of growth duration, the carrier concentration values are in the order of  $10^{18} \text{ cm}^{-3}$  which is in accord with the reported values by Lui et al [69] and Fernandes et al [68].

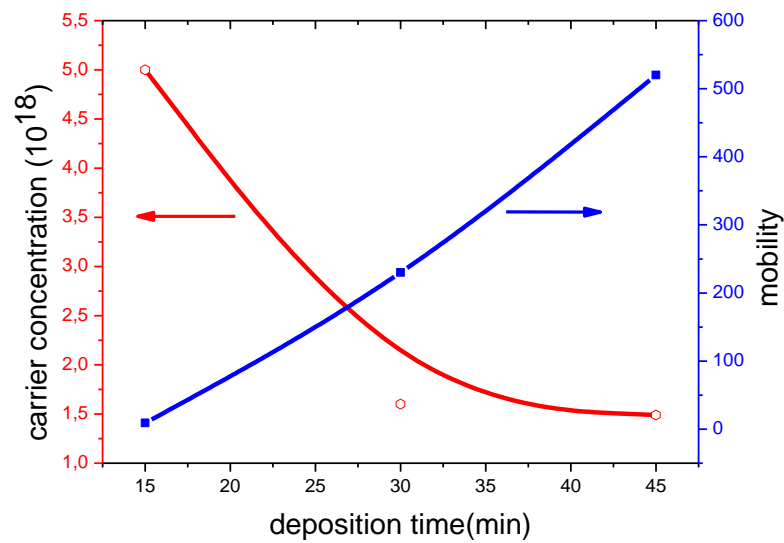


**Figure III.17:** The variation of carrier concentration and mobility as function of deposition time

Holes nobilities of CZTS varied from 9 to 520  $\text{cm}^2/\text{VS}$  for the film deposited at 45 minutes whereas the film deposited for at 15 minutes shows an optimal value of mobility which reported generally for CZTS film [72], we know that the mobility of free carriers in film network is controlled by the number of carriers and the grain size of the film. The films deposited at 30 and 45 minutes show high value of mobility which can refer to the presence of CuS conductive phase which characterized by large crystallites size. Further, the mobility of free carriers increases with the decrease of carrier concentration and the increase of the conductivity for the samples deposited for 45 minutes, since the film conductivity was always found to be higher than the typical values reported in the literature, this increase can refer to presence of conductive secondary phases such as CuS and to the Cu rich: Zn poor condition.

### ***III.3 Copper concentration effect***

In this part, we have studied and discussed the results obtained in the study of copper salt concentration effect on the structural, optical, and electrical properties of CZTS thin films. The samples are denoted as (C1, C2, C3 and C4) corresponding to the preparation molarities 0.01, 0.15, 0.02 and 0.25 M respectively.

### III.3.1 Structural properties

The XRD diffraction patterns of CZTS thin films prepared with different copper concentration salt are shown in Figure III.18, the dependence of the structural properties on copper salt concentration is observed clearly from the evolution of phases with copper molarity. The intense peak position at  $2\theta=28.6^\circ$  along (112) plan confirmed the phase formation of kesterite CZTS according to (JCPDS 26-0575) card with the apparition of other peaks associated to CZTS with lower intensity at (200) and (312) planes.

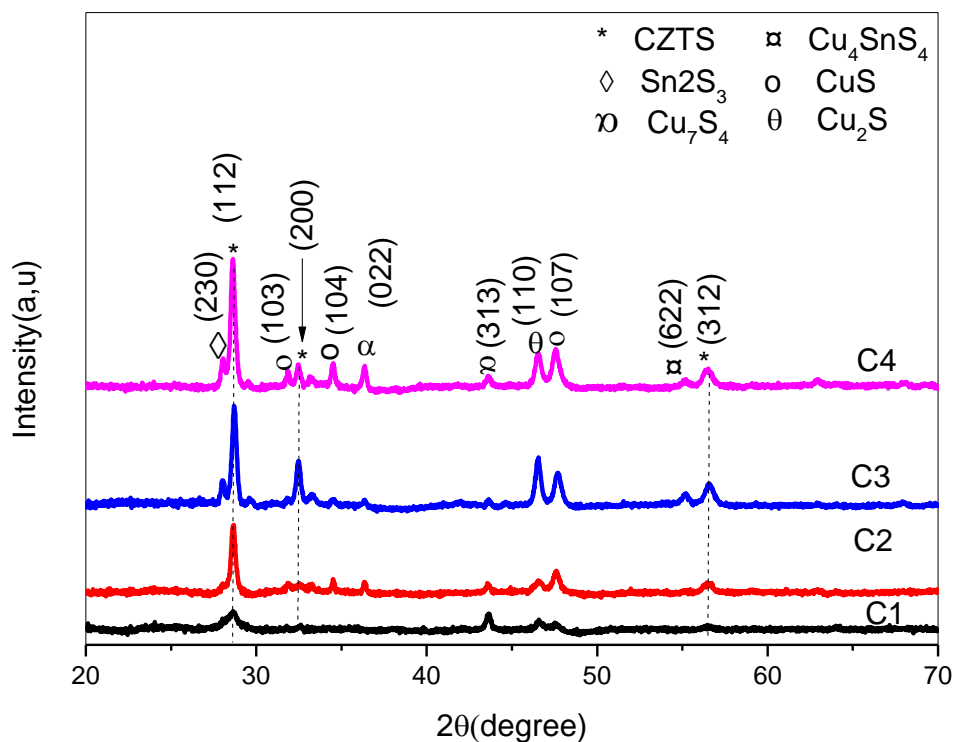


**Figure.III.18.** XRD patterns of CZTS thin film with various copper concentrations

As seen in figure III.18, as the copper molarities increase the intensity of the preferential orientation along (112) increase, the same results were observed by Mkawi et al. [159]. Furthermore, as the copper molarity increase the emergence of secondary phases increase, such as CuS (PDF#850620), Cu<sub>2</sub>S (PDF#722276), Sn<sub>2</sub>S<sub>3</sub> (PDF#301378) Cu<sub>4</sub>SnS<sub>3</sub> (PDF#7290584) and annilite phase Cu<sub>7</sub>S<sub>4</sub> (PDF#720617) the same secondary phases was reported by Mbhosel et al. [130]. The presence of the CuS (or Cu<sub>2</sub>S) and annilite phase Cu<sub>7</sub>S<sub>4</sub> in CZTS thin film is likely to be related with the Cu-rich condition in CZTS as reported by Lin Sun et al. [160]. Mkawi et al. observed the effect of copper concentration on the properties of CZTS films deposited by electrochemical method and found that the formation of such

undesired secondary compounds is due to incomplete conversion of sulfides [159]. The presence of

$\text{Cu}_{2-x}\text{S}$  phases is very detrimental to the performance of the absorber layer and especially the solar cell performance, since they are degenerate semiconductors, but they may be removed by chemical etching in aqueous cyanide.

The crystallites sizes (D) were calculated from XRD data using (III.1) formula, while the average lattice microstrain was calculated using (III.3) formula, the calculated values are resumed in Table III.4.

	<i>Crystallite size(nm)</i>	<i>Strain</i>
<i>C1</i>	33.48	0.0044
<i>C2</i>	83.74	0.0018
<i>C3</i>	83.76	0.0017
<i>C4</i>	51	0.0028

**Table III.4.** Crystallites size and strain of CZTS thin films as function of copper salt concentration

From table III.4, we can see that as the copper concentration increase the crystallite size increase and reach a maximum value of 83.76 nm then it decreases for the sample C4 which refer to apparition of many secondary phases. The sample C3 with 0.02 M of copper salt shows the best crystallinity of the film, it can be seen that the increase of copper molarity enhances the structural properties by increasing crystallites size but for a certain value undesirable conductive phase will appear such as Cu-S and Cu-Sn-S phases which have negative effect on the film properties and on solar cell performance which will create shunting paths through the solar cell or the absorber layer. Camara et al. [161] have synthesized CZTS nano-particles with different copper concentration and the best result were found for the one with Cu rich condition but for a high value of copper concentration the film became amorphous and the structure of the film was degraded. M.Bhosele et al. [130] was studied the effect of copper concentration on CZTS solar cells and reveal that the efficiency increase with the increase of copper salt. Thus, the enrichment of the Cu concentration leads to formation of faster crystal growth and enhance the density of nucleation for a single crystal as result the increase in film thicknesses

Figure III.19.a, illustrate the shifted of the preferential peak position with the increase of copper concentration, as seen, as the copper concentration increase the shifted of (112) peak position increase toward the high angles because of the formation of secondary phases and the presence of internal lattice strain in the films. While, figure III.19.b displays the variation of both XRD shift and lattice strain as function of copper concentration.

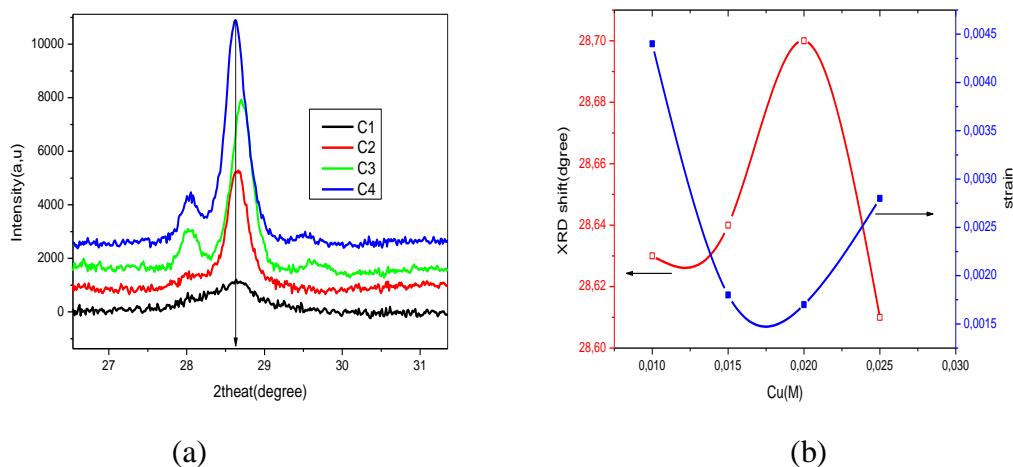


**Figure III 19:** (a) The variation of (112) peak position in XRD pattern of CZTS films as a function of Cu molarity and ( b) their variation with lattice strain.

As seen in figure III.19.b, the sample C1 show the high strain value, which are probably a result of the Cu poor composition of the layer and it is associated to the presence of a disordered kesterite phase in the film [162]. Then lattice strain decrease steeply for the sample C2. After that, the strain increase slightly for the sample C3 with a strain value equal to 0.0017. The sample C4 show the lower values of XRD shift and a considerable value of lattice strain. Hence, lattice strain in film network is related to crystallites size and the disorder in film network. The sample C3 and C2 have the large crystallites size and lower strain values whereas samples C1 and C4 show the worst crystallographic properties. The increase of copper concentration lead to the appeared of many secondary phase as seen in XRD pattern of C4 sample. Further, in quaternary compound the composition of the film plays an important role and affect strongly on the film properties. Hence, we can conclude that the choice of a moderate copper concentration is important for gotten good properties of CZTS thin film which are required to enhance CZTS solar cell's efficiencies.

### III.4.3 Optical properties

#### a. Transmittance

Figure.III.20. Shows the transmittance spectra of CZTS thin films with varied copper molarities in UV-Visible range wavelength (200-1000 nm), the whole films exhibit a low transmittance in the UV-visible range (less than 18 %) for the high wavelength and less than 4 % for the range of  $\lambda$  lower than 600 nm which is decrease with the increase of copper content and as consequence the increase of film thickness.

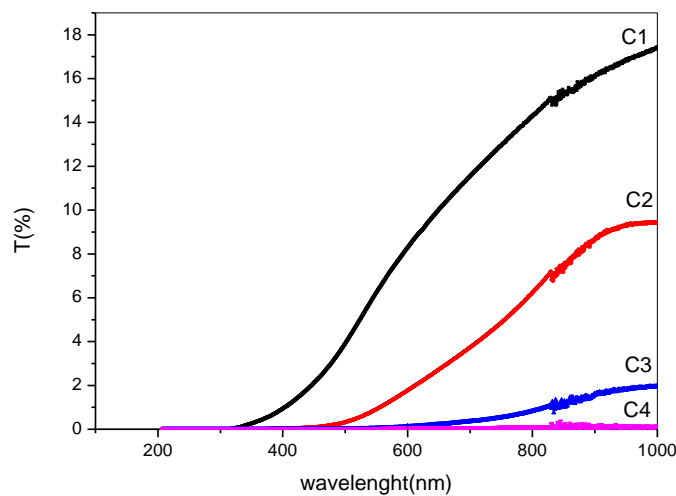


**Figure III.20:** Transmittance spectra of CZTS thin with different copper concentration.

The films are characterized by high absorption coefficient more than  $10^4 \text{ cm}^{-1}$  and near  $10^5 \text{ cm}^{-1}$  for the film with high copper concentration which is in agreement with the reported work in [37, 48]. We can resume that the molarity of copper salt affect strongly on the optical properties of CZTS and especially in the transparency of the film, the film deposited with a copper concentration equal to 0.025 M show a value about 0 % of transparency.

#### b. Band gap energy

The optical band gaps of CZTS thin films have been determined, as shown in Figure.III.21, from the fitting of transmission data, the extracted of gap energy has been done using Tauc's formula for direct band gap semiconductors (III.4). The obtained values of the optical band gap energy were found equal to 1.9, 1.7, 1.5 and 1.2eV when the copper concentration equal to: 0.01,0.015,0.02, and 0.025 M.

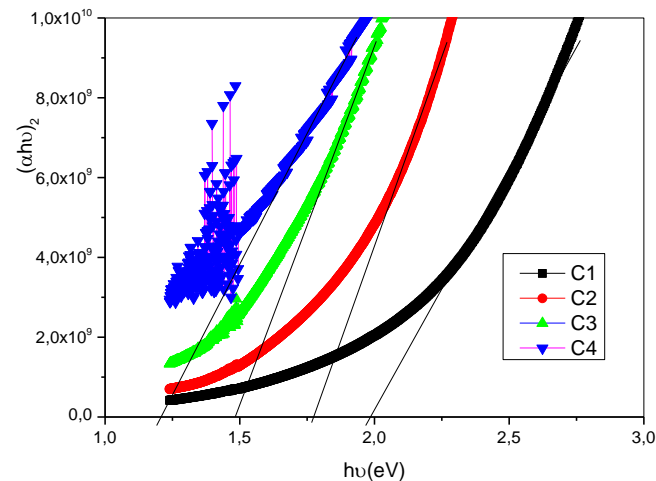


**Figure III. 21:** Tauc's plot of CZTS thin film with different copper molarities

The decrease in the band gap energy with the increase of copper concentration may refer to many reasons: the increase of films thickness, increase in the crystallinity (table.III.4) and also apparition of secondary phase (CuS) which has narrow band gap energy. It should be noted that the disorder between Cu and Zn cations is occurs generally in CZTS network with the variation of the film compositions which affect the band gap energy as cited by Scragg et al [163]. The moderate gap's values are required for a good absorber layer and match well with solar spectrum and specially the sample contain 0.02 M of copper salt.

### III.3.3. Electrical properties

The electrical conductivity, hole concentration and mobility were measured using Hall Effect measurement. The p-type conductivity of CZTS thin film is confirmed from the positive sign of hall coefficient. Table.III.5 resumed the obtained values for CZTS thin film with different copper concentration. As can be observed the electrical properties is largely sensitive to copper salt concentration. It has to be pointed out that the excess of Cu in the film favorite the formation of different defects and especially  $Cu_{Zn}$  and  $V_{Cu}$  intrinsic acceptor defects. As seen, as copper molarity increase the conductivity increased from 180 to 400 ( $\Omega \cdot cm$ )<sup>-1</sup>, the conductivity of our films is higher than the reported values in [70,77]. The high values of the conductivity can refer to the Cu rich condition, the high concentration of holes in film network and the presence of CuS conductive phase as cited by tanaka et al. [71], whereas the carrier concentration varied in the range  $10^{20}$ - $10^{21} \text{Cm}^{-3}$  which as higher than the reported value which are in the range  $10^{16}$ - $10^{18} \text{cm}^{-3}$ . [ 67-69].

	$\rho(\text{Cm}^{-3})$	$\mu(\text{cm}^2/\text{v.s})$	$\sigma (\Omega .\text{cm})^{-1}$
C1	$1.22 \cdot 10^{20}$	9.4	$1.8 \cdot 10^2$
C2	$1.6 \cdot 10^{21}$	0.53	$1.9 \cdot 10^2$
C3	$1 \cdot 10^{21}$	0.8	$2 \cdot 10^2$
C4	$9.94 \cdot 10^{20}$	2.67	$4 \cdot 10^2$

**Table III.5:** Carrier concentration, mobility and conductivity of CZTS thin film.

Figure III.22.a reported the variation of the carrier concentration and mobility as function of copper molarities, these two parameters are varied in contracted way.

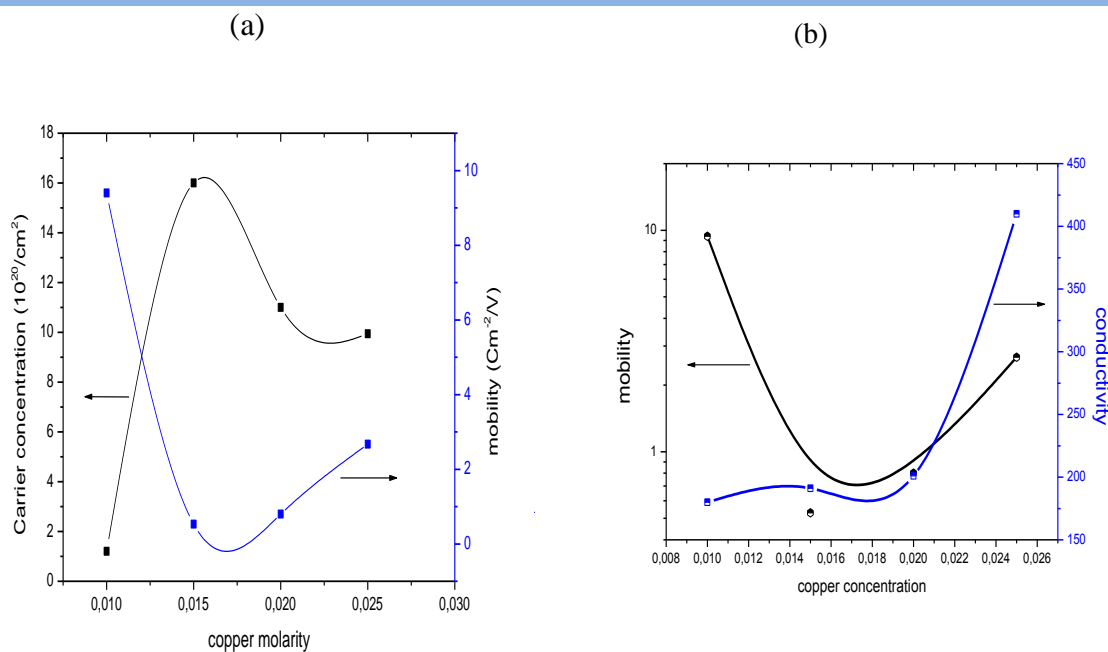


**Figure III.22.** (a, b) Variation of carrier concentration and conductivity with mobility as function of copper concentration

As the carrier concentration augments, the mobility increases which due to the high number of free carriers which limit their movement in the film network. Whereas in figure. III.22.b we have reported the variation of both conductivity and carrier concentration as function of copper concentration. In chalcopyrite thin films, it is generally observed that conductivity of films can be improved by increasing the concentration of copper. We speculate with increasing Cu concentration in the starting solution the number of  $\text{Cu}_{\text{Zn}}$  defect increase which

caused the increase of free carriers as seen in Table III.5. It's evident that the conductivity increase with the increase of free carrier's mobility.

### III.4 Zinc molarity effect

Kesterite thin films with different zinc content have been prepared by varying the zinc acetate molarity as discussed in chapter II. Films are noted CZTS1, CZTS2, and CZTS3 for zinc concentration values 0.01, 0.015, and to 0.025 M. Their related results with discussions are presented in the following paragraphs

#### III.4.1 Structural properties

- X-Ray Diffraction

The XRD patterns of CZTS thin films obtained at different zinc concentration are shown in figure.III.23 the diffraction angles varied from 20 to 80 °.

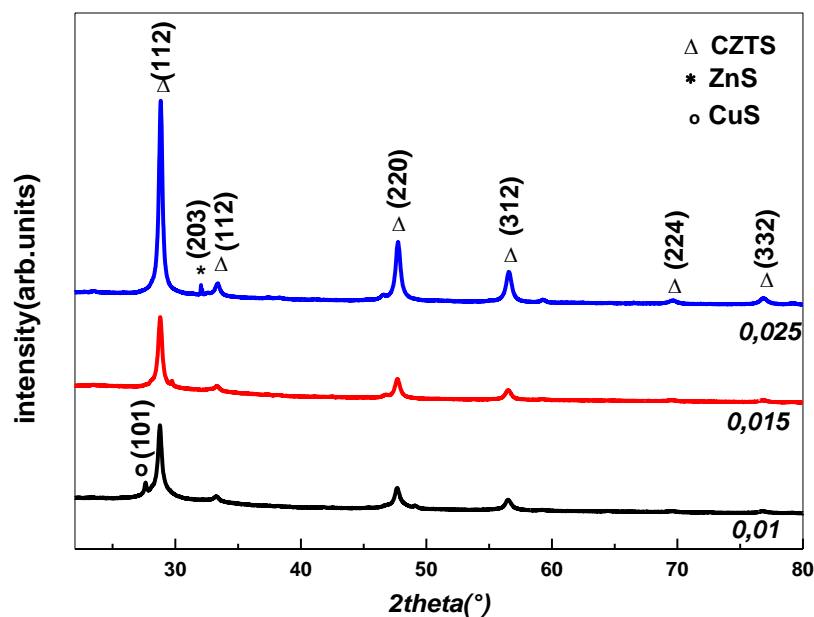


*Figure III.23: XRD patterns of CZTS thin films prepared under different zinc salt concentration*

Actually, it is well known that it is hard to clearly detect secondary phases [164,165]. Due to the negative influence of secondary phases on CZTS based solar cell performances, one of the

major challenges for these solar cells is the growth of single phase material. In the case of films prepared at low Zn concentration, no secondary phases were detected, while, as the zinc acetate concentration in the solution increases the tendency of undesired phases formation increases. CuS is the first formed secondary phase (according to (JCPDS-85-0620)). CuS phase formation in this sample is due to the fact that the film is prepared in Cu rich condition since the Zn source precursor molarity is lower than Cu one. While, with Zn molarity increase, ZnS phase (JCPDS-01-0677) is formed in the detriment of CuS one. The same observation of the effect of Zn in the composition of CZTS thin films prepared by sequential reactive sputtering have been outlined by Sing et al [166] with varying the Zn thickness layer, at low Zn content, secondary CuS is formed, while with increasing Zn concentration the ZnS phase appears then.

In a theoretical calculation of the defect formation and stoichiometry of CZTS thin films, Chen et al. [63] have climbed that chemical-potential control is very important in growing good-quality crystals with no secondary phase formation and low-defect density. The chemical-potential control is very important for growing good-quality  $\text{Cu}_2\text{ZnSnS}_4$  crystals. In particular, due to the strong binding between Zn and S, Zn content control should be taken very carefully. Thus, perfect  $\text{Cu}_2\text{ZnSnS}_4$  crystals are thermodynamically unstable when Zn is rich. It is experimentally observed that under Cu poor and Zn-rich conditions, the secondary phase segregation of ZnS may occurs [118, 167]. Actually, CZTS thin films deposition is usually accompanied by secondary phase formation. The most formed one is CuS due to its low formation enthalpy -0, 45 eV. However, due to its larger formation enthalpy -1.47 eV, ZnS is inevitably formed in high Zn rich condition. This explains the formation of ZnS with increasing Zn concentration in the solution. Berg et al [168] have proved that the presence of ZnS secondary phase in CZTS thin films causes the (112) peak position shift towards the higher angles. This is consistent with observed peak shift as depicted in figure III.24.

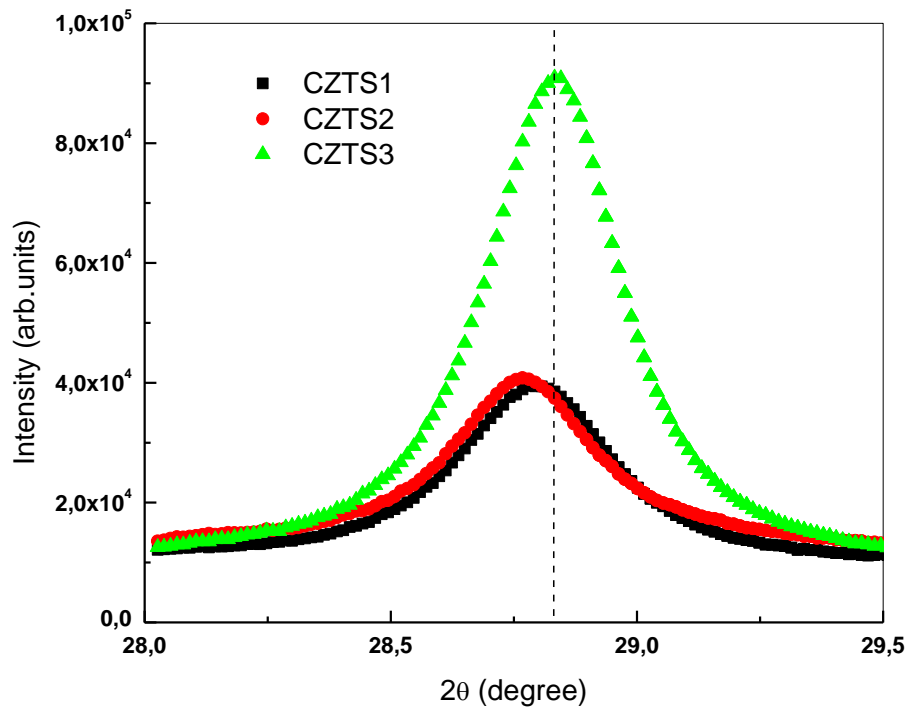


**Figure III.24** The shift of (112) peak position as function of Zn concentration

As seen the peak (112) position is shifted with increasing Zn concentration due to the formation of ZnS phase.

The crystallites sizes (D) were deduced from XRD data using III.1 formula. The values of FWHM and the determinate crystallites size are resumed in Table III.6.

<i>Sample</i>	<i>CZTS1</i>	<i>CZTS2</i>	<i>CZTS3</i>
<i>Zinc concentration</i>	<i>0.01</i>	<i>0.015</i>	<i>0.025</i>
<i>FWHM (2θ°)</i>	<i>0.2303</i>	<i>0.2326</i>	<i>0.2814</i>
<i>Crystallite size(nm)</i>	<i>29.23</i>	<i>35.46</i>	<i>133.51</i>

**Table III.6:** The FWHM values of (112) orientation and crystallites size of the CZTS thin films obtained at different zinc concentrations.

The crystallites size of the film increases from 28 to 133 nm with increasing zinc concentration in the starting solution. Thereafter, increasing zinc salt concentration improves the crystallite size of CZTS thin film. This could be due to the formation of ZnS phase with

increasing Zn salt in the starting solution. The same conclusion has been reported by Berg et al in a study of detection limit of secondary phase in CZTS thin films [168] and they concluded that increasing Zn composition in the starting solution used for CZTS deposition by electro-deposition technique enlarges enormously the crystallite size. Singh et al [164] have prepared CZTS by sequential sputtering of metallic targets they investigated Zn influence and concluded that sample with higher Zn content have better crystallinity.

### III.4.2 Morphological properties

AFM measurement are performed at room temperature, AFM 3-dimensional micrographs obtained in different films are depicted in (figure.III.25).

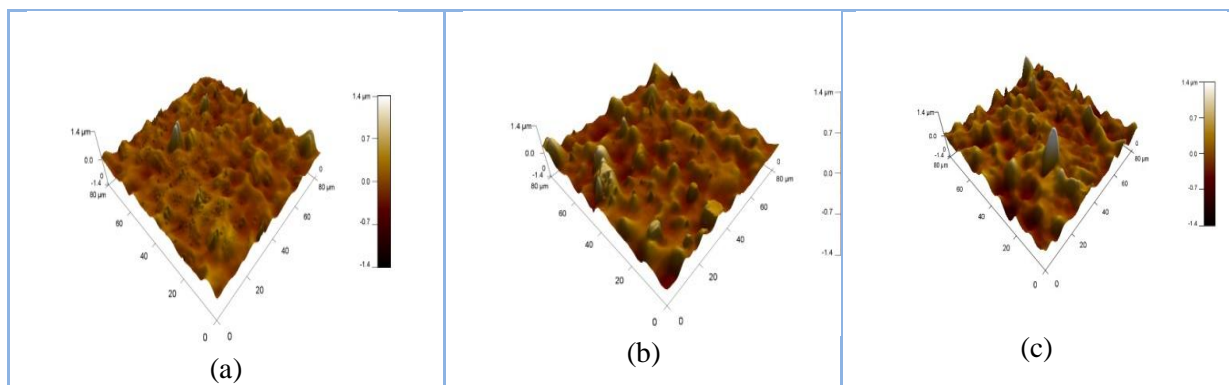


**Figure III.25:** 3D AFM images of CZTS thin films deposited with various zinc salt concentrations.

The films are dense and continuous; the surface is well covered with a relatively large grains and pinholes free. The surface films roughness increases with zinc concentration, the roughness values are resumed in table.III.7

As can be deduced from table III.7, film crystallites size is larger in films prepared with higher zinc molarity, this is in good agreement with the crystallites size enlargement deduced from DRX measurement.

<i>Zinc concentration</i>	<i>RMS(nm)</i>
<i>CZTS1</i>	<i>146.36</i>
<i>CZTS2</i>	<i>215.95</i>
<i>CZTS3</i>	<i>248.50</i>

**Table III.7.** RMS values of CZTS thin films deposited with various zinc concentration

Figure III.26. Shows the variations of both crystallites size and surface roughness as function of zinc salt concentration, we observed clearly the dependence between these two parameters

as the crystallites size increase the surface of the films became rough which can refer to the apparition of multiple sites of nucleation in CZTS thin films.

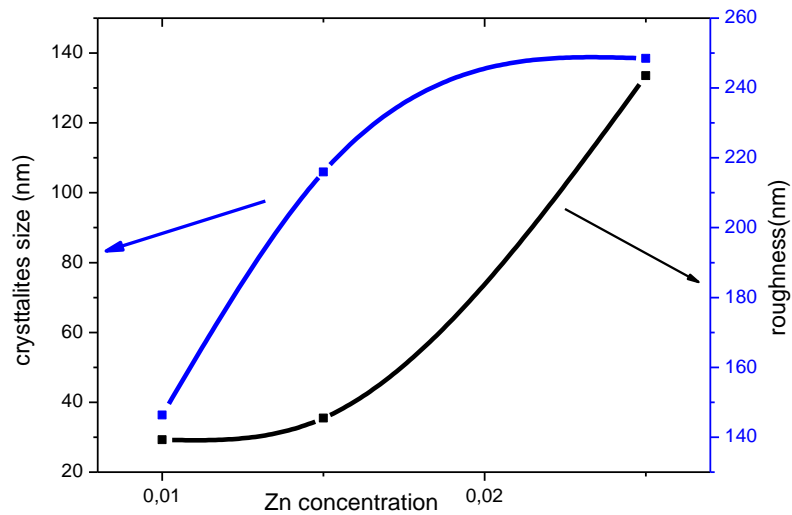


*Figure III.26: Crystallites size and roughness as function of zinc concentration*

### III.3.4. Optical properties

#### a. Transmittance

The transmission spectra of sprayed CZTS films deposited at different zinc concentrations were investigated using UV-Visible spectrophotometer in spectral range of (400-900) nm. The variation of the transmittance as function of wavelength is depicted in figure III.27.

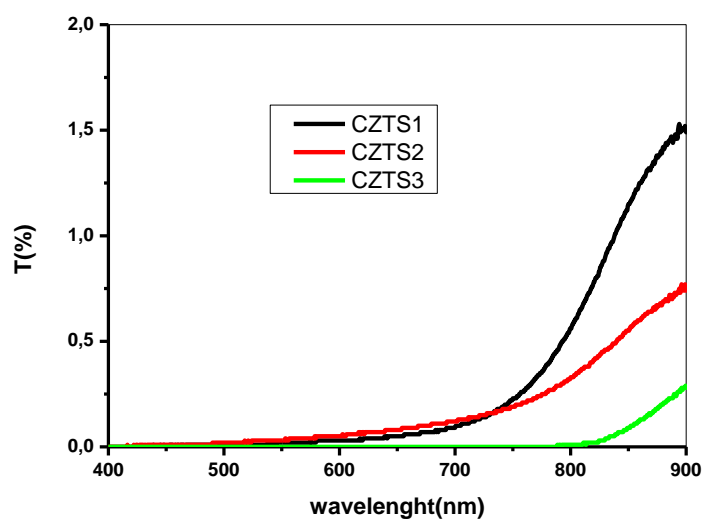


*Figure III.27: Transmittance spectra of CZTS thin film with the variation of zinc salt molarity*

As can be seen, the whole films have very low transmission coefficient (<2%), consequently, with an absorption coefficient larger than  $10^4 \text{ cm}^{-1}$ , which is in agreement with those reported in literature [167,42]. This large absorption coefficient is highly recommended for application as absorber layer in thin films solar cells. The concentration of zinc acetate reduces films transmittance; this is due to the increase in film thickness.

***b. Band gap energy***

The band gaps energy ( $E_g$ ) of CZTS films were estimated from the analysis of the optical transmission using tauc's formula (III.4). As explained earlier, the band gap energy is determined from the variation of  $(\alpha h\nu)^2$  Vs  $(h\nu)$ .  $E_g$  is determined by extrapolating the linear portion of the spectrum to  $\alpha h\nu = 0$ , as shown in figure III.28. The obtained energy gap values are in the range of 1.3 to 1.37 eV which are in good concordance with the reported gap values of CZTS [81]. The gap energy decreases slightly with zinc concentration. The same behavior of optical band enlargement has been reported by Malbera et al [40] with increasing tin concentration and Zn concentration [164].

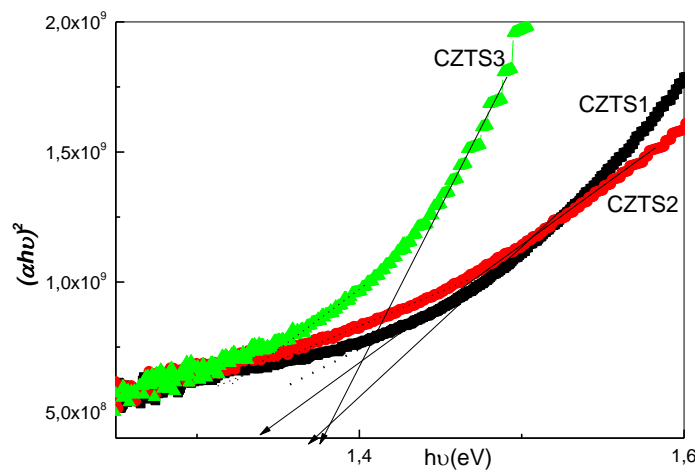


**Figure III.28:** Tauc's plot of CZTS films elaborated with various zinc salt molarities

From ab initio calculations Chen et al. [170,171] has climbed that a reduction in Zn or Sn content introduces a large density of acceptor defects such as  $V_{zn}$ ,  $Cu_{zn}$ ,  $V_{sn}$ ,  $Cu_{sn}$ , and  $Zn_{sn}$  anti-sites. These defects may create shallow acceptor levels responsible for the change in material absorption edge and optical band gap shrinking. This variation can be also explained in term of the disorder as depicted in the drawing insert in figure III.29. While, the optical gap

broadening of sample (CZTS3) can be related to the apparition of ZnS secondary phase as suggested from XRD analysis. It is well argued [164,172] that ZnS secondary phase is responsible for optical band gap enlargement.

### c. Urbach energy

The disorder in the film network is described by the band tail width which is called Urbach tail and expressed as [173].

$$\alpha = \alpha_0 \exp\left(\frac{h\nu}{Eu}\right) \quad (\text{III.4})$$

Where  $\alpha_0$  is the pre-exponential factor,  $h\nu$  the photon energy and  $Eu$  is the Urbach tail

The Urbach tail ( $Eu$ ) can be estimated from the inverse slope of the linear plot of  $\ln(\alpha)$  versus photons energy. The both energy gap and Urbach tail as function of photon energy are plotted in figure III.29. From the graphs we can see that the variation is in contradiction and here we can say the disorder in the film network affect strongly the optical band gap energy.

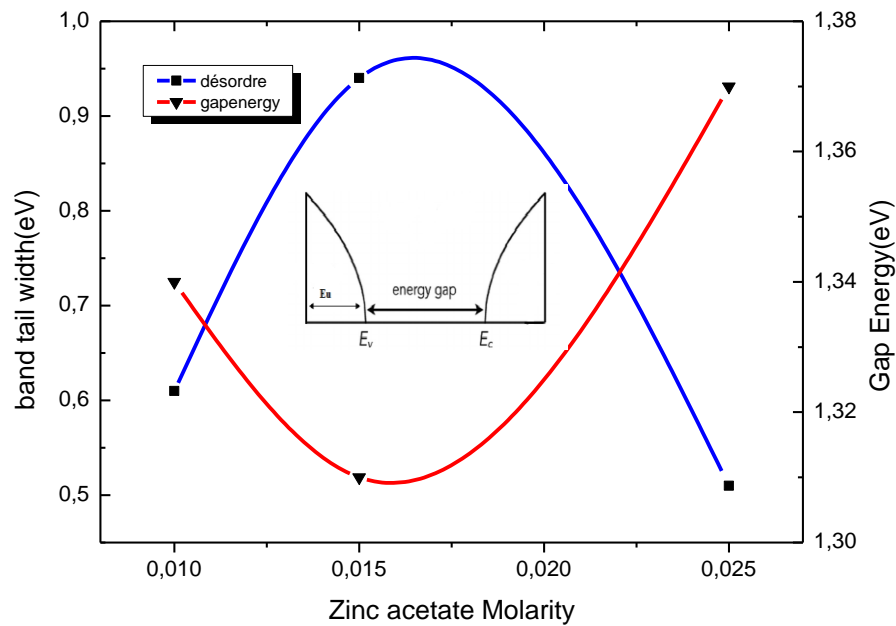


**Figure III.29:** Band tails width and gap energy variation as function of zinc molarity

### III.4.3 Electrical properties

The electrical properties of sprayed CZTS thin films are performed by Hall Effect at room temperature, the carrier concentration, hall mobility and electrical conductivity values are reported in Table III.8

	<i>Carrier concentration (cm<sup>-3</sup>)</i>	<i>Conductivity (Ω<sup>-1</sup>cm)<sup>-1</sup></i>
<i>CZTS1</i>	$1.082 \cdot 10^{22}$	14.35
<i>CZTS2</i>	$3.36 \cdot 10^{23}$	12.44
<i>CZTS3</i>	$3.32 \cdot 10^{16}$	2.2

**Table III.8.** Electrical parameters of CZTS thin films at different zinc concentration

The whole prepared films have p-type conductivity according to Hall constant sign. Several authors found the same order of conductivity in CZTS thin films [174, 175]. In figure.III.30: we have presented the variation of both carrier concentration and conductivity as function of zinc molarities. As well known that, the conductivity variation is controlled by the free carrier concentration.

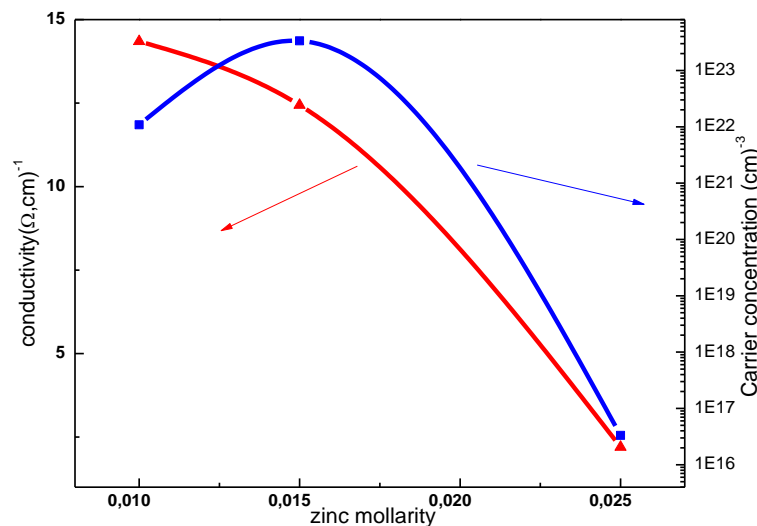


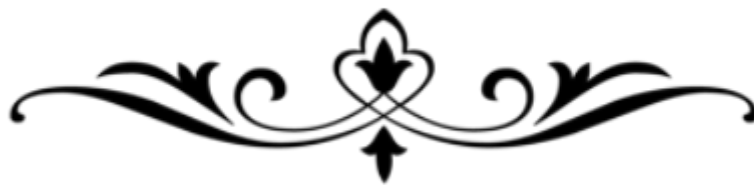
**Figure III.30.** Conductivity and carrier concentration of CZTS film as function of zinc salt concentration

The carrier concentration decreases with Zn molarity, this can be due to reduction of acceptor defects responsible for free carrier p type carriers. It is well known that intrinsic point defects in CZTS play a major role and may control CZTS electrical properties. Several authors have calculated the formation energies of defects in CZTS, based on first-principle theory [122,63-65,171,42,176-177]. It has been climbed that copper vacancies ( $V_{Cu}$ ) and  $Cu_{Zn}$  can be easily formed and are the dominant acceptor defects in CZTS material [65,171,176-177]. They form shallow acceptor levels in CZTS lead to p-doping. Thereafter, we speculate that with increasing Zn concentration in the starting solution the  $Cu_{Zn}$  defect is reduced causing the

decrease in the free carrier as shown in figure III.30. It is well known that lattice mismatch between CZTS and the secondary phase give rise to interface states within the band gap (due to the dangling bonds), hence a shorter carrier lifetime and carriers loss at the CZTS/secondary phase interfaces leading to free carrier's concentration reduction. On the other hand, the resistive ZnS secondary phase that appears with increasing Zn concentration could be the cause of conductivity reduction of the obtained CZTS film. This is consistent with Mitzi et al conclusion [176] where they inferred that ZnS is responsible for the high series resistance observed in CZTS based solar cells. While the relative high conductivity measured in film prepared with low Zn molarity may originate from the segregation of conductive  $Cu_xS$  phases.

# Chapter IV

Device properties, results and  
discussions



In this chapter, we will present and discuss the electrical properties of some realized devices, in which we have studied the effect of back contact nature in CZTS based hetero-junction, the effect of ZnO intrinsic layer, and the effect of sulfurization temperature on CZTS solar cells performance.

### *IV.1 Back contact study of CZTS/ZnS heterojunction*

In this section of chapter IV, we will present with discussions the obtained results concerning the effect of back contact metals nature (Al, Ag, and Au) on CZTS/ZnS properties, such as on current-voltage (I-V) and capacitance (conductance)-frequency (C-G-f) characterizations.

#### *IV.1.1. Films properties*

The structural, optical, and electrical properties of the layers composed our devices are presented and discussed in details in the following paragraphs.

##### **IV.1.1.1 Structural properties**

In figures IV.1 (a, b) and c we have reported the Raman and XRD patterns of CZTS thin film. The XRD pattern (figure IV.1.a) of CZTS layer matches well with the Kesterite CZTS phase JCPDS  $\neq$ No°. 26-0575 card.

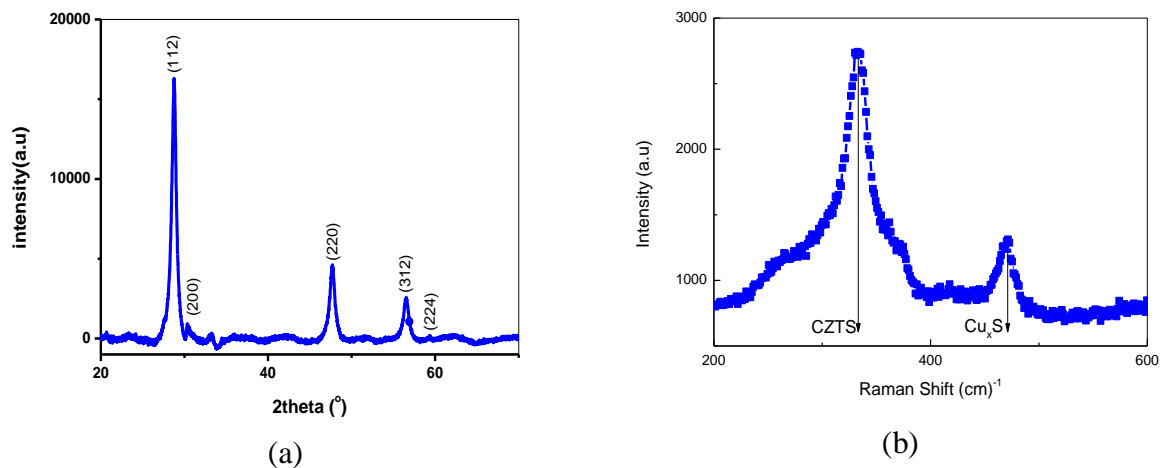


*Figure.IV.1. a: XRD and b: Raman spectra of CZTS thin films*

As can be seen, five clear diffraction peaks corresponding to the (112), (200), (220), (312) and (224) planes of kesterite CZTS structure are detected with the direction (112) as preferential orientation. No other peaks, in XRD pattern, related to any secondary phase are

observed. It is generally reported that CZTS regardless the deposition technique is usually accompanied with a binary secondary phases [152,71]. However, it hard to asses from XRD analysis that CZTS is pure this is due to the fact that the lattice constants of CZTS are similar to  $\text{Cu}_2\text{SnS}_3$  (CTS) and  $\text{ZnS}$ , the obtained peaks could be related to either CZTS or CTS or  $\text{ZnS}$  phases [168].

Thereafter to confirm the secondary phase's formation we further analyzed the film by Raman spectroscopy since it is a very sensitive tool for phase identification.

As shown in figure IV.1. b the existence of kesterite phase is confirmed with Raman scattering spectroscopy by the presence of intense Raman peak at  $337\text{cm}^{-1}$  and the shoulder peaks at  $282$  and  $362\text{cm}^{-1}$ . The same results have been reported by several authors [178-180]. While, the additional peak at  $472\text{cm}^{-1}$  is attributed to the  $\text{Cu}_x\text{S}$  phase, the same results were reported by Fernandes et al. [58]. The formation of sulfide cupric secondary phase is due to the excess Cu in the used starting solution by comparison to Zn.

In figure IV.2.a, we have reported the DRX spectrum of  $\text{ZnS}$  film. The obtained diffraction pattern suggests the evidence of Zn (O.S) thin film formation rather than pure  $\text{ZnS}$ . Peaks assigned to  $\text{ZnO}$  and  $\text{ZnS}$  phases are present. As shown in figure IV.2.b, the plane (101) of hexagonal  $\text{ZnO}$  Wurtzite structure is clearly visible along with the planes (220), (311) and (204) of the hexagonal  $\text{ZnS}$  cubic According to JCPDS card N° 77–2100.

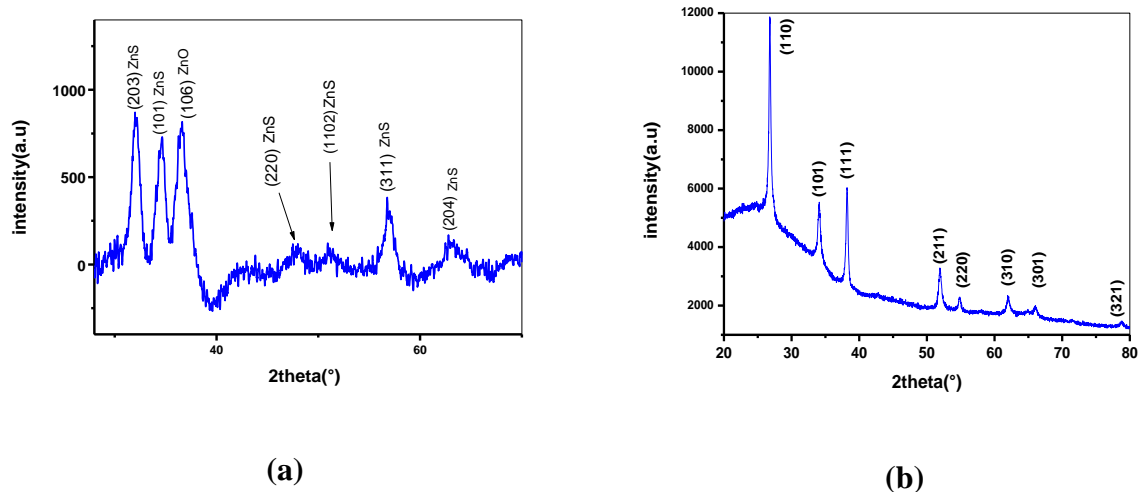


**Figure IV.2:** (a, b). XRD patterns of  $\text{ZnS}$  and FTO thin films

Actually, in contrary to PVD deposition (Sputtering, thermal evaporation), chemical route techniques such as: spray pyrolysis, chemical bath, SILAR and sol gel techniques yield to

ZnS formation mixed with ZnO phase. This is due to the fact that in these techniques films are achieved in air or in aqueous solution [181-183] which favors oxygen contamination.

The performances of CZTS based solar cells is lowered by different causes such as MoS<sub>2</sub> layer formation at the back contact [184], the presence of secondary phases in the bulk [185], and especially the alignment lack of conduction bands at the absorber/buffer interface [186]. Recently Ericson et al. [187] have investigated Zn (O, S) system as buffer layer in CZTS solar cell, they have shown that conduction band gap offset can be tailored through the conduction band variation by controlling the ratio of oxygen to sulfur [188], and that the optimum conduction band alignment for CZTS lies in between the ZnO and the ZnS values. This has been experimentally observed [189]. It has been claimed also that ZnOS film is more preferable partner than ZnS to form an ideal hetero-junction due the lower conduction band offset at the interface with SnS absorber layer [190].

The XRD diffraction of FTO film is shown in figure IV.2.b. Several peaks assigned to the tetragonal rutile SnO<sub>2</sub> phase such as (110), (101) and (111) are present, indicating the formation of polycrystalline SnO<sub>2</sub> with (110) as preferential orientation, the same results are recently reported in SnO<sub>2</sub> thin films prepared by spray pyrolysis [191,192] and Sol gel deposited SnO<sub>2</sub> thin films [193].

#### IV.1.1.2 Optical and electrical properties

##### a. Transmittance

Figure IV.3 shows the transmittance spectra of different layers CZTS, ZnS and FTO in the visible range.

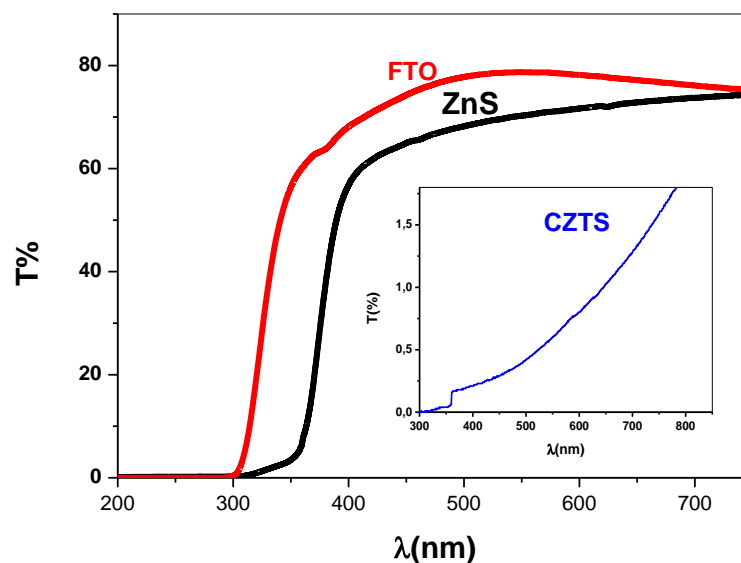


*Figure IV.3: Transmittance spectra of CZTS, ZnS, and FTO thin films*

Both FTO and ZnS layer exhibit large transmittance spectra due to the fact that they are large gap semiconductors. For application in thin film solar cells, these two layers should be transparent, since they are used as windows for visible wavelength to allow the incident photons to reach the CZTS absorber layer. While, as shown in insert figure IV.3, CZTS layer is highly absorbent with an absorption coefficient higher than  $10^4 \text{ cm}^{-1}$ .

Moreover, FTO layer should be also a highly conducting. The fluorine is introduced in  $\text{SnO}_2$  in order to enhance its conductivity since the two requirements for FTO use as transparent electrode is a high transparency and a large conductivity. The measured conductivity of the deposited FTO is equal to  $10^2 (\Omega.\text{cm})^{-1}$ , the efficiency introduction of fluorine as donor is also assessed from the transmittance spectrum in the UV visible near infrared range as shown in figure IV.4, the reduction in the transmittance in the near infrared range is caused by the reflection due the large free carriers concentration which is equal  $3 \times 10^{19} \text{ cm}^{-3}$  as reported in table VI.1.

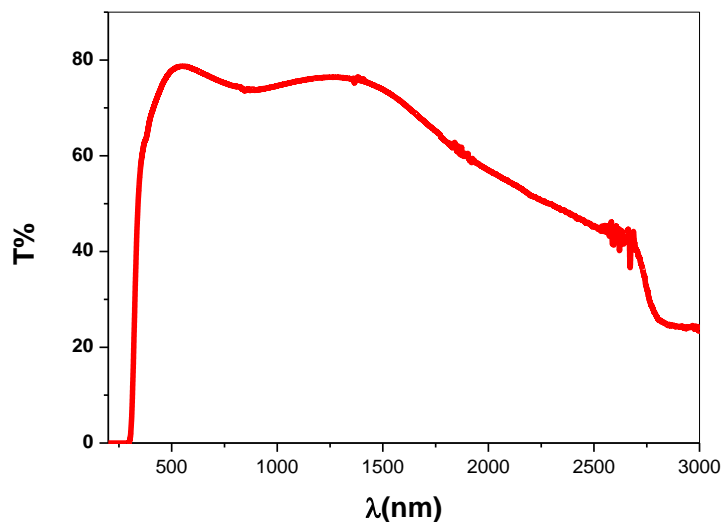


*Figure IV.4: Transmittance spectra of FTO in UV-Visible-IR range*

#### ***b. Gap energy***

The optical gap energies of CZTS, ZnS and FTO were calculated from the plot of  $(\alpha h\nu)^2$  vs  $h\nu$ , where  $h\nu$  represent the energy of incident photon and  $\alpha$  is the absorption coefficient estimated from the transmittance values.

Figures IV.5 a, b and c show the plots of  $(\alpha h\nu)^2$  vs  $h\nu$  plots of the three thin films, the values of optical band gaps measured of CZTS, ZnS and FTO are 1.6, 3.3 and 3.9 eV respectively.

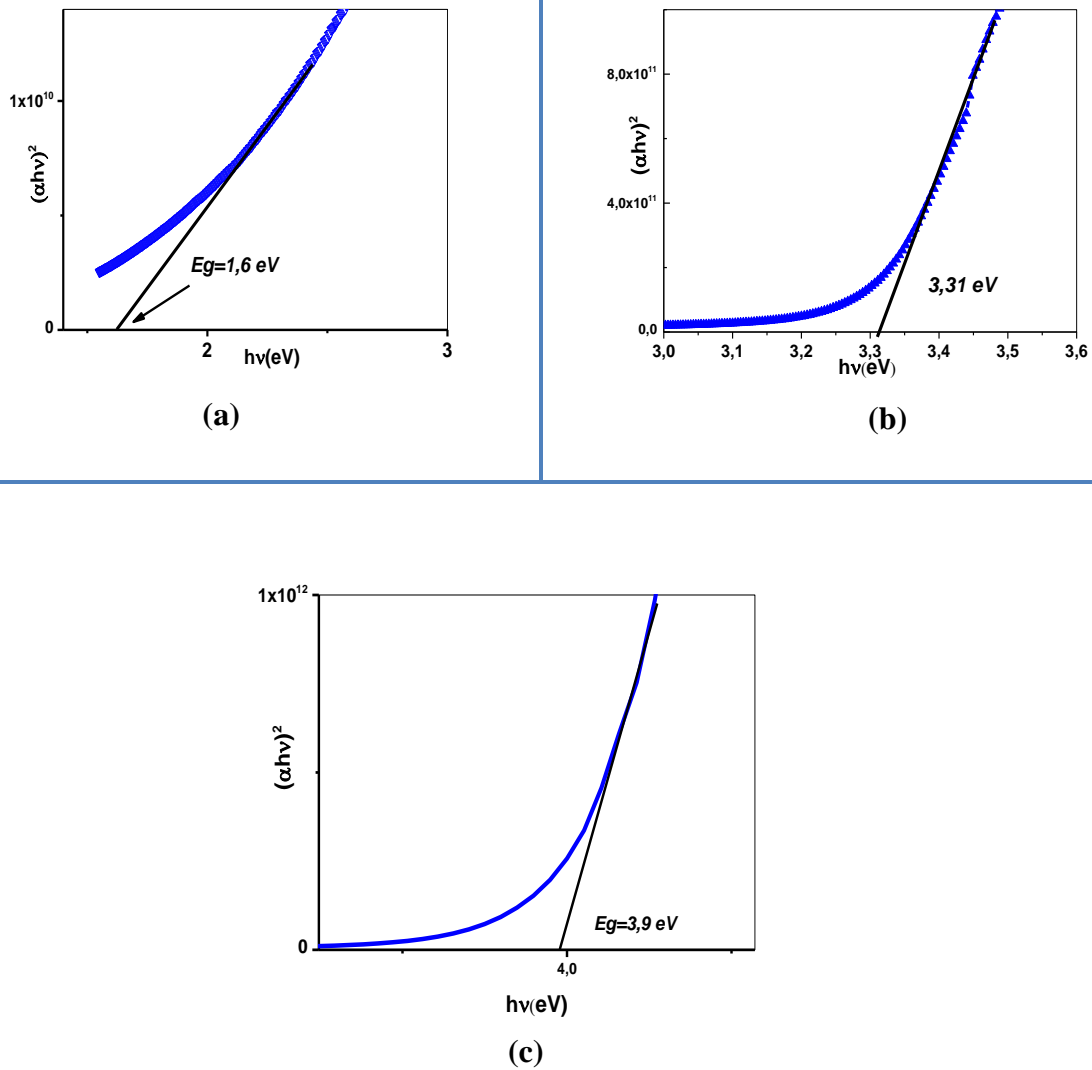


**Figure IV.5.** (a-c):  $(\alpha hv)^2$  vs  $hv$  of (a): CZTS, (b): ZnS and (c): FTO thin films

**c. Electrical properties.**

The electrical properties of the film are measurement used Hall effect in the dark, CZTS film mobility exhibit a high value of mobility more than  $800$  ( $\text{cm}^2/\text{Vs}$ ) which due to the low value of carrier concentration compared to the values reported in various work [168] and has a conductivity in the order the  $10^{-2}$  ( $\text{cm}\Omega$ ) $^{-1}$ . The deposited FTO thin film show a good conductivity about  $10^2$  ( $\text{cm}\Omega$ ) $^{-1}$  and a carrier concentration about  $10^{19}$   $\text{cm}^{-3}$ . Whereas, ZnS film characterized by a low value of conductivity which was about  $10^{-4}$  ( $\text{cm}\Omega$ ) $^{-1}$ , ZnS pure film has in general resistive behavior with a large band gap energy (3.9 eV). The calculated optical band gap and film thickness (d) together with electrical properties free carrier concentration, mobility and dark conductivity of different films deduced from Hall Effect measurements are reported in Table IV.1

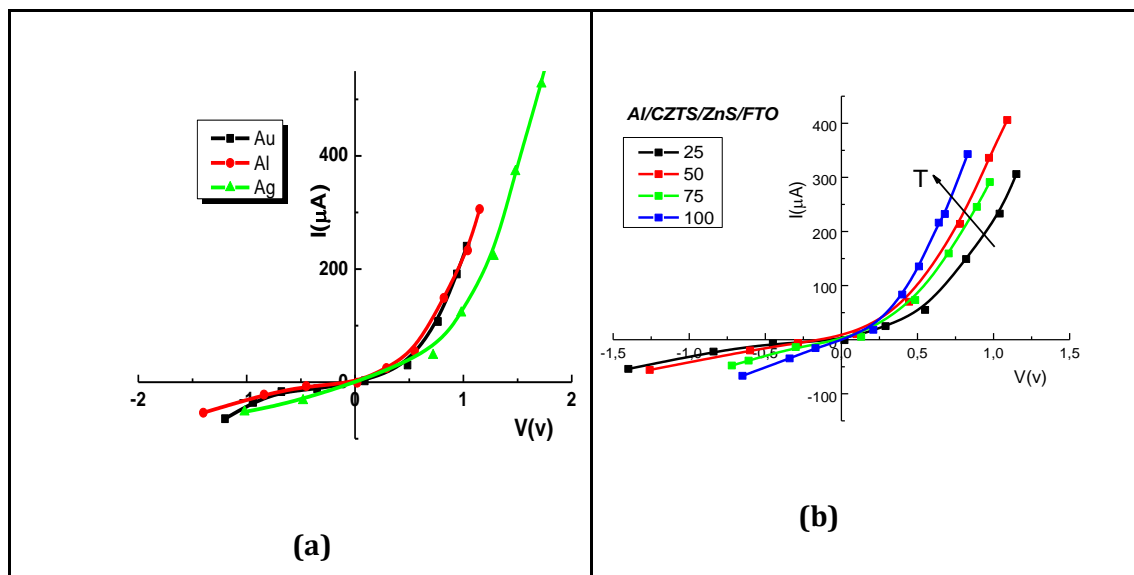
	$\delta$ ( $cm^{-3}$ )	$\mu$ ( $cm^2/Vs$ )	$\sigma$ ( $cm\Omega$ ) <sup>-1</sup>	$E_g$ (eV)	$d$ (nm)
<b>CZTS</b>	$4 \times 10^{13}$	$8.15 \times 10^3$	$5.2 \times 10^{-2}$	1.6	1400
<b>FTO</b>	$3,3 \times 10^{19}$	19.42	$10^2$	3.9	50
<b>ZnS</b>	-	-	$10^{-4}$	3.3	100

**Table IV.1** Electrical parameters and gap energy of CZTS, ZnS, and FTO

### IV.1.2. Device properties

#### IV.1.2 .1 Current-Voltage characterization

The device current–voltage (I-V) characteristics are done using Tektronix tracer (diodoscope) (figure II.4) and yields to important information about junction electrical properties such as: series resistance ( $R_s$ ), diode ideality factor ( $n$ ), saturation current ( $I_s$ ) barrier height ( $\phi_b$ ) and for knowing the major conduction mechanisms through the junction. In figure IV.6.a we have reported the I-V characteristics of CZTS/ZnS hetero-junction with different back contact aluminum (Al), silver (Ag), and gold (Au) measured in the dark and at room temperature, whereas figure IV.6. (c-d) shows the I-V characterization of CZTS/ZnS hetero-junction with different back contact measured at a variable temperature from 25 to 90 °C.



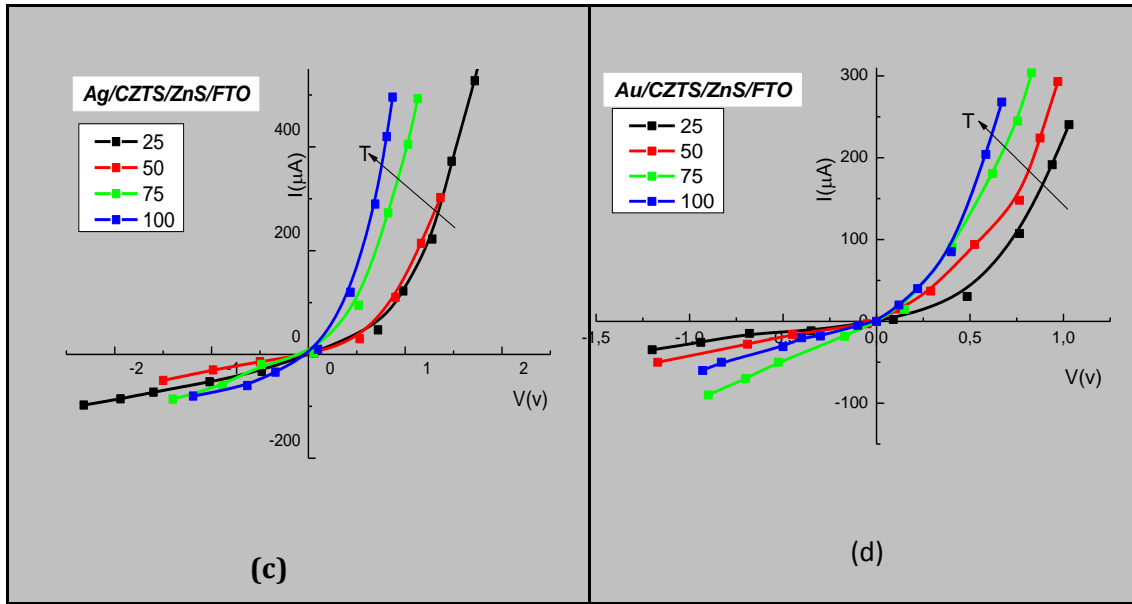


**Figure.IV.6:** Characterization of heterojunctions (a)-CZTS/ZnS with different back contact in the dark and at room temperature and (b) CZTS/Al;(c)- CZTS/Ag; (d)- CZTS/Au heterojunctions at different measurement temperature

As can be seen in Figure IV.6.a there is no noticeable difference between the three characteristics. All hetero-structure exhibit a rectifying behavior. Moreover, the reverse voltage characteristics show no saturation, indicating that defect-assisted generation or tunneling mechanism occur [43]. Their characteristics can be described by equation (I.1):

The ideality factor determined from the slope of the linear region of forward bias  $\ln(I)-V$  plot and defined as mentioned in equation (I.2)

The barrier heights were calculated from the variation of current saturation ( $I_s$ ) as function of the temperature, it can be described and expressed as (IV.1):

$$I_s \sim T^2 \exp\left(\frac{-q\phi_b}{KT}\right) \quad (\text{IV.1})$$

Where:  $T$  is the temperature;  $q$  is elementary charge,  $K$  Boltzmann constant.

The barrier height was calculated from the variation of saturation current with measurement temperature (fig.IV.5.c-d), is thermally activated, the barrier height was estimated according to the relation (IV.2) from the slope of the Arrhenius plot of  $\ln(I_s/T^2)$  as function of  $10^3/T$ .

The deduced values of ideality factor, saturation current, series resistance, and barrier height of heterojunctions are resumed in Table IV.2.

<i>Structure</i>	<i>CZTS/Al</i>	<i>CZTS/Ag</i>	<i>CZTS/Au</i>
<i>n</i>	11.4	10.5	5.9
<i>I<sub>s</sub> x 10<sup>-6</sup>(A)</i>	18.57	30	1.27
<i>R<sub>s</sub>(kΩ)</i>	2.1	1.42	2
<i>Φ<sub>b</sub>(eV)</i>	0.38	0.29	0.28

**Table.IV.2** Electrical parameters of CZTS/ZnS hetero-junction with different back contacts.

As reported in table IV.2, The lower saturation current and barrier height are measured in the hetero-junction using Au as a back contact. Whereas, the ideality factors calculated in the realized hetero-junctions are large and depend on the nature of the used metal contact, they are respectively equal to 11.4, 10.5 and 5.9 for Al, Ag and Au. Several authors have reported anomalous ideality factor values in different hetero-junction and p-n junction [193-196] where an ideality factor ( $n > 5$ ) is reported.

The origin of the large value of  $n$  may be due to the metal /CZTS contact. Indeed, when the contact is not ohmic, the hetero-junction can be modeled as a series of diodes and resistors in series, according to Shah–Li–Schubert [197] the ideality factor is the sum of ideality factors of each diode. Jing-Jing et al [198] have explained the measured 18,8 ideality factor in ZnO(Al)/ (p)Si hetero-junction in terms of metal contact nature. The same reason has been proposed by Shah et al. [199] to explain the anomalous ideality factor of 6.9 measured in the hetero-structure p-type AlGaN/GaN.

To assess the nature of contact between CZTS and the used contact metal one should compare the work functions of the metal  $\Phi_M$  and  $\Phi_S$  of the semiconductor as seen in figure IV.7 which illustrate de band diagram of ohmic and schottky contacts.

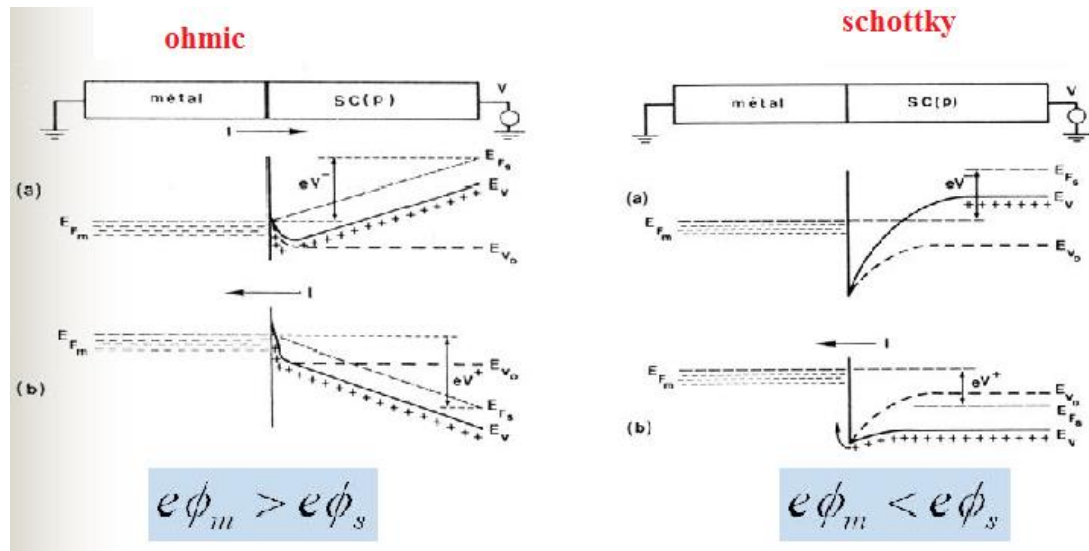


**Figure.IV.7:** band diagram of ohmic and Schottky contact of metal/sc (p) diode [x]

The optical gap of the prepared CZTS film is equal to 1.6 eV, the conductivity activation energy (which equal to the difference  $E_F - E_V$ ) is equal to 250 meV. Thereafter, knowing that CZTS affinity is given equal to 4.21 eV, the work function of CZTS is then equal to 5.57 eV.

It is well known that in the case of  $\Phi_M < \Phi_S$ , the metal semiconductor contact is ohmic if the semiconductor is n type and if Schottky contact is p type. Thereafter, since CZTS is a p type semiconductor and according of the work function of the used metals (4.26, 4.28 and 5.1 eV for Ag, Al and Au respectively), Al and Ag are candidates to yield a Schottky contact with CZTS, in contrary in the case of Au, where the contact with CZTS could be ohmic. This can explain then the large ideality factor measured in the hetero-junction obtained when using Al and Ag as back contacts. While, the large value measured in the structure obtained with Au back contact ( $n=5.9$ ) can be due to the defects located at the interface. Similar results ( $n > 20$ ) were reported by Raddy et al. [200] in the n-ZnO nanorods /p-Si devices; they suggested that the large value of  $n$  is probably due to the presence of defect states in ZnO lattice and/or the presence of traps at the interface [201]. Actually, the large value of ideality factor could be also due to numerous reasons such as recombination of electrons and holes in depletion region, the presence of interfacial layer [202,203] the trap-assisted tunneling [204,205] and carrier leakage [205] and the in-homogeneities in junction barrier heights [206,207].

Tables IV.3. (a-c): resumed the electrical properties of CZTS/ZnS hetero-junction with Ag, Al. and Au back contact respectively, measured at different temperature. It clear that the series resistance decrease and the saturation current increase with the temperature.

$T(k)$	$n$	$I_s(A) 10^{-6}$	$R_s(k\Omega)$
293	10.5	3.4	1.42
323	6.24	1.5	2.42
348	4.4	1.86	1.55
373	4.1	4.6	1.18

**Table.IV.3. a** Ag/CZTS diode parameters determined from I-V plots

$T(k)$	$n$	$I_s(A)10^{-6}$	$R_s(k\Omega)$
298	11.4	9.13	2.1
323	6.2	5.6	1.91
348	4.8	2.71	2.06
373	3.87	3.35	1.8

**Table.IV.3. b** Al/CZTS diode parameters determined from I-V plots

$T(k)$	$n$	$I_s(A) 10^{-6}$	$R_s(k\Omega)$
293	5.9	1.27	2
323	6.4	6.14	2.3
348	4.6	6.79	2.05
373	3.7	7.3	1.65

**Table.IV.3.c** Au/CZTS diode parameters determined from I-V characteristic

The value of ideality factor of devices measured at different temperatures is found to be sensitive to the measurement temperature, it decreases with increasing temperature. This phenomenon, commonly referred as “To-effect”, was first proposed by [208]. The variation of  $n$  with  $T$  has been explained by several authors [209-210]. According to the proposed model, the temperature dependence of  $n$  suggests that the carrier generation-recombination involves defect states. The temperature dependence of  $n$  may be modeled as [xx]:

$$n = n_0 + T_0 / T \quad (IV.2)$$

Where  $n_0$  and  $T_0$  are constants which are independent of temperature and voltage

The variation of  $n$  with temperature is shown in figure IV.7, the variation of  $n$  as function of reverse temperature (insert figure IV.7) firstly to a straight line as predicted from eq.IV.2. This

suggests the involvement of several defect levels in carrier generation-recombination processes and also the tunneling effects contribution in carrier transport [211].

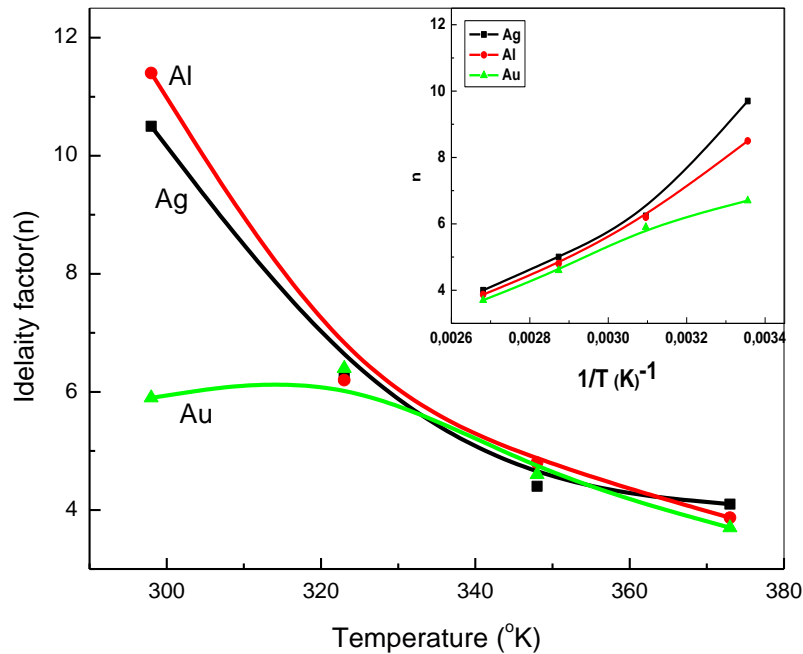


*Figure IV.8: Ideality factor variation as function of measured temperature of CZTS/ZnS with different back contact metals*

## IV.2.2 Conductance-frequency characteristic

### IV.2.2.a Conductance-frequency at room temperature

The capacitance and conductance versus frequency are important techniques to extract the interface state properties in hetero-junction or homo-junction devices [212]. However, the conductance technique determines the interfaces state with more accuracy than capacitance technique [213], this is due to the fact that conductance comes only from the interface states [214]. Capacitance-conductance measurements were carried out in dark with a frequency range varied from 1.2 KHZ to 1 MHZ and voltage about  $V=0.3$  V at ambient and variable temperature. In figures IV.9 and IV.10 we have reported the measured capacitance (C) and conductance (G) as function of measurement frequency for the different structures Au/CZTS/ZnS/FTO, Ag/CZTS/ZnS/FTO and Al/CZTS/ZnS/FTO in the dark and at room temperature.

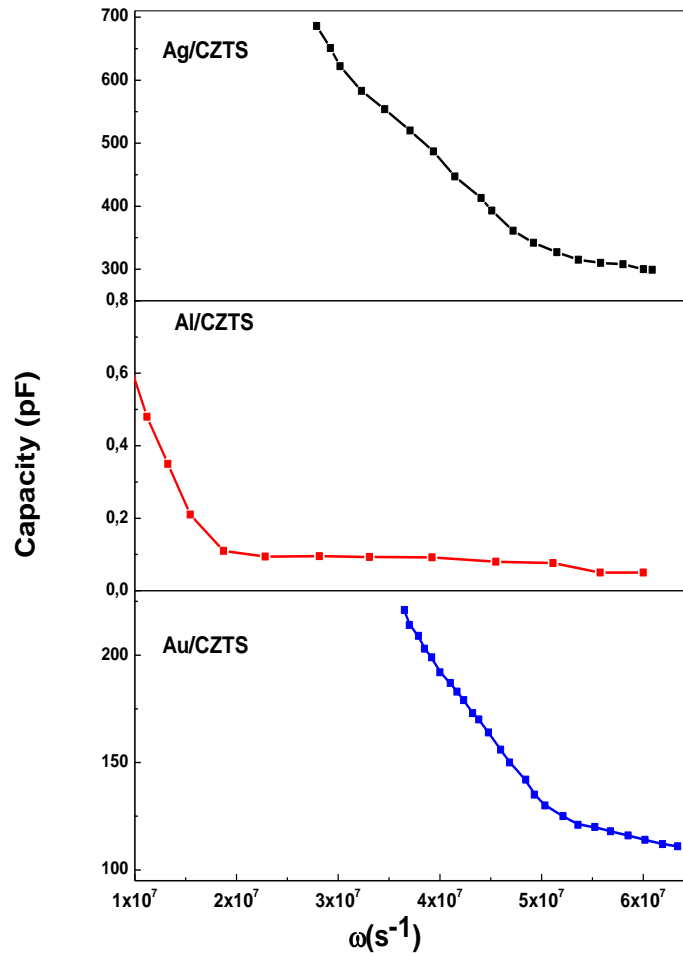


**Figure IV.9:**  $C$ - $\omega$  variation of CZTS/ZnS hetero-junction with different back contact

The high value of capacitance measured at low frequency (figure IV.9), is due to the fact that the trapped electrons at the interface can follow the ac signal at low frequency. With further frequency increase, trapped electrons cannot follow the high frequency signal [215] and the capacitance decreases to reach its smallest value at 1MHz. Therefore, the capacitance at high frequency ( $\omega > \omega_r$ ) represents the free-carrier response. Whereas, at low frequency (lower than the thermal emission rate of deep level) the defects can be charged and discharged, which allow them to contribute in the total junction capacitance. Thereafter, the capacitance represents the response of both free carriers and traps [216, 217], it can be then described as: [218].

$$C = C_{sc} + C_{ss} \quad (\text{at low frequency } \omega < \omega_r)$$

Whereas,  $C = C_{sc}$  (at high frequency  $\omega > \omega_r$ )

Where:  $C_{sc}$  is the capacitance of space charge region  $C_{ss}$ : is the interfacial capacitance

The presence of interfacial state in a hetero-junction is accompanied by a flexion in the C–f curve and by a resonant peak in conductance ( $G/w$ ) versus angular frequency, as can be seen in figures IV.9.

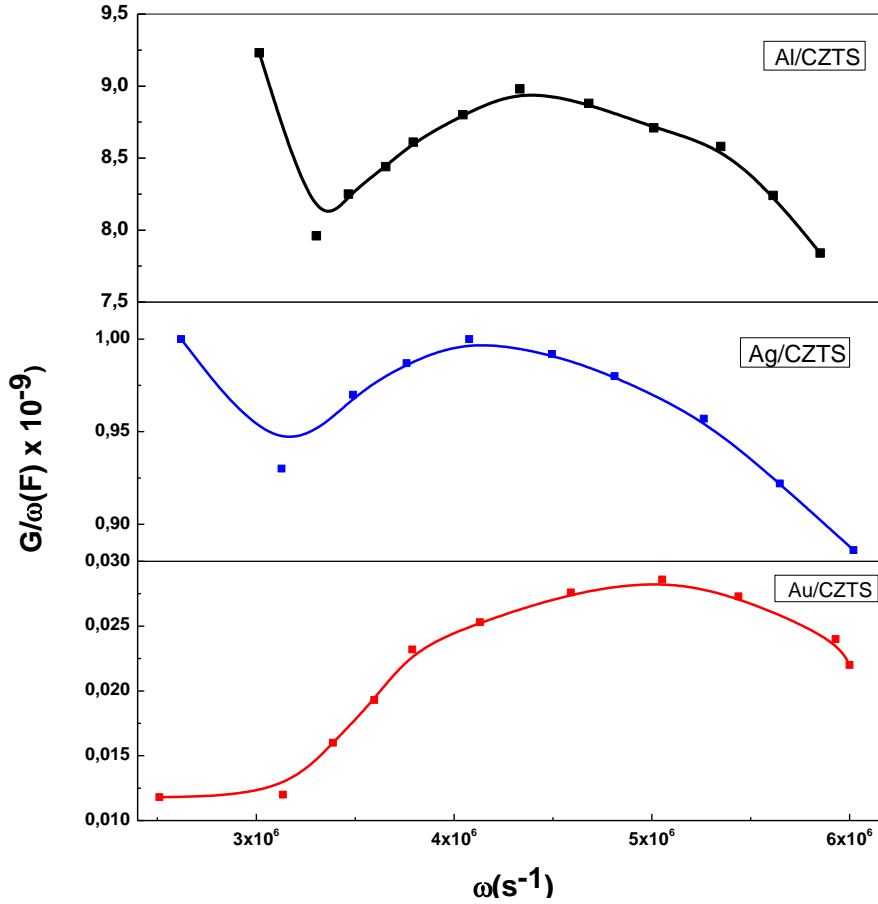


**Figure.IV.10:**  $G$ - $\omega$  variation of CZTS/ZnS with different back contact

The resonant peak in  $G/\omega(\omega)$  occurs when the trapped carriers emission rate ( $\omega_r$ ) is the same order than the angular frequency of the ac signal ( $\omega = \omega_r$ ). The angular frequency  $\omega_r$  of the resonant peak is expressed by the following relation [141] eq. (IV.3):

$$\omega_{r(T)} = 2e_t(T) = A \cdot T^2 \exp\left(-\frac{Ea}{KT}\right) \quad (\text{IV.3})$$

Where:  $\omega_r$  is the inflection frequency  $e_t$  is the emission rate of trapped charges and  $Ea$  is the activation energy.

The interface state density ( $N_{ss}$ ) can be deduced from  $(G/\omega)$  max using the following relation [142] eq. (IV.4):

$$N_{ss} = \frac{(G/\omega)_{\max}}{0.402qS} \quad (\text{IV.4})$$

Where  $q$  is the electronic charge and  $S$  is the diode area.

The time constant  $\tau$  for electrons exchange between interface states and valence band can be calculated using the relation  $\tau = 1/\omega_r$  [143].

The interface state densities of the hetero-structures were found in the order of  $10^{10} \text{ cm}^{-2} \cdot \text{eV}^{-1}$  and the trap time constant about  $10^{-7}$  s for the two structures prepared with Al and Ag as back contact, while in the case of the hetero-junction prepared with Au contact, we have measured a defect interface density lower by one order of decade (table IV.4). The larger measured interface states in the devices prepared with Al and Ag back contacts can be associated to the contribution of the depletion layer formed between the metal and CZTS due to the Schottky contact nature as suggested by the ideality factor values. Thereafter, Au metal can be used as back contact in CZTS based solar cell, this is consistent with the Aaron et al. [219] recent Us patent where they succeeded in improving the efficiency of CZTS/CdS and CZTS /ZnS solar cells by using Au or Pt as back contact due to their relative large work function.

The calculated value of state density ( $N_{ss}$ ) and life time are resumed in table IV.4.

<i>Structure</i>	<i><math>N_{ss} \times 10^{10} (\text{eV}^{-1} \cdot \text{cm}^{-2})</math></i>	<i><math>\tau \times 10^{-7} (\text{s})</math></i>
<i>Al/CZTS/ZnS/FTO</i>	<i>1.39</i>	<i>2.64</i>
<i>AG/CZTS/ZnS/FTO</i>	<i>3.48</i>	<i>2.65</i>
<i>Au/CZTS/ZnS/FTO</i>	<i>0.28</i>	<i>1.9</i>

**Table.IV.4:** Density of state and life time of carriers of CZTS /ZnS hetero-junction with different back contact at room temperature

#### IV.2.2.b. Conductance -Frequency-Temperature

The interface state density characterization using capacitance–conductance–frequency measurements in CZTS/ZnS structures with different back contact (Al, Ag, and Au) were carried out in the dark with various measurement temperatures. The Ac voltage amplitude kept to 0.3 V and the frequency varied from 1.2 KHz to 1 MHz. Figure IV.11.b shows the C-f characteristics of CZTS/ZnS hetero-junction with different back contacts and at various measurement temperature, we can see clearly a decrease in capacitance with the increase of

frequency and with a decrease of measured temperature which referred to the generation of additional charge carriers at the interface when the measurement temperature increases. As known that the total capacitance of the hetero-junction consists of the free carrier's capacitance across the space charge region and the additional capacitance contribution from charging and discharging of the defects located at the interface of the junction (hetero-junction).

The conductance measurements yield more exact and reliable results to determine the interface state density distribution. The variation of  $G/\omega - \omega$  with measurement temperature is shown in figure IV.11.a; the whole structure have the same trend of  $G/\omega - \omega$ , with the increase of measurement temperature and frequency. Knowing that the presence of state defect in the rectifying junction is determined by a peak in  $G/\omega$  vs  $\omega$  graph, no shift in  $G/\omega$  vs  $\omega$  plots were seen with the increase of temperature which suggest that the emission rate stay constant ( $e_t = \frac{1}{2\tau}$ ) and didn't affect by the temperature. The effect of measurement temperature on interface state density were calculated from the variation of  $(G/\omega) - \omega$  it has been seen that interface state density ( $N_{ss}$ ) value augment with increasing of the temperature from  $3.48 \cdot 10^{10}$  to  $3.76 \cdot 10^{10} \text{ eV}^{-1} \cdot \text{cm}^{-2}$  for CZTS/ZnS hetero-junction with Al back contact and from  $1.22 \cdot 10^{10}$  to  $1.52 \cdot 10^{10} \text{ eV}^{-1} \cdot \text{cm}^{-2}$  for the one with Ag back contact while for Au back contact the  $N_{ss}$  was varied from 0.28 to  $0.86 \cdot 10^{10} \text{ eV}^{-1} \cdot \text{cm}^{-2}$  which present the lower interface state density. Same variation was reported by A. Turut et al. [220] who has calculated the density of state in Au/Ni/n-GaN structures and observed the increase of state density with the increase of measurement temperature and explain this increase of state density by the increase of active charge in the interface with the increase of measurement temperature and same observation was reported in Ni/n-GaP structure in [221]. Few (or no) works were reported in the literature related to the study of interfacial defect in CZTS/ZnS device which is an important part of the device and affect strongly on the solar cell performance. A density of defect in the order of  $10^{10} \text{ eV}^{-1} \cdot \text{cm}^{-2}$  is an import value, these states present in the forbidden gap as recombination (generation) of free carriers which may cause short circuited path in the solar cell.

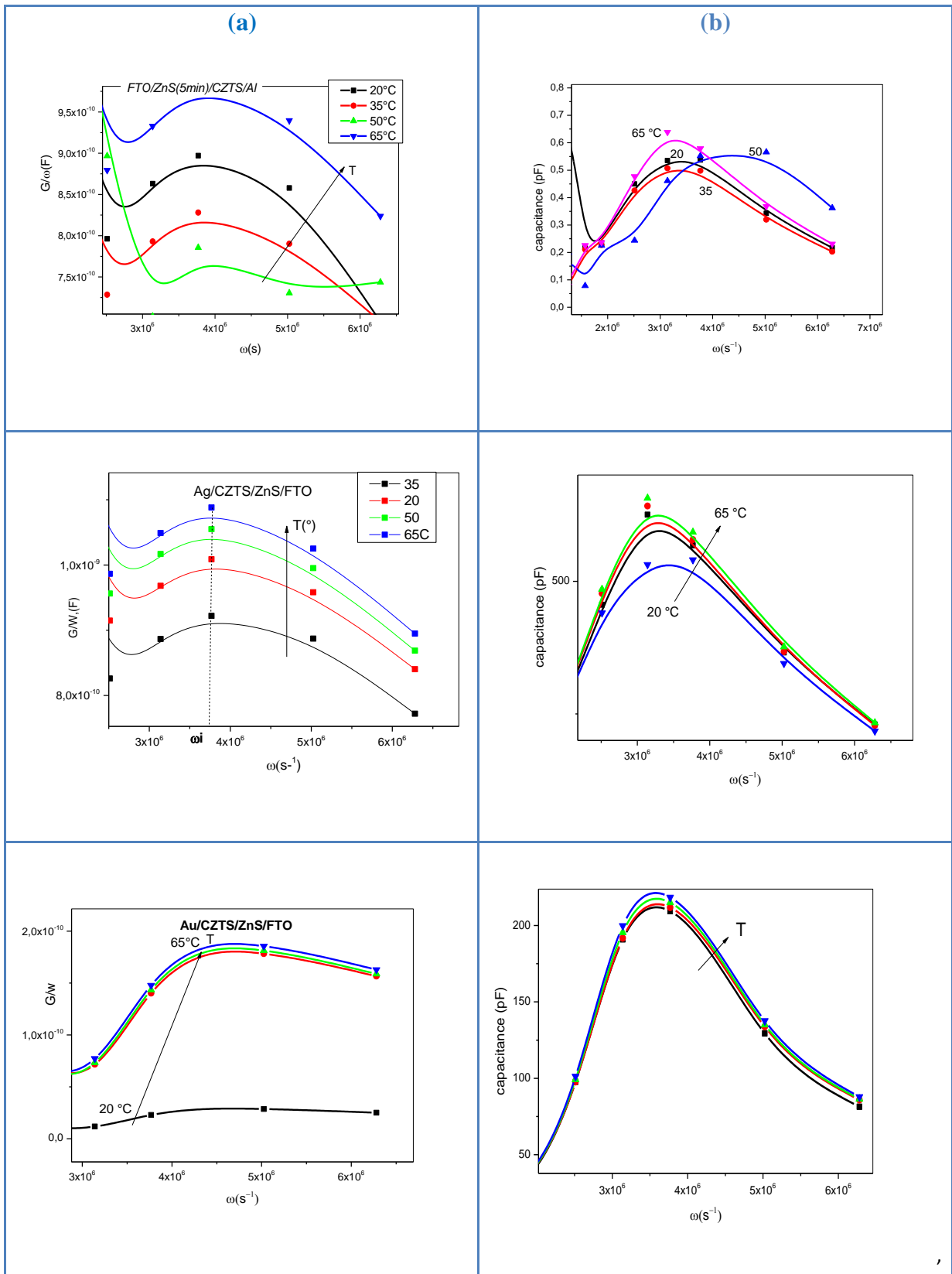


**Figure.IV.11** (a)  $G/\omega - \omega$  and (b):  $C-\omega$  variation of CZTS/ZnS hetero-junction with Al, Ag, and Au back contacts at different temperature

The activation energy of defect was calculated from the Arrhenius plot  $\ln(\omega_r/T^2)$  vs.  $1000/T$ , where,  $E_a$  correspond to the slope of the linear part as seen in figure IV.12.

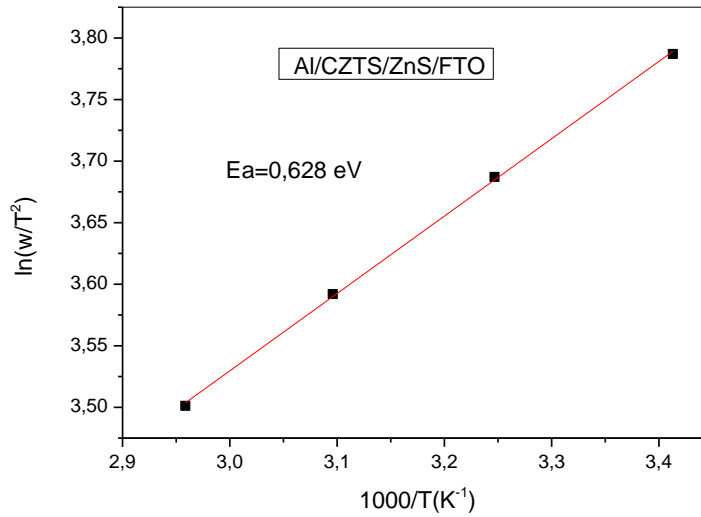


**Figure IV.12:** Arrhenius plot of CZTS/ZnS hetero-junction

The calculated values of interface state density, time constant and activation energy are resumed in table IV.5

Structure	$N_{ss} (eV^{-1} \cdot cm^{-2}) 10^{10}$	$\tau (s) 10^{-7}$	Energy level (eV)
Al/CZTS/ZnS	3.48-3.76	2.65	0.62
Ag/CZTS/ZnS	1.22-1.58	2.64	-
Au/CZTS/ZnS	0.28-0.86	1.9	-

**Table IV.5:** Density of state, life time and energy level of CZTS/ZnS hetero-junction with different back contacts

## IV.2 The effect of *i*-ZnO intrinsic layer and measurement temperature

### IV.2.1 I-V characteristic in the dark

Figure IV.13 report the I-V characteristic measured at room temperature of the both devices with *i*-ZnO (a) and without *i*-ZnO (b). As shown, the I-V characteristic of the realized hetero-structures can be described by eq. (I.1).

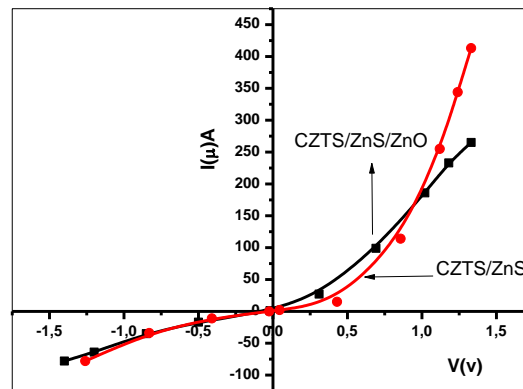


**Figure IV.13:** *I-V characteristic in the dark and at room temperature of CZTS/ZnS hetero-junction (a) with ZnO and (b) without ZnO layer.*

I-V graphs of CZTS/ZnS/(ZnO) hetero-junctions show rectification behavior, which confirms the junction formation. The series resistance ( $R_s$ ) was calculated directly from the I-V plot, as seen in table IV.6, the device with ZnO layer shows lower series resistance than the CZTS/ZnS hetero-junction. Knowing that ZnO thin film is characterized by a high resistivity as reported in [222]. The same conclusion was reported by Obahiagbon [223] who have reported the decrease of series resistance with the addition of ZnO intrinsic layer in the realized device. However, no clear explication was understood yet about the origin of the series resistance reduction with the addition of ZnO layer. The ideality factor decreases when ZnO layer add in the fabricated devise which can refer to the reduction of interface state between CZTS and ZnS buffer layer. Further, those interface states are origin from the band alignment which caused their apparition. The electrical characterization such as ideality factor ( $n$ ), series resistance ( $R_s$ ), and saturation current ( $I_s$ ) are resumed in table IV.6.

$T(^{\circ}\text{C})$	$n$	$R_s(\Omega)$	$I_s(\mu\text{A})$
CZTS/ZnO/ZnS	8	1330	0.47
CZTS/ZnS	11	3917	0.4

**Table IV.6.** Electrical characterization of CZTS hetero-junction with ZnO and without ZnO layer.

#### IV.2.2 I-V-T characteristic in the dark

Figure.IV.14 shows the effect of measurement temperature on the electrical parameters of CZTS/ZnS/ZnO hetero-junction. Different parameters such as series resistance ( $R_s$ ), saturation current ( $I_s$ ), ideality factor ( $n$ ), and activation energy of the saturation current ( $E_a$ ) were extracted from the I-V data at different measurement temperature.

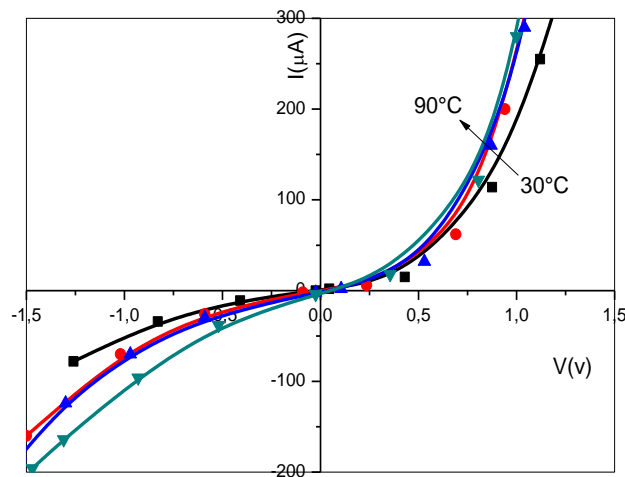


**Figure.IV.14:** The I-V characteristic of CZTS/ZnS/ZnO hetero-junction in the dark at different temperature

The series resistance ( $R_s$ ) decreases with the increases of substrate temperature accompanied with an increase of the saturation current, this was explained by the thermal activation of carriers, the same behavior was reported by Guitouni et al. [224]. The increase of saturation current with the temperature come from the recombination of free carriers at interface state which caused the diminution of ( $I_{sc}$ ). The relation of saturation current with the temperature is expressed as the following expression (IV.5) [225].

$$I_s \propto \exp\left(\frac{-E_a}{KT}\right) \quad (\text{IV.5})$$

The activation energy of the saturation current ( $E_a$ ) was extracted from the variation of the saturation current with  $1000/T$ , as shown in figure.IV.15.

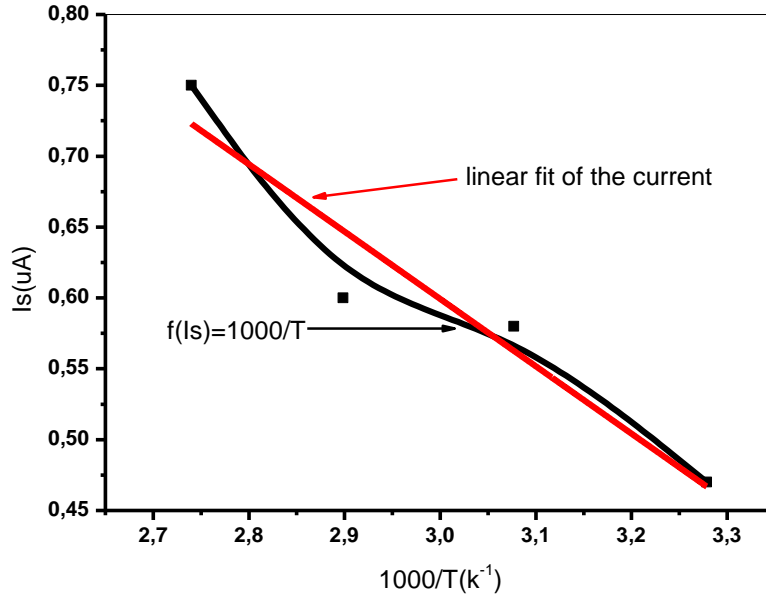


**Figure IV.15:** saturation current as function of  $1000/T$

From the variation of the saturation current with temperature we have determined the activation energy of the saturation current, its value was equal to 0.46 eV. This is attributed to the presence of Sn vacancies deep acceptor defects which have the same activation energy, as reported by Courel et al. [226]. The activation energy of saturation current is closely related to the presence of defects at the interface of CZTS/ZnS hetero-junction, the ideality factor ( $n$ ) is calculated from equation (IV.3) which is represent the slope of the plot  $\ln(I)$  as function of the applied voltage. The calculated ideality factor is reported in table IV.7. As can be seen,  $n$  is depending on the measurement temperature, as the temperature increases the ideality factor decreases from 7 to 1,8. At high measurement temperature, the generation and recombination on the space charge region is the dominant transport mechanism, whereas at low temperature as mentioned above, Brotzmann et al. [15] suggest the presence of amorphous interface at the junction.

$T(^{\circ}C)$	$n$	$R_s(\Omega)$	$I_s(\mu A)$
30	8	1330	0.47
50	3.7	776	0.58
70	2	636	0.6
90	1.5	702	0.75

**Table IV.7:** Electrical properties of realized devices at various measurement temperatures

### IV.2.3 I-V characteristic under illumination

The realized devices were tested under illumination and the photovoltaic effect was observed on a cell area equal to  $0.16 \text{ cm}^2$ . Figure IV.16 illustrated the semi-logarithmic of the I-V curves of the cells.

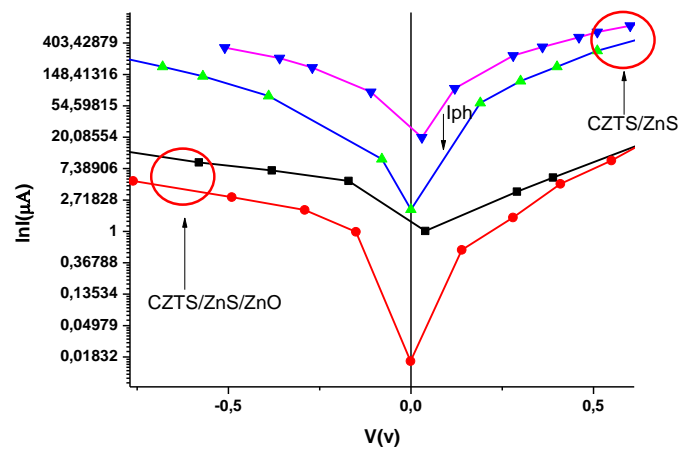


**Figure IV.16:** semi-log plot of I-V characteristic under-illumination

The different parameters of the solar cell were extracted such as open circuit voltage ( $V_{oc}$ ), short circuit current ( $I_{sc}$ ), fill factor (FF), and the efficiency are resumed in table IV.8.

	$V_{oc}$ (mV)	$I_{sc}$ (uA)	FF(%)	$\eta$ (%)
ZnS/ZnO	43	1.2	22	$7.10^{-3}$
ZnS	34	3.16	20	$5.10^{-3}$

**Table IV.8:** Electrical parameters of the fabricated solar cells

As seen in table IV.8, the best efficiency was obtained for the cell with ZnO with a value equal to  $7.10^{-3}$  % and a  $V_{oc}=43\text{mV}$ , and  $FF=0.2$ . These values are low compared to the ones obtained by other process and especially the physical routes in which we can cite: Zhi et al. [227] who reported an efficiency about 3.6 % and a  $V_{oc} = 629 \text{ meV}$  by sputtering and Katagiri et al. [102] who reported in 2003 a value of 5.45% with a  $V_{oc}=582\text{mV}$  and  $J_{sc}=15.5 \text{ mA/cm}^2$  of by thermal evaporation. The low efficiency reported by Bhosale et al. [180] and Vigil-Gal et al. [131] of CZTS solar cells using spray pyrolysis is generally due to the low value of open circuit voltage ( $V_{oc}$ ). This is due to the presence of interface states which act as recombination centre of the free carriers. The presence of these states was confirmed by admittance spectroscopy in our previous work. However, we have reports a density of state in the order of  $10^{10} \text{ cm}^2/\text{eV}$  [228] and Patel et al. [229] reported a value about  $10^9 \text{ cm}^2/\text{eV}$ . Furthermore, Courel et al. [230] have studied the poor performance of spray CZTS solar cells. They declared that beside the low value of  $V_{oc}$ , sprayed CZTS material is characterized by a low value of length diffusion of minority carriers which is related to the crystallites size which don't exceed 300 nm. Indeed, Emrani et al.[231] report a grain size up to  $2.5 \mu\text{m}$  by sputter and  $0.4\mu\text{m}$  was reported by Shin et al.[105] using thermal evaporation. Also another factor who limit CZTS performance is the cliff like band alignment between absorber/buffer (CZTS/ZnS) because of the difference band gap energy (CZTS=1.5 eV and 3.7 for ZnS), the deposition of an intrinsic layer may cause a reduction in the band offset between CZTS and ZnS layers. The depositing of a ZnS/ZnO buffer layer can be retrieve the loss in CZTS solar cells efficiency. In this work the best efficiency was obtained for the cell with ZnO layer. This value still low and need more work to understand and enhance sprayed CZTS solar cell efficiency.

---

### *IV.3 Effect of sulfurization temperature*

---

In this section of chapter IV, we will discuss the obtained results concerning the effect of sulfurized temperature on the properties of sprayed CZTS thin films and related devices. The annealing temperature was varied from 450 to 550 °C.

### III.3.1 Films properties

Films properties were studied using XRD and Raman spectroscopy for the structural properties, Atomic Force microscopy for morphological properties and UV-Visible for the study of the optical properties and Hall effect for the electrical properties.

#### III.3.1.1 Structural properties

##### *a. X Ray Diffraction*

The XRD patterns of CZTS thin films annealed at different sulfurization temperatures are shown in figure IV.17, the observed peaks are related to (112), (220), and (312) planes, they are assigned to CZTS kesterite tetragonal phase (according to #27-0575 card), (112) plane exhibits the higher intensity indicating the preferential orientation the same peaks position were observed in [37,48]. Generally, CZTS thin films deposition is accompanied by the formation of several secondary phases such as SnS, SnS<sub>2</sub>, Sn<sub>2</sub>S<sub>3</sub>, ZnS, and Cu<sub>3</sub>SnS<sub>4</sub> [232-233]

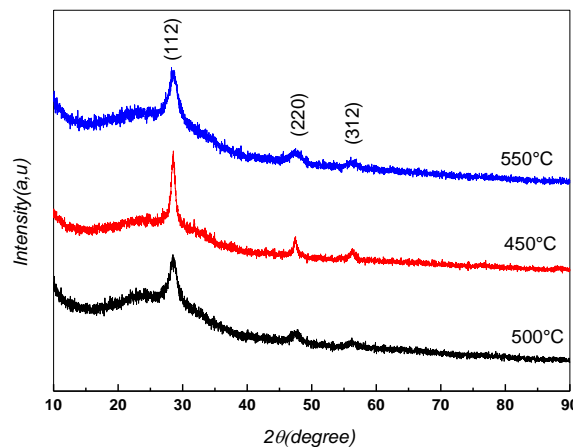


**Figure.IV.17:** XRD patterns of CZTS films sulfurized at different temperatures

It is interesting to note that no peaks related to any secondary phase has been detected. The absence of secondary phase can be a result of the thermal sulfurization, which is a good solution for the reduction of undesirable phases as mention. The same observation has been reported after CZTS sulfurization in [234,235]. Moreover, according to XRD patterns Mo<sub>2</sub>S phase is not formed during sulfurization step. While, it is reported that sulfurization yields to the formation of undesirable Mo<sub>2</sub>S phase [236,79]. With increasing the annealing sulfurization temperature, XRD peaks intensities are reduced, the sample sulfurized at 450 °C exhibits the most intense and sharp peak. This indicated that high temperature sulfurization degrades CZTS sprayed films microstructure.

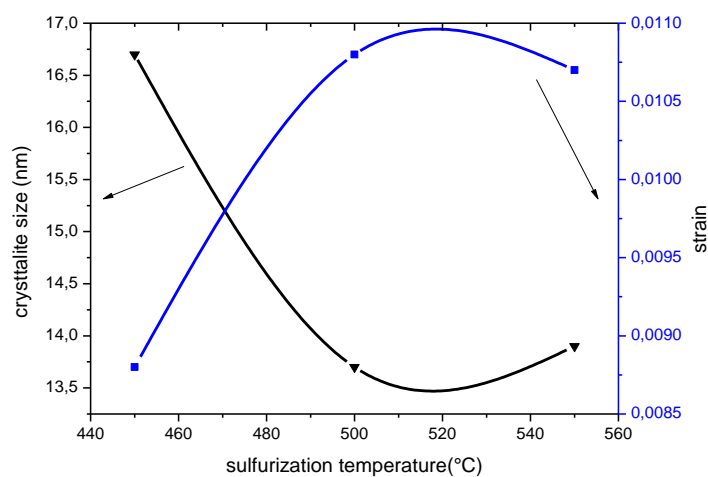
The crystallites sizes were calculated from the most intense peak along (112) plane using Debye Scherer's equation [145] according to (III.2) formula. The lattice strain ( $\epsilon$ ) was calculating using: equation (III.3).

The calculated values of D, FWHM, and strain are regrouped in table IV.9. As can be seen, increasing the sulfurization temperature yields to the reduction of the crystallites size in one hand and the increase in films strain in the other hand. This confirms the microstructure deterioration in films annealed at temperatures above 450 °C.

<i>Annealed T(°C)</i>	<i>FWHM(°)</i>	<i>Crystallite size(nm)</i>	<i>Strain</i>
<b>450</b>	<i>0.5117</i>	<i>16.7</i>	<i>0.0088</i>
<b>500</b>	<i>0.624</i>	<i>13.7</i>	<i>0.0108</i>
<b>550</b>	<i>0.614</i>	<i>13.9</i>	<i>0.0107</i>

**Table IV.9.** FWHM, crystallites size, and strain of CZTS films sulfurized at various temperatures

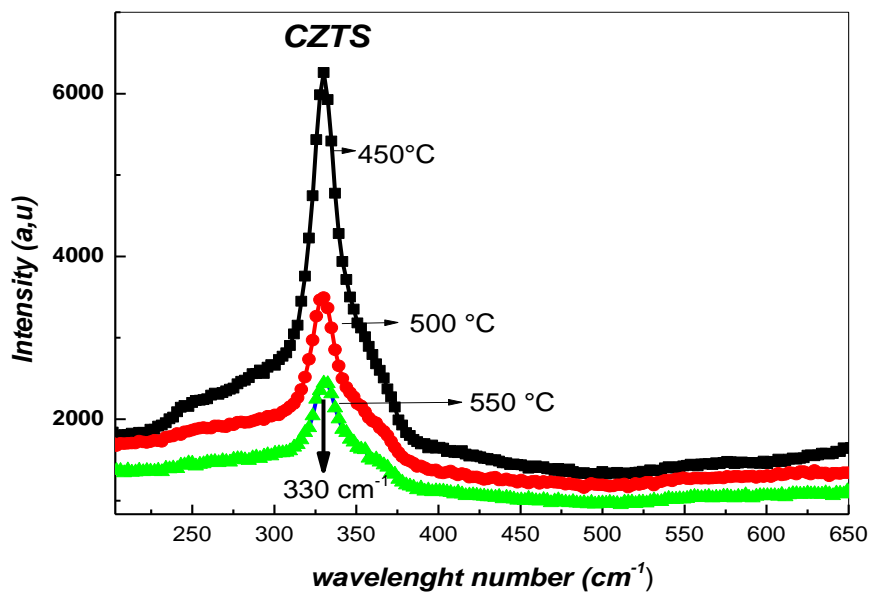
The variation of crystallites size and strain as function of sulfurization temperature is presented in figure IV.18, as seen in the graph their variation are opposite, the low value of strain yield to a large crystallite size whereas the high value of strain yield to small values of crystallites size. Knowing that the strain is related to the presence of the disorder in film network,



**Figure IV.18:** Crystallites size and strain as function of sulfurized temperature.

**b. Raman analysis**

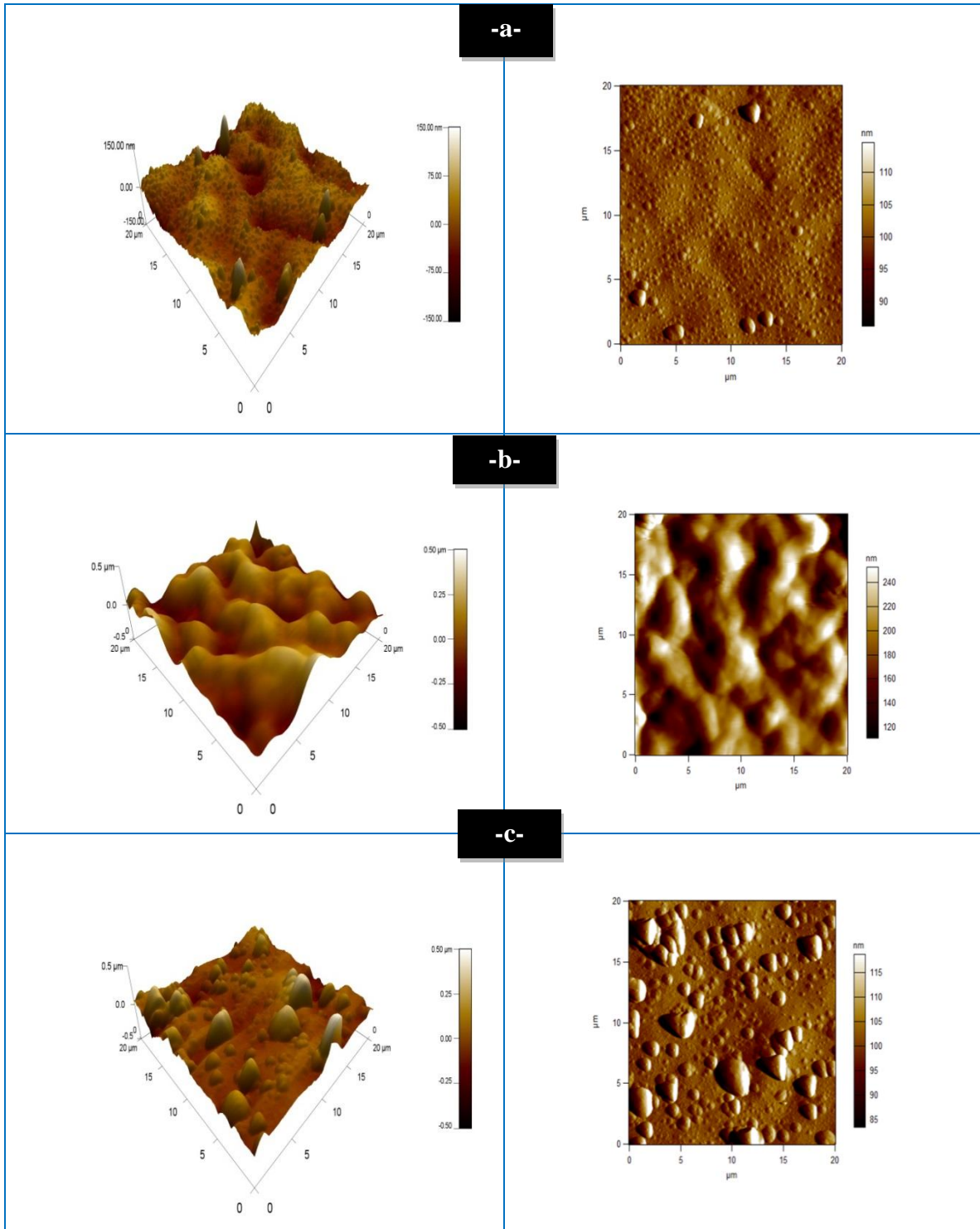
Raman spectra of CZTS are shown in figure IV.19. The single Raman intense peak located at  $330\text{ cm}^{-1}$  is assigned to bulk CZTS [238- 241]. As can be seen no peaks related to any secondary phases is observed confirming CZTS monophas formation. The single phase formation may two origins: (i) the used spray pyrolysis technique, since similar results have been reported by several authors in films prepared by spray pyrolysis method [242-243]. (ii) The sulfurization temperature, Xu et al have investigated the post sulfurization of CZTS thin deposited by sputtering they concluded that after sulfurization pure CZTS without significant amount of secondary phases is obtained after sulfurization at temperatures above  $400^\circ\text{C}$  [244]. It is important to note that film annealed at  $450^\circ\text{C}$  present the most intense peak. This suggests that increasing sulfurization temperature reduces the film crystallinity as concluded from XRD analysis.



*Figure.IV.19: Raman spectroscopy of CZTS at various sulfurized temperature*

**IV.3.1.2 Morphological properties**

CZTS thin films surface morphology was characterized by using AFM images, as shown in Fig.IV.20.



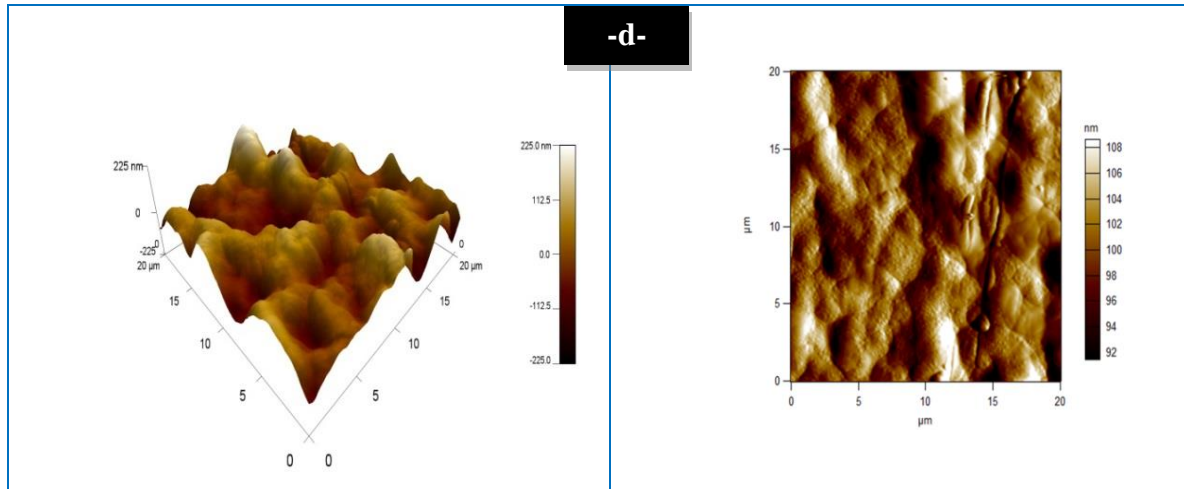


**Figure IV.20.** 3D and 2D AFM images of CZTS thin films (a) as deposited, (b-d) annealed at 450, 500, and 550°C respectively.

As can be seen, annealing temperature increasing results in films grains size enlargement and in films surface roughness increase, as reported in Table IV.10

<i>Annealing (T°C)</i>	<i>As deposited</i>	<i>450</i>	<i>500</i>	<i>550</i>
<b><i>RMS (nm)</i></b>	23	98	80	53

**Table IV.10.** RMS values of CZTS films annealed at various temperatures

Figure IV.21 (a and b) show the variation of both crystallite size and lattice strain with film roughness of CZTS thin films sulfurized at different annealing temperatures, these two parameters lattice strain and roughness have an inverse variation, as the surface of the film became rough, lattice strain became small, whereas the crystallites size became large. Generally, the surfaces roughness increase with the increase of grain (crystallites) size, the surface roughness depends on many conditions such as substrate type, deposition temperature and the thickness of the film or deposition time. Knowing that, the rough surfaces have more nucleation sites, and as a result many crystallites will appear. We can say that the roughness may be depending on the size of grain and also on the shape and the orientation of the grains.

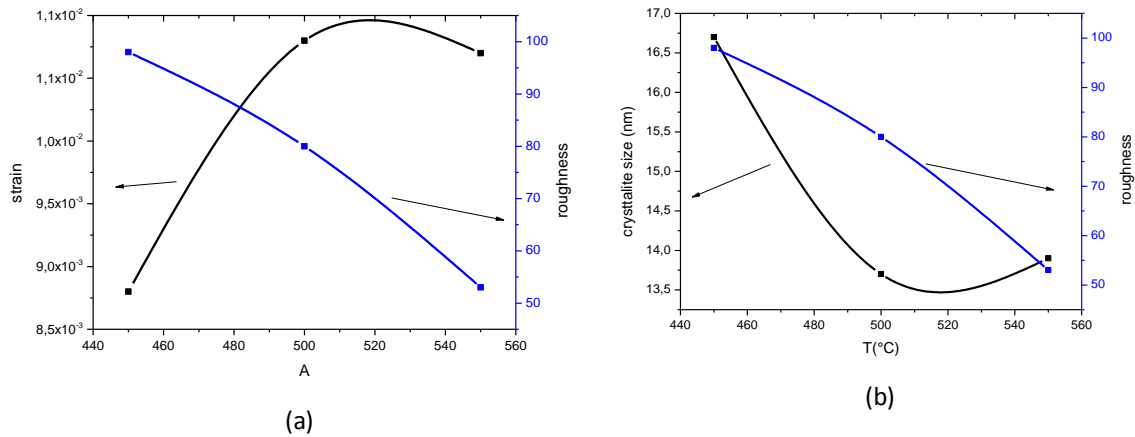


*Figure IV.21:(a) Lattice strain and (b) crystallite size variation with surface roughness as function of sulfurized temperature*

### IV.3.1.3 Optical properties

#### a. Transmittance

The transmittance spectra of CZTS thin films at different annealing temperature are depicted in figure IV.22.

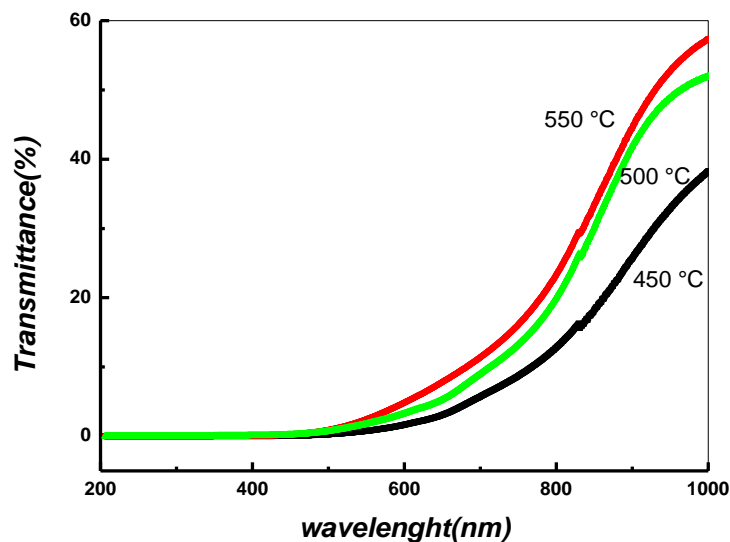


*Figure IV.22: Transmittance spectra of CZTS film as function of sulfurized temperature*

As seen, the whole films exhibiting low transmission in the visible range (400-800nm) lower than 20 %. While, the transmission is enhanced with increasing sulfurization temperature, this can be explained by the reduction of the films thickness. Films annealing tends to the films

densification by reducing its thickness, the same results were reported in CZTS films prepared by sol-gel method [245] and in sputtered CZTS films after sulfurization at 450°C [244].

The absorption coefficient of CZTS thin film was calculated from transmission data. The measured low optical transmittance and large absorption coefficient (higher than  $10^4 \text{ cm}^{-1}$ ) of CZTS films after sulfurization implies that the obtained films are suitable candidates for application as absorber in thin film solar cell technology.

### b. Gap energy

The optical band gap energy was extracted from transmission data fitting, their values were estimated from the extrapolation of the linear section of  $(\alpha h\nu)^2$  plot as function of photon energy ( $h\nu$ ), as illustrated in figure.IV.23.

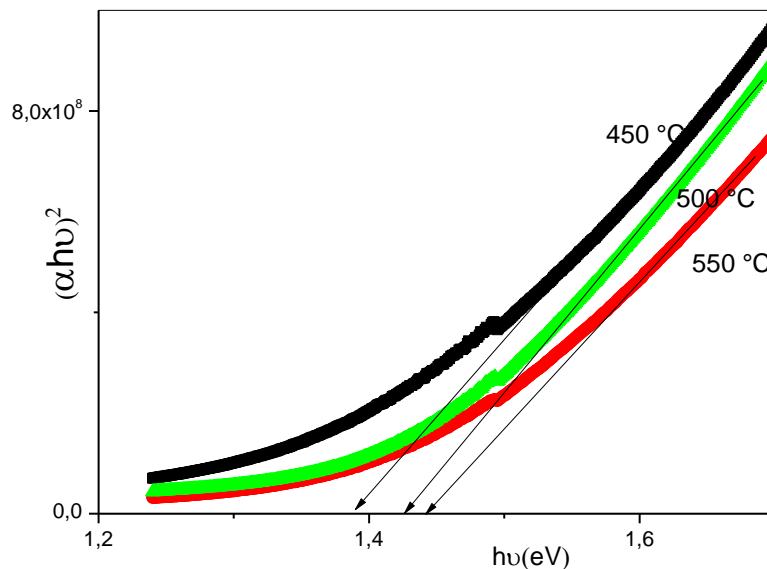


**Figure IV.23:** Tauc's plot of CZTS thin film sulfurized at various temperatures

The measured gap energies are reported in table IV.11. They are in concurrence with the reported band gap energy of sprayed CZTS thin film [81,153-154]. As seen, films optical gap is enlarged with increasing the sulfurization temperature; it varies from 1.38 eV at 450 °C to 1.45 eV at 550 °C. The same results were reported in electrodeposited  $\text{CuIn}(\text{Se}, \text{S})_2$  sulfurized at a temperature varied between 450-550 °C [246]. The optical band gap broadening may originate from the films densification and disorder reduction in films network as a consequence of thermal annealing. Indeed, the film thickness is reduced from 1420 nm to 1220 nm with increasing annealing temperature. Actually, the network disorder reduction yields to films optical band gap enlargement as observed in various thin film semiconductors

[247]. Higher band gap values up to 1.7 eV have been reported this was referred to the presence of secondary phases which enlarges the gap energy and specially ZnS given that this phase has a large band gap energy about 3.7eV.

### IV.3.1.3 The electrical properties

The electrical properties of CZTS thin films at different annealing temperatures were carried out in the dark and at room temperature using Hall Effect. The p-type conductivity of CZTS semiconductor was assessed by the positive Hall coefficient. The measured values of carrier concentration, conductivity and mobility are resumed in Table IV.11. The measured mobility is in agreement with the reported values lying between 0.1 and 10 cm<sup>2</sup>/Vs [248-249]. While, film conductivity and mobility are reduced after thermal sulfurization due to the reduction in the crystallites size as concluded from XRD analysis. The reduction in the crystallite size increases the number of grain boundaries that may cause larger electrons scattering during their transport.

	$d$ (nm)	$E_g$ (eV)	$\rho$ (cm <sup>-3</sup> )	$\mu$ (cm <sup>2</sup> /V s)	$\sigma$ ( $\Omega$ cm) <sup>-1</sup>
450 °C	1420	1.38	$7.23 \times 10^{15}$	9.16	$10.61 \times 10^{-3}$
500 °C	1260	1.42	$8.58 \times 10^{14}$	0.41	$0.56 \times 10^{-3}$
550 °C	1220	1.45	$8.78 \times 10^{16}$	0.18	$2.52 \times 10^{-3}$

*Table IV.11: Film thickness, band gap, carrier concentration, Hall mobility and conductivity of CZTS thin film sulfurized at different annealing temperature*

## IV.3.2 Characteristic of the devices

### IV.3.2.1. Current-Voltages characteristic

The realized devices are tested under illumination using a simulator solar cell with a halogen lamp using a light source with intensity equal to 100mW/cm<sup>2</sup>, the cell area is equal to 0.16 cm<sup>2</sup>.

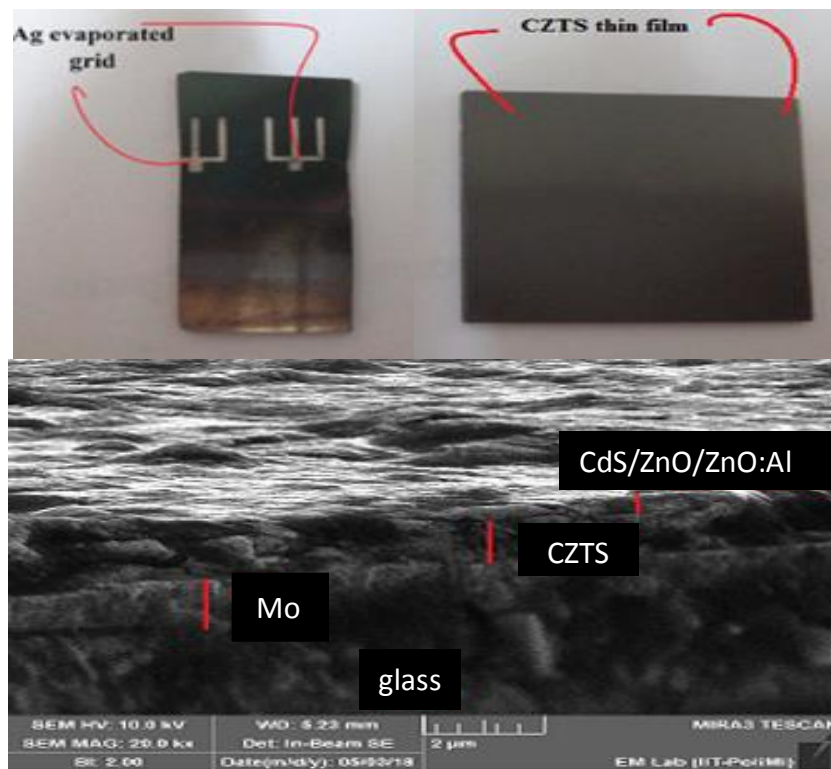


**Figure.IV.24:** Images of CZTS thin film, solar cell, and the cross section of our device.

The silver grid was deposited by thermal evaporation on the top (n-) contact is also visible as seen in figure IV.24 which show the images of CZTS film with related device and the cross section of the cell using scanning electronic spectroscopy.

Figure IV.25 shows the semi-logarithmic plot of current-voltage measurement of different CZTS/CdS hetero-junctions in the dark at room temperature and under illumination.

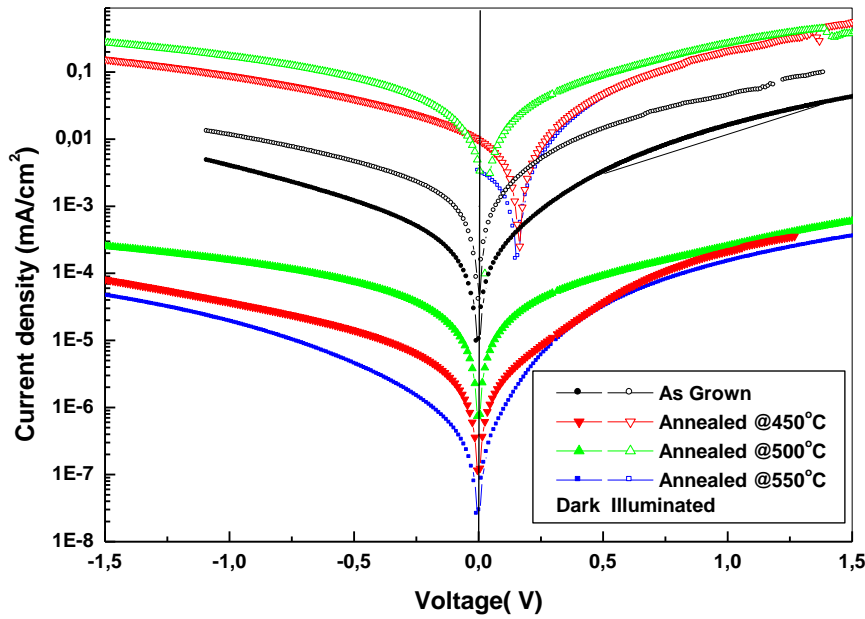


*Figure IV.25: semi log plot of CZTS/CdS solar cells sulfurized at various annealing temperatures*

The values of rectification ratio (RR) were varied between 8 and 5 with the large rectification ratio for the device annealed at 450 °C. The current across the hetero-junction varies exponentially with the applied voltage and their variation can be described by the standard Schottky diode equation III.3. The ideality factor was found equal to 2.2 in the device realized with non-annealed CZTS layer.

However, in treated CZTS films the obtained ideality factor lays between 1.6 and 1.8 when the temperature varied between 450 and 550 °C. This implies that generation-recombination process at the depletion layer is the dominate transport mechanism through the hetero-junction. This suggests also the presence of interface states and defect in the space charge region which is act as charge carriers traps. Mali et al. [250] reported an ideality factor in the range of 2.2-2.9 for CZTS solar cells by SILAR method, they claimed that current transport in CZTS solar cell is controlled by recombination at high defected grain boundary region. In a previous work, we measured an ideality factor more than 5 in CZTS/ZnS hetero-junction; this was explained by the presence of interfacial state defects with a density about  $10^{10} \text{ cm}^{-2} \text{ eV}^{-1}$  [228]. Patel et al. [229] reported a value of interfacial states equal to  $10^9 \text{ cm}^{-3}$  at CZTS/CdS interface.

The saturation current ( $I_s$ ) was calculated from the semi-log plot is reported in table IV.12. The saturation current increase from 291  $\mu\text{A}$  to 587  $\mu\text{A}$  with the increase of sulfurization temperature indicates clearly the defects enhancement due to the grain boundary number increases as a consequence of crystallite size reduction with sulfurization temperature. The series resistance varies between 11-8  $\Omega$ , it decreases with sulfurization temperature increase. Amerani et al. [231] has observed the same trend, they reported a decrease in  $R_s$  from 48 to 14  $\Omega$  when the sulfurization temperature increases from 500 to 575  $^\circ\text{C}$ . Actually, the series resistance regroups the back and front metal contacts resistances, the semiconductors bulk resistances and the interfaces resistance [251]. Thereafter, it is hard to assess the origin of  $R_s$  variation. Despite that the film annealed at 450  $^\circ\text{C}$  exhibits the highest conductivity, it has the largest series resistance, this is due to the film thickness, as shown in table IV.11, the film annealed at 450  $^\circ\text{C}$  is the thicker one. The drawback of the series resistance is the short current circuits reduction and consequently the cell efficiency.

The other parameter affecting the solar cell performance is the shunt resistance ( $R_{sh}$ ) which is due mainly to the defects presence in the bulk of semiconductors and at interfaces. It is estimated from the reverse bias I-V characteristics branch. Shunt resistance reduces drastically the open circuit voltage  $V_{oc}$ . It should be as high as possible in order to prevent losses [21]. The measured  $R_{sh}$  values are reported in table IV.12. The highest  $R_{sh}$  value was found for the cell annealed at 550 $^\circ\text{C}$  (304 $\Omega$ ) and 120 $\Omega$  for the one annealed at 450 $^\circ\text{C}$ , whereas the low value is measured in the cell annealed at 500 $^\circ\text{C}$ , therefore, the latter presents the low efficiency and  $V_{oc}$  values (table IV.12).

As seen in Figure IV.24, all devices exhibit photovoltaic behavior except the un-annealed device. The cell annealed at 450 $^\circ\text{C}$  exhibits the best  $V_{oc}$  equal to 161 mV and  $I_{sc}$  equal to 1.56 mA with a fill factor of 28 % and an efficiency of 0.43 %. This is due to the good crystallinity of the film sulfurized at 450  $^\circ\text{C}$  compared to the other films. The film annealed at 500  $^\circ\text{C}$  leads to the lower efficiency, this can be attributed to its inferior crystalline quality according to XRD and Raman analysis. This is consistent with the measured high series resistance, low shunt resistance and high current saturation in this cell (table IV.12).

T(°)	Voc(meV)	Jsc(mA.cm <sup>-2</sup> )	Rs(Ω)	n	Rsh(Ω)	FF (%)	PCE (%)	Is(μA)
450	161	9.73	11.48	1.7	120	28	0.43	291.6
500	25.3	4.25	10.77	1.8	37	25	0.02	587
550	156	1.41	8.5	1.6	304	31	0.06	336
As deposited	-	-	11.83	2.2	-	-	-	120

**Table. IV.12:** The calculated parameters of the realized solar cells.

In table IV.13 we have compiled parameters of CZTS based solar cells reported by several authors working with different deposition techniques and CZTS films treatments.

CZTS preparation technique and treatment	Voc (mV)	Is (mA/cm <sup>2</sup> )	FF (%)	η(%)	Rs (Ω)	Rsh (Ω)	ref
<i>Thermal evaporation + annealing in air at 570°C</i>	661	19.5	65.8	8.4	4.5	-	[105]
<i>Thermal evaporation +sulfurization at 520°C</i>	629	12,53	58	4.53	8.5	428	[252]
<i>Thermal co- evaporation + sulfurization at 550°C</i>	633	21.5	60.1	8.27	5.85	2.2 10 <sup>4</sup>	[253]
<i>Evaporation + sulfurization 550 °C</i>	400	5.8	45	1.05	-	-	[254]
<i>Dc rf co-sputtering of Cu , Sn, and ZnS target annealing at 250°C in N<sub>2</sub> +sulfurization at 600 °C</i>	629	13.14	42	3.6	126	189	[227]
<i>Multi target magnetron sputtering +sulfurization at 570°C</i>	600.4	11.82	40.4	2.87	25.1	144. 5	[255]
<i>Dc and Rf sputtering of Cu ,Zn ,Sn targets +sulfurization at 575 °C</i>	593	20.5	48	5.75	19	620	[236]
<i>Electrodeposition + sufurization at 590°C</i>	673	18.7	44	5.5	68	1101	[256]
<i>Sol gel sulfurization at 500°C</i>	390	7.81	33	1.01			[257]
<i>SIAR + sulfurization at 575 °C</i>	400	8.27	52	1.06	-	-	[258]
<i>Spray pyrolysis at 500 °C substrate temperature</i>	390	7.31	30	0.86	190	400	[180]
<i>Spray heated in Air + Sulfur and tin atmosphere at 550°C</i>	173	10	28	0.5			[131]

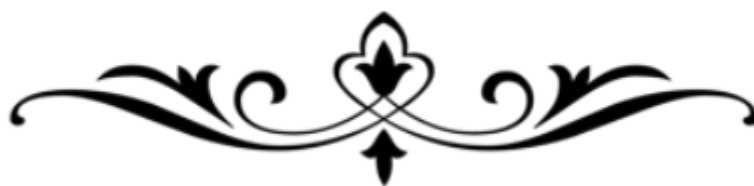
<i>Spray in Ar + Sulfur and tin atmosphere At 550°C</i>	361	7.5	37	1.0			[131]
<i>Spray pyrolysis at 500 °C substrate temperature</i>	510	8.88	23	1.09	278.5	250	[180]
<i>Spray pyrolysis at Ts 450 °C with Ar carrier gas</i>	246	3.9	39	0.4	14	95	[259]
<i>Spray pyrolysis + sulfurization at 450°C in H<sub>2</sub>S+Ar</i>	161	9.73	28	0.43	11.5	120	This work

**Table IV.13:** The electrical parameters of CZTS solar cells calculated by several authors.

The most important conclusions that can be retained are: the results are too spread; best results are achieved by the physical deposition methods namely thermal evaporation and sputtering. While, spray pyrolysis technique yields to inferior solar cell performances, even though the sulfurization treatments are applied, Thereafter, despite that spray pyrolysis, technique is considered as one of the most appropriate growth methods to develop low-cost devices, it yields to low solar cell efficiency. As can be seen, our result remains in the range of efficiency achieved by spray pyrolysis. This discrepancy may originate from the films microstructure differences. We speculate that the major reason of spray pyrolysis inferiority is due to the achieved low material grain sizes. Indeed, grain size up to 2.5-1  $\mu\text{m}$  [252, 255] and 0.4  $\mu\text{m}$  [4] were reported in sputtered and thermally evaporated CZTS thin films respectively. While in sprayed films the grain size does not exceed 300 nm [257, 131] in our case, we have measured a crystallite size of 16 nm. Grain boundaries introduce additional defects acting as recombination centers. The same conclusion has been outlined by Courel et al. [230], they explained that the inferiority of spray pyrolysis solar cells is originated from the low mobility of electron and recombination that may reduce drastically the open circuit, which is in concordance with our conclusion. It has been reported that this problem is particularly more detrimental in CZTS-based devices, than in chalcopyrites (CuInGsa) Sn-based ones [260]. Any reduction in the grain size is accompanied by the increase in the grain boundaries and consequently a recombination enhancement, reduction in carrier's mobility due to the scattering and the photo-generated carrier's lifetime reduction. In fact, low mobility values are usually reported in CZTS thin films, particularly in samples deposited using spray pyrolysis technique due to the microstructure [261, 262]. Both these effects concur to Voc, FF and cell efficiency reduction. Courel et al. had studied the loss mechanism in sprayed CZTS solar cells

and find that CZTS is characterized by a low minority carrier lifetime and defects in CZTS bulk [71]. This is in concordance with several authors conclusion claiming that spray pyrolysis technique produces low efficiency solar cells [131,180,259].

# Conclusion



# Conclusion

The main objective of this PhD thesis was the realization and the electrical characterization of hetero-junction and related solar cells from a stack of different layers such as ( $\text{Cu}_2\text{ZnSnS}_4$ ,  $\text{ZnS}$ ,  $\text{CdS}$ ,  $\text{FTO}$ ,  $\text{ZnO}$ , and  $\text{ZnO: Al}$ )

To tackle this task, the first step of own project is to enhance and establish the moderate experimental condition for synthesizing high quality of CZTS film which used in this work as the active layer of the realized photovoltaic devices. Fourth parameters were studied namely substrate temperature, deposition time, copper and zinc salt molarities. After the elaborated CZTS layer, several characterization techniques were adapted for analyzed their properties such as X Ray Diffraction and Raman spectroscopy for the structural properties, Atomic Force microscopy for the morphological properties, UV-Visible and Hall effect for study the optical and electrical properties.

The study of the effect of substrate temperature ( $T_s$ ) on the structural properties of CZTS film revealed that the whole films crystallize in tetragonal structure (Kesterite) with a preferential orientation along (112) plan, the increase of substrate temperature yield to an increase of crystallite size from 33 to 60 nm. The peak position at (112) plane shifted with the increase of  $T_s$  toward the high angles because of the presence of lattice strain in film network. With the increase of temperature, the number of secondary phases increase such as  $\text{CuS}$ ,  $\text{Cu}_7\text{S}_4$  and  $\text{ZnS}$ . The Raman spectroscopy analysis show an intense and sharp peak at  $335 \text{ cm}^{-1}$  position and a little shift with the increase of  $T_s$  because of the presence of micro strain and the increase of film's thickness whereas the presence of  $\text{CuS}$  phase was observed for the film elaborated at 300 and 390 °C. The whole films exhibit a high absorption coefficient with a direct band gap energy lie between 1.6~1.4 eV. Hall Effect confirms the p-type conductivity of kesterite films with a high mobility, the conductivity was varied between 1 and 150  $(\text{cm}.\Omega)^{-1}$ . These results reveal that CZTS material is eco-friendly candidate absorber layer for solar energy application, however, their properties are depending on growing temperature.

From the investigation of deposition time ( $Dt$ ) effect, we see that the whole grown films have tetragonal structure with a preferential orientation along (112) plane. With the increase of deposition time (15-45 min), we observed the emergence of zinc sulfide ( $\text{ZnS}$ ) for de sample grown for 45 min with the increase of secondary phases number. The Raman spectrum of the whole films are characterized by a strong peak position located at  $335 \text{ cm}^{-1}$  with a peak

## Conclusion

---

position at  $472\text{ cm}^{-1}$  attributed to the  $\text{Cu}_x\text{S}$  binary phase. The film deposited at 15 min show pure kesterite CZTS phase then this phase appeared in the film grown for 30 and 45 min. The optical analysis show a high absorption coefficient more than  $10^4\text{ cm}^{-1}$  which increase with deposition time and referred to the increase of film thickness, the gap energy decrease from 1.6 to 1.3 eV with the increase of Dt. Hall effect confirm the p-type conductivity of CZTS film with the increase of conductivity with Dt from 7,3 to  $124\text{ (cm}\cdot\Omega)^{-1}$  accompanied by an increase of carriers mobility from 9 to  $520\text{ cm}^2/\text{vs}$  and the carrier concentration was in the order of  $10^{18}\text{ cm}^{-3}$ .

Copper concentrations salt effect on CZTS thin films revealed a strong influence of this parameter on CZTS properties. XRD patterns indicated the formation of CZTS films with a preferential orientation along (112) plane with an increase of the intensity with the augmentation of Cu molarity. Furthermore, as the copper molarity increase the emergence of secondary phases increase, such as CuS,  $\text{Cu}_2\text{S}$ ,  $\text{Sn}_2\text{S}_3$ ,  $\text{Cu}_4\text{SnS}_3$  and annilite phase  $\text{Cu}_7\text{S}_4$ . The crystallite size increases and reaches a maximum value of 83,76 nm then it decreases for the sample C4 which refer to apparition of many secondary phases at high concentration of copper salt. Hence, the transmittance spectra reveal a strong absorption of the films with a band gap energy decrease with the increase of copper salt concentration from 1.9 to 1.3 eV. Hall Effect measurement confirms the p-type conductivity of the film with a high carrier concentration in the order of  $10^{21}\text{ cm}^{-3}$  whereas the film conductivity varies from 180 to  $400\text{ (cm}\cdot\Omega)^{-1}$  wich refer to the high concentration of Cu and the possibly of formation of several acceptor defect such as  $\text{Cu}_{\text{Zn}}$  antisite which related to Cu rich composition of the film.

The whole films grown with various zinc content crystallize in tetragonal structure with a preferential orientation along (112) plan. Films are composed of secondary phases such as CuS at low Zn molarity and ZnS phase when film is deposited with higher zinc precursor molarities. Film's crystallites size increase from 29 to 133 nm with the increase of zinc content. Atomic Force Microscopy images show that the film roughness increases with Zinc concentration from 146 to 248 nm. Increasing the Zn molarity improved the film crystallinity and the optical band gap broadening due to the presence of disorder in the network. Due to the presence of ZnS phase the electrical conductivity is lowered from 14.2 to  $2.4\text{ (}\Omega\cdot\text{cm)}^{-1}$  due to the reduction of free carrier concentration

In the second part which is the main of this work, we have realized various structure such as CZTS/ZnS with different back contacts, Au/CZTS/ZnS/ZnO/FTO for studying the effect of

## Conclusion

---

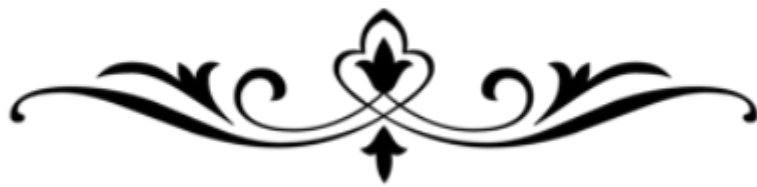
ZnO layer on the electrical properties of the fabricated device, and CZTS/CdS solar cells in which we have studied the effect of sulfurization temperature on the solar cells performance. Three different back metals contact (Al, Au and Ag) were tested to investigate the influence of metal contact nature on device properties in order to find an alternative metal of the commonly used Molybdenum. CZTS and ZnS layers were prepared by a simple pneumatic spray pyrolysis technique. The electrical characterization of the devices was achieved by (I-V) at ambient and at different temperatures and C-G-f measurements. The whole IV characteristics exhibit a rectifying behavior. The ideality factor of all devices were found to be large, it is found equal to 5.9 when using Au contact and equal to 10.5 and 11.4 in heterojunction prepared with Ag and Al back contacts respectively. The anomalous ideality factors greater than unity are explained in terms of the Schottky contact nature between CZTS, Al and Ag in one hand and by the presence of interface states and the series resistance on the other hand. The high value of the ideality factor suggests that the current transport mechanism in the devices is achieved by tunneling assisted by interface states emission-recombination rather than by the thermionic emission. The capacitance and conductance versus frequency characteristic reveals the presence of defects in CZTS/ZnS interface with a density in the order the  $10^{10} \text{ cm}^{-3}$  when using Al or Ag as back contacts, while it is found one order of decade lower when using Au metal contact. The defects time constant is found equal to  $10^{-7}$ s. Finally, we inferred that Au metal can be use as back contact for based CZTS heterojunction solar cells as alternative to Mo. The effect of the intrinsic layer (i-ZnO) and the measurement temperature on the electrical behavior of the realized devices reveal that Zn (O,S) can be a viable buffer layer for CZTS solar cells which present better electrical properties of the realized devices. Further, we have observed the dependence of the electrical parameters on the measurement temperature, the ideality factor decreases from 7 to 1.8 when the temperature varied between 30 and 90°C, a decrease of the series resistance with the increase of the saturation current was obtained. The activation energy of the saturation current is about 0.46 eV and attributed to the presence of Sn vacancies acceptor defect. The photovoltaic effect was observed on the fabricated cells with a best efficiency equal to  $7.10^{-3}$  % and a  $V_{oc}$  equal to 0.043V for the cells with Zn (O, S) buffer layer, the low efficiency of sprayed CZTS solar cells can be explained by the low diffusion length of minority carriers and the cliff like band alignment buffer/ absorber layer which allows the formation of interface state defect at absorber/buffer interface. CZTS cells were sulfurized at various temperatures (450-550 °C). The sample sulfurized at 450°C show the best crystallinity of the film with a high absorption coefficient and low band gap energy. All the realized devices

## Conclusion

---

Mo/CZTS/CdS/ZnO/ZnO: Al show rectification behavior with an ideality factor varied between 1.6 and 1.8 which implies that the electron-hole or interfacial recombination is the dominant transport mechanism at the hetero-junction. Nevertheless, the solar cell sulfurized at 450° C shows an efficiency about 0.43 % whereas the cell annealed at 500 and 550 show an efficiency about 0.02 and 0.06 % respectively, the low efficiency of CZTS by spray pyrolysis compared to other routes is due mainly to the low  $V_{oc}$  because of the recombination in the CZTS bulk and at interfaces whereas the fabricated cell with the best efficiency give a current density equal to 9.8 mA/Cm<sup>2</sup>.

# References



---

## References Introduction

---

- [1] Bell, M.L.; Davis, D.L. & Fletcher, T. (2004). "A Retrospective Assessment of Mortality from the London Smog Episode of 1952: The Role of Influenza and Pollution". *Environ Health Perspect.* 112 (1; January)
- [2] Smith, Bruce, Balakrishnan et al (2014), *Annual Review of Public Health*, in press.
- [3] E. Becquerel, C. R. *Hebd. Seances Acad. Sci.* 9, 561 (1839).
- [4] Ohl R. S. (1941), 'Light-sensitive electric device', U.S. Patent No. 2,402,662; 'Electrical translating device utilizing silicon', U.S. Patent No. 2,402,839; 'Light-sensitive device including silicon', U.S. Patent No. 2,443,542.
- [5] Kingsbury E. F. and Ohl R. S. (1952), 'Photoelectric properties of ionically bombarded silicon', *Bell Syst. Tech. J.* 31, 8092.
- [6] Pearson G.L., 18th IEEE Photovoltaic Specialists Conference, PV founders award luncheon (1985)
- [7] Fuller C.S., Pearson G.L., *J.Appl.Phys.*, 25, 676 (1954)
- [8] Green MA, Blakers AW, Osterwald CR. Characterization of high-efficiency silicon solar cells. *Journal of Applied Physics* 1985; 58: 4402–4408.
- [9] Kunta Yoshikawa, Hayato Kawasaki, Wataru Yoshida, Toru Irie, Katsunori Konishi, Kunihiro Nakano, Toshihiko Uto, Daisuke Adachi, Masanori Kanematsu, Hisashi Uzu and Kenji Yamamoto' Silicon heterojunction solar cell with interdigitated back contacts for a photoconversion efficiency over 26%' *NATURE ENERGY* 2, 17032 (2017).
- [10] Shockley, W.; Queisser, H. J. Detailed Balance Limit of Efficiency of P-N Junction Solar Cells. *J. Appl. Phys.* 1961, 32, 510
- [11] G.Liu, T. Schulmeyer, J. Brotz, A. Klein and W. Jaegermann, *Thin Solid Films* 431(2003)477.
- [12] Green, M.A., Emery, K., Hishikawa, Y., Warta, W., Dunlop, E.D.: Solar cell efficiency table (version 42). *Prog. Photovoltaics Res. Appl.* 21, 827–837 (2013)
- [13] Sandip Das, Krishna C. Mandal and Raghu N. Bhattacharya, 'Earth-Abundant Cu<sub>2</sub>ZnSn(S,Se)<sub>4</sub> (CZTSSe) Solar Cells', *Semiconductor Materials for Solar Photovoltaic Cells*, Springer Series in Materials Science 218.

---

## References Chapter I

---

- [12] <https://www.google.dz/url?sa=i&source=images&cd=&cad=rja&uact=8&ved2ahUKEwiiyvnl1t6feAhUNzoUKHf5tBtgQjRx6BAgBEAU&url=http%3A%2F%2Fzigorat.co%2Fdiagram-of-photovoltaic-cell.html&psig=AOvVaw2qi9yBjrKZrBEUKorOyKUs&ust=154075769019362>
- [13] Sze SM1981 Physics of Semiconductor Devices (New York: Wiley)
- [14] ShahCT, Noyce RNand ShockleyW1957 Proc. IRE 45 1228–43
- [15] Brotzmann M, VetterUand HofsassHJ 2009 Appl. Phys. 106 063704
- [16] Schenk A and KrumbeinUJ 1995 Appl. Phys. 78 3185
- [17] Green MA.Solarcell:operatingprinciple,technologyandsystemapplication. EnglewoodCliffs,NJ,USA:Prentice-HallInc.;1982.
- [18] LuqueA,HegeudusS.Handbookofphotovoltaicscienceandengineering.2nd ed. NewYork,USA:JohnWileyandSonsLtd.;2011.
- [19] CuevasA,SintonRA,MidkiffNE,SwansonRM.26%efficient pointcontact junction concentratorsolarcellwithafrontmetalgrid.IEEEElectronDevice Lett 1990;11:6–08.
- [20] Solanki CS.Solarphotovoltaics:fundamentalstechnologiesandapplications. India: PHILearningPvt.Ltd.;2009.
- [21] Altamura G2014,”Development of CZTSSe thin films based solar cells “,PhD Thesis Joseph-Fourier—Grenoble I university
- [22] Bao Wujisiguleng,” First Principles Study on Band Offsets at the Cu<sub>2</sub>ZnSnS<sub>4</sub>-Based Heterointerfaces”, Thesis for Doctor of Engineering ,Department of Engineering Physics, Nagoya Institute of Technology,Nagoya, JAPAN.March 2014.
- [22x] A. Niemegeers, M. Burgelman and A. De Vos, Appl. Phys. Lett. 67 (1995) 843
- [23] D. A. Cusano, 1963, Solid-State Electronics, vol. 6, pp. 217-232
- [24] E. I. Andirovich, Y. M. Yuabov, and G. R. Yagudaev, 1969, Sov. Phys. Semicond., 3, pp. 61
- [25] S. Wagner, J. Shay, P. Migliorato, H.M. Kasper, Applied Physics Letters 25 (1974) 434.
- [26] L. L. Kazmerski, F. R. White and G. K. Morgan, Thin-film CuInSe<sub>2</sub>/CdS heterojunction solar cells, Appl. Phys. Lett., 1976, 29, 268–269.
- [27] M Konagai, M Sugimoto, K Takahashi;”High efficiency GaAs thin film solar cells by peeled film technology “, Journal of crystal growth, 1978
- [28] Todorov, T.K., Tang, J., Bag, S., Gunawan, O., Gokmen, T., Zhu, Y., Mitzi, D.B.: Beyond 11 % efficiency: characteristics of state-of-the-Art Cu<sub>2</sub>ZnSn(S,Se)<sub>4</sub> solar cells. Adv. Energy Mater. 3, 34–38 (2013)
- [29] W. Wang, M. T. Winkler, O. Gunawan, T. Gokmen, T. K. Todorov, Y. Zhu andD. B. Mitzi, Device Characteristics of CZTSSe Thin-Film Solar Cells with 12.6 % Efficiency, Advanced Energy Materials,
- [30] R. Shabu , A. Moses Ezhil Raj , C. Sanjeeviraja, C. Ravidhas Materials Research Bulletin 68 (2015) 1.
- [31] Benagli S, Borrello D, Vallat-Sauvain E, Meier J, Kroll U, Hötzel J, Spitznagel J,

Steinhauser J, Castens L, Djeridane Y. High-efficiency amorphous silicon devices on LPCVD-ZNO TCO prepared in industrial KAI-M R&D reactor. 24th Europea Photovoltaic Solar Energy Conference, Hamburg, September 2009.

- [32] S. Ahn, S. Lee and H. Lee, 27th European Photovoltaic Solar Energy Conference, Frankfurt, 2012.
- [33] Y. Gu'lena, F. Bayansalb, B.S-ahinb, H.A.C- Etinkarab, H.S.Guderb *Ceramics International* 39 (20&13) 6475.
- [34] [http://www.pvtech.org/news/first\\_solar\\_surpasses\\_ges\\_cdte\\_cell\\_efficiency\\_record](http://www.pvtech.org/news/first_solar_surpasses_ges_cdte_cell_efficiency_record)
- [35] M.A. Green, K. Emery, Y. Hishikawa, W. Warta, E.D. Dunlop, *Solar cell efficiency tables (version 46)*, *Prog. Photovolt.: Res. Appl.* 23 (2015) 805–812
- [36] P. Jackson, D. Hariskos, E. Lotter, S. Paetel, R. Wuerz, R. Menner, W. Wischmann, M. Powalla, *Progress In Photovoltaics: Research and Applications* 19 (2011), pp. 894–897
- [37] Wang, K., Gunawan, O., Todorov, T., Shin, B., Chey, S.J., Bojarczuk, N.A., Mitzi, D., Guha, S.: Thermally evaporated Cu<sub>2</sub>ZnSnS<sub>4</sub> solar cells. *Appl. Phys. Lett.* 97, 143508 (2010)
- [38] Guo, Q., Ford, G.M., Yang, W.-C., Walker, B.C., Stach, E.A., Hillhouse, H.W., Agrawal, R.: Fabrication of 7.2 % efficient CZTSSe solar cells using CZTS nanocrystals. *J. Am. Chem. Soc.* 132, 17384–17386 (2010)
- [39] [https://commons.wikimedia.org/wiki/File:Elemental\\_abundances.svg](https://commons.wikimedia.org/wiki/File:Elemental_abundances.svg)
- [40] Song X., Ji X., Li M., Luo X. and Zhang H., (2014), A review on development prospect of CZTS Based Thin Film Solar Cell, *international Journal of Photoenergy*, Article ID 613173, 11pages
- [41] Vasekar S. P. and Dhakal T. P., (2013), Thin film solar cells using Earth abundant materials, in *Tech open* 145-168
- [42] Chen S., Gong X. G., Walsh A. and Wei S., (2009), Crystal and electronic band structure of Cu<sub>2</sub>ZnSnX<sub>4</sub> (X=S and Se) photovoltaic absorbers: First-principles insights, *Applied Physics Letters*, 94, 041903 1-3
- [43] S. Schorr, *Solar Energy Materials and Solar Cells*, 95 (2011), pp. 1482–1488
- [44] J. J. Scragg, L. Choubrac, A. Lafond, T. Ericson, C. Platzer-Björkman, *Applied*
- [45] R. Palitha Wejisundera, *Ceramics Silikáty* 54 (2010) 19.
- [46] J. R. Tuttle, M. Contreras, D. S. Albin and R. Noufi. Physical, chemical and structural modifications to thin-film CuInSe<sub>2</sub>-based photovoltaic devices. In *Proceedings of the 22nd IEEE Photovoltaic Specialists Conference*, volume 2, pages 1062–1067, 1991.
- [47] T. Tanaka, A. Yoshida, D. Saiki, K. Saito, Q. Guo, M. Nishio and T. Yamaguchi. Influence of composition ratio on properties of Cu<sub>2</sub>ZnSnS<sub>4</sub> thin films fabricated by co-evaporation. *Thin Solid Films*, 518(21, Supplement 1), S29–S33, 2010.
- [48] A. Ennaoui, M. Lux-Steiner, A. Weber, D. Abou-Ras, I. Kötschau, H.W. Schock, R. Schurr, A. Hölzing, S. Jost, R. Hock, T. Voß, J. Schulze and A. Kirbs. Cu<sub>2</sub>ZnSnS<sub>4</sub> thin film solar cells from electroplated precursors: Novel low-cost perspective. *Thin Solid Films*, 517(7), 2511–2514, 2009.
- [49] K. Jimbo, R. Kimura, T. Kamimura, S. Yamada, S. M. Win, H. Araki, K. Oishi and H. Katagiri. Cu<sub>2</sub>ZnSnS<sub>4</sub>-type thin film solar cells using abundant materials. *Thin Solid Films*, 515(15), 5997–5999, 2007.
- [50] R. Wagner and H. D. Wiemhöfer. Hall effect and conductivity in thin films of low temperature chalcocite Cu<sub>2</sub>S at 20°C as a function of stoichiometry. *Journal of*

- Physics and Chemistry of Solids, 44, 801–805, 1983.
- [51] Z. Zhou, Y. Wang, D. Xu and Y. Zhang. Fabrication of Cu<sub>2</sub>ZnSnS<sub>4</sub> screen printed layers for solar cells. *Solar Energy Materials and Solar Cells*, 94, 2042–2045, 2010.
- [52] T. Kato, H. Hiroi, N. Sakai, S. Muraoka and H. Sugimoto. Characterization of front and back interfaces on Cu<sub>2</sub>ZnSnS<sub>4</sub> thin-film solar cells. In *Proc. of the 27th EU-PVSEC*, 2012.
- [53] A. Weber, R. Mainz, T. Unold, S. Schorr and H.-W. Schock. In-situ XRD on formation reactions of Cu<sub>2</sub>ZnSnS<sub>4</sub> thin films. *Physica Status Solidi C*, 6(5), 1245–1248, 2009.
- [54] Chen, S., Yang, J.-H., Gong, X.G., Walsh, A., Wei, S.-H., 2010. Intrinsic point defects and complexes in the quaternary kesterite semiconductor Cu<sub>2</sub>ZnSnS<sub>4</sub>. *Phys. Rev. B* 81, 245204.
- [55] A. Walsh, S. Chen, S.-H. Wei and X.-G. Gong. Kesterite thin-film solar cells: Advances in materials modelling of Cu<sub>2</sub>ZnSnS<sub>4</sub>. *Adv. Energy Mater.* 2(4), 400–409, 2012.
- [56] P.A. Fernandes, P.M.P. Salomé and A.F. da Cunha. Study of polycrystalline Cu<sub>2</sub>ZnSnS<sub>4</sub> films by Raman scattering. *Journal of Alloys and Compounds*, 509(28), 7600–7606, 2011.
- [57] Schäfer, W., & Nitsche, R. *Mat. Res. Bull.* 1974, 9, 645-654.
- [58] M. Altosaar, J. Raudoja, K. Timmo, M. Danilson, M. Grossberg, J. Krustok and E. Mellikov. Cu<sub>2</sub>Zn<sub>1-x</sub>Cd<sub>x</sub>Sn(Se<sub>1-y</sub>S<sub>y</sub>)<sub>4</sub> solid solutions as absorber materials for solar cells. *Physica Status Solidi (a)*, 205, 167–170, 2008.
- [59] P. A. Fernandes, P. M. P. Salomé and A. F. da Cunha. Growth and Raman scattering characterization of Cu<sub>2</sub>ZnSnS<sub>4</sub> thin films. *Thin Solid Films*, 517(7), 2519–2523, 2009.
- [60] W.G. Nilsen. *Phys. Rev.*, 182, 838, 1969.
- [61] P. A. Fernandes, P. M. P. Salomé and A. F. da Cunha. Cu<sub>x</sub>SnS<sub>x+1</sub> (x = 2,3) thin films grown by sulfurization of metallic precursors deposited by dc magnetron sputtering. *Physica Status Solidi (c)*, 7(3-4), 901–904, 2010.
- [62] P. A. Fernandes, P. M. P. Salomé and A. F. da Cunha. A study of ternary Cu<sub>2</sub>SnS<sub>3</sub> and Cu<sub>3</sub>SnS<sub>4</sub> thin films prepared by sulfurizing stacked metal precursors. *Journal of Physics D: Applied Physics*, 43(21), 215403, 2010.
- [63] L. S. Price, I.P. Parkin, A. M. E. Hardy and R. J. H. Clark. Atmospheric Pressure Chemical Vapor Deposition of Tin Sulfides (SnS, Sn<sub>2</sub>S<sub>3</sub> and SnS<sub>2</sub>) on Glass. *Chem. Mater.*, 11(7), 1792-1799, 1999.
- [64] S. Chen, X. G. Gong, A. Walsh and S.H. Wei. Defect physics of the kesterite thin-film solar cell absorber Cu<sub>2</sub>ZnSnS<sub>4</sub>. *Applied Physics Letters*, 96(2), 021902, 2010.
- [65] S. Chen, J.H. Yang, X. G. Gong, A. Walsh and S.H. Wei. Intrinsic point defects and complexes in the quaternary kesterite semiconductor Cu<sub>2</sub>ZnSnS<sub>4</sub>. *Physical Review B*, 81(24), 245204, 2010.
- [66] A. Nagoya, R. Asahi, R. Wahl and G. Kresse. Defect formation and phase stability of Cu<sub>2</sub>ZnSnS<sub>4</sub> photovoltaic material. *Physical Review B*, 81(11), 113202, 2010.
- [67] Katagiri, H., Saitoh, K., Washio, T., Shinohara, H., Kurumadani, T., & Miyajima, S. *Sol. Energy. Mater. Sol. Cells* 2001., 65, 141-148.
- [68] Scragg, J. J., Dale, P. J., Peter, L. M., Zoppi, G., & Forbes, I. *Phys. Stat. Sol. B.* 2008, 245, 1772-1778.
- [69] Fernandes, P. A., Salomé, P. M. P., da Cunha, A. F., & Schubert, B. *Thin Solid Films* 2011., 519, 7382-7385.
- [70] Liu, F., Zhang, K., Lai, Y., Li, J., Zhang, Z., & Liu, Y. *Electrochem-StateSolid.Lett.* 2011,H379-H381.

- [71] Tanaka, K.; Fukui, Y.; Moritake, N.; Uchiki, H. Chemical composition dependence of morphological and optical properties of Cu<sub>2</sub>ZnSnS<sub>4</sub> thin films deposited by sol-gel sulfurization and Cu<sub>2</sub>ZnSnS<sub>4</sub> thin film solar cell efficiency. *Sol. Energy Mater. Sol. Cells* 2011, 95, 838–842.
- [72] J. Zhang and L. Shao. Cu<sub>2</sub>ZnSnS<sub>4</sub> thin films prepared by sulfurizing different multilayer metal precursors. *Science in China Series E: Technological Sciences*, 52(1), 269–272, 2009.
- [72] I. L. Repins, H. Moutinho, S. G. Choi, A. Kanevce, D. Kuciauskas, P. Dippo, C. L. Beall, J. Carapella, C. DeHart, B. Huang, S. H. Wei, *J. Appl. Phys.* 114, 084507 (2013)
- [74] N. Nakayama and K. Ito. Sprayed films of stannite Cu<sub>2</sub>ZnSnS<sub>4</sub>. *Applied Surface Science*, 92, 171–175, 1996.
- [75] Claudia Malerba, 'Cu<sub>2</sub>ZnSnS<sub>4</sub> thin fillms and solar cells: materiall and device characterization', University of Trento, Department of Industrial Engineering June 2014
- [76] F. Z. Boutebakh·A. Beloucif· M. S. Aida· A. Chettah· N. Attaf, 'Zinc molarity effect on Cu<sub>2</sub>ZnSnS<sub>4</sub> thin film properties prepared by spray pyrolysis', *Journal of Materials Science: Materials in Electronics*, 6/12/2017
- [77] J. Zhang and L. Shao. Cu<sub>2</sub>ZnSnS<sub>4</sub> thin films prepared by sulfurizing different multilayer metal precursors. *Science in China Series E: Technological Sciences*, 52(1), 269–272, 2009.
- [78] H. Tanaka, T. Shimakawa, T. Miyata, H. Sato and T. Minami. Effect of AZO film deposition conditions on the photovoltaic properties of AZO-Cu<sub>2</sub>O heterojunctions. *Applied Surface Science*, 244(1-4), 568–572, 2005.
- [79] Z. Zhou, Y. Wang, D. Xu and Y. Zhang. Fabrication of Cu<sub>2</sub>ZnSnS<sub>4</sub> screen printed layers for solar cells. *Solar Energy Materials and Solar Cells*, 94, 2042–2045, 2010.
- [80] J. Paier, R. Asahi, A. Nagoya and G. Kresse. Cu<sub>2</sub>ZnSnS<sub>4</sub> as a potential photovoltaic material: A hybrid Hartree-Fock density functional theory study. *Physical Review B*, 79(11), 115126, 2009.
- [81] C. Persson. Electronic and optical properties of Cu<sub>2</sub>ZnSnS<sub>4</sub> and Cu<sub>2</sub>ZnSnSe<sub>4</sub>. *Journal of Applied Physics*, 107(5), 053710, 2010.
- [82] K. Hönes, E. Zscherpel, J. Scragg and S. Siebentritt. Shallow defects in Cu<sub>2</sub>ZnSnS<sub>4</sub>. *Physica B: Condensed Matter*, 404(23-24), 4949–4952, 2009.
- [83] H. Matsushita and A. Katsui. Materials design for Cu-based quaternary compounds derived from chalcopyrite-rule. *Journal of Physics and Chemistry of Solids*, 66, 1933–1936, 2005.
- [84] P.A. Fernandes, P.M.P. Salomé, A.F. da Cunha and Björn-Arvid Schubert. Cu<sub>2</sub>ZnSnS<sub>4</sub> solar cells prepared with sulphurized dc-sputtered stacked metallic precursors. *Thin Solid Films*, 519(21), 7382–7385, 2011.
- [85] T. Kato, H. Hiroi, N. Sakai, S. Muraoka and H. Sugimoto. Characterization of front and back interfaces on Cu<sub>2</sub>ZnSnS<sub>4</sub> thin-film solar cells. In *Proc. of the 27th EU-PVSEC*, 2012.
- [86] McCandless BE, Hegedus SS. *Proc. of the 22<sup>th</sup> IEEE Photovoltaic Specialists Conference*, (1991) 967–972
- [87] A. Ennaoui, S. Siebentritt, M.Ch. Lux-Steiner, W. Riedl, F. Karg, *Sol. Energy Mater. Sol. Cells* 67 (2001) 31.
- [88] W. Eisele, A. Ennaoui, P. Schubert-Bischoff, M. Giersig, C. Pettenkofer, J. Krauser, M. Lux-Steiner, S. Zweigart, F. Karg, *Sol. Energy Mater. Sol. Cells* 75(2003) 17.

- [89] M. Gloeckler and J. R. Sites, *Thin Solid Films* 480–481, 241 (2005).
- [90] R. Haight, A. Barkhouse, O. Gunawan, B. Shin, M. Copel, M. Hopstaken, and D. B. Mitzi, *Appl. Phys. Lett.* 98(25), 253502 (2011).
- [91] J. Li, Q. Du, W. Liu, G. Jiang, X. Feng, W. Zhang, J. Zhu, and C. Zhu, *Electron. Mater. Lett.* 8(4), 365 (2012).
- [92] M. Bar, B.-A. Schubert, B. Marsen, R. G. Wilks, S. Pookpanratana, M. Blum, S. Krause, T. Unold, W. Yang, L. Weinhardt, C. Heske, and H.-W. Schock, *Appl. Phys. Lett.* 99(22), 222105 (2011).
- [93] A. Santoni, F. Biccari, C. Malerba, M. Valentini, R. Chierchia, and A. Mittiga, *J. Phys. D: Appl. Phys.* 46(17), 175101 (2013).
- [94] Chang Yan, Fangyang Liu, Ning Song, Boon K. Ng, John A. Stride, Anton Tadich, and Xiaojing Hao, 'Band alignments of different buffer layers (CdS, Zn(O,S), and In<sub>2</sub>S<sub>3</sub>) on Cu<sub>2</sub>ZnSnS<sub>4</sub>', *APPLIED PHYSICS LETTERS* 104, 173901 (2014)
- [95] T. Minemoto, T. Matsui, H. Takakura, Y. Hamakawa, T. Negami, Y. Hashimoto, T. Uenoyama, and M. Kitagawa, *Sol. Energy Mater. Sol. Cells* 67(1–4), 83 (2001).
- [96] Metzger, W. K., Repins, I. L. & Contreras, M. A. Long lifetimes in high-efficiency Cu(In,Ga)Se<sub>2</sub> solar cells. *Appl. Phys. Lett.* 93, 022110 (2008).
- [97] Deleted or change
- [98] K. Ito, and T. Nakazawa, *Jpn. J. Appl. Phys.* **27**, 2094 (1988).
- [99] Ito, K., Nakazawa, T.: *Proceedings of the 4th international conference on photovoltaics science and engineering, Sydney, Australia*, p. 341 (1989)
- [100] Katagiri, H., Sasaguchi, N., Hando, S., Hoshino, S., Ohashi, J., Yokota, T.: Preparation and evaluation of Cu<sub>2</sub>ZnSnS<sub>4</sub> thin films by sulfurization of E-B evaporated precursors. *Sol. Energy Mater. Sol. Cells* 49, 407–414 (1997)
- [101] Katagiri, H., Saitoh, K., Washio, T., Shinohara, H., Kurumadani, T., Miyajima, S.: Development of thin film solar cell based on Cu<sub>2</sub>ZnSnS<sub>4</sub> thin films. *Sol. Energy Mater. Sol. Cells* 65, 141–148 (2001)
- [102] Katagiri, H., Jimbo, K., Moriya, K., Tsuchida, K.: Solar cell without environmental pollution by using CZTS thin film. In: *Proceedings of the 3rd World conference on photovoltaic energy conversion, Osaka*, pp. 2874–2879 (2003)
- [103] Katagiri, H., Jimbo, K., Yamada, S., Kamimura, T., Maw, W.S., Fukano, T., Ito, T., Motohiro, T.: Enhanced conversion efficiencies of Cu<sub>2</sub>ZnSnS<sub>4</sub>-based thin film solar cells by using preferential etching technique. *Appl. Phys. Exp.* 1, 041201 (2008)
- [104] Todorov, T.K., Reuter, K.B., Mitzi, D.B.: High-efficiency solar cell with earth-abundant liquid-processed absorber. *Adv. Mater.* 22, E156–E159 (2010)
- [105] Shin, B., Gunawan, O., Nestor, Y.Z., Bojarczuk, A., Chey, S.J., Guha, S.: Thin film solar cell with 8.4 % power conversion efficiency using an earth-abundant Cu<sub>2</sub>ZnSnS<sub>4</sub> absorber. *Prog. Photovoltaics Res. Appl.* 21, 72–76 (2013)
- [106] Todorov, T.K., Tang, J., Bag, S., Gunawan, O., Gokmen, T., Zhu, Y., Mitzi, D.B.: Beyond 1 % efficiency: characteristics of state-of-the-Art Cu<sub>2</sub>ZnSn(S,Se)<sub>4</sub> solar cells. *Adv. Energy Mater.* 3, 34–38 (2013)
- [107] W. Wang, M. T. Winkler, O. Gunawan, T. Gokmen, T. K. Todorov, Y. Zhu and D. B. Mitzi. Device characteristics of CZTSe thin-film solar cells with 12.6 efficiency. *Advanced Energy Materials*, 2013.

---

## References Chapter II

---

- [108] Friedlmeier, T.M., Wieser, N., Walter, T., Dittrich, H., Schock, H.-W.: Heterojunctions based on Cu<sub>2</sub>ZnSnS<sub>4</sub> and Cu<sub>2</sub>ZnSnSe<sub>4</sub> thin films. In: Proceedings of the 14<sup>th</sup> European PVSEC and Exhibition, P4B.10, 1242 (1997)
- [108x] <http://www.semicore.com/71-thin-film-deposition-thermal-evaporation>
- [109] Chalapathy, R.B.V., Jung, G.S., Ahn, B.T.: Fabrication of Cu<sub>2</sub>ZnSnS<sub>4</sub> films by sulfurization of Cu/ZnSn/Cu precursor layers in sulfur atmosphere for solar cells. *Sol. Energy Mater. Sol. Cells* 95, 3216–3221 (2011)
- [110] Zoppi, G., Forbes, I., Miles, R.W., Dale, P.J., Scragg, J.J., Peter, L.M.: Cu<sub>2</sub>ZnSnSe<sub>4</sub> thin film solar cells produced by selenisation of magnetron sputtered precursors. *Prog. Photovoltaics Res. Appl.* 17, 315–319 (2009)
- [111] Momose, N., Htay, M.T., Yudasaka, T., Igarashi, S., Seki, T., Iwano, S., Hashimoto, Y., Ito, K.: Cu<sub>2</sub>ZnSnS<sub>4</sub> thin film solar cells utilizing sulfurization of metallic precursor prepared by simultaneous sputtering of metal targets. *Jpn. J. Appl. Phys.* 50, 01BG09 (2011)
- [112] Fernandes, P.A., Salomé, P.M.P., da Cunha, A.F., Schubert, B.: Cu<sub>2</sub>ZnSnS<sub>4</sub> solar cells prepared with sulphurized dc-sputtered stacked metallic precursors. *Thin Solid Films* 519, 7382–7385 (2011)
- [113] Seol, J.S., Lee, S.Y., Lee, J.C., Nam, H.D., Kim, K.H.: Electrical and optical properties of Cu<sub>2</sub>ZnSnS<sub>4</sub> thin films prepared by rf magnetron sputtering process. *Sol. Energy Mater. Sol. Cells* 75, 155–162 (2003)
- [114] Tanaka, T., Nagatomo, T., Kawasaki, D., Nishio, M., Guo, Q.X., Wakahara, A., Yoshida, A., Ogawa, H.: Preparation of Cu<sub>2</sub>ZnSnS<sub>4</sub> thin films by hybrid sputtering. *J. Phys. Chem. Solids* 66, 1978–1981 (2005)
- [115] Chrisey, D.B., Hubler, G.K.: Pulsed laser deposition of thin films, vol. 14. Wiley, New York (1994)
- [116] Sekiguchi, K., Tanaka, K., Moriya, K., Uchiki, H.: Epitaxial growth of Cu<sub>2</sub>ZnSnS<sub>4</sub> thin films by pulsed laser deposition. *Phys. Status Solidi C* 3, 2618–2621 (2006)
- [117] Moriya, K., Tanaka, K., Uchiki, H.: Fabrication of Cu<sub>2</sub>ZnSnS<sub>4</sub> thin-film solar cell prepared by pulsed laser deposition. *Jpn. J. Appl. Phys.* 46, 5780–5781 (2007)
- [118] Scragg, J. J., Dale, P. J. & Peter, L. M. (2009) Synthesis and characterization of Cu<sub>2</sub>ZnSnS<sub>4</sub> absorber layers by an electrodeposition-annealing route. *Thin Solid Films*, **517**(7), 2481–2484.
- [119] Ennaoui, A., Steiner, M.L., Weber, A., Ras, D.A., Kotschau, I., Schock, H.W., Schurr, R., Holzinger, A., Jost, S., Hock, R., Vob, T., Schulze, J., Kirbs, A.: Cu<sub>2</sub>ZnSnS<sub>4</sub> thin film solar cells from electroplated precursors: novel low-cost perspective. *Thin Solid Films* 517, 2511–2514 (2009)

- [120] Ahmed, S., Reuter, K.B., Gunawan, O., Guo, L., Romankiw, L.T., Deligianni, H.: A high efficiency electrodeposited Cu<sub>2</sub>ZnSnS<sub>4</sub> solar cell. *Adv. Energy Mater.* 2, 253–259 (2012)
- [121] Tanaka, K., Oonuki, M., Moritake, N., Uchiki, H.: Cu<sub>2</sub>ZnSnS<sub>4</sub> thin film solar cells prepared by non-vacuum processing. *Sol. Energy Mater. Sol. Cells* 93, 583–587 (2009)
- [122] Maeda, K., Tanaka, K., Fukui, Y., Uchiki, H.: Influence of H<sub>2</sub>S concentration on the properties of Cu<sub>2</sub>ZnSnS<sub>4</sub> thin films and solar cells prepared by sol–gel sulfurization. *Sol. Energy Mater. Sol. Cells* 95, 2855–2860 (2011)
- [123] WooK, Kim Y and Moon J 2012 *Energy Environ. Sci.* 5 5340–5
- [124] J.B. Mooney and S.B. Radding, *Annu. Rev. Mater. Sci.*, **12**, 81 (1982).
- [125] M.S. Tomar and F.J. Garcia, *Progress in Crystal Growth and Characterization of Materials*, **4**(3), 221 (1981).
- [126] D.S. Albin and S.H. Risbud, *Advanced Ceramic Materials*, (3A), 243 (1987).
- [127] B.R. Pamplin, *Progress in Crystal Growth and Characterization of Materials*, **1**(4), 395 (1979).
- [128] P.S. Patil, *Mater. Chem. Phys.*, **59**(3), 185 (1999).
- [129] Nakayama, N. & Ito, K. (1996) Sprayed films of stannite Cu<sub>2</sub>ZnSnS<sub>4</sub>. *Applied Surface Science*, **92**, 171–175.
- [130] Bhosale SM, SuryawanshiaMP, Kim JHand Moholkar AV2015 *Ceram. Intern.* **41** 8299
- [131] Vigil-Galan O, Courel M, Espindola-Rodriguez M, Izquierdo-Roca V, Saucedo E and Fairbrother A 2013 *J. Renew. Sustain. Energy* **5**
- [132] RajeshmonVG, KarthaCS, VijayakumarKP, Sanjeeviraja C, Abe T and Kashiwaba Y 2008 *Sol. Energy* **85** 249
- 133 Espindola-Rodríguez, M. , López-García, J. , Sylla, D. , Fontané, X. , Sánchez, Y. , López-Marino, S. , Izquierdo-Roca, V. , Riedel, W. , Ohm, W. , Gledhill, S. , Vigil-Galán, O. and Saucedo, E. (2015), Cu<sub>2</sub>ZnSnS<sub>4</sub>absorber layers deposited by spray pyrolysis for advanced photovoltaic technology. *Phys. Status Solidi A*, 212: 126-134. doi:[10.1002/pssa.201431460](https://doi.org/10.1002/pssa.201431460)
- [134] Moholkar, A.V., Shinde, S.S., Babar, A.R., Sim, K., Lee, H., Rajpure, K.Y., Patil, P.S., Bhosale, C.H., Kim, J.H.: Synthesis and characterization of Cu<sub>2</sub>ZnSnS<sub>4</sub> thin films grown by PLD: solar cells. *J. Alloy. Compd.* 509, 7439–7446 (2011)
- [135] Prabhakar, T., Nagaraju, J.: Device parameters of Cu<sub>2</sub>ZnSnS<sub>4</sub> thin film solar cell. *Photovoltaic Specialists Conference (PVSC)*, 37th IEEE, Seattle, pp. 001346–001351 (2011)
- [136] Steinhagen, C., Panthani, M.G., Akhavan, V., Goodfellow, B., Koo, B., Korgel, B.A.: Synthesis of Cu<sub>2</sub>ZnSnS<sub>4</sub> nanocrystals for use in low-cost photovoltaics. *J. Am. Chem. Soc.* 131, 12554–12555 (2009)
- [137] Wangperawong, A., King, J.S., Herron, S.M., Tran, B.P., Pangan-Okimoto, K., Bent, S.F.:Aqueous bath process for deposition of Cu<sub>2</sub>ZnSnS<sub>4</sub> photovoltaic

- absorbers. *Thin Solid Films* 519, 2488–2492 (2011) (0.16)
- [138] M. Pinczlits, G. Spingholz and G. Bauer, *Appl. Phys. Lett.*, 73 250 (1998)
- [139] P. Nollet, M. Burgelman, S. Degrave, J. Beier, *Proc. 29th IEEE Photovolt. Specialists Conf.*, IEEE, Priscataway, 2002, p. 704.
- [140] U. Rau, M. Schmidt, F. Engelhart, O. Seifert, J. Parisi, W. Riedl, J. Rimmasch and F. Karg, *Solid State Commun.*, **107**, (1998), 59.
- [141] R. Herberholz, M. Igalson, H.W. Schock, *J. Appl. Phys.* 83 (1998) 318.
- [142] H.M. Baran, A. Tatar˘oglu, *Chin. Phys. B* 22 (2013) 047303.
- [143] Vincent, D. Bois, P. Pinard, *J. Appl. Phys.* 46 (1975) 5173.

---

## References Chapter III

---

- [144] Y.M. Sun, B. Yao, X.C. Meng, D. Wang, D. Long, Z. Hua.” ACTA PHYSICA POLONICA A ,Vol. 126 (2014)
- [145] L. A. Goodman,” Liquid-crystal displays—Electro-optic effects and addressing techniques”, RCA Rev, 35, 613, (1974).
- [146] T. M. Razykov, K. M. Kouchkarov, Solar energy 80 (2006)182-184.
- [147] <http://www.techno-science.net/?onglet=glossaire&definition=6765>
- [148] Persson, C.: Electronic and optical properties of Cu<sub>2</sub> Zn Sn S<sub>4</sub> and Cu<sub>2</sub> Zn Sn Se<sub>4</sub>. J. Appl. Phys. 107, 710 (2010).
- [149] W. Daranf, M.S. Aida, N. Attaf, J. Bougdira, H. Rinnert,”Cu<sub>2</sub> ZnSnS<sub>4</sub> thin films deposition by ultrasonic spray pyrolysis” ,J. of Alloys and Compounds 542 (2012) 2227.
- [150] Kamoun N., Bouzouita H. and Rezig B., Fabrication and characterization of Cu<sub>2</sub>ZnSnS<sub>4</sub> thin films deposited by spray pyrolysis technique, Thin Solid Films, 515(15), 5949–5952 (2007)
- [151] Yoo, H., Kim, J.: Comparative study of Cu<sub>2</sub> Zn Sn S<sub>4</sub> film growth. Sol Energy Mater. Sol. Cells 95(1), 239–244 (2011)
- [152] J. Wang, S. Li, J. Cai, B. Shen, Y. Ren, G. Qin, Cu<sub>2</sub>ZnSnS<sub>4</sub>thinfilms: facile andcost-effective preparation by RF-magnetron sputtering and texture control, J.Alloys Compd. 552 (2014) 418–422.
- [153] Kahraman S., Çetinkaya S., Podlogar M., Bernik S.,Çetinkara H.A. and Güder H.S., Effects of the sulfurization temperature on sol- gel processed Cu<sub>2</sub>ZnSnS<sub>4</sub> thin films,Ceram. Int., 39(8), 9285-9292 (2013).
- [154] Touati R., Ben Rabeh M. and Kanzari M., Structural and Optical Properties of the New Absorber Cu<sub>2</sub>ZnSnS<sub>4</sub> Thin Films Grown by Vacuum Evaporation Method, Energy Procedia, 44, 44 – 51 (2014).
- [155] Sheng C. Y., Jun Y. W., Rui L., Hua G. J., Xiao L. J., and Shi E. Y., (2014), Preparing Cu<sub>2</sub>ZnSnS<sub>4</sub> films using the co-electrodeposition method with ionic liquids, China Physics B, 21(5) 058801 1-4
- [156] bShinde N.M., Deokate R. J., and Lokhande C. D., (2013), Properties of spray deposited Cu<sub>2</sub>ZnSnS<sub>4</sub> (CZTS) thin films, Journal of Analytical and Applied Pyrolysis, 100 12-16
- [157] Lydia R. and Reddy S. P., (2013), Structural and optical properties of Cu<sub>2</sub>ZnSnS<sub>4</sub> nanoparticles for solar cell applications, Journal of Nano- and Electronic Physics, 5(3) 03017(4pp).
- [158] Pranab Sarker, Mowafak M.Al-Jassim, and Muhammad N.Huda Journal of Applied Physics 117, 035702 (2015)10.
- [159] E. M. Mkawi, K. Ibrahim, M. K. M. Ali, A. S. Mohamed, Int. J. Electrochem.

- Sci., 8 (2013) 359.
- [160] L. Sun, J. He, H. Kong, F. Yue, P. Yang, and J. Chu, *Sol. Energy Mater. Sol. Cells* 95, 2907–2913 (2011) .
- [161] *S. M. Camara, L. Wang, X. Zhang, Nanotechnology, 24 (2013) 495401.*
- [162] Chen, S., Gong, X. G., Walsh, A., and Wei, S.-H. Crystal and electronic band structure of  $\text{Cu}_2\text{ZnSnX}_4$  (X = S and Se) photovoltaic absorbers: First-principles insights. *Appl. Phys. Lett.* 94(4), 041903 (2009).
- [163] *Scragg, Jonathan J.S.Larsen, Jes K.Kumar, MukeshPersson, ClasSandler, JanSiebentritt, Susanne, Physica Status Solidi Basic Research,253(2)(2016)*
- [164] O.Pal Singh , N.Muhunthan , K.Singh Gour , R.Parmar , M.Dalai , P.Kulriya S.Pillai , V.N.Singh,” Effect of sputter deposited Zn precursor film thickness and annealing time on the properties of  $\text{Cu}_2\text{ZnSnS}_4$  thin films deposited by sequential reactive sputtering of metal targets”, *Mater. Sci. in Semicond. Process.* 52(2016)38.
- [165] P.J. Dale, K. Hoenes, J.J. Scragg and S.Siebentritt, 34<sup>th</sup> IEEE Photovoltaic Specialist Conf. IEEE, Philadelphia (2009) 1956.
- [166] X. Fontané, L. Calvo-Barrio, V. Izquierdo-Roca, E. Saucedo, A. Pérez-Rodríguez, J. R. Morante, D. M. Berg, P. J. Dale, and S. Siebentritt,” In-depth resolved Raman scattering analysis for the identification of secondary phases: characterization of  $\text{Cu}_2\text{ZnSnS}_4$  layers for solar cell applications”, *Appl. Phys. Lett.*(2011)181905
- [167] T. Todorov, M. Kita, J. Carda, and P. Escribano,”  $\text{Cu}_2\text{ZnSnS}_4$  films deposited by a soft-chemistry method”, *Thin Solid Films* 517 (2009) 2541.
- [168] D.M. Berg, M. Arasimowicz , R.Djemour , L. Gütay , S. Siebentritt, S. Schorr , X. Fontané, V.Izquierdo-Roca, A. Pérez-Rodríguez and P. J. Dal, *Thin Solid Films* 569 (2014) 113.
- 169 C. Malerba, C. Ricardo, M.Valentini,F. Biccari, M.Muller, L. Rebuffi, E. Esposito, P.Mangiapane, P.Scardi and A.Mittiga,” Stoichiometry effect on  $\text{Cu}_2\text{ZnSnS}_4$  thin films morphological and optical properties”, *J. of Renewable and Sust. Energy* 6 (2014)011404.
- 170 S. Chen, A. Walsh, X. Gong, and S. Wei,” Classification of Lattice Defects in the Kesterite  $\text{Cu}_2\text{ZnSnS}_4$  and  $\text{Cu}_2\text{ZnSnSe}_4$  Earth-Abundant Solar Cell Absorbers”, *Adv. Mater.* 25(2013)1522.
- 171 S. Chen, L.-W. Wang, A. Walsh, X. Gong, and S.-H. Wei,” Abundance of  $\text{CuZn} + \text{SnZn}$  and  $2\text{CuZn} + \text{SnZn}$  defect clusters in kesterite solar cells”, *Appl. Phys. Lett.* 101, (2012)223901.
- 172 S. Schorr, V. Riede, D. Spemann and T. Doering,” Electronic band gap of  $\text{Zn}_{2x}(\text{CuIn})_{1-x}\text{X}_2$  solid solution series (X=S, Se, Te)”, *J. of Alloys and Compounds* 414 (2006) 26.
- 173 F. Urbach,” The Long-Wavelength Edge of Photographic Sensitivity and of the Electronic Absorption of Solids”, *Phys. Rev.* 92 (1953) 1324.
- 174 S. Kumar Swami, A. Kumar and V.Dutta,” Deposition of Kesterite  $\text{Cu}_2\text{ZnSnS}_4$  (CZTS) Thin Films by Spin Coating Technique for Solar Cell Application”,

- Energy Procedia 33 ( 2013 ) 198 .
- [175] Z.Shadrokh , H.Eshghi , A.Yazdan, Mater.Sci. in Semicond. Process. 40 (2015) 752.
- [176] D. Mitzi, O. Gunawan, T. Todorov, K .Wang and S.Guha, ” The path towards a high-performance solution-processed kesterite solar cell”,Sol. Ener. Mater, & Solar Cells; 95(201)1421
- [177] J. M. Raulot, C. Domain and J. F. Guillemoles, ”Ab initio investigation of potential indium and gallium free chalcopyrite compounds for photovoltaic application”,Jo.of Phys.and Chem. of Solids, 66 (2005) 2019.

---

## References Chapter VI

---

- [178] Gurav, K.V., Yun, J.H., Pawar, S.M., Shin, S.W., Suryawanshi, M.P., Kim, Y.K., Kim, J.H., *Mater. Lett.* 108, (2013). 316.
- [179] M.P. Suryawanshi a,b, S.W. Shin , U.V. Ghorpade , K.V. Gurav , G.L. Agawane , Chang Woo Hong , Jae Ho Yun , P.S. Patil , Jin Hyeok Kim , A.V. Moholkar, *Solar Energy* 110 (2014) 221.
- [180] S.M. Bhosale , M.P.Suryawanshi , M.A.Gaikwad , P.N.Bhosale , J.H.Kim , A.V.Moholkar, *Mater. Lett.* 129(2014)153.
- [181] Fei Long , Wei-Min Wang, Zhan-kui Cui , Li-Zhen Fan , Zheng-guang Zou , Tie-kun Ji, *Chemical Physics Letters* 462 (2008) 84
- [182] Johnston D A, Carletto M H, Reddy K T R, Forbes I and Miles R W, 2002 *Thin Solid Films* 403–404 102–6.
- [182] L.V. Makhova, I. Konovalov, R. Szargan, N. Aschkenov, M. Schubert, T. Chasse, *Phys. Stat. Sol.* 2 (3) (2005) 1206.
- [184] O. Gunawan, T. Todorov, and D. Mitzi, *Appl. Phys.Lett.*, vol. 97, pp. 233506, Dec, 2010.
- [185] A. Redinger, M. Mousel, M. H. Wolter, N. Valle, and S. Siebentritt, *Thin Solid Films*, vol. 535, pp. 291–295, May, 2013
- [186] M. Bär, B. A. Schubert, B. Marsen, R. G. Wilks, S. Pookpanratana, M. Blum, S. Krause, T. Unold, W. Yang, L. Weinhardt, C. Heske, and H. W. Schock, "", *Appl. Phys. Lett.*, vol. 99 (2011) 222105-3.
- [187] Ericson, T., Scragg, J., Hultqvist, A., Wätjen, J., Szaniawski, P.. (2013). *IEEE J. of Photovoltaics* <http://dx.doi.org/10.1109/JPHOTOV.2013.2283058>.
- [188] C. Platzer-Björkman, T. Törndahl, D. Abou-Ras, J. Malmström, J. Kessler, and L. Stolt, , *J. Appl. Phys.*, vol. 100, pp.044506, Aug, 2006.
- [189] D. A. R. Barkhouse, R. Haight, N. Sakai, H. Hiroi, H. Sugimoto, and D. B. Mitzi, *Appl. Phys. Lett.*, vol. 100, pp. 193904, May, 2012.
- [190] P. Sinsermsuksakul, K. Hartman, S. B. Kim, J. Heo, L. Sun, H.H. Park, R. Chakraborty, T. Buonassisi, and R. G. Gordon, *Appl. Phys. Lett.* **102**, 053901 (2013).
- [191] F. El Akkad, T. A.P. Paulose, *Appl. Surf. Sci.* 295 (2014) 8– 17
- [192] E. Mocaripoor, M.M. Bagheri-Mohagheghi *Mater. Sci. in Semicond. Process.* 30(2015)400–405.
- [193] Q.P. Tran , J.S. Fang and T. S. Chin , *Mater. Sci. in Semicond. Process.* 40(2015)664–669
- [194] J. M. Shah, Y.-L. Li, Th. Gessmann, and E. F. Schubert, *JOURNAL OF APPLIED PHYSICS VOLUME 94, NUMBER 4 15 AUGUST 2003*,
- [195] Ben-Chorin M, Moller F and Koch F 1995 *J. Appl. Phys.* 77 4482.
- [196] MA Jing-Jing, JIN Ke-Xin, LUO Bing-Cheng, FAN Fei, XING Hui, ZHOU Chao-

- Chao, CHEN Chang-Le, CHIN. PHYS. LETT. Vol. 27, No. 10 (2010) 107304.
- [197] Shah J M, Li L Y, Gessmann T and Schubert E F 2003J. Appl. Phys. 94 2627.
- [198] MA Jing-Jing, JIN Ke-Xin, LUO Bing-Cheng, FAN Fei, XING Hui,ZHOU Chao-Chao, CHEN Chang-Le, CHIN. PHYS. LETT. Vol. 27, No. 10 (2010) 107304.
- [199] Jay M. Shah, Y.-L. Li, Th. Gessmann, and E. F. Schubert JOURNAL OF APPLIED PHYSICS VOLUME 94, NUMBER 4 15 AUGUST 2003.
- [200] Raddy N K, Ahsanulhaq Q, Kim J H and Hahn Y B 2008 Appl. Phys. Lett. 92 043127.
- [201] Mridha S and Basak D 2007 J. Appl. Phys. 101 083102
- [202] R. Singh, A.K. Narula, Appl. Phys. Lett. 71 (1997) 2845 .
- [203] R.S. Ajimsha, K.A. Vanaja, M.K. Jayaraj, P. Misra, V.K. Dixit, L.M. Kukreja, Thin Solid Films 515 (2007) 7352.
- [204] 4H. C. Casey, Jr., J. Muth, S. Krishnankutty, and J. M. Zavada, Appl. Phys.Lett. **68**, 2867 (1996).
- [205] K. Mayes, A. Yasan, R. McClintock, D. Shiell, S. R. Darvish, P. Kung, and M. Razeghi, Appl. Phys. Lett. **84**, 1046 (2004).
- [206] J P Sullivan, R T Tung, and M R Pinto 1991 J. Appl.Phys. 70, 7403
- [207] Tung R T 1992 Phys. Rev. B 45, 13509.
- [208] Padovani, F. A. & Sumner, G.G. (1965). Experimental Study of Gold-Gallium Arsenide Schottky Barriers, J. Appl. Phys. 36(12), 3744-3746.
- [209] J P Sullivan, R T Tung, and M R Pinto 1991 J. Appl.Phys. 70, 7403
- [210] Tung R T 1992 Phys. Rev. B 45, 13509,
- [211] Kiziroglou M E, Zhukov A A, Li X, Gonzalez D C, de-Groot P A J and Bartlett P N 2006 Solid StateCommun. 140, 508.
- [212] Roderick E H, 1978 Metal Semiconductor Contacts London (Oxford Press)
- [213] S. Logothetidis, J. Appl. Phys. 82, 5017 (1997).
- [214] E.H. Nicillian, A. Goetzberger, Appl. Phys. Lett. 7,216 (1965).
- [215] J. Fernandez, P. Godignon, S. Berberich, J. Rebollo,G. Brezenanu, J. Millan, Solid-State Electron. 39,1359 (996)
- [216] J.P. Sullivan, R.T. Tung, M.R. Pinto, W.R. Graham, J. Appl. Phys. 70 (1991) 7403.
- [217] M. Cakar, Y. Onganer, A. Turut, Synth. Met. 126 (2002) 213.
- [218] A. Singh, Solid State Electron. 28 (1985) 223.
- [219] D. Aaron, R. Barkhouse, T. Gokmen, O. Gunawan and R. A. Haight ,Us patent N<sup>0</sup> US20130269764 A1,(2013).
- [220] A.Turut,,H.Dğoan, and N.Yldirim, ‘The interface state density characterization by temperature-dependent capacitance–conductance–frequency measurements in Au/Ni/ n -GaN structures’, Materials Research Express 2(9):096304’ September 2015
- [221] K. EJDERHA,I. ORAK,S. DUMAN,and A. TURUT,’ The Effect of Thermal Annealing and Measurement Temperature on Interface State Density Distribution and TimeConstant in Ni/n-GaP Rectifying Contacts, Journal of Electronic Materials ,March 2018.
- [222] S.M. Sze(1981), Physics of Semiconductor Devices, John Wiley and Sons, New

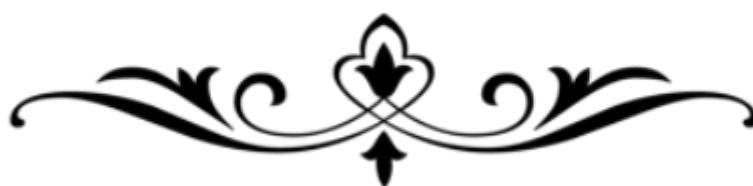
York.

- [223] Uwadiae Obahiagbon, Christopher P. Thompson, William N. Shafarman, Steven S. Hegedus (2015), "The Role of the Intrinsic Zinc Oxide Layers on the Performance of Wide-bandgap (AgCu)(InGa)Se<sub>2</sub> Thin-Film Solar Cells", 978-1-4799-7944-8/15/\$31.00 © IEEE
- [224] S. Guitouni, M. Khammar, M. Messaoudi, N. Attaf, and M. S. Aida (2016), "Electrical properties of Cu<sub>2</sub>ZnSnS<sub>4</sub>/ZnS heterojunction prepared by ultrasonic spray pyrolysis", *Journal of Semiconductors*, Vol. 37, No. 12.
- [225] S.M. Sze (1981), *Physics of Semiconductor Devices*, John Wiley and Sons, New York,.
- [226] Maykel Courel, O. Vigil-Galán, D. Jiménez-Olarte, M. Espindola-Rodriguez, and E. Saucedo, (2013) "Thermally Stimulated Current in Sprayed Cu<sub>2</sub>ZnSnS<sub>4</sub> Thin Films, Energy and Environment Focus Vol. 2, pp. 294–298.
- [227] J. Zhi, W. Shurong, L. Zhishan, Y. Min, L. Sijia, L. Yilei, Z. Qichen, H. Ruiting (2017), "Effects of temperature-time profile on Cu<sub>2</sub>ZnSnS<sub>4</sub> films and cells based on sulfur-contained precursors", *Mater. Sci. in Semicond. Process.* 57 239–243]
- [228] F.Z. Boutebakh, M. Lamri Zeggar, N. Attaf, M.S. Aida, (2017), "Electrical properties and back contact study of CZTS/ZnS heterojunction", *Optik - International Journal for Light and Electron*, 144 • 2017
- [229] M. Patel, Indrajit Mukhopadhyay and Abhijit Ray (2013), "Study of the junction and carrier life time properties of a spray-deposited CZTS thin-film solar cell", *Semicond. Sci. Technol.* 28 055001.
- [230] Maykel Courel, E. Valencia-Resendiz, J.A. Andrade-Arvizu, E. Saucedo, O. Vigil Galán, (2017), "Towards understanding poor performances in spray-deposited Cu<sub>2</sub>ZnSnS<sub>4</sub> thin film solar cells", *Solar Energy Materials and Solar Cells* Volume 159, Pages 151-15
- [231] A. Emrani, P. Vasekar, Charles R. Westgate, (2013) "Effects of sulfurization temperature on CZTS thin film solar cell performances", *Solar Energy* 98 335–340.
- [232] Y.L. Zhou, W.H. Zhou, M. Lei, Y.F. Du and S.X. Wu, *J. Phys. Chem. C* 115(2011)19632-19639.
- [233] I.P. Parkin, L.S. Price, T.G. Hibbert, K.C. Molloy, *J. Mater Chem* 11(2001)1486-1490.
- [234] A. Khalkar, K.S. Lim, S.M. Yu, D.W. Shin, T.S. Oh, J.B. Yoo, "Effects of sulfurization pressure on the conversion efficiency of co sputtered Cu<sub>2</sub>ZnSnS<sub>4</sub> thin film solar cells". *Int. J. Photoenergy*. (2015). doi:10.1155/2015/750846
- [235] J. Zhi, W. Shurong, L. Zhishan, Y. Min, L. Sijia, L. Yilei, Z. Qichen, H. Ruiting, *Mater. Sci. in Semicond. Process.* 57 (2017) 239–243
- [236] Y. Li, T. Yuan, L. Jiang, Z. Su, F. Liu, *J. of Alloys and Compnds.*; 610(2014)331–336.
- [237] Y. Cui, S. Zuo, J. Jiang, S. Z. Yuan, J. Chu, *Solar Energy Materials & Solar Cells*, 95(2011)2136-2140
- [238] D. Tang, Q. Wang, F. Liu, L. Zhao, Z. Han, K. Sun, Y. Lai, J. Li and Y. Liu, *Surf.*

- Coat. Technol. 232 (2013)53.
- [239] A. Shavel, D. Cadavid, M. Ibáñez, A. Carrete, A. Cabot, J. Am. Chem. Soc. 134 (2012) 1438.
- [240] M. Zhou, Y. Gong, J. Xu, G. Fang, Q. Xu, J. Dong, J. Alloy. Compd.;574(2013)272–277.
- [241] Y. Xia, Z. Cheng, Z. Zhang, X. Fang, G. Liang, Nanoscale Res Lett 2014;9:208-214
- [242] X. Zhai, H. Jia, Y. Zhang, Y. Lei, J. Wei, Y. Gao, J. Chu, W. He, J. Yin, Z. Zheng, Cryst Eng Comm;16(2014)6244-6249.
- [243] K. Diwatea, K. Mohiteb, M. Shindec, S. Rondiyaa, A. Pawbakea, A. Dated, H. Pathane, S. Jadhare, Energy Procedia 110 ( 2017 ) 180 – 187
- [244] J. Xu, Z. Cao, Y. Yang, and Z. Xie J. of Renewable and Sustainable Energy 6, (2014)053110
- [245] K. Maeda, K. Tanaka, Y. Fukui, and H. Uchiki; Jpn. J. of Appl. Phys. 50 (2011) 01BE10
- [246] D. Kim, Y. Kwon, D. Lee, S. Yoon, S. Leed and B. Yoo, J. Electrochem. Soc. 162(2015) D36-D41.
- [247] S. Jamil Ikhmayies, R. N. Ahmed Bitar; J. of Mater. Res. and Technol. 2 (2013)221-227
- [248] O. Gunawan, T. Gokmen, and D. B. Mitzi, J. Appl. Phys. 116 (2014) 1–9.
- [249] J. C. Gonzalez, G. M. Ribeiro, E. R. Viana, P. A. Fernandes, P. M. P. Salome, K. Gutierrez, A. Abelenda, F. M. Matinaga, J. P. Leit , and A. F. da Cunha, J. Phys. D: Appl. Phys., 46 (2013) 155107-1–155107-7.
- [250] S. Mali, P. S. Shinde, C. A. Betty , P. N. Bhosale , Y. W. Oh, P. S. Patil , J. Phys. Chem. Solids 73 (2012), 735–740.
- [251] A. Luque and S. Hegedus, “*Handbook of Photovoltaic Science and Engineering*” Wiley 3<sup>rd</sup> edition (2011).
- [252] H. Katagiri Thin Solid Films 480–481 (2005) 426–432
- [253] T. Gershon, B. Shin, N. Bojarczuk, T. Gokmen, S. Lu, and S. Guha J. of Appl. Phys. 114 (2013)154905.
- [254] F. Biccari, R. Chierchia, M. Valentini, P. Mangiapane, E. Salza, C. Malerba, C. L. Azanza Ricardo, L. Mannarino, P. Scardi and A. Mittiga, Energy Procedia 10 (2011 ) 187 – 191
- [255] W. Li, J. Chen, C. Yan, X. Hao J. of Alloys and Compd. 632 (2015) 178–184.
- [256] J. Ge, J. Jiang, P. Yang, C. Peng, Z. Huang, S. Zuo , L. Yang and J. Chu, Solar Energy Materials & Solar Cells 125(2014)20–26
- [257] K. Tanaka, M. Oonuki, N. Moritake and H. Uchiki , Solar Energy Materials & Solar Cells 93 (2009) 583–587
- [258] M. P. Suryawanshi, S. W. Shin, U. V. Ghorpade, K. V. Gurav , G. L. Agawane , C. Woo Hong , J. Ho Yun , P. S. Patil , J. H. Kim and A. V. Moholkar , Solar Energy 110 (2014) 221–230
- [259] O. Vigil-Galán , M. Courel, M. Espindola-Rodriguez, D. Jiménez-Olarte, M. Aguilar-Frutos and E. Saucedo , Solar Energy Materials & solar cells 132(2015)557–56
- [260] J. Li, D. B. Mitzi, and V. B. Shenoy, ACS Nano 5(2011) 8613–8619.

- [261] Kishore Kumar Y B, Suresh Babu G, Uday Bhaskar P and Sundara Raja V 2009 Sol. Energy Mater. Sol. Cells 93 1230
- [262] Y.B. K. Kumar, P.U. Bhaskar, G.S. Babu, V.S. Raja, Phys. Status Solidi A 207(2010)149–156

# Publications





# Electrical properties and back contact study of CZTS/ZnS heterojunction



F.Z. Boutebakh<sup>a</sup>, M. Lamri Zeggar<sup>a</sup>, N. Attaf<sup>a</sup>, M.S. Aida<sup>b,\*</sup>

<sup>a</sup> Laboratoire Couches minces et interfaces faculté de Sciences, Université frères Mentouri Constantine 1, Constantine, Algeria

<sup>b</sup> Departement of physics faculty of sciences, King Abdulaziz university, Djeddah, KSA

## ARTICLE INFO

### Article history:

Received 27 March 2017

Accepted 20 June 2017

### Keywords:

Heterojunctions

Thin films

Solar cells

Spray pyrolysis

## ABSTRACT

In the present work, we have studied the effect of metal back contact nature on the electrical properties of CZTS/ZnS based heterojunction prepared by spray pyrolysis. Three different back contact metals (Al, Au and Ag) were tested as alternative of the commonly used Molybdenum. Structural and optical properties of different layers are characterized. The electrical devices characterization were achieved by (I–V) at ambient and at different temperatures and capacitance–conductance vs frequency (C–G–f) measurements. The realized structures exhibit a rectifying behavior. The ideality factor of all devices were found to be large, it is found equal to 5.9 when using Au contact and equal to 10.5 and 11.4 in heterojunction prepared with Ag and Al back contact respectively. The anomalous ideality factor is due to the Schottky contact between Al, Ag and CZTS and to the presence of density of defect at the interface CZTS/ZnS. The latter was estimated from conductance measurement as a function of frequency and found equal to  $10^{10} \text{ cm}^{-2} \text{ eV}^{-1}$ . From this study we inferred that Au contact can be an alternative of Mo as back contact of CZTS based solar cell.

© 2017 Elsevier GmbH. All rights reserved.

## 1. Introduction

Thin films solar cells technologies has emerged earlier in 1960 with  $\text{Cu}_2\text{S}/\text{CdS}$  cell, the achieved efficiency with this heterostructure was about 10% [1]. However, the instability due to Cu migration dictated the research of more stable materials. Thereafter, copper indium gallium diselenide (CIGS) and cadmium telluride (CdTe) have been used and extensively studied. The recent recorded efficiency with these materials are equal to 20.8 and 19.6% respectively [2]. However, despite this reached efficiencies, these materials suffer from severe issues namely: selenium and cadmium toxicity and indium scarcity. Consequently, research of alternative materials composed of abundant and non toxic elements is necessary. In this research activity, the quaternary chalcogenide compound copper zinc tin sulfide  $\text{Cu}_2\text{ZnSnS}_4$  (CZTS) has recently attracted much attention due to the fact that it is composed of earth-abundant and environmental friendly elements. Moreover, CZTS is a p type semiconductor with direct band gap energy between 1.2 and 1.6 eV, and an absorption coefficient greater than  $10^4 \text{ cm}^{-1}$ . This confers to CZTS the status of a promising candidate, and a serious alternative for application as absorber layer in thin film solar cells. During the current decade, several studies on the quaternary chalcogenide CZTS for solar cell application have been carried [3–10]. The theoretical predicted efficiency of CZTS based solar cell is larger than 30% [11–13].

\* Corresponding author.

E-mail address: [aida\\_salah2@yahoo.fr](mailto:aida_salah2@yahoo.fr) (M.S. Aida).

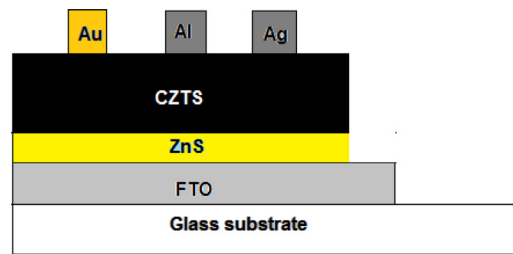


Fig. 1. Schematic drawn of the realized CZTS based heterojunctions.

CZTS solar cell is formed of a stack of two layers mainly CZTS as absorber layer and a buffer layer to form an heterojunction and two electrodes. Cadmium sulfide (CdS) thin film is the most used buffer layer. While, Mo film is the commonly used back contact. However, concerns are stressed about Cd due to its toxicity and Mo back contact due to the formation of MoS<sub>2</sub> at the interface [14,15]. Few studies have been devoted to less hazardous buffer layer such as ZnS and to the effect of metal back contact nature. The only compiled papers dealing with back contact metal are Vigin-Galan et al. paper [16] where they carried a preliminary study in the specific contact resistance on sprayed CZTS thin films and Altamura et al. paper [17], they studied several alternative back contact in CZTSSe solar cells such as (Au, W, Pd, Pt, and Ni).

To date the highest efficiency achieved with CZTS based solar cell is 9.2% with a large deficit in the open circuit voltage (708 mV) [18]. This is due to the interface recombination due to the cliff like band alignment [19] in one hand and to the lattice misfit between CZTS and buffer layer on the other hand [20]. This results in the appearance of a large density at the interface causing a minority carrier recombination at the heterojunction interface [21]. Few experimental studies have been devoted to the determination of the interface density of states in CZTS heterojunction based.

In the present study we investigated the electrical properties of Cd free CZTS based heterojunction using ZnS buffer layer in replacement of CdS. The investigated structure is formed with FTO/ZnS/CZTS/Au(Ag,Al). The advantage of the present work is that all active layers are deposited by the same system using spray pyrolysis technique. Three different metals (Au, Ag and Al) are tested as back contact instead of commonly used Mo. The interface state density is also determined using the conductance measurements.

## 2. Experimental details

The studied heterojunctions are formed with the heterostructure FTO/ZnS/CZTS/Metal on glass substrate (as depicted in Fig. 1). Both FTO (fluorine doped tin oxide), ZnS and CZTS layers are deposited with the same ultrasonic spray pyrolysis deposition system. FTO used as transparent front contact layer was prepared by dissolving 0.1 M tin chloride (SnCl<sub>2</sub>·2H<sub>2</sub>O) in distilled water with NH<sub>4</sub>F with the ratio F/Sn = 12%. Whereas, ZnS film was prepared from a solution composed of dissolved 0.1 M zinc acetate (Zn(CH<sub>3</sub>COO)<sub>2</sub>·2H<sub>2</sub>O) in distilled water and 0.05 M of thiourea. The active layer CZTS was prepared from a solution composed with a mixture: copper chloride (0.03 M), zinc acetate (0.01 M), tin chloride (0.01 M) and thiourea (0.12 M). The solutions were thoroughly mixed by magnetic stirring (during 10 min), until an homogeneous transparent solutions were obtained. The deposition temperature was fixed at 350 °C. Three metals are tested as back contact namely gold (Au), aluminum(Al) and silver(Ag), the former was deposited by DC sputtering, while Al and Ag contacts are prepared by thermal evaporation. The contacts are deposited successively of the top surface of the device (as shown in Fig. 1) in order to have the same heterojunction.

The structural characterizations of different layers were achieved using high resolution X-ray diffractometer (XRD, X'pert Pro) with Cu K $\alpha$  line to confirm films formation and structure. The optical properties were studied by means of UV-vis spectrometry. The electrical characterization was achieved by Hall Effect measurements. The heterojunctions electrical properties were studied using current-voltage characteristic in the dark and at different temperatures ranged from ambient to 100 °C. While the interface properties between (CZTS/ZnS) study were investigated using the Conductance-Capacitance versus frequency technique.

## 3. Results and discussion

### 3.1. Films properties

In Fig. 2a–c we have reported the XRD patterns of different layers. The XRD pattern (Fig. 2a) of CZTS layer matches well with the Kesterite CZTS phase JCPDS No. 26-0575 card. As can be seen, four clear diffraction peaks corresponding to the (112), (200), (220), (312) and (224) planes of kesterite CZTS structure with the direction (112) as preferential orientation. No other peaks, in XRD pattern, related to any secondary phase are observed. It is generally reported that CZTS regardless the deposition technique is usually accompanied with a binary secondary phases [22–24]. However, it hard to asses from XRD analysis that CZTS is pure this is due to the fact that the lattice constants of CZTS are similar to Cu<sub>2</sub>SnS<sub>3</sub> (CTS) and ZnS, the obtained peaks could be related to either CZTS or CTS or ZnS phases [25]. Thereafter to confirm secondary phases formation

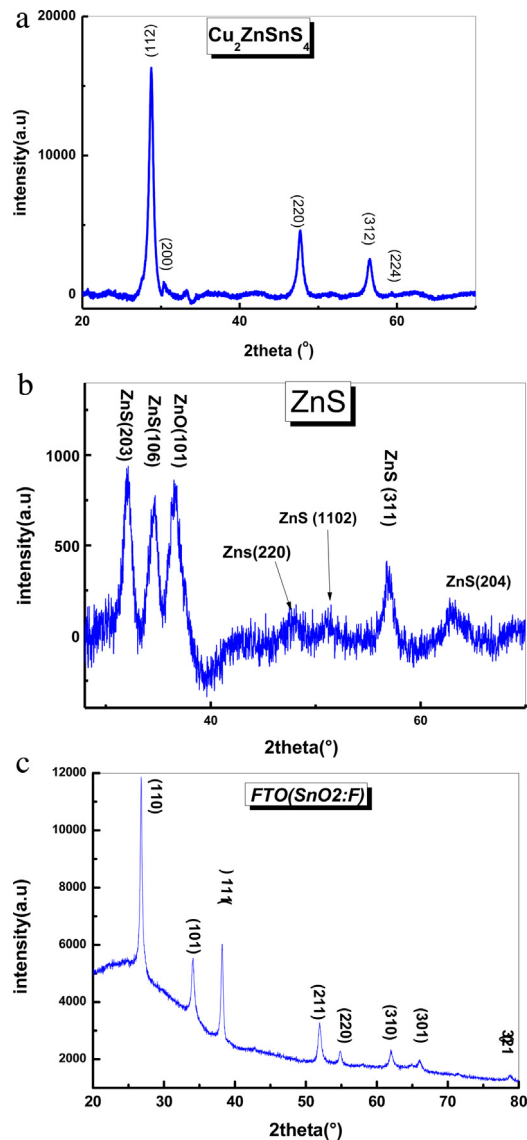


Fig. 2. XRD diffraction pattern of different layers deposited by spray pyrolysis (a) CZTS (b) ZnS and (c) FTO.

we further analyzed the film by Raman spectroscopy since it is a very sensitive tool for phase identification. As shown in Fig. 3 the existence of kesterite phase is confirmed with Raman scattering spectroscopy by the presence of intense Raman peak at  $337\text{ cm}^{-1}$  and the shoulder peaks at  $282$  and  $362\text{ cm}^{-1}$ . The same results has been reported by several authors [26–28]. While, the additional peak at  $472\text{ cm}^{-1}$  is attributed to the  $\text{Cu}_x\text{S}$  phase, the same results was reported by Thiruvankadam et al. [29]. The formation of sulfide cupric secondary phase is due to the excess Cu in the used starting solution by comparison to Zn.

In Fig. 2b, we have reported the DRX spectrum of ZnS film. The obtained diffraction pattern suggests the evidence of Zn(O,S) thin film formation rather than pure ZnS. Peaks assigned to ZnO and ZnS phases are present. As shown in Fig. 2b, the plane (101) of hexagonal ZnO Wurtzite structure is clearly visible along with the planes (220), (311) and (204) of the hexagonal ZnS cubic According to JCPDS card N 77-2100.

Actually, in contrary to PVD deposition (Sputtering, thermal evaporation), chemical route techniques such as: spray pyrolysis, chemical bath, SILAR and sol gel techniques yield to ZnS formation mixed with ZnO phase. This is due to the fact that in these techniques films are achieved in air or in aqueous solution [30–32] which favors oxygen contamination.

The performances of CZTS based solar cells is lowered by different causes such as  $\text{MoS}_2$  layer formation at the back contact [33], the presence of secondary phases in the bulk [34], and especially the alignment lack of conduction bands at the absorber/buffer interface [35]. Recently Ericson et al. [36] have investigated Zn(O,S) system as buffer layer in CSTZ solar cell, they have shown that conduction band gap offset can be tailored through the conduction band variation by controlling the

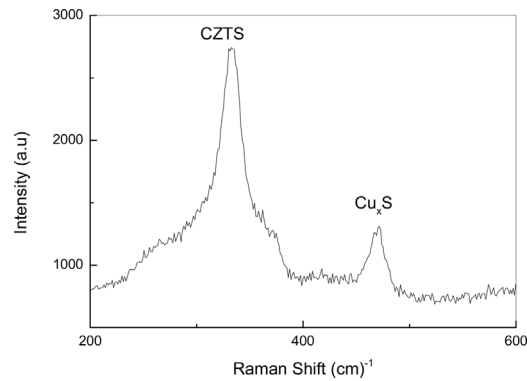


Fig. 3. Raman spectrum of CZTS layer.

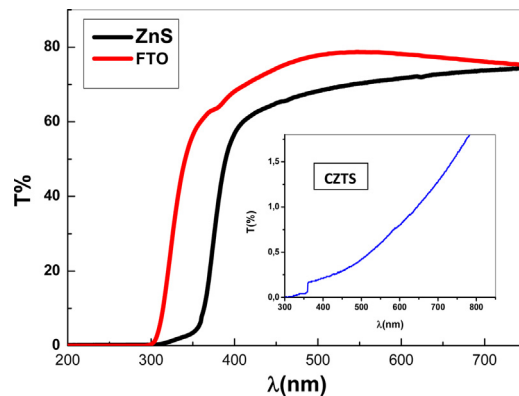


Fig. 4. Optical transmittance spectra of different layers in the Uv visible range.

Table 1

Majority carrier concentration, electrical conductivity, optical band gap and mobility measured in different layers.

	concentration( $\text{cm}^{-3}$ )	$\mu(\text{cm}^2/\text{Vs})$	$\sigma(\text{cm}\Omega)^{-1}$	$E_g(\text{eV})$
CZTS	$4 \times 10^{13}$	$8.15 \times 10^3$	$5.2 \times 10^{-2}$	1.6
FTO	$3.3 \times 10^{19}$	19.42	$10^2$	3.3
ZnS	–	–	$10^{-4}$	3.9

ratio of oxygen to sulfur [37], and that the optimum conduction band alignment for CZTS lies in between the ZnO and the ZnS values. This has been experimentally observed [38]. It has been claimed also that ZnOS film is more preferable partner than ZnS to form an ideal heterojunction due the lower conduction band offset at the interface with SnS absorber layer [39].

The XRD diffraction of FTO film is shown in Fig. 2c. Several peaks assigned to the tetragonal rutile  $\text{SnO}_2$  phase such as (110), (101) and (111) are present, indicating the formation of polycrystalline  $\text{SnO}_2$  with (110) as preferential orientation, the same results is recently reported in  $\text{SnO}_2$  thin films prepared by spray pyrolysis [40,41] and sol gel technique [42].

Fig. 4 shows the transmittance spectra of different layers CZTS, ZnS and FTO in the visible range. Both FTO and ZnS layer exhibit a large transmittance spectra due to the fact that they are wide band gap semiconductors. For application in thin film solar cells, these two layers should be transparent, since they are used as windows for visible wavelength to allow the incident photons to reach the CZTS absorber layer. While, as shown in insert Fig. 4, CZTS layer is highly absorbent.

Moreover, FTO layer should be also highly conducting. The fluorine is introduced in  $\text{SnO}_2$  in order to enhance its conductivity since the two requirements for FTO use as transparent electrode is a high transparency and a large conductivity. The measured conductivity of the deposited FTO is equal to  $10^2 (\Omega \text{ cm})^{-1}$ , the efficient introduction of fluorine as donor is also assed from the transmittance spectrum in the uv visible near infrared rang as shown in Fig. 5, the reduction in the transmittance in the near infra red range is caused by the reflection due the large free carriers concentration which is equal  $3 \times 10^{19} \text{ cm}^{-1}$  as reported in Table 1.

The optical gap energies of CZTS, ZnS and FTO were calculated from the plot of  $(\alpha h\nu)^2$  vs  $h\nu$ , where  $h\nu$  represent the energy of incident photon and  $\alpha$  is the absorption coefficient estimated from the transmittance values.

Fig. 6a–c shows the plots of  $(\alpha h\nu)^2$  vs  $h\nu$  plots of the three layers, the value of band gap energy are deduced from the linear extrapolation of the plot  $(\alpha h\nu)^2$  versus  $h\nu$  with  $h\nu$  axis, the values of optical band gaps measured of CZTS, ZnS and FTO are 1.6, 3.3 and 3.9 eV respectively.

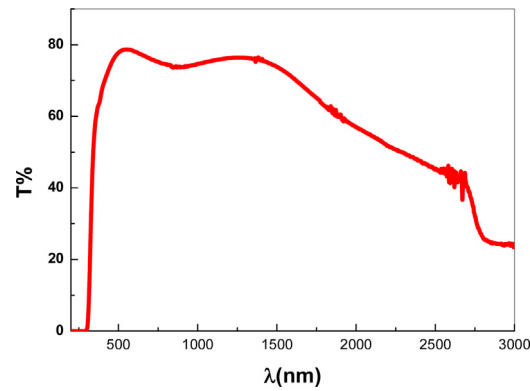


Fig. 5. Optical transmittance spectrum of FTO layer in visible and near infrared wavelength region.

Table 2

Electrical parameters of heterojunctions prepared with different metal back contact measured in dark and ambient temperature.  $n$  ideality factor,  $I_s$  saturation current  $R_s$  series resistance and  $\Phi_b$  junction barrier height.

Structure	CZTS/Al	CZTS/Ag	CZTS/Au
$n$	11.4	10.5	5.9
$I_s \times 10^{-6} (A)$	18.57	30	1.27
$R_s (k\Omega)$	2.1	1.42	2
$\Phi_b (eV)$	0.38	0.29	0.28

The calculated optical band gap together with electrical properties (free carrier concentration, mobility and dark conductivity) of different films deduced from Hall Effect measurements are reported in Table 1. The FTO thin film deposition show a good conductivity about  $10^2 (\text{cm}\Omega)^{-1}$  and a carrier concentration about  $10^{19} \text{cm}^{-3}$  whereas CZTS film has a conductivity in the order the  $10^{-2} (\text{cm}\Omega)^{-1}$ .

### 3.2. Device properties

The device current–voltage (IV) characteristics yields to important information about junction parameters such as: series resistance ( $R_s$ ), diode ideality factor ( $n$ ), saturation current ( $I_s$ ), barrier height ( $\phi_b$ ) and the major conduction mechanisms through the junction. In Fig. 7 we have reported the IV characteristics of different heterojunctions obtained with the three studied back contact. As can be seen there is no noticeable difference between the three characteristics. All heterostructure exhibit a rectifying behavior. Moreover, the reverse voltage characteristics show no saturation, indicating that defect-assisted generation or tunneling mechanism occurring [43].

Their characteristics can be described by the following equation:

$$I(V) = I_s \left( \exp \left( \frac{qV}{kTn} \right) - 1 \right) \quad (1)$$

Where  $k$  is the Boltzmann constant,  $T$  is the absolute temperature,  $q$  is the elementary electronic charge and  $n$  is the ideality factor.  $I_s$  is the saturation current, it can be expressed as:

$$I_s \sim T^2 \exp \left( \frac{-q\phi_b}{kT} \right) \quad (2)$$

The ideality factor is determined from the slope of the linear region of forward bias  $\ln(I)-V$  plot and defined as:

$$n = \frac{q}{kT} \left( \frac{dV}{d(\ln I)} \right) \quad (3)$$

In Table 2 we have reported the calculated values of the ideality factor. The ideality factor indicates how closely the structure IV characteristic follows the ideal diode equation. The diode-ideality factor is directly related to the carrier transport mechanisms. According to Sah–Noyce–Shockley theory [44], it is equal to 1 if the forward current is dominated by the recombination in the quasi-neutral regions. While, recombination in the space charge region yields to an ideality factor equal to 2, as reported in Table 2, the ideality factors calculated in the realized heterojunctions are large and depend on the nature of the used metal contact, they are respectively equal to 11.4, 10.5 and 5.9 for Al, Ag and Au contact. Several authors have reported anomalous ideality factor values in different heterojunction and pn junction [45–47] where an ideality factor ( $n > 5$ ) is found.

The origin of the large value of  $n$  may be due to the metal/CZTS contact. Indeed when the contact is not ohmic, the heterojunction can be modeled as a series of diodes and resistors in series, according to Shah-Li-Schubert [45] the ideality

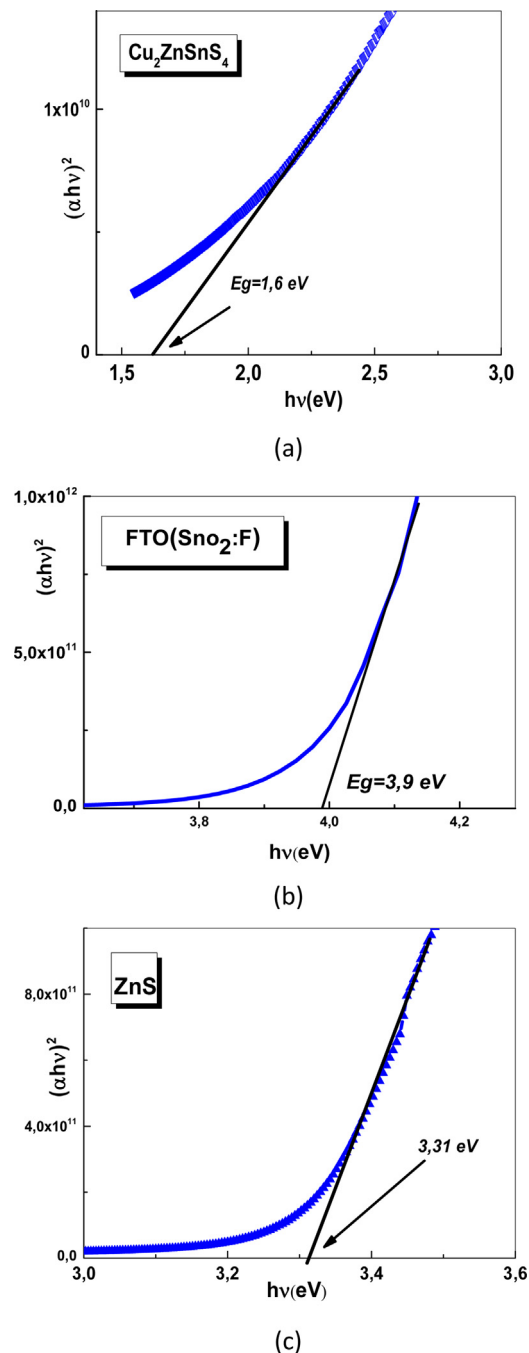


**Fig. 6.** Tauc plots used for optical band gap calculation of different layers: (a) CZTS, (b) ZnS and (c) FTO.

factor is the sum of ideality factor of each diode. Jing-Jing et al. [47] have explained the measured 18.8 ideality factor in ZnO(Al)/(p)SI heterojunction in terms of metal contact nature. The same reason has been proposed by Shah et al. [45] to explain the anomalous ideality factor of 6.9 measured in the heterostructure p-type AlGaIn/GaN.

To assess the nature of contact between CZTS and the used contact metal one should compare the work function  $\Phi_M$  of the metal to  $\Phi_S$  of the semiconductor. The optical gap of the prepared CZTS film is equal to 1.6 eV, the conductivity activation energy (which equal to the difference  $E_F - E_V$ ) is equal to 250 meV. Thereafter, knowing that CZTS affinity is given equal to 4.21 eV, the work function of CZTS is then equal to 5.57 eV.

It is well known that in the case of  $\Phi_M < \Phi_S$ , the metal semiconductor contact is ohmic if the semiconductor is n type and is Schottky contact if p type. Thereafter, since CZTS is a p type semiconductor, and according of the work function of the used

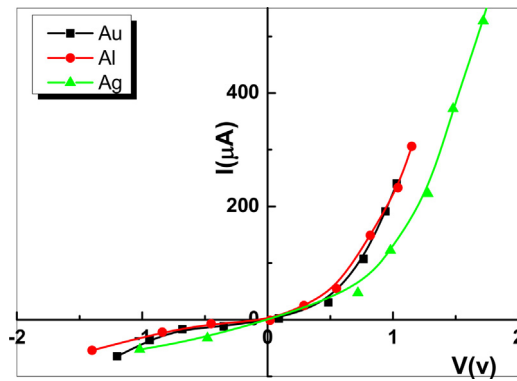


Fig. 7. IV characteristics of different CZTS/ZnS heterojunctions prepared with various back contact metals.

metals (4.26, 4.28 and 5.1 eV for Ag, Al and Au respectively), Al and Ag are candidates to yield a Schottky contact with CZTS, in contrary in the case of Au, the contact with CZTS could be ohmic. This can explain then the large ideality factor measured in the heterojunction obtained when using Al and Ag back contact. While, the large value measured in the structure obtained with Au back contact ( $n=5.9$ ) can be due to the defects located at the interface. Similar results ( $n > 20$ ) were reported by Raddy et al. [48] in the n-ZnO nanorods/p-Si devices, they suggested that the large value of  $n$  is probably due to the presence of defect states in ZnO lattice and/or the presence of traps at the interface [49]. Actually, the large value of ideality factor could be also due to numerous reasons such as recombination of electrons and holes in depletion region, the presence of interfacial layer [50,51], the trap-assisted tunneling [52,53] and carrier leakage [53] and the non-homogeneities in junction barrier heights [54,55].

In Fig. 8 we have reported the variation of IV characteristics measured at different temperatures. The reverse saturation current ( $I_s$ ) derived from the straight line intercept of  $\log(I)$  at  $V=0$ . The saturation current is thermally activated, the barrier height was estimated according to the relation (3) from the slope of the Arrhenius plot of  $\ln(I_s/T^2)$  as function of  $10^3/T$ . In Table 2 we have reported the estimated saturation current at the ambient temperature and the barrier height. The lower saturation current and barrier height are measured in the heterojunction using Au as a back contact.

The value of ideality factor of devices measured at different temperatures is found to be sensitive to the measurement temperature, it decreases with increasing temperature. This phenomenon, commonly referred as “To-effect”, was first proposed by [56]. The variation of  $n$  with  $T$  has been explained by several authors [57,58]. According to the proposed model, the temperature dependence of  $n$  suggests that the carrier generation-recombination process involves defect states. The temperature dependence of  $n$  may be modeled as [59]:

$$n = n_0 + T_0/T \quad (4)$$

where  $n_0$  and  $T_0$  are constants which are independent of temperature and voltage.

The variation of  $n$  with temperature is shown in Fig. 9, the variation of  $n$  as function of reverse temperature (insert Fig. 9) fits to a straight line as predicted from Eq. (4). This suggests the involvement of several defect levels in carrier generation-recombination processes and also the tunneling effects contribution in carrier transport [59].

The series resistances were calculated from  $I-V$  curve at high bias, their values are in the order of  $K\Omega$  as reported in Table 2, and these values can explain the obtained large ideality factor as mentioned above. The resistance series is lower when using Ag as back contact this can be due to the low work function of Ag by comparison to other metals.

### 3.2.1. Conductance-frequency characteristic

The capacitance and conductance versus frequency are an important techniques to extract the interface states properties in heterojunction or homojunction devices [60]. However, the conductance technique determines the interface states with more accuracy than capacitance technique [61], this is due to the fact that conductance comes only from the interface states [60].

Capacitance and conductance measurements are carried out in dark with a frequency range varied from 1.2 KHZ to 1 MHZ and voltage about  $V=0.3V$  at ambient temperature. In Fig. 10 we have reported the measured capacitance ( $C$ ) and conductance ( $G$ ) as function of measurement frequency in different structures Au/CZTS/ZnS/FTO, Ag/CZTS/ZnS/FTO and Al/CZTS/ZnS/FTO. The high value of capacitance measured at low frequency is due to the fact that the trapped electrons at the interface can follow the ac signal at low frequency. With further frequency increase, trapped electrons cannot follow the high frequency signal [62] and the capacitance decreases to reach its smallest value at 1MHZ. Therefore, the capacitance at high frequency ( $\omega > \omega_r$ ) represents the free-carrier response. Whereas, at low frequency (lower than the thermal emission rate of deep level) the defects can be charged and discharged, which allow them to contribute in the total junction capacitance. Thereafter, the capacitance represents the response of both free carriers and traps [63,64], it can be then described as: [65].

$$C = C_{sc} + C_{ss}(\text{at low frequency } \omega < \omega_r)$$

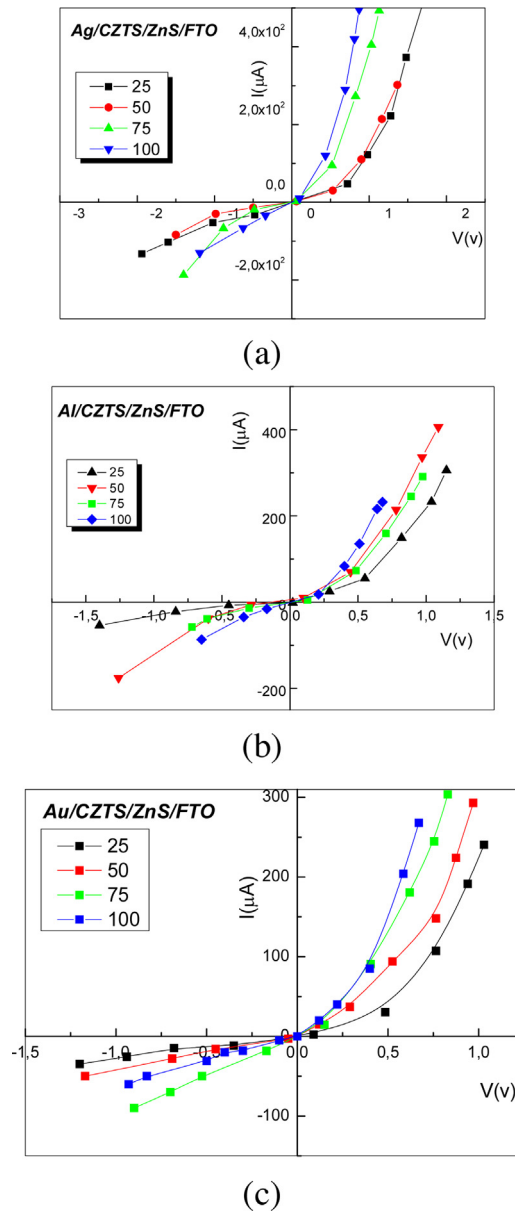


**Fig. 8.** IV characteristics measured at various temperatures of different CZTS based heterojunctions using different back contact metals: (a) Ag, (b) Al and (c) Au.

Whereas,  $C = C_{sc}$  (at high frequency  $\omega > \omega_r$ )

Where:  $C_{sc}$  is the capacitance of space charge region  $C_{ss}$ : is the interfacial capacitance

The presence of interfacial state in a hetero-junction is accompanied by a flexion in the  $C$ - $f$  curve and by a resonant peak in conductance ( $G/w$ ) versus angular frequency, as can be seen in Fig. 11. This resonant peak occurs when the trapped carriers emission rate ( $\omega_r$ ) is the same order than the angular frequency of the ac signal ( $\omega = \omega_r$ ). The frequency  $wr$  of the resonant peak is expressed by the following relation [66]:

$$\omega_r(T) = 2e_t(T) = A.T^2 \exp\left(-\frac{Ea}{KT}\right) \tag{4}$$

Where:  $\omega_r$  is the inflection frequency  $e_t$  is the emission rate of trapped charges and  $Ea$  is the activation energy.

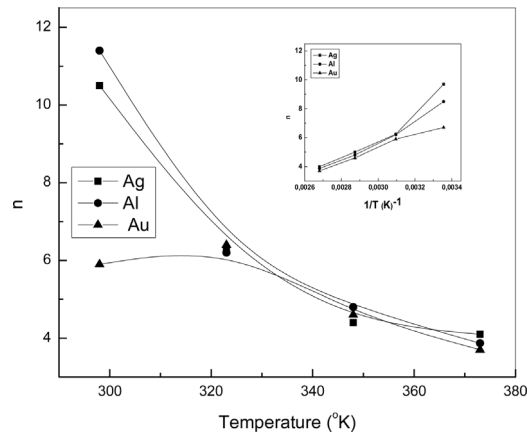


Fig. 9. variation of the ideality factor  $n$  of different heterojunction as a function of temperature, insert variation of  $n$  as a function of temperature reverse.

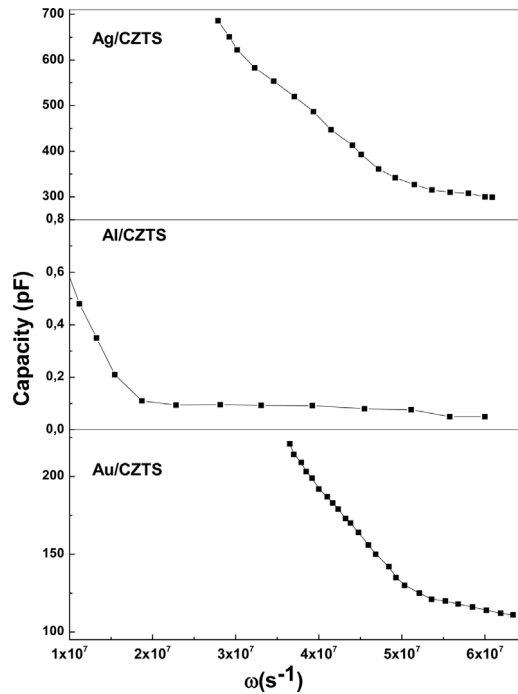


Fig. 10. Capacity dependence on frequency measurement recorded in the prepared heterojunctions with various back contact metals.

The interface state density ( $N_{ss}$ ) can be deduced from the conductance peak by using the following relation [67]:

$$N_{ss} = \frac{(G/\omega) \max}{0.402qS} \tag{5}$$

Where  $q$  is the electronic charge and  $S$  is the diode area.

The time constant  $\tau$  for electrons exchange between interface states and valence band can be calculated using the relation  $\tau = 1/\omega_r$  [68].

The interface states densities of the hetero-structures were found in the order of  $10^{10} \text{ cm}^{-2} \text{ eV}^{-1}$  and the trap time constant about  $10^{-7} \text{ s}$  for the two structures prepared with Al and Ag as back contact, while in the case of the heterojunction prepared with Au contact, we have measured a defect interface density lower by one order of decade (Table 3). The larger measured interface states in the devices prepared with Al and Ag back contacts can be associated to the contribution of the depletion layer formed between the metal and CZTS due to the Schottky contact nature as suggested by the ideality factor values. Thereafter, Au metal can be used as back contact in CZTS based solar cell, this is consistent with the Aaron et al. recent US patent [69] where they succeeded in improving the efficiency of CZTS/CdS and CZTS/ZnS solar by using Au or Pt as back contact due to their relative large work function.

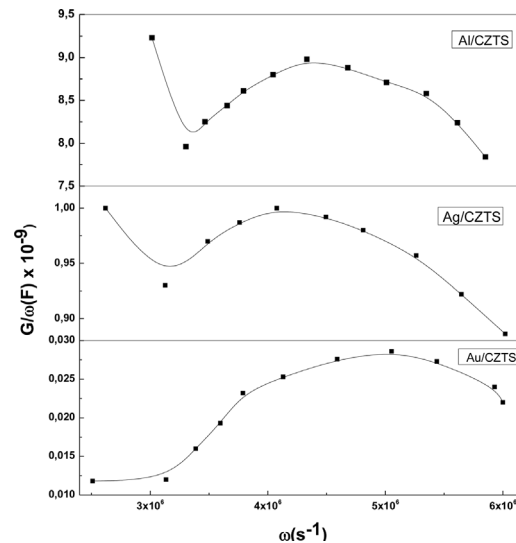


Fig. 11. Conductance dependence on frequency measurement recorded in the prepared heterojunctions with various back contact metals.

Table 3

Interface density of states and their time constant estimated from G-f measurement in heterojunctions prepared with different metal back contact.

Structure	$N_{ss} \times 10^{10}$ (ev <sup>1</sup> cm <sup>2</sup> )	$\tau \times 10^{-7}$ (s)
Al/CZTS/ZnS/FTO	1.39	2.64
Ag/CZTS/ZnS/FTO	3.48	2.65
Au/CZTS/ZnS/FTO	0.28	1.9

#### 4. Conclusions

In the present work, the electrical properties of CZTS/ZnS based heterojunctions were studied. ZnS layer is used as alternative of CdS buffer layer. Three different back metals contact (Al, Au and Ag) were tested to investigate the influence of metal contact nature on device properties in order to find an alternative metal of the commonly used Molybdenum. FTO, CZTS and ZnS layers were prepared by a simple pneumatic spray pyrolysis technique. The electrical devices characterization were achieved by (I–V) at ambient and at different temperatures and C–G–f measurements. The whole IV characteristics exhibit a rectifying behavior. The ideality factor of all devices were found to be large, it is found equal to 5.9 when using Au contact and equal to 10.5 and 11.4 in heterojunction prepared with Ag and Al back contact respectively. The anomalous ideality factors greater than unity are explained in terms of the Schottky contact nature between CZTS, Al and Ag in one hand and by the presence of interface states and the series resistance on the other hand. The high value of the ideality factor suggests that the current transport mechanism in the devices is achieved by tunneling assisted by interface states emission-recombination rather than by the thermionic emission. The capacitance and conductance versus frequency characteristic reveals the presence of defects in CZTS/ZnS interface with a density in the order the  $10^{10}$  cm<sup>-3</sup> when using Al or Ag as back contact, while it is found one order of decade lower when using Au metal contact. The defects time constant is found equal to  $10^{-7}$  s. Finally we inferred that Au metal can be use as back contact for based CZTS heterojunction solar cells as alternative to Mo.

#### References

- [1] G. Liu, T. Schulmeyer, J. Brotz, A. Klein, W. Jaegermann, *Thin Solid Films* 431 (2003) 477.
- [2] M.A. Green, K. Emery, Y. Hishikawa, W. Warta, E.D. Dunlop, *Prog. Photovoltaics Res. Appl.* 21 (2013) 827.
- [3] Z. Seboui, A. Gassoumi, N. Kamoun-Turki, *Mater. Sci. Semicond. Process.* 26 (2014) 360.
- [4] A. Tombak, Y.S. Ocak, M.F. Genişel, T. Kilicoglu, *Mater. Sci. Semicond. Process.* 28 (2014) 98.
- [5] O. Pal Singh, N. Muhunthan, K. Singh Gour, R. Parmar, M. Dalai, P. Kulriya, S. Pillai, V.N. Singh, *Mater. Sci. Semicond. Process.* 52 (2016) 38.
- [6] M. Placidi, M. Espindola-Rodríguez, S. Lopez-Marino, Y. Sanchez, S. Giraldo, L. Acebo, M. Shubhra Kala, H. Kaur, A. Rastogi, V.N. Singh, T.D. Senguttuvan, *J. Alloys Compds.* 675 (2016) 158.
- [7] A. Neuschitzer, X. Alcobé, A. Pérez-Rodríguez, E. Saucedo, *J. Alloys Compds.* 658 (2016) 324.
- [8] A. Sagna, K. Djessas, C. Sene, M. Belaqqiz, H. Chehouani, O. Briot, M. Moret, *Superlatt. Microstruct.* 85 (2015) 918.
- [9] Q.Y. Wen, Y. Li, J.J. Yan, J. Wang, C.W. Wang, *Superlatt. Microstruct.* 85 (2015) 331.
- [10] M.I. Khalil, O. Atici, A. Lucotti, S. Binetti, A. Le Donne, L. Magagnin, *Appl. Surf. Sci.* 379 (2016) 91.
- [11] W. Shockley, H.J. Queisser, *J. Appl. Phys.* 32 (1961) 510.
- [12] T.K. Todorov, K.B. Reuter, D.B. Mitzi, *Adv. Mater.* 22 (2010) E156.
- [13] Q.J. Guo, H.W. Hillhouse, R. Agrawal, *J. Am. Chem. Soc.* 131 (2009) 11672.
- [14] J.J. Scragg, T. Ericson, T. Kubart, M. Edoff, C. Platzer-Bjorkman, *Chem. Mater.* 23 (2011) 4625.

- [15] D.B. Mitzi, O. Gunawan, T.K. Todorov, K. Wang, S. Guha, *Sol. Energy Mater. Sol. Cells* 95 (2011) 1421.
- [16] O. Vigil-Gal-an, Maykel Courel, M. Espindola-Rodriguez, V. Izquierdo-Roca, E. Saucedo, A. Fairbrother, *J. Renew. Sustain. Energy* 5 (2013) 053137.
- [17] G. Altamura, L. Grenet, C. Roger, F. Roux, V. Reita, R. Fillon, H. Fournier, S. Perraud, H. Mariette, *J. Renew. Sustain. Energy* 6 (2014) 011401.
- [18] H. Hiroi, N. Sakai, T. Kato, H. Sugimoto, *IEEE 39th Photovoltaic Specialists Conf. (PVSC)* (2013), 0863.
- [19] K. Wang, O. Gunawan, T. Todorov, B. Shin, S.J. Chey, N.A. Bojarczuk, D. Mitzi, S. Guha, *Appl. Phys. Lett.* 97 (2010) 143508.
- [20] D. Zi-Yuan, L. Yong-Feng, Y. Bin, D. Zhan-Hui, Y. Gang, D. Rui, F. Xuan, W. Zhi-Peng, L. Lei, *J. Phys. D: Appl. Phys.* 47 (2014) 075304.
- [21] A. Nagoya, R. Asahi, G. Kresse, *J. Phys. Cond. Matter* 23 (2011) 404203.
- [22] A. Redinger, K. Hönes, X. Fontané, V. Izquierdo-Roca, E. Saucedo, N. Valle, A. Pérez-Rodríguez, S. Siebentritt, *Appl. Phys. Lett.* 98 (2011) 101907.
- [23] M. Bär, B.-A. Schubert, B. Marsen, S. Krause, S. Pookpanratana, T. Unold, L. Weinhardt, C. Heske, H.-W. Schock, *Appl. Phys. Lett.* 99 (2011) 152111.
- [24] K. Wang, B. Shin, K.B. Reuter, T. Todorov, D.B. Mitzi, S. Guha, *Appl. Phys. Lett.* 98 (2011) 051912.
- [25] D.M. Berg, M. Arasimowicz, R. Djemour, L. Gütay, S. Siebentritt, S. Schorr, X. Fontané, V. Izquierdo-Roca, A. Pérez-Rodríguez, P.J. Dale, *Thin Solid Films* 569 (2014) 113.
- [26] K.V. Gurav, J.H. Yun, S.M. Pawar, S.W. Shin, M.P. Suryawanshi, Y.K. Kim, J.H. Kim, *Mater. Lett.* 108 (2013) 316.
- [27] M.P. Suryawanshi, S.W. Shin, U.V. Ghorpade, K.V. Gurav, G.L. Agawane, C.W. Hong, J.H. Yun, P.S. Patil, J.H. Kim, A.V. Moholkar, *Sol. Energy* 110 (2014) 221.
- [28] S.M. Bhosale, M.P. Suryawanshi, M.A. Gaikwad, P.N. Bhosale, J.H. Kim, A.V. Moholkar, *Mater. Lett.* 129 (2014) 153.
- [29] S. Thiruvenkadam, D. Jovina, A. Leo Rajesh, *Sol. Energy* 106 (2014) 166.
- [30] F. Long, W.M. Wang, Z.K. Cui, L.Z. Fan, Z. Zou, T.K. Ji, *Chem. Phys. Lett.* 462 (2008) 84.
- [31] D.A. Johnston, M.H. Carletto, K.T.R. Reddy, I. Forbes, R.W. Miles, *Thin Solid Films* 403–404 (2002) 102.
- [32] L.V. Makhova, I. Kononov, R. Szargan, N. Aschkenov, M. Schubert, T. Chasse, *Phys. Stat. Sol. 2* (2005) 1206.
- [33] O. Gunawan, T. Todorov, D. Mitzi, *Appl. Phys. Lett.* 97 (2010) 233506.
- [34] A. Redinger, M. Mousel, M.H. Wolter, N. Valle, S. Siebentritt, *Thin Solid Films* 535 (2013) 291.
- [35] M. Bär, B.A. Schubert, B. Marsen, R.G. Wilks, S. Pookpanratana, M. Blum, S. Krause, T. Unold, W. Yang, L. Weinhardt, C. Heske, H.W. Schock, *Appl. Phys. Lett.* 99 (2011), 222105–3.
- [36] T. Ericson, J. Scragg, A. Hultqvist, J.P. Wätjen Szaniawski, *IEEE J. Photovoltaics JPHOTOV* 4 (2014), 465.
- [37] C. Platzer-Björkman, T. Törndahl, D. Abou-Ras, J. Malmström, J. Kessler, L. Stolt, *J. Appl. Phys.* 100 (2006) 044506.
- [38] D.A.R. Barkhouse, R. Haight, N. Sakai, H. Hiroi, H. Sugimoto, D.B. Mitzi, *Appl. Phys. Lett.* 100 (2012) 193904.
- [39] P. Sinsersuksakul, K. Hartman, S.B. Kim, J. Heo, L. Sun, H.H. Park, R. Chakraborty, T. Buonassisi, R.G. Gordon, *Appl. Phys. Lett.* 102 (2013) 053901.
- [40] F. El Akkad, T.A.P. Paulose, *Appl. Surf. Sci.* 295 (2014) 8.
- [41] E. Mokaripour, M.M. Bagheri-Mohagheghi, *Mater. Sci. Semicond. Process.* 30 (2015) 400.
- [42] Q.P. Tran, J.S. Fang, T.S. Chin, *Mater. Sci. Semicond. Process.* 40 (2015) 664.
- [43] G.A.H. Wetzelaer, M. Kuik, M. Lenes, P.W.M. Blom, *Appl. Phys. Lett.* 99 (2011) 153506.
- [44] C. Sah, R.N. Noyce, W. Shockley, *Proc. IRE* 45 (1957) 1228.
- [45] J.M. Shah, Y.-L. Li, Th. Gessmann, E.F. Schubert, *J. Appl. Phys.* 94 (2003) 2627.
- [46] M. Ben-Chorin, F. Moller, F. Koch, *J. Appl. Phys.* 77 (1995) 4482.
- [47] M. Jing-Jing, J. Ke-Xin, L. Bing-Cheng, F. Fei, X. Hui, Z. Chao-Chao, C. Chang-Le, *Chin. Phys. Lett.* 27 (2010) 107304.
- [48] N.K. Raddy, Q. Ahsanulhaq, J.H. Kim, Y.B. Hahn, *Appl. Phys. Lett.* 92 (2008) 043127.
- [49] S. Mridha, D. Basak, *J. Appl. Phys.* 101 (2007) 083102.
- [50] R. Singh, A.K. Narula, *Appl. Phys. Lett.* 71 (1997) 2845.
- [51] R.S. Ajimsha, K.A. Vanaja, M.K. Jayaraj, P. Misra, V.K. Dixit, L.M. Kukreja, *Thin Solid Films* 515 (2007) 7352.
- [52] H.C. Casey Jr., J. Muth, S. Krishnankutty, J.M. Zavada, *Appl. Phys. Lett.* 68 (1996) 2867.
- [53] K. Mayes, A. Yasan, R. McClintock, D. Shiell, S.R. Darvish, P. Kung, M. Razeghi, *Appl. Phys. Lett.* 84 (2004) 1046.
- [54] J.P. Sullivan, R.T. Tung, M.R. Pinto, *J. Appl. Phys.* 70 (1991) 7403.
- [55] R.T. Tung, *Phys. Rev. B* 45 (1992) 13509.
- [56] F.A. Padovani, G.G. Sumner, *J. Appl. Phys.* 36 (1965) 3744.
- [57] J.P. Sullivan, R.T. Tung, M.R. Pinto, *J. Appl. Phys.* 70 (1991) 7403.
- [58] M.E. Kiziroglou, A.A. Zhukov, X. Li, D.C. Gonzalez, P.J. de-Groot, P.N. Bartlett, *Solid Stat. Commun.* 140 (2006) 508.
- [59] E.H. Roderick, *Metal Semiconductor Contacts*, Oxford Press, London, 1978.
- [60] S.E.H. Logothetidis, *J. Appl. Phys.* 82 (1997) 5017.
- [61] E.H. Nicillian, A. Goetzberger, *Appl. Phys. Lett.* 7 (1965) 216.
- [62] J. Fernandez, P. Godignon, S. Berberich, J. Rebollo, G. Brezenanu, J. Millan, *Solid-State Electron.* 39 (1996) 1359.
- [63] J.P. Sullivan, R.T. Tung, M.R. Pinto, W.R. Graham, *J. Appl. Phys.* 70 (1991) 7403.
- [64] M. Cakar, Y. Onganer, A. Turut, *Synth. Met.* 126 (2002) 213.
- [65] A. Singh, *Solid State Electron.* 28 (1985) 223.
- [66] R. Herberholz, M. Igalson, H.W. Schock, *J. Appl. Phys.* 83 (1998) 318.
- [67] H.M. Baran, A. Tataröglu, *Chin. Phys. B* 22 (2013) 047303.
- [68] G. Vincent, D. Bois, P. Pinard, *J. Appl. Phys.* 46 (1975) 5173.
- [69] D. Aaron, R. Barkhouse, T. Gokmen, O. Gunawan, R.A. Haight, US patent No US20130269764 A1 (2013).



# Zinc molarity effect on $\text{Cu}_2\text{ZnSnS}_4$ thin film properties prepared by spray pyrolysis

F. Z. Boutebakh<sup>1</sup> · A. Beloucif<sup>2</sup> · M. S. Aida<sup>3</sup> · A. Chettah<sup>4</sup> · N. Attaf<sup>1</sup>

Received: 12 September 2017 / Accepted: 29 November 2017  
© Springer Science+Business Media, LLC, part of Springer Nature 2017

## Abstract

In the present work,  $\text{Cu}_2\text{ZnSnS}_4$  (CZTS) thin films were deposited by spray pyrolysis, the effect of zinc molarity on films structural, optical and electrical properties was investigated. CZTS films were grown by pneumatic spray pyrolysis with various zinc salt molarities. The structural properties reveal that all prepared CZTS films have a kesterite structure with a preferential orientation along (112) plan with the presence of secondary phases. Film composition and structural property vary with Zn molarity: at relatively low Zn molarity CuS secondary phase is formed, while with increasing Zn molarity ZnS secondary phase is formed. The crystallite size increases from 25 to 125 nm with increasing Zn molarity. Films transmission spectra show low transmission in the visible range, whereas the band gaps varies slightly with Zn salt molarity, it lies between 1.3 and 1.37 eV. Hall Effect measurements were employed to determine the electrical properties of CZTS films. The films conductivity is a p type, it is reduced with increasing Zn molarity due to the reduction of free carriers concentration caused by carriers loss at ZnS/CZTS interface and the presence of the resistive ZnS phase.

## 1 Introduction

Among quaternary semiconductors,  $\text{Cu}_2\text{ZnSnS}_4$  compound has drawn much interest due to its application in thin films based solar cells. This material belongs to the  $\text{I}_2\text{-II-IV-VI}_4$  class, CZTS has similar optical and electronic properties as compared to CIGS (copper indium gallium selenium). CZTS is composed of abundant, non-toxic and cheaper elements, in contrast to indium high cost and cadmium toxicity encountered in CIGS and CdTe materials.

The first report dealing with CZTS thin films was by Ito and Nakazawa, they have prepared CZTS thin films by sputtering technique [1]. CZTS material has a p-type electrical conductivity with a direct band gap energy around 1.5 eV and a high absorption coefficient in the visible range

( $\alpha > 10^4 \text{ cm}^{-1}$ ) [2]. The efficiency of CZTS based solar cell exceeds 12% with films deposited by physical technique [3]. While, for chemical technique, Ahmed et al. [4] have reported a conversion efficiency about more than 7.3% in CZTS based solar cell prepared by electrodeposition route. However, the experimental record efficiency of CZTS based solar cells is still far from the theoretical value 32% [5]. Actually, thin films solar cell efficiency is greatly influenced by the absorber layer deposition technique. Beside this, the other CZTS solar cell efficiency limiting factor is the formation of secondary phases that could be present in CZTS network such as: ZnS,  $\text{Cu}_x\text{S}$ , SnS,  $\text{Cu}_2\text{SnS}_3$ . Actually, ZnS secondary phase can absorb the shorter wavelengths which causes the photocurrent reduction; whereas,  $\text{Cu}_x\text{S}$  phase acts as recombination centre and thereafter reduces the device open circuit voltage [6]. Bhosale et al. investigated copper concentration effect under Cu rich-Zn poor condition and inferred that efficiency and open circuit rise with copper concentration increasing [7]. Therefore, well understanding of CZTS properties, investigation of deposition parameters influence upon device performances are still open studies and ambitious tasks. Till now, there is no general agreement and unanimity about which are the ideal conditions to obtain efficient devices from CZTS films: Zn-rich Cu-poor [8, 9] or Zn-poor Cu-rich [10–12].

✉ M. S. Aida  
aida\_salah2@yahoo.fr

<sup>1</sup> Laboratoire couches minces et interface université Frères Mentouri Constantine 1, Annaba, Algeria  
<sup>2</sup> Département de Physique, Faculté des Sciences, Université 20 Aout, 1955 Skikda, Algeria  
<sup>3</sup> Department of Physics, Faculty of Sciences, King Abdulaziz University, Jeddah, Kingdom of Saudi Arabia  
<sup>4</sup> Laboratoire LGMM, Groupe des matériaux fonctionnels, Université 20 Aout, 1955 Skikda, Algeria

Several deposition techniques were employed to prepare CZTS thin films namely: electron beam evaporation [13], pulsed laser deposition [14, 15], sputtering [16], electro-deposition [17], sol gel method [18], photochemical deposition [19] and spray pyrolysis [20–22].

Among these techniques, spray pyrolysis appears as an interesting technique for preparing  $\text{Cu}_2\text{ZnSnS}_4$  thin films [23]. This technique is very attractive because it is simple, inexpensive and non vacuum based technique, it is suitable for homogeneous thin films production on large surface.

In spray pyrolysis technique, several parameters that may alter the post deposited films properties can be controlled such as: substrate temperature, precursors salts source nature, flow rate solution molarities. Nakayama and Ito [24] studied the effect of ethanol and zinc concentration in the starting solution on the properties of spray deposited CZTS films using  $\text{N}_2$  as the carrier gas. Films grown from aqueous solution are near stoichiometric CZTS films were obtained with a solution containing 30% ethanol. Subsequent annealing of the films in sulphur ambient was found to be necessary. Madara et al. [25] deposited CZTS films by spray pyrolysis using thiourea complexes. Kamoun et al. [20], Kishore et al. [21] and Darenfed et al. [21] have investigated the effect of substrate temperature and the spray duration on CZTS films growth.

Regardless the deposition technique, the major concern with CZTS thin films preparation is the difficulty of stoichiometry control due the inevitable presence of secondary phases, their formation depend on the experimental conditions. Several studies revealed that the conditions to obtain a stoichiometric quaternary CZTS films are too narrow due to its stability limit region regarding the compositional ratios of different constituents [26, 27].

Moreover, CZTS electrical properties are extremely sensitive to the Zn and Cu amount in film network. Few reports were devoted to study the effect of precursor molarities on the properties of CZTS thin films prepared by spray pyrolysis. In the present paper we have studied the effect of zinc molarity on CZTS thin films properties. CZTS films were grown by a pneumatic spray pyrolysis technique, the concentration of Zn is varied with a fixed concentration of Cu in order to vary their relative composition in the film.

## 2 Experimental details

CZTS films were grown onto well cleaned glass substrates by pneumatic spray pyrolysis technique. The solution was prepared by dissolving four precursors, cupric chloride  $\text{CuCl}_2 \cdot 2\text{H}_2\text{O}$  (0.02 M), tin chloride (0.01 M), thiourea  $\text{SC}(\text{NH}_2)_2$  (0.12 M) and zinc acetate  $[\text{Zn}(\text{C}_2\text{H}_3\text{O}_2)_2 \cdot 2\text{H}_2\text{O}]$  with a varied molarities ranged from 0.01 to 0.025 M. All precursors were dissolved in distilled water. The obtained

solutions were thoroughly mixed by magnetic stirring during 10 min, until homogeneous transparent solutions are obtained. The solution was sprayed on heated glass substrates at 350 °C for 30 min. The used carrier gas is air with a flow rate of 10 l/min. The samples are denoted as (CZTS1, CZTS2 and CZTS3) corresponding to the preparation molarity 0.01, 0.015 and 0.025 M respectively. Film thicknesses are respectively 1.14, 1.45 and 1.75  $\mu\text{m}$ .

Structural, morphological, optical and electrical properties of films were analyzed. The structural properties were determined using Philips X'Pert system with Cu  $K\alpha$  radiation ( $\lambda_{\text{Cu}}=0.154056$  nm) at room temperature with  $2\theta$  varied in the range 20°–80°. The films surface morphology is studied by using the Atomic Force Microscopy AFM. The optical properties were studied by Shimadzu UV-3101 PC spectrophotometer transmissions in the UV–visible range (400–900 nm). Films thickness, gaps energy were calculated from the fitting of transmission data. Finally carriers concentration, mobility and electrical conductivity were determined from Hall effect measurement performed at home temperature.

## 3 Results and discussion

### 3.1 Structural properties

The XRD patterns of CZTS thin films obtained at different zinc concentration are shown in Fig. 1. The diffraction angles varied from 20° to 80°. For the whole samples, peaks assigned to (112), (220), (321), (224) and (332) planes are present, indicating the formation of kesterite type CZTS according to (JCPDS cards-26-0575). As seen, the increase in zinc concentration improves CZTS films crystallinity with

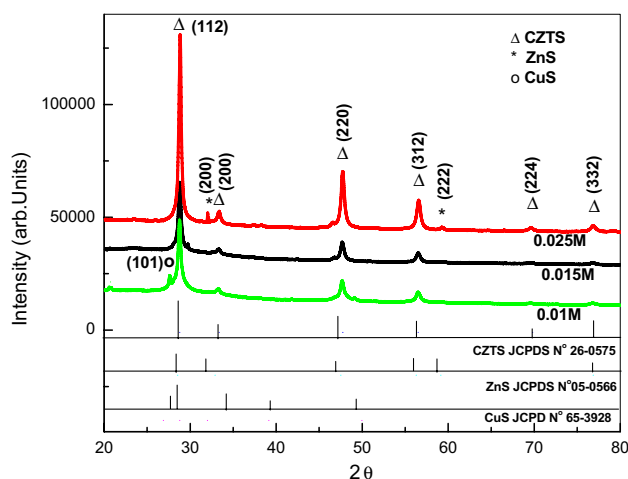


**Fig. 1** The XRD patterns of CZTS films prepared at different zinc concentrations

emerging the preferential orientation along (112) direction. This preferential orientation is commonly observed in CZTS thin films regardless the deposition technique [28, 29].

It is generally reported that CZTS, regardless the deposition technique, is usually accompanied with a binary secondary phases such as: CuS, Cu<sub>2</sub>SnS<sub>3</sub> (CTS) and ZnS [22–24]. However, it is hard to clearly detect these secondary phases, this is due to the fact that the lattice constants of CZTS are similar to CTS and ZnS, the obtained peaks could be related to either CZTS or CTS or ZnS phases [29, 30]. Due to the negative influence of secondary phases on CZTS based solar cell performances, one of the major challenges for these solar cells is the growth of single phase material.

In the case of films prepared at relatively low Zn concentration, CuS phase was detected; it is confirmed by the presence of the diffraction peak assigned to the (101) plane of CuS phase [according to (JCPDS No. 65-3928)]. While, as the zinc acetate concentration increases in the solution, ZnS phase is formed. The presence of ZnS phase is confirmed by the presence of two diffraction peaks assigned only to (200) and (222) plane related to ZnS phase (JCPDS No. 05-0566).

CuS phase is the first formed secondary phase, this is due to the fact that the film is prepared under Cu rich condition since the Zn source precursor molarity is lower than Cu one. While, with Zn molarity increase, ZnS phase is formed in the detriment of CuS one. The same observation of Zn effect in the composition of CZTS thin films prepared by sequential reactive sputtering have been observed by Sing et al. [31] with varying Zn thickness layer. They reported that at low Zn content, secondary CuS is formed, while with increasing Zn concentration the ZnS phase appears then.

In a theoretical calculation of the defect formation and stoichiometry of CZTS thin films, Chen et al. [27] have claimed that chemical-potential control is very important in growing good-quality crystals with no secondary phase formation and low-defect density. The chemical-potential control is necessary for growing good-quality Cu<sub>2</sub>ZnSnS<sub>4</sub> crystals. In particular, due to the strong binding between Zn and S, Zn content control should be taken very carefully. Thus, perfect Cu<sub>2</sub>ZnSnS<sub>4</sub> crystals are thermodynamically unstable when Zn is rich. It is experimentally observed that under Cu poor and Zn-rich conditions, the secondary phase segregation of ZnS is more likely to occur [32, 33]. Thereafter, CZTS thin films deposition is usually accompanied by secondary phase formation. The most formed one is CuS due to its low formation enthalpy –0.45 eV. However, due to its larger formation enthalpy –1.47 eV ZnS is inevitably formed in high Zn rich condition. This explains the formation of ZnS with increasing Zn concentration in the solution. Berg et al. [34] have proved that the presence of ZnS secondary phase in CZTS thin films causes the (112) peak position shift towards the higher angles. This is consistent with observed peak shift

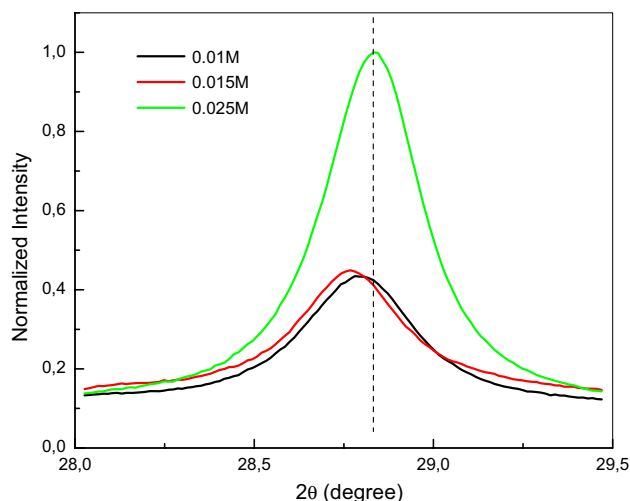


**Fig. 2** The variation of (112) peak position in XRD pattern of CZTS films as a function of Zn molarity

**Table 1** The FWHM values and grains size of (112) orientation of CZTS thin films obtained at different zinc concentrations

Sample	CZTS1	CZTS2	CZTS3
Zinc concentration	0.01	0.015	0.025
FWHM (2θ°)	0.2303	0.2326	0.2814
Crystallite size (nm)	29.23	35.46	133.51

as depicted in Fig. 2. As seen the peak position is shifted with increasing Zn concentration due to the formation of ZnS phase.

The crystallites size ( $D$ ) in the films has been determined from the XRD data using the Scherer's formula [35].

$$D = \frac{(0.9\lambda)}{\Delta(2\theta) \times \cos \theta} \quad (1)$$

where  $\lambda$  is the wavelength of the X-ray used,  $\Delta(2\theta)$  is the full width at half maximum of the peak and  $\theta$  is the Bragg angle.

The value of FWHM and the calculated crystallite size are summarized in Table 1. The crystallites size increases from 28 to 133 nm with increasing zinc concentration in the starting solution. Thereafter, one can conclude that increasing zinc salt concentration improves the crystallite size of CZTS thin films. We speculate that Zn atoms acts as nucleation center. Thereafter, increasing Zn molarity may enhances the nucleation step during film formation and then the crystallite size. The same conclusion has been reported by Berg et al. in a study of detection limit of secondary phase in CZTS thin films [34], they concluded that increasing Zn composition in the starting solution

used for CZTS deposition by electrodeposition technique enlarges the crystallite size. Singh et al. [29] investigated Zn influence in CZTS films prepared by sequential sputtering of metallic targets, they investigated Zn influence and concluded that sample with higher Zn content have better crystallinity .

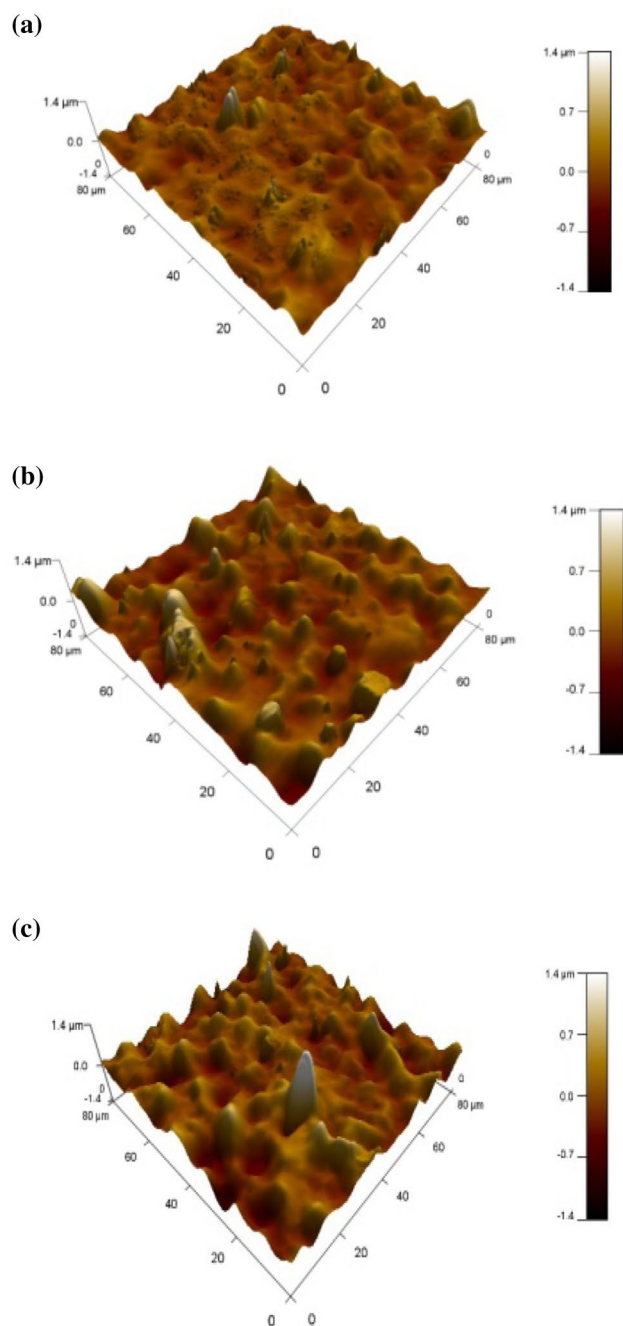


**Fig. 3** AFM images of CZTS thin films prepared at different zinc molarities: **a** 0.01 M, **b** 0.015 M and **c** 0.02 M

### 3.2 Morphological properties

AFM 3-dimensional micrographs obtained in different films are depicted in (Fig. 3). The AFM measurements are performed at room temperature. The films are dense and continuous, the surface is well covered with a relatively large grains and pinholes free. The surface films roughness increases with zinc concentration, the roughness values are summarized in Table 2. As can be deduced from Table 2, film gains size is larger in films prepared with higher zinc molarity, this is in good agreement with the crystallites size enlargement deduced from XRD measurements.

### 3.3 Optical and electrical properties

The transmission spectra of sprayed CZTS films deposited at different zinc concentrations were investigated using UV–visible spectrophotometer in spectral range of (400–900) nm. The variation of the transmittance as function of wavelength is depicted in Fig. 4. As can be seen, the whole films have low transmission (<2%) with an absorption coefficient larger than  $10^4 \text{ cm}^{-1}$ , which is in agreement with that reported results in the literature [33, 36, 37]. This large absorption coefficient is highly recommended for application as absorber layer in thin films solar cells. The concentration of zinc acetate reduces films transmittance, due to the increase in film thickness.

**Table 2** RMS values as function of zinc concentration

Zinc concentration	RMS (nm)
CZTS1	146.36
CZTS2	215.95
CZTS3	248.50

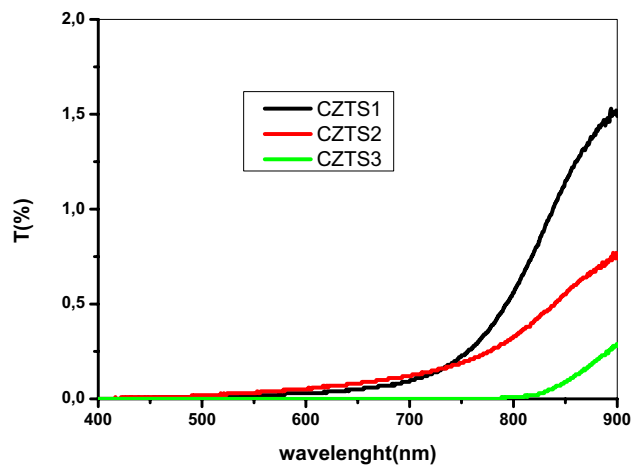


**Fig. 4** Optical transmission spectra in the visible range of CZTS thin films deposited with different zinc molarities

The band gaps energy ( $E_g$ ) of CZTS films were estimated from the analysis of the optical transmission. The relation between the absorption coefficient  $\alpha$  and the photon energy  $h\nu$  is given by (2):

$$(\alpha h\nu)^2 = B(h\nu - E_g) \tag{2}$$

where  $B$  is a constant,  $E_g$  the band gap energy which is determined from the variation of  $(\alpha h\nu)^2$  vs.  $(h\nu)$ .  $E_g$  is determined by extrapolating the linear portion of the spectrum to  $\alpha h\nu = 0$ , as shown in Fig. 5. The band gap energy calculated values are reported in Fig. 6, they vary in the range of 1.3–1.37 eV which is in good concordance with the reported gap values of CZTS [38].

The gap energy decreases slightly with zinc concentration. The same behavior of optical band enlargement has been reported by Malbera et al. [39] with increasing tin and Zn concentration [29].

From ab initio calculations Chen et al. [40, 41] has climbed that a reduction in Zn or Sn content introduces a large density of acceptor defects such as  $V_{zn}$ ,  $Cu_{zn}$ ,  $V_{Sn}$ ,  $Cu_{Sn}$ , and  $Zn_{Sn}$  antisites. These defects may create shallow acceptor levels responsible for the change in material absorption edge and optical band gap shrinking. This variation can be also explained in terms of the disorder as depicted in the drawing insert in Fig. 6. The optical gap broadening of sample(CZTS3) can be related to the apparition of ZnS secondary phase as suggested from XRD analysis. It is well argued [29, 42] that ZnS secondary phase is responsible for optical band gap enlargement.

The disorder in the film network is described by the band tail width which is called Urbach tail and expressed as [43].

$$\alpha = \alpha_0 \exp\left(\frac{h\nu}{E_u}\right) \tag{3}$$

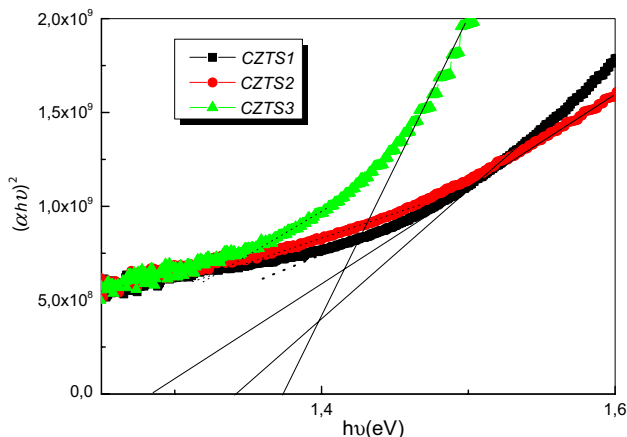


Fig. 5 Plot of  $(\alpha h\nu)^2$  as a function of photon energy ( $h\nu$ ) of films deposited at different zinc molarities used for optical band gap determination

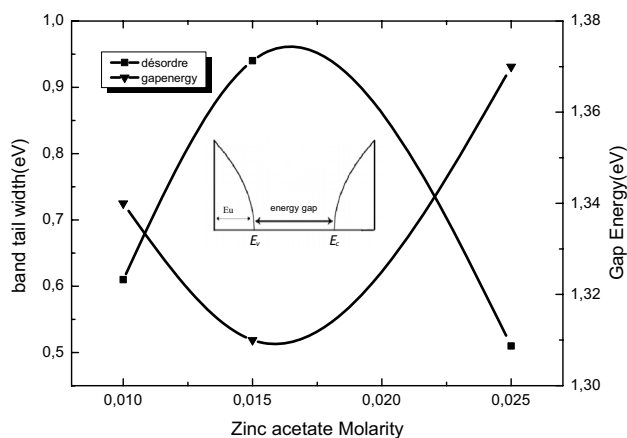


Fig. 6 Variations of band tail with and band gap energy as a function of zinc molarity in the solution

where  $\alpha_0$  is the pre-exponential factor,  $h\nu$  the photon energy and  $E_u$  is the Urbach tail.

The Urbach tail ( $E_u$ ) can be estimated from the inverse slope of the linear plot of  $\ln(\alpha)$  versus photons energy. Both energy band gap and Urbach tail are plotted as function of photon energy in Fig. 6. From this figure, we observe that the variations of band gap and Urbach energies have opposite trends. Hence one can conclude that the disorder in film network controls the optical band gap energy variation .

The electrical properties of sprayed CZTS thin films are performed by Hall effect at room temperature, the carriers concentration. Hall mobility and electrical conductivity are tabulated in Table 3. The whole prepared films have p type conductivity according to Hall constant sign. Several authors found the same order of conductivity in CZTS thin films [44, 45]. In Fig. 7 we have presented the variation of both carrier concentration and conductivity as function of zinc molarities. According to Fig. 7, the conductivity variation is not only controlled by the free carriers concentration. Since, despite that the film prepared at 0.015 M enjoys the higher carrier concentration, its conductivity is not the higher one. It is well known that intrinsic point defects in CZTS play a major role and control CZTS electrical properties. Several authors have calculated the defects formation energies in CZTS, based on first-principle theory [27, 41, 46–49].

Table 3 The electrical parameters of CZTS thin films at different zinc concentration

Carrier concentration ( $\text{cm}^{-3}$ )	Conductivity ( $(\Omega \times \text{m})^{-1}$ )	
CZTS1	$1.082 \times 10^{22}$	14.35
CZTS2	$3.36 \times 10^{23}$	12.44
CZTS3	$3.32 \times 10^{16}$	2.2

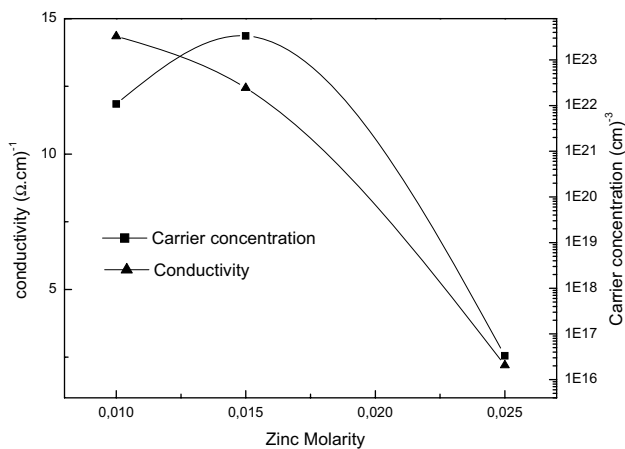


**Fig. 7** Variation electrical conductivity and free carriers of CZTS thin films concentration as a function of Zinc molarity in the preparing solution

It has been claimed that copper vacancies ( $V_{Cu}$ ) and  $Cu_{Zn}$  can be easily formed and are the dominant acceptor defects in CZTS [41, 48, 49]. They form shallow acceptor levels in CZTS leading to p-doping. Thereafter, with increasing Zn concentration in the starting solution,  $Cu_{Zn}$  defects are reduced causing the decrease in free carriers concentration as shown in Fig. 7.

The films conductivity is also controlled by the secondary phases present in film network. It is well known that lattice mismatch between CZTS and the secondary phase give rise to interface states within the band gap (due to the dangling bonds). Hence a shorter carrier lifetime and carriers loss at the CZTS/secondary phase interface cause the conductivity reduction. On the other hand, the resistive ZnS secondary phase that appears with increasing Zn concentration could be the cause of conductivity reduction of CZTS film. This is consistent with Mitzi et al. conclusion [50] where they inferred that ZnS is responsible for the high series resistance observed in CZTS based solar cells. While the relative high conductivity measured in film prepared with low Zn molarity may originate from the segregation of conductive  $Cu_xS$  phase.

## 4 Conclusion

CZTS thin films were successively deposited by a simple and economic spray pyrolysis technique. The effect of zinc salt molarity on films properties was investigated. The XRD patterns confirm the formation of kesterite structure of the obtained CZTS thin film with a preferential orientation along (112) plan. Films are composed of secondary phases such as CuS at relatively low Zn molarity and ZnS phase when film is deposited with higher Zn precursor molarities.

Atomic Force Microscopy images shows that the film roughness increases with zinc concentration. Increasing the Zn molarity improved the film crystallinity and the optical band gap broadening. Electrical characterization reveals that films conductivity is a p type. Due to the presence of ZnS phase the electrical conductivity is reduced due to the reduction of free carriers concentration. Thereafter, we concluded from the obtained results that in order to avoid the negative ZnS phase, it is recommended to use a relatively low Zn salt molarity concentration.

## References

1. K. Ito, T. Nakazawa, Electrical and optical properties of stannite-type quaternary semiconductor thin films. *Jpn. J. Appl. Phys.* **27**, 2094 (1988)
2. F. Liu, Y. Li, K. Zhang, B. Wang, C. Yan, Y. Lai, Z. Zhang, J. Li, Y. Liu, In situ growth of  $Cu_2ZnSnS_4$  thin films by reactive magnetron co-sputtering. *Sol. Energy Mater. Solar Cells* **94**, 2431 (2010)
3. W. Wang, M.T. Winkler, O. Gunawan, T. Gokmen, T.K. Todorov, Y. Zhu, D.B. Mitzi, Device characteristics of CZTSSe thin-film solar cells with 12.6% efficiency. *Adv. Energy Mater.* **4** (2014)
4. S. Ahmed, K.B. Reuter, O. Gunawan, L. Guo, L.T. Romankiw, H. Deligianni, A high efficiency electrodeposited  $Cu_2ZnSnS_4$  solar cell. *Adv. Energy Mater.* **2**, 253 (2012)
5. W. Shockley, H.J. Queisser, Detailed balance limit of efficiency of p-n junction solar cells. *J. Appl. Phys.* **32**, 510 (1961)
6. J.J. Scragg, in *Copper Zinc Tin Sulfide Thin Films for Photovoltaics* (Springer, Berlin, 2011)
7. S.M. Bhosale, M.P. Suryawanshi, J.H. Kim, A.V. Moholkar, Influence of copper concentration on sprayed CZTS thin films deposited at high temperature. *Ceram. Int.* **41**, 8299 (2015)
8. T.K. Todorov, K.B. Reuter, D.B. Mitzi, High-efficiency solar cell with Earth-abundant liquid-processed absorber. *Adv. Mater.* **22**, E156 (2010)
9. C.P. Bjorkman, J. Scragg, H. Flammersberger, T. Kubart, M. Edoff, Influence of precursor sulfur content on film formation and compositional changes in  $Cu_2ZnSnS_4$  films and solar cells. *Sol. Energy Mater. Solar Cells* **98**, 110 (2012)
10. M.P. Suryawanshi, S.W. Shin, U.V. Ghorpade, K.V. Gurav, G.L. Agawane, C.W. Hong, J.H. Yun, P.S. Patil, J.H. Kim, A.V. Moholkar, A chemical approach for synthesis of photo electrochemically active  $Cu_2ZnSnS_4$  (CZTS) thin films. *Solar Energy* **110**, 221 (2014)
11. B. Shin, O. Gunawan, Y. Zhu, N.A. Bojarczuk, S.J. Chey, S. Guha, Thin film solar cell with 8.4% power conversion efficiency using an earth-abundant  $Cu_2ZnSnS_4$  absorber. *Prog. Photovoltaics Res. Appl.* **21**, 72 (2013)
12. S. Chen, X.G. Gong, A. Walsh, S. Wei, Defect physics of the kesterite thin-film solar cell absorber  $Cu_2ZnSnS_4$ . *Appl. Phys. Lett.* **96**, 021902 (2010)
13. J. Zhang, L. Shao, Y. Fu, E. Xie,  $Cu_2ZnSnS_4$  thin films prepared by sulfurization of ion beam sputtered precursor and their electrical and optical properties. *Rare Met.* **25**, 315 (2006)
14. K. Moriyama, K. Tanaka, H. Uchiki, Fabrication of  $Cu_2ZnSnS_4$  thin-film solar cell prepared by pulsed laser deposition. *Jpn. J. Appl. Phys.* **46**, 5780 (2007)
15. S.M. Pawar, A.V. Moholkar, I.K. Kim, S.W. Shin, J.H. Moon, J.I. Rhee, J.H. Kim, Effect of laser incident energy on the structural,

- morphological and optical properties of  $\text{Cu}_2\text{ZnSnS}_4$  (CZTS) thin films. *Curr. Appl. Phys.* **10**, 565 (2010)
16. T. Tanaka, T. Nagatomo, D. Kawasaki, M. Nishio, Q. Guo, A. Wakahara, A. Yoshida, H. Ogawa, Preparation of  $\text{Cu}_2\text{ZnSnS}_4$  thin films by hybrid sputtering. *J. Phys. Chem. Solids* **66**, 1978 (2005)
  17. K. Tanaka, N. Moritake, H. Uchiki, Preparation of  $\text{Cu}_2\text{ZnSnS}_4$  thin films by sulfurizing sol-gel deposited precursors. *Sol. Energy Mater. Sol. Cells* **91**, 1199 (2007)
  18. S. Siebentritt, U. Rau eds., in *Wide-Gap Chalcopyrites* (Springer, Berlin, 2006)
  19. K. Moriya, K. Tanaka, H. Uchiki, Characterization of  $\text{Cu}_2\text{ZnSnS}_4$  thin films prepared by photochemical Deposition. *Jpn. J. Appl. Phys.* **44**, 715 (2005)
  20. N. Kamoun, H. Bouzouita, B. Rezig, Fabrication and characterization of  $\text{Cu}_2\text{ZnSnS}_4$  thin films deposited by spray pyrolysis technique. *Thin. Solid Films* **515**, 5949 (2007)
  21. Y.B. Kishore Kumar, G. Suresh Babu, P. Uday Bhaskar, V.S. Raja, Preparation and characterization of spray-deposited  $\text{Cu}_2\text{ZnSnS}_4$  thin films. *Solar Energy Mater. Solar Cells* **93**, 1230 (2009)
  22. W. Daranf, M.S. Aida, N. Attaf, J. Bougdira, H. Rinnert,  $\text{Cu}_2\text{ZnSnS}_4$  thin films deposition by ultrasonic spray pyrolysis. *J. Alloys Compd.* **542**, 2227 (2012)
  23. H. Afif, S.A. Mahmoud, A. Ashour, Structural study of ZnS thin films prepared by spray pyrolysis. *Thin Solid Films* **263**, 248 (1995)
  24. N. Nakayama, K. Ito, Sprayed films of stannite  $\text{Cu}_2\text{ZnSnS}_4$ . *Appl. Surf. Sci.* **92**, 171 (1996)
  25. J. Madara, P. Bombicz, M. Okuya, S. Kaneko, Thermal decomposition of thiourea complexes of Cu(I), Zn(II), and Sn(II) chlorides as precursors for the spray pyrolysis deposition of sulfide thin films". *Solid State Ionics* **141–142**, 439 (2001)
  26. I.D. Olekseyuk, I.V. Dudchak, L.V. Piskach, Phase equilibria in the  $\text{Cu}_2\text{S}-\text{ZnS}-\text{SnS}_2$  system. *J. Alloys Compd.* **368**, 135 (2004)
  27. S. Chen, J.H. Yang, X.G. Gong, A. Walsh, S.H. Wei, Intrinsic point defects and complexes in the quaternary kesterite semiconductor  $\text{Cu}_2\text{ZnSnS}_4$ . *Phys. Rev. B* **81**, 245204 (2010)
  28. H. Yoo, J. Kim, Growth of  $\text{Cu}_2\text{ZnSnS}_4$  thin films using sulfurization of stacked metallic films. *Thin Solid Films* **518**, 6567 (2010)
  29. O.P. Singh, N. Muhunthan, K.S. Gour, R. Parmar, M. Dalai, P. Kulriya, S. Pillai, V.N. Singh, Effect of sputter deposited Zn precursor film thickness and annealing time on the properties of  $\text{Cu}_2\text{ZnSnS}_4$  thin films deposited by sequential reactive sputtering of metal targets. *Mater. Sci. Semicond. Process* **52**, 38 (2016)
  30. P.J. Dale, K. Hoenes, J.J. Scragg, S. Siebentritt, in *34th IEEE Photovoltaic Specialist Conference*. (IEEE, Philadelphia, 2009), p. 1956
  31. X. Fontané, L. Calvo-Barrío, V. Izquierdo-Roca, E. Saucedo, A. Pérez-Rodríguez, J.R. Morante, D.M. Berg, P.J. Dale, S. Siebentritt, In-depth resolved Raman scattering analysis for the identification of secondary phases: characterization of  $\text{Cu}_2\text{ZnSnS}_4$  layers for solar cell applications. *Appl. Phys. Lett.* **98**, 181905 (2011)
  32. J. Scragg, P. Dale, L. Peter, Synthesis and characterization of  $\text{Cu}_2\text{ZnSnS}_4$  absorber layers by an electrodeposition-annealing route. *Thin Solid Films* **517**, 2481 (2009)
  33. T. Todorov, M. Kita, J. Carda, P. Escribano,  $\text{Cu}_2\text{ZnSnS}_4$  films deposited by a soft-chemistry method. *Thin Solid Films* **517**, 2541 (2009)
  34. D.M. Berg, M. Arasimowicz, R. Djemour, L. Gütay, S. Siebentritt, S. Schorr, X. Fontané, V. Izquierdo-Roca, A. Pérez-Rodríguez, P.J. Dal, Discrimination and detection limits of secondary phases in  $\text{Cu}_2\text{ZnSnS}_4$  using X-ray diffraction and Raman spectroscopy. *Thin Solid Films* **569**, 113 (2014)
  35. L.A. Goodman, Liquid-crystal displays—electro-optic effects and addressing techniques. *RCA Rev.* **35**, 613 (1974)
  36. C. Steinhagen, M.G. Panthani, V. Akhavan, B. Goodfellow, B. Koo, B.A. Korgel, Synthesis of  $\text{Cu}_2\text{ZnSnS}_4$  nanocrystals for use in low-cost photovoltaics. *J. Am. Chem. Soc.* **131**, 12554 (2009)
  37. S. Chen, X.G. Gong, A. Walsh, S.-H. Wei, Crystal and electronic band structure of  $\text{Cu}_2\text{ZnSnX}_4$  (X = S and Se) photovoltaic absorbers: first-principles insights. *Appl. Phys. Lett.* **94**, 041903 (2009)
  38. C. Persson, Electronic and optical properties of  $\text{Cu}_2\text{ZnSnS}_4$  and  $\text{Cu}_2\text{ZnSnSe}_4$ . *J. Appl. Phys.* **107**, 053710 (2010)
  39. C. Malerba, C. Ricardo, M. Valentini, F. Biccari, M. Muller, L. Rebuffi, E. Esposito, P. Mangiapane, P. Scardi, A. Mittiga, Stoichiometry effect on  $\text{Cu}_2\text{ZnSnS}_4$  thin films morphological and optical properties. *J. Renew. Sust. Energy* **6**, 011404 (2014)
  40. S. Chen, A. Walsh, X. Gong, S. Wei, Classification of lattice defects in the Kesterite  $\text{Cu}_2\text{ZnSnS}_4$  and  $\text{Cu}_2\text{ZnSnSe}_4$  earth-abundant solar cell absorbers. *Adv. Mater.* **25**, 1522 (2013)
  41. S. Chen, L.-W. Wang, A. Walsh, X. Gong, S.-H. Wei, Abundance of  $\text{CuZn} + \text{SnZn}$  and  $2\text{CuZn} + \text{SnZn}$  defect clusters in kesterite solar cells. *Appl. Phys. Lett.* **101**, 223901 (2012)
  42. S. Schorr, V. Riede, D. Spemann, T. Doering, Electronic band gap of  $\text{Zn}_2\text{x}(\text{CuIn})_{1-x}\text{X}_2$  solid solution series (X = S, Se, Te). *J. Alloys Compd.* **414**, 26 (2006)
  43. F. Urbach, The long-wavelength edge of photographic sensitivity and of the electronic absorption of solids. *Phys. Rev.* **92**, 1324 (1953)
  44. S. Kumar Swami, A. Kumar, V. Dutta, Deposition of kesterite  $\text{Cu}_2\text{ZnSnS}_4$  (CZTS) thin films by spin coating Technique for solar cell application. *Energy Procedia* **33**, 198 (2013)
  45. Z. Shadrokh, H. Eshghi, A. Yazdan, *Mater. Sci. Semicond. Process* **40**, 752 (2015)
  46. T. Maeda, S. Nakamura, T. Wada, First principles calculations of defect formation in in-free photovoltaic semiconductors  $\text{Cu}_2\text{ZnSnS}_4$  and  $\text{Cu}_2\text{ZnSnSe}_4$ . *Jpn. J. Appl. Phys.* **50**, 04DP07 (2011)
  47. S. Chen, X.G. Gong, A. Walsh, S.-H. Wei, Defect physics of the kesterite thin-film solar cell absorber  $\text{Cu}_2\text{ZnSnS}_4$ . *Appl. Phys. Lett.* **96**, 021902 (2010)
  48. A. Nagoya, R. Asahi, R. Wahl, G. Kresse, Defect formation and phase stability of  $\text{Cu}_2\text{ZnSnS}_4$  photovoltaic material. *Phys. Rev. B*, **81**, 113202 (2010)
  49. J.M. Raulot, C. Domain, J.F. Guillemoles, Ab initio investigation of potential indium and gallium free chalcopyrite compounds for photovoltaic application. *J. Phys. Chem. Solids*, **66**, 2019 (2005)
  50. D. Mitzi, O. Gunawan, T. Todorov, K. Wang, S. Guha, The path towards a high-performance solution-processed kesterite solar cell. *Sol. Ener. Mater. Solar Cells*, **95**, 1421 (2011)

PAPER

# Thermal sulfurization effect on sprayed CZTS thin films properties and CZTS/CdS solar cells performances

To cite this article: F Z Boutebakh *et al* 2018 *Mater. Res. Express* **5** 015511

View the [article online](#) for updates and enhancements.



## PAPER

## Thermal sulfurization effect on sprayed CZTS thin films properties and CZTS/CdS solar cells performances

RECEIVED  
11 October 2017REVISED  
13 December 2017ACCEPTED FOR PUBLICATION  
11 January 2018PUBLISHED  
24 January 2018F Z Boutebakh<sup>1</sup>, D Batibay<sup>2</sup>, M S Aida<sup>3</sup> , Y S Ocak<sup>2</sup> and N Attaf<sup>1</sup><sup>1</sup> Laboratoire couches minces et interface université Frères Mentouri Constantine 1, Algérie<sup>2</sup> Department of Science, Faculty of Education, Dicle University, 21280 Diyarbakir, Turkey<sup>3</sup> Department of Physics, Faculty of Sciences, King Abdulaziz University Djeddah, Saudi ArabiaE-mail: [aida\\_salah2@yahoo.fr](mailto:aida_salah2@yahoo.fr)

Keywords: thin films, solar cells, spray pyrolysis, CZTS

**Abstract**

Cu<sub>2</sub>ZnSnS<sub>4</sub> (CZTS) thin films were successfully deposited by a simple and inexpensive technique such as ultrasonic spray pyrolysis. The effect of sulfurization temperature on CZTS films properties and on Mo/CZTS/CdS/ZnO/ZnO:Al solar cell performances were studied. The investigated sulfurization temperatures were ranged from 450 °C to 550 °C. X-ray-diffraction pattern and Raman scattering spectroscopy confirmed the formation of monophase kesterite CZTS, the best crystallinity was obtained in the sample sulfurized at 450 °C. Atomic forces microscopy images indicated that annealing temperature increase yields to rough films with large grain size. UV–visible optical transmittance spectroscopy reveals that films enjoy a strong absorption with an absorption coefficient as high as 104 cm<sup>-3</sup>. Whereas, the optical band gap energy was found to decrease with sulfurization temperature. Hall effect measurements confirm the films p-type conductivity; the carriers concentration varies between 10<sup>14</sup> and 10<sup>16</sup> cm<sup>-3</sup> when the sulfurization temperature changes from 450 °C to 550 °C. The *I*–*V* characteristics of the realized Mo/CZTS/CdS/ZnO/ZnO:Al cells indicated that all the devices show a rectification behavior with an ideality factor ranged from 1.6 to 1.8. The current transport is dominated by the interfacial recombination process. The photovoltaic effect was observed, the best performance was achieved in the device prepared with CZTS sulfurized film at 450 °C, the recorded characteristics are: 0.43% efficiency, 9.8 mA cm<sup>-2</sup> short circuit current, 161 mV open circuit voltage and 28% fill factor. A comparison between the reported results obtained by different techniques reveals the superiority of the cells prepared with CZTS deposited by physical deposition technique such as thermal evaporation or sputtering.

**1. Introduction**

During the last two decades, CZTS thin films has emerged as promising material for thin films solar cells production as an alternative of CuIn(Ga)Se and CdTe solar cells due to the scarcity of In and toxicity of Se. CZTS is composed with abundant and environmental friendly materials. Besides this, CZTS film is characterized by a large absorption coefficient ( $\alpha \sim 10^4$  cm<sup>-1</sup>) in the UV–visible range and an optical band gap of 1.5 eV, thus making CZTS thin films suitable for application as an absorber layer in solar cell [1, 2]. Furthermore, CZTS based solar has a theoretical Shockley–Queisser conversion efficiency limit as high as 32.2% [3]. The best recorded efficiency of CZTS solar cell prepared by non-vacuum route was about 7.4% reported by Ahmad *et al* [4], whereas Cu<sub>2</sub>ZnSnS<sub>4</sub>Se CZTS(Se) material achieved an efficiency about 12.6% [5]. Actually, the formation of p–n rectifying hetero-junction responsible for the photo-generated carriers separation is achieved by CdS/CZTS hetrostructure. Cadmium sulfide (n-type semiconductor) layer, the most popular buffer layer this buffer, provides the best performance due to the moderate CdS gap energy of (2.4 eV) [6–10].

CZTS thin films can be prepared by several methods, either vacuum or no vacuum processes. The reached efficiency in laboratory is about 8.4% in the case of CZTS based solar cell deposited by vacuum process such as sputtering technique [11], while, 4.13% of efficiency was achieved by pulsed laser deposition [12]. Katagiri *et al*

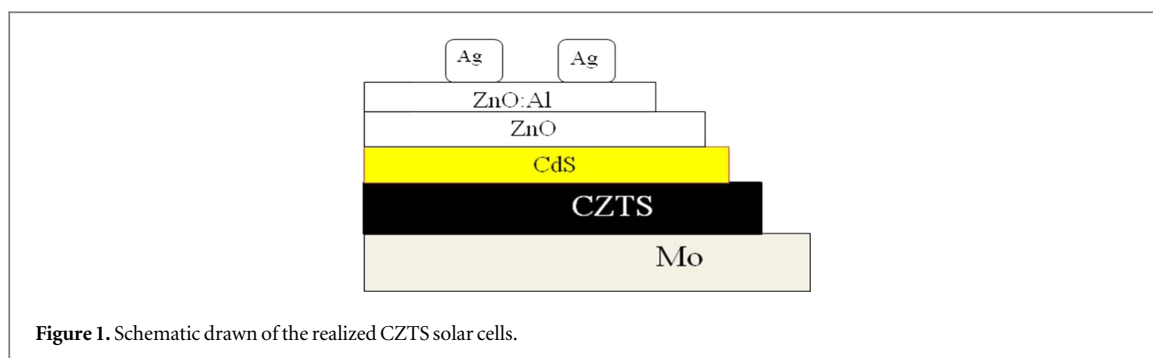


Figure 1. Schematic drawn of the realized CZTS solar cells.

[13] reported an efficiency of about 6.48% and 6.7% by using magnetron sputtering and co-sputtering technique of Cu, SnS, and ZnS targets [14]. However, in the case of non-vacuum techniques, Ahmed *et al* [4] had reported the best record efficiency using chemical route as equal as 7.4%. An efficiency of 5.1% was reported in CZTS spin coating coated solar cell [15].

Among chemical route techniques, spray pyrolysis is the most suitable one for films deposition on large area. Moreover, it is inexpensive and simple. Several authors have used this technique for CZTS thin films deposition and solar cells production [16–19]. Bhosale *et al* [19] have studied the effect of copper concentration on CZTS/CdS solar cells performance and found an efficiency ranged between 0.2% and 1.09% when the copper concentration change from 0.15 to 0.25, suggesting that CZTS thin films deposition under Cu-rich Zn-poor may enhance the solar cell efficiency. Vigil-Gal *et al* [20] had studied the effect of gas carrier on CZTS solar cell performance, they found an efficiency of about 1% under argon gas and 0.5% using air as carrier gas. Up to date, less studies are devoted to CZTS solar cell compared to CIGS technology even they have similar properties. Additionally, the low performance of CZTS solar cell is generally due to its low open circuit voltage ( $V_{oc}$ ) [21]. Lowering the open circuit voltage is mainly due to the carriers recombination at CZTS/CdS interface [22–24] because of the cliff-like band alignment between CZTS and CdS layers. Courel *et al* [25] have studied the loss mechanisms in sprayed-CZTS solar cells; they inferred that CZTS thin film device low performance is due to the low minority carriers diffusion length values that affects strongly the short circuit current density.

The drawback of spray pyrolysis method is the lack of sulfur due to its volatility, thereafter; generally, CZTS films prepared by spray pyrolysis are subsequently post-annealed in  $H_2S$  atmosphere to improve the film stoichiometry. Thermal sulfurization of CZTS was widely used [26–29]; since his benefit in CZTS solar cells efficiency enhancement has been proved. However, the best CZTS solar cell was produced by co-sputtering continued with vapor phase sulfurization method; efficiencies of up to 5.74% were reached [30].

In the present work we have investigated the effect of sulfurization temperature on the properties of sprayed CZTS thin film and on the electrical parameters of Mo/CZTS/CdS/ZnO/ZnO:Al solar cells.

## 2. Experimental

Ultrasonic spray pyrolysis system was used for CZTS thin film deposition on molybdenum coated glasses substrates. Glass substrates were cleaned firstly in a bath of acetone after rinsing in distilled water and drying under  $N_2$  gas. The starting solution used for CZTS deposition was prepared by dissolving 0.01 M of zinc acetate and tin chloride 0.04 M of copper acetate monohydrate and 0.12 M of thiourea. All precursors were dissolved in distilled water and stirred for 15 min until transparent solution obtained, then the solution was sprayed on Mo-coated glass heated at 350 °C, nitrogen was used as carrier gas. The Mo/CZTS structure was annealed at different temperature (450 °C–550 °C) in  $H_2S:Ar$  gas (30 sccm) gas mixture atmosphere for 30 min. After annealing, 50 nm thickness cadmium sulfide CdS layer was deposited onto CZTS using DC sputtering at 175 °C, followed by DC sputtering deposition of an intrinsic ZnO layer and ZnO:Al layer as window layer with thicknesses of 50 nm. Finally, the device structure (figure 1) was completed by silver grids deposition on the top by thermal evaporation technique. The structural properties of CZTS films were studied using x-ray diffraction (XRD) and Raman scattering spectroscopy. Films morphology was studied by means of atomic forces microscopy (AFM). 2D and 3D AFM topography were obtained with scanning in area of  $20 \times 20 \mu m^2$  size using contact mode with 0.65 Hz scan rate in air and at room temperature. The optical properties were characterized by means of optical transmittance spectrophotometry in the UV–visible wavelength range. CZTS films electrical measurements were carried out using Hall effect measurements. The  $I$ – $V$  characteristics of the realized solar cells were analyzed in dark and under illumination by a simulator solar with lamp intensity about  $100 \text{ mW cm}^{-2}$ .

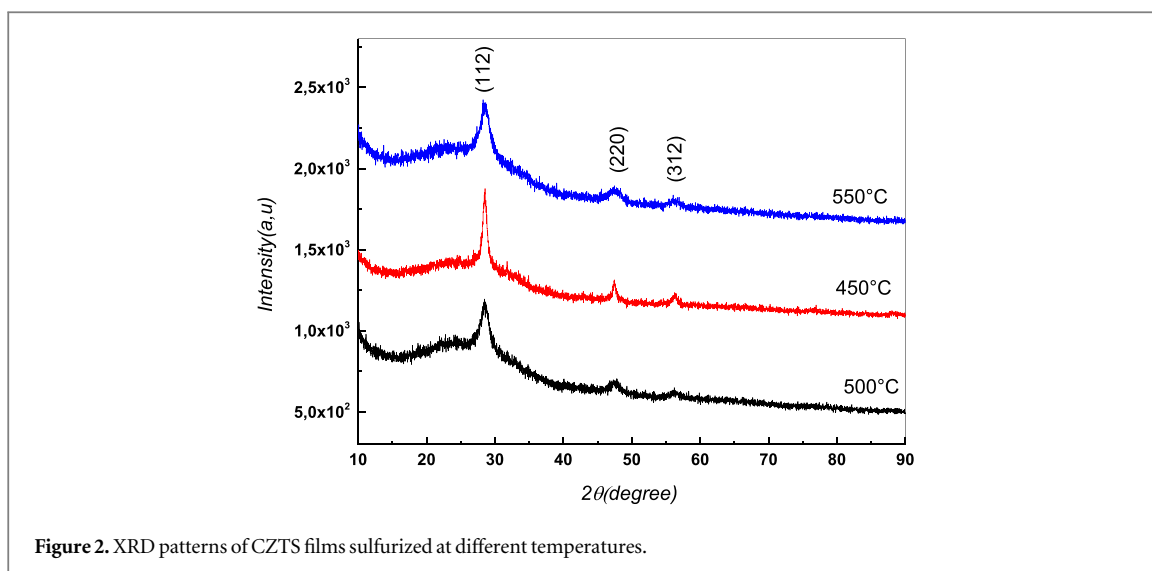


Figure 2. XRD patterns of CZTS films sulfurized at different temperatures.

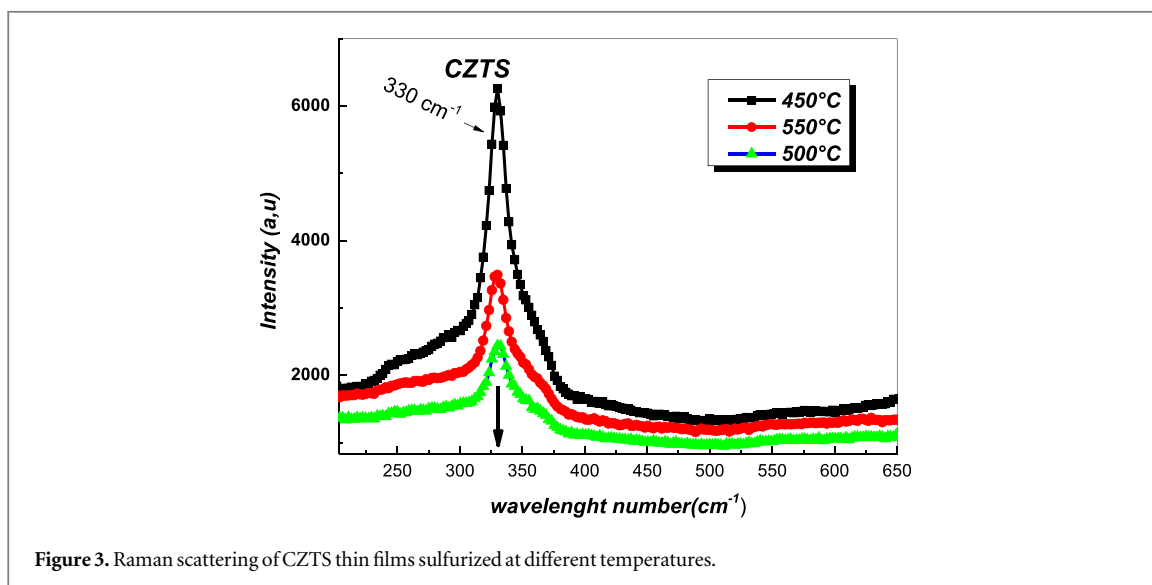


Figure 3. Raman scattering of CZTS thin films sulfurized at different temperatures.

### 3. Results and discussions

#### 3.1. Films properties

The XRD patterns of CZTS thin films annealed at different sulfurization temperatures are shown in figure 2, the observed peaks are related to the planes (112), (220) and (312) planes, they are assigned to CZTS kesterite tetragonal phase (according to #27-0575 card), (112) plane exhibits the higher intensity indicating the preferential orientation the same peaks position were observed in [31, 32]. Generally, CZTS thin films deposition is accompanied by the formation of several secondary phases such as SnS, SnS<sub>2</sub>, Sn<sub>2</sub>S<sub>3</sub>, ZnS, and Cu<sub>3</sub>SnS<sub>4</sub> [33–36]

It is interesting to note that no peaks related to any secondary phase has been detected; this is confirmed by Raman analysis, as show in figure 3. The absence of secondary phase can be a result for the thermal sulfurization, which is a good solution for the reduction of undesirable phases as mention. The same observation has been reported after CZTS sulfurization [37, 38]. Moreover, according to XRD patterns Mo<sub>2</sub>S phase is not formed during sulfurization step. While, it is reported that sulfurization yields to the formation of undesirable Mo<sub>2</sub>S phase [39–41]. With increasing the annealing sulfurization temperature, XRD peaks intensities are reduced, the sample sulfurized at 450 °C exhibits the most intense and sharp peak. This indicated that high temperature sulfurization degrades CZTS sprayed films microstructure.

The crystallites sizes were calculated from the most intense peak along (112) plane by Debye Scherer's equation [42].

**Table 1.** The FWHM, crystallite sizes and strain values of CZTS films annealed at different temperatures.

Annealed $T$ (°C)	FWHM (°)	Crystallite size (nm)	Strain
450	0.5117	16.7	0.0088
500	0.624	13.7	0.0108
550	0.614	13.9	0.0107

$$D = \frac{(0, 9, \lambda)}{\Delta(2\theta) \cdot \cos \theta}, \quad (1)$$

where:  $\lambda$  is the wavelength of the x-ray used,  $\beta$  is the full width at half maximum of the peak and  $\theta$  is the Bragg angle.

The lattice strain ( $\varepsilon$ ) was calculating using the following relation:

$$\varepsilon = \frac{\beta \cos \theta}{4}. \quad (2)$$

The calculated values of  $D$ , FWHM and strain are regrouped in table 1. As can be seen, increasing the sulfurization temperature yields to the reduction of the crystallites size in one hand and the increase in films strain in the other hand. This confirms the microstructure deterioration in films annealed at temperatures above 450 °C.

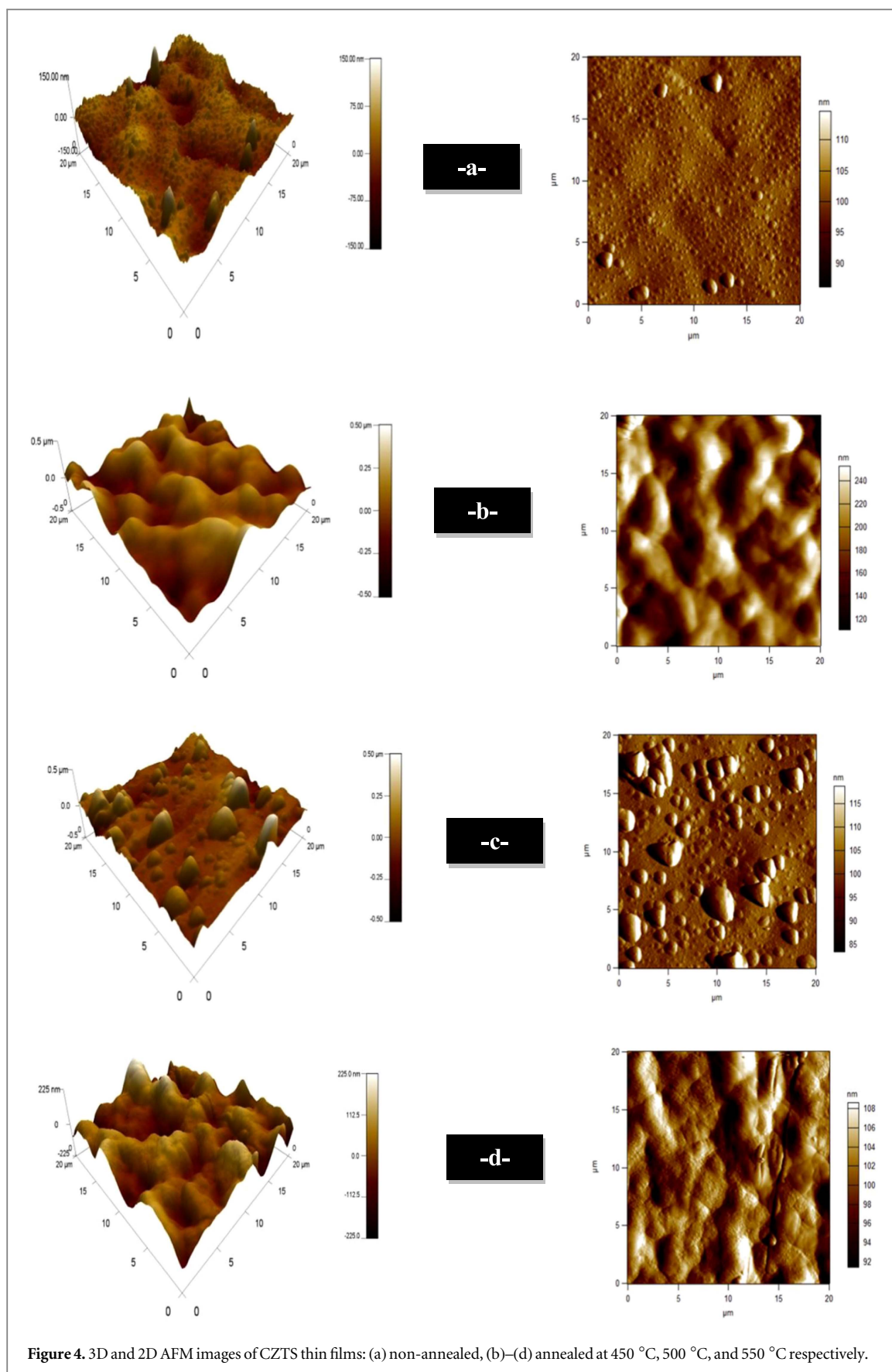
The structural properties were analyzed also via Raman scattering spectroscopy. Raman spectroscopy gives the vibrational modes of bulk CZTS, it is a powerful tool for secondary phases detection which is not evident by XRD analysis. Raman spectra of CZTS are shown in figure 3. The single Raman intense peak located at 330  $\text{cm}^{-1}$  is assigned to bulk CZTS [43–46]. As can be seen no peaks related to any secondary phases is observed confirming CZTS monophase formation. The single phase formation may two origins: (i) the used spray pyrolysis technique, since similar results have been reported by several authors in films prepared by spray pyrolysis method [32, 47]. (ii) The sulfurization temperature, Xu *et al* have investigated the post sulfurization of CZTS thin deposited by sputtering they concluded that after sulfurization pure CZTS without significant amount of secondary phases is obtained after sulfurization at temperatures above 400 °C [48]. It is important to note that film annealed at 450 °C present the most intense peak. This suggests that increasing sulfurization temperature reduces the film crystallinity as concluded from XRD analysis.

CZTS thin films surface morphology was characterized by using AFM images, as shown in figure 4. As can be seen, annealing temperature increasing results in films grains size enlargement and in films surface roughness increase, as reported in table 2.

The transmittance specters of CZTS thin films at different annealing temperature are depicted in figure 5. As seen, the whole films exhibiting low transmission in the visible range (400–800 nm) smaller than 20%. While, the transmission is enhanced with increasing sulfurization temperature, this can be explained by the reduction of the films thickness. Films annealing tends to the films densification by reducing its thickness, the same results were reported in CZTS films prepared by sol–gel method [49] and in sputtered CZTS films after sulfurization at 450 °C [48].

The absorption coefficient of CZTS thin film was calculated from transmission data. The measured low optical transmittance and large absorption coefficient (higher than  $10^4 \text{ cm}^{-1}$ ) of CZTS films after sulfurization implies that the obtained films are suitable candidates for application as absorber in thin film solar cell technology. The optical band gap energy was extracted from transmission data fitting, their values were estimated from the extrapolation of the linear section of  $(\alpha h\nu)^2$  plot as function of photon energy ( $h\nu$ ), as illustrated in figure 6. The measured gap energies are reported in table 1. They are in concurrence with the reported band gap energy of sprayed CZTS thin film [16, 50–52]. As seen, films optical gap is enlarged with increasing the sulfurization temperature; it varies from 1.38 eV at 450 °C to 1.45 eV at 550 °C. The same results were reported in electrodeposited  $\text{CuIn}(\text{Se,S})_2$  sulfurized at a temperature varied between 450 °C and 550 °C [53]. The optical band gap broadening may originate from the films densification and disorder reduction in films network as a consequence of thermal annealing. Indeed, the film thickness is reduced from 1420 to 1220 nm with increasing annealing temperature. Actually, the network disorder reduction yields to films optical band gap enlargement as observed in various thin film semiconductors [54]. Higher band gap values up to 1.7 eV have been reported this was referred to the presence of secondary phases which enlarges the gap energy and specially ZnS given that this phase has a large band gap energy about 3.7 eV.

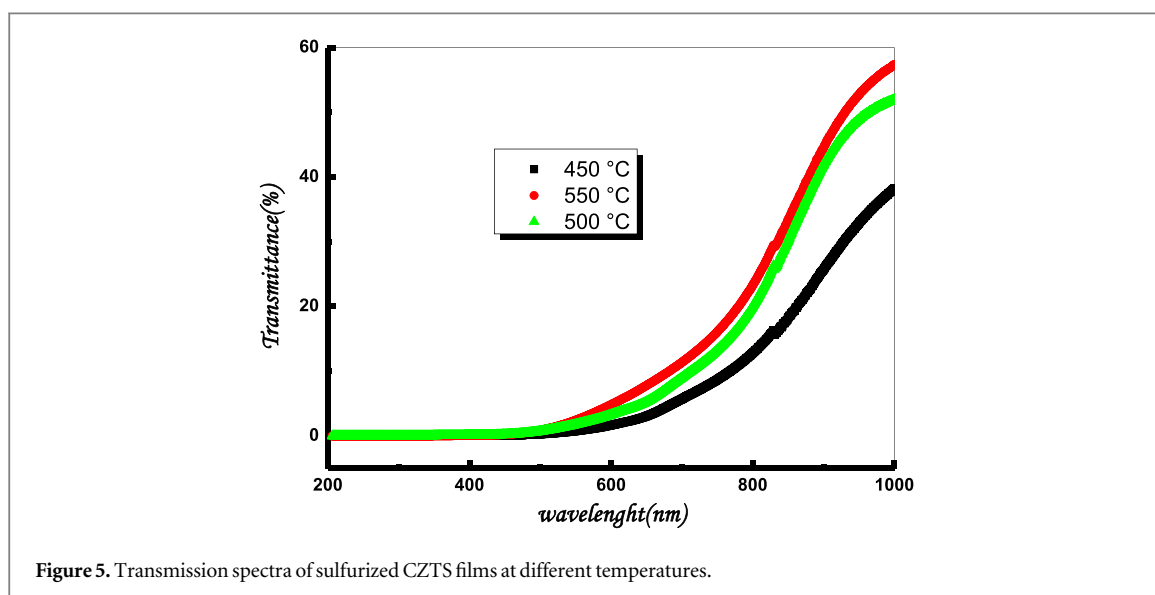
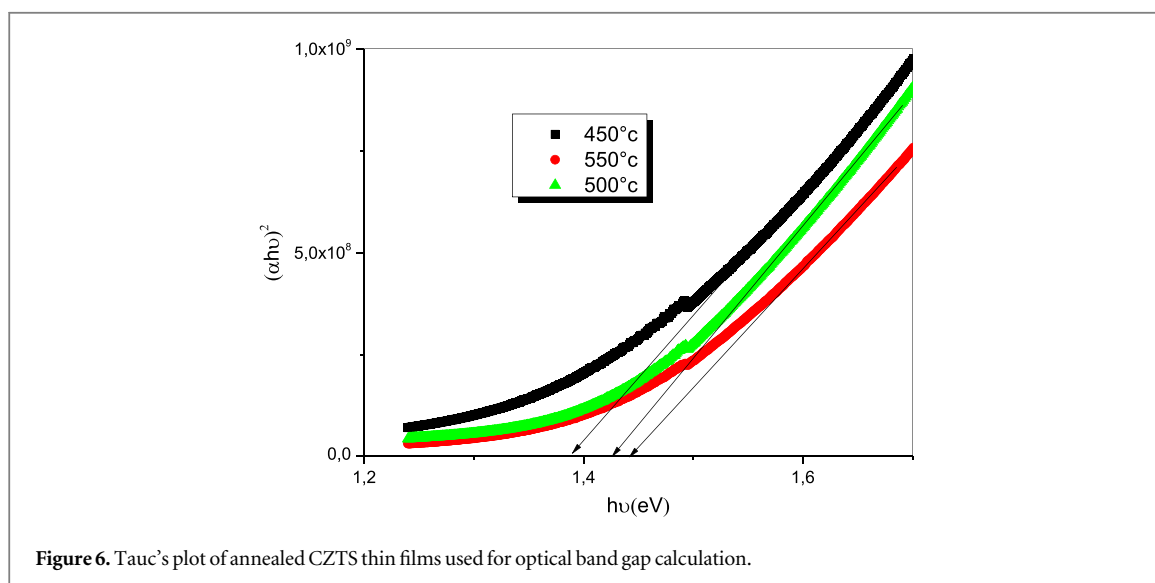
The electrical properties of CZTS thin films at different annealing temperatures were carried out in the dark and at room temperature using Hall effect. The p-type conductivity of CZTS semiconductor was assessed by the positive Hall coefficient. The measured values of carrier concentration, conductivity and mobility are resumed in table 3. The measured motilities are in agreement with the reported values laying between 0.1 and



$10 \text{ cm}^2 \text{ V}^{-1} \text{ s}^{-1}$  [55, 56]. While, film conductivity and mobility are reduced after thermal sulfurization due to the reduction in the crystallites size as concluded from XRD analysis. The reduction in the crystallite size increases the number of grain boundaries that may cause larger electrons scattering during their transport.

**Table 2.** Rms values of CZTS thin films at different condition.

Annealing ( $T^{\circ}\text{C}$ )	As deposited	450	500	550
Rms (nm)	23	98	80	53

**Figure 5.** Transmission spectra of sulfurized CZTS films at different temperatures.**Figure 6.** Tauc's plot of annealed CZTS thin films used for optical band gap calculation.**Table 3.** Carrier concentration, Hall mobility and conductivity of CZTS films annealed at different temperatures.

	Film thickness (nm)	Band gap (eV)	Carrier concentration ( $\text{cm}^{-3}$ )	Hall mobility ( $\text{cm}^2 \text{V}^{-1} \text{s}^{-1}$ )	Conductivity ( $\Omega \text{cm}$ ) <sup>-1</sup>
450 °C	1420	1.38	$7.23 \times 10^{15}$	9.16	$10.61 \times 10^{-3}$
500 °C	1260	1.42	$8.58 \times 10^{14}$	0.41	$0.56 \times 10^{-3}$
550 °C	1220	1.45	$8.78 \times 10^{16}$	0.18	$2.52 \times 10^{-3}$

### 3.2. Characteristic of the devices

#### 3.2.1. Current–voltages characteristic

The realized devices are tested under illumination using a simulator solar cell with a halogen lamp using a light source with intensity equal to  $100 \text{ mW cm}^{-2}$ , the cell area is of  $0.16 \text{ cm}^2$ . Figure 7 shows the semi-logarithmic plot of current–voltage measurement of different CZTS/CdS hetero-junctions in the dark at room temperature

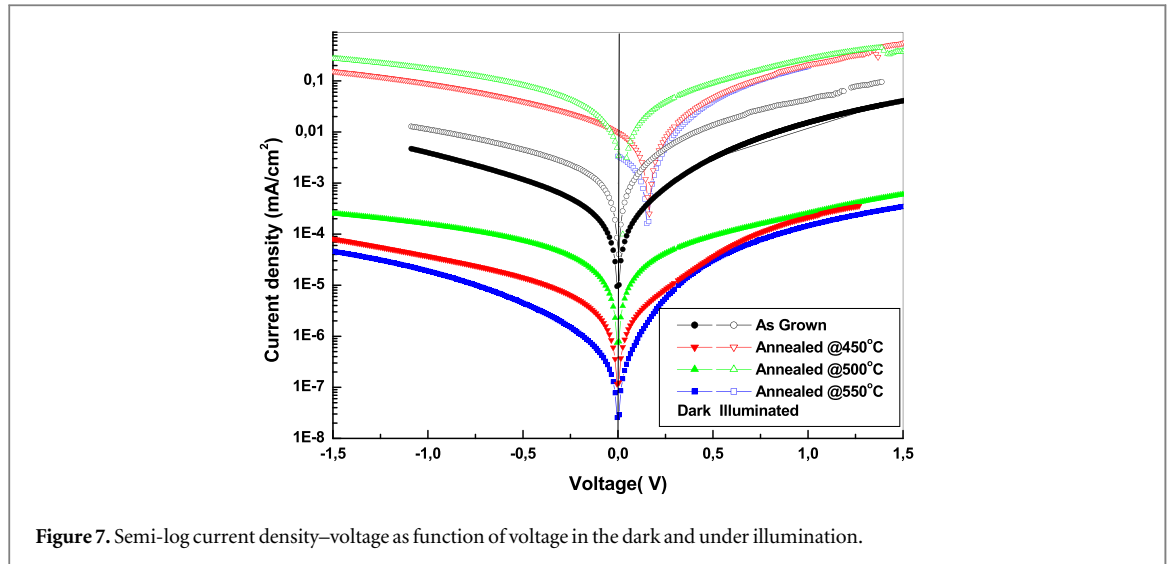


Figure 7. Semi-log current density–voltage as function of voltage in the dark and under illumination.

Table 4. The extracted electrical parameters of realized solar cells.

$T(^{\circ})$	$V_{oc}(meV)$	$J_{sc}(mA\ cm^{-2})$	$R_s(\Omega)$	$n$	$R_{sh}(\Omega)$	FF (%)	PCE (%)	$I_s(\mu A)$
450	161	9.73	11.48	1.7	120	28	0.43	291.6
500	25.3	4.25	10.77	1.8	37	25	0.02	587
550	156	1.41	8.5	1.6	304	31	0.06	336
As deposited	—	—	11.83	2.2	—	—	—	120

and under illumination. The whole devices exhibit a rectification behavior. The rectification ratio (RR) was calculated at a direct and reverse voltage value at  $V = \pm 1$ . The values of RR were varied between 8 and 5 with the large RR for the device annealed at 450 °C. The current across the hetero-junction varies exponentially with the applied voltage and their variation can be described by the standard Schottky diode equation [57].

$$I(V) = I_s \left( \exp\left(\frac{qV}{kTn}\right) - 1 \right), \quad (3)$$

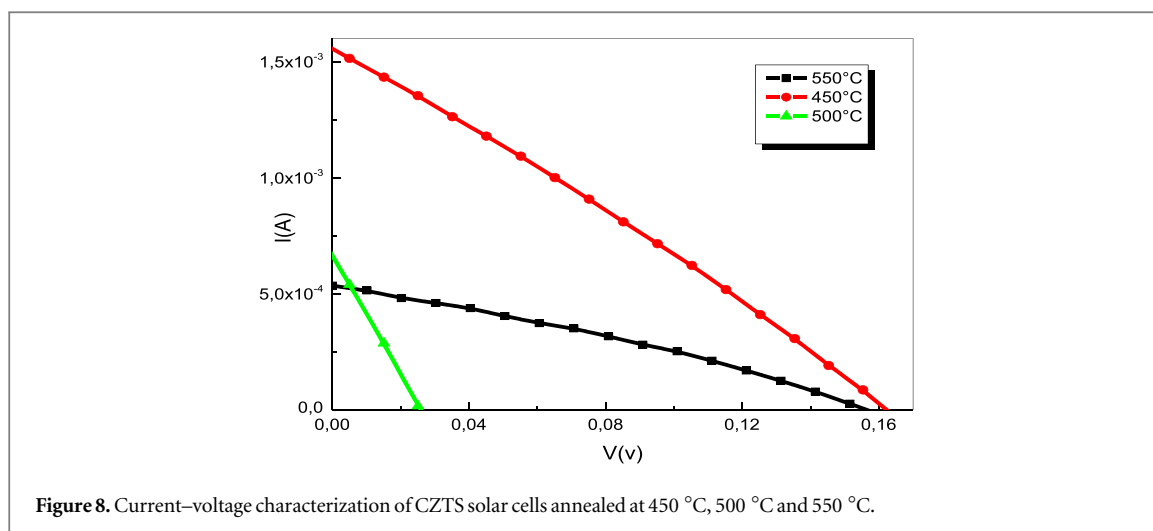
where:  $I_s$ : saturation current;  $n$  is the ideality factor and  $V$  applied voltage,  $k$  is the Boltzmann constant,  $T$  is the absolute temperature,  $q$  is the elementary electronic charge.

The ideality factor ( $n$ ) was calculated from the variation of the slope of the linear portion of  $\ln(I)-V$  and it can be expressed as the following formula:

$$n = \frac{q}{kT} \left( \frac{dV}{d(\ln I)} \right). \quad (4)$$

The ideality factor  $n$  is an important parameter characterizing the diode behavior. It is used to determine which transport mechanism across the hetero-junction is the dominant. In the case of  $n$  equal the unity, the diffusion is the dominant mechanism, whereas if  $n \leq 2$ , the recombination and generation in the depletion layer is the dominant one [58]. Whereas when  $n > 6$  it has been suggested that the interface states contribute mainly in the transport [59, 60]. The ideality factor was found equal to 2.2 in the device realized with non annealed CZTS layer. However in treated CZTS films the obtained ideality factor lays between 1.6 and 1.8 when the temperature varied between 450 °C and 550 °C. This implies that generation-recombination process at the depletion layer is the dominate transport mechanism through the hetero-junction. This suggests also the presence of interface states and defect in the space charge region which is act as charge carriers traps. Mali *et al* [61] reported an ideality factor in the range of 2.2–2.9 for CZTS solar cells by SILAR method, they claimed that current transport in CZTS solar cell is controlled by recombination at high defected grain boundary region. In a previous work, we measured an ideality factor more than 5 in CZTS/ZnS hetero-junction; this was explained by the presence of interfacial state defects with a density about  $10^{10}\ cm^{-2}\ eV^{-1}$  [62]. Patel *et al* [63] reported a value of interfacial states equal to  $10^9\ cm^{-3}$  at CZTS/CdS interface.

The saturation current ( $I_s$ ) was calculated from the semi-log plot and equation (3) and reported in table 4. The saturation current increase from 291 to 587  $\mu A$  with sulfurization temperature indicates clearly the defects



enhancement due to the grain boundary number increases as a consequence of crystallite size reduction with sulfurization temperature.

The series resistances ( $R_s$ ) were calculated directly from the linear portion of  $I$ – $V$  curve plot in the dark. The obtained values are reported in table 4. The series resistance varies between 11 and 8  $\Omega$ , it decreases with sulfurization temperature increase. Amerani *et al* [64] has observed the same trend, they reported a decrease in  $R_s$  from 48 to 14  $\Omega$  when the sulfurization temperature increase from 500 °C to 575 °C. Actually, the series resistance regroups the back and front metal contacts resistances, the semiconductors bulk resistances and the interfaces resistance [65]. Thereafter, it is hard to assess the origin of  $R_s$  variation. Despite that the film annealed at 450 °C exhibits the highest conductivity, it has the largest series resistance, this is due to the film thickness, as shown in table 3, the film annealed at 450 °C is the thicker one. The drawback of the series resistance is the short current circuits reduction and consequently the cell efficiency.

The other parameter affecting the solar cell performance is the shunt resistance ( $R_{sh}$ ) which is due mainly to the defects presence in the bulk of semiconductors and at interfaces. It is estimated from the reverse bias  $I$ – $V$  characteristics branch. Shunt resistance reduces drastically the open circuit voltage  $V_{oc}$ . It should be as high as possible in order to prevent losses [66]. The measured  $R_{sh}$  values are reported in table 4. The highest  $R_{sh}$  value was found for the cell annealed at 550 °C (304  $\Omega$ ) and 120  $\Omega$  for the one annealed at 450 °C, whereas the low value is measured in the cell annealed at 500 °C, thereof, the latter presents the low efficiency and  $V_{oc}$  values (table 3).

Figure 8 depicts the  $I$ – $V$  characteristics of CZTS thin film solar cells under illumination. All devices exhibit photovoltaic behavior. While the photovoltaic effect was not observed in the un-annealed device (figure 7). The cell annealed at 450 °C exhibits the best  $V_{oc}$  equal to 161 mV and  $I_{sc}$  equal to 1.56 mA with a fill factor of 28% and an efficiency of 0.43%.

This is due to the good crystallinity of the film sulfurized at 450 °C compared to the other films. The film annealed at 500 °C leads to the lower efficiency, this can be attributed to its inferior crystalline quality according to XRD and Raman analysis. This is consistent with the measured high series resistance, low shunt resistance and high current saturation in this cell (table 4).

In table 5 we have compiled parameters of CZTS based solar cells reported by several authors working with different deposition techniques and CZTS films treatments. The most important conclusions that can be retained are: the results are too spread, best results are achieved by the physical deposition methods namely thermal evaporation and sputtering. While, spray pyrolysis technique yields to inferior solar cell performances, even though the sulfurization treatments is applied. Thereafter, despite that spray pyrolysis, technique is considered as one of the most appropriate growth methods to develop low-cost devices, it yields to low solar cell efficiency. As can be seen, our result remains in the range of efficiency achieved by spray pyrolysis. This discrepancy may originate from the films microstructure differences. We speculate that the major reason of spray pyrolysis inferiority is due to the achieved low material grain sizes. Indeed, grain size up to 2.5–1  $\mu\text{m}$  [64, 67] and 0.4  $\mu\text{m}$  [4] were reported in sputtered and thermally evaporated CZTS thin films respectively. While in sprayed films the grain size do not exceed 300 nm [20, 68] in our case, we have measured a crystallite size of 16 nm. Grain boundaries introduce additional defects acting as recombination centers. The same conclusion has been outlined by Courel *et al* [25], they explained that the inferiority of spray pyrolysis solar cells is originated from the low mobility of electron and recombination that may reduce drastically the open circuit, which is in concordance with our conclusion. It has been reported that this problem is particularly more detrimental in

**Table 5.** Characteristics of CZTS based thin films solar cells prepared by different techniques reported by different authors.

CZTS preparation technique and treatment	$V_{oc}$ (mV)	$I_s$ (mA cm <sup>-2</sup> )	FF (%)	$\nu$ (%)	$R_s$ ( $\Omega$ )	$R_{sh}$ ( $\Omega$ )	Reference
Thermal evaporation + annealing in air at 570 °C	661	19.5	65.8	8.4	4.5	—	[4]
Thermal evaporation + sulfurization at 520 °C	629	12.53	58	4.53	8.5	428	[73]
Thermal co-evaporation + sulfurization at 550 °C	633	21.5	60.1	8.27	5.85	2.2 104	[74]
Evaporation + sulfurization 550 °C	400	5.8	45	1.05	—	—	[75]
Dc rf co-sputtering of Cu, Sn, and ZnS target annealing at 250 °C in N <sub>2</sub> + sulfurization at 600 °C	629	13.14	42	3.6	126	189	[38]
Multi target magnetron sputtering + sulfurization at 570 °C	600.4	11.82	40.4	2.87	25.1	144.5	[67]
Dc and rf sputtering of Cu, Zn, Sn targets + sulfurization at 575 °C	593	20.5	48	5.75	19	620	[64]
Electrodeposition + sulfurization at 590 °C	673	18.7	44	5.5	68	1101	[76]
Sol gel sulfurization at 500 °C	390	7.81	33	1.01	—	—	[77]
SIAR + sulfurization at 575 °C	400	8.27	52	1.06	—	—	[78]
Spray pyrolysis at 500 °C substrate temperature	390	7.31	30	0.86	190	400	[68]
Spray heated in air + sulfur and tin atmosphere at 550 °C	173	10	28	0.5	—	—	[20]
Spray in Ar + sulfur and tin atmosphere At 550 °C	361	7.5	37	1.0	—	—	[20]
Spray pyrolysis at 500 °C substrate temperature	510	8.88	23	1.09	278.5	250	[19]
Spray pyrolysis at Ts 450 °C with Ar carrier gas	246	3.9	39	0.4	14	95	[79]
Spray pyrolysis + sulfurization at 450 °C in H <sub>2</sub> S + Ar	161	9.73	28	0.43	11.5	120	This work

CZTS-based devices, than in chalcopyrites (CuInGsa) Sn-based ones [69]. Any reduction in the grain size is accompanied by the increase in the grain boundaries and consequently a recombination enhancement, reduction in carriers mobility due to the scattering and the photo-generated carriers lifetime reduction. In fact, low mobility values are usually reported in CZTS thin films, particularly in samples deposited using spray pyrolysis technique due to the microstructure [17, 70]. Both these effects concur to  $V_{oc}$ , FF and cell efficiency reduction. Courel *et al* had studied the loss mechanism in sprayed CZTS solar cells and find that CTZS is characterized by a low minority carrier lifetime and defects in CZTS bulk [28]. This is in concordance with several authors conclusion claiming that spray pyrolysis technique produces low efficiency solar cells [52, 71, 72].

#### 4. Conclusion

In the present work, the effect of sulfurization temperature on sprayed CZTS thin films and on solar cells performance was investigated. XRD analysis and Raman spectroscopy reveal that after sulfurization CZTS films are monophasic exempt from any secondary phases. Increasing the sulfurization temperature reduces slightly the crystallite size and enhances the films strain. Films conductivity and mobility are reduced after thermal sulfurization due to the reduction in the crystallites size. Films optical gap is enlarged with increasing the sulfurization temperature; it varies from 1.38 eV at 450 °C to 1.45 eV at 550 °C. All the realized devices Mo/CZTS/CdS/ZnO/ZnO:Al show a rectification behavior with an ideality factor varied between 1.6 and 1.8. The best results are achieved in the cell prepared with CZTS sulfurized at 450 °C, the obtained characteristics are: 0.43% efficiency, 161 mV open circuit, 9.8 A cm<sup>-2</sup> short circuit and 28% fill factor. A comparison with the reported results, in the literature, by different authors and techniques indicates clearly that spray pyrolysis technique yields to lower cell efficiencies due to the small crystallites size of CZTS films prepared by the latter technique.

#### ORCID iDs

M S Aida  <https://orcid.org/0000-0001-8420-1835>

#### References

- [1] Wang K, Gunawan O, Todorov T, Shin B, Chey S J, Bojarczuk N A, Mitzi D and Guha S 2010 *Appl. Phys. Lett.* **97** 143508
- [2] Chung C H, Bob B, Lei B, Li S H, Hou W W and Yang Y 2013 *Sol. Energy Mater. Sol. Cells* **113** 148–52
- [3] Shockley W and Queisser H 1961 *Japan. J. Appl. Phys.* **32** 510–9
- [4] Ahmed S, Reuter K B, Gunawan O, Guo L, Romankiw L T and Deligiani H 2011 *Adv. Energy Mater.* **20** 1–7

- [5] Wang W, Winkler M T, Gunawan O, Gokmen T, Todorov T K, Zhu Y and Mitzi D B 2013 *Adv. Energy Mater.* **4** 1301465
- [6] Roy P and Srivastava S K 2006 *Mater. Chem. Phys.* **95** 235–41
- [7] Alexander J N, Higashiya S, Caskey D, Efstathiadis H and Haldar P 2014 *Sol. Energy Mater. Sol. Cells* **125** 47–53
- [8] Oliva A I, Solis-Canto O, Castro-Rodriguez R and Quintana 2001 *Thin Solid Films* **391** 28
- [9] Nair P K et al 1998 *Sol. Energy Mater. Sol. Cells* **52** 313
- [10] Battisha I K, Afify H H, Abd El Fattah G and Badr Y 2002 *Fizika A* **11** 31
- [11] Shin B, Gunawan O, Zhu Y, Bojarczuk N A, Chey S J and Guha S 2013 *Prog. Photovolt., Res. Appl.* **21** 72–6
- [12] Moholkar A V, Shinde S S, Agawane G L, Jo S H, Rajpure K Y, Patil P S, Bhosale C H and Kim J H 2012 *J. Alloy. Compd.* **544** 145–51
- [13] Katagiri H and Jimbo K 2011 *Proc. 37th IEEE Photovoltaic Specialists Conf.* pp 3516–21
- [14] Katagiri H, Jimbo K, Yamada S, Kamimura T, Maw W S, Fukano T, Ito T and Motohiro T 2008 *Appl. Phys. Express* **1** 041201
- [15] Woo K, Kim Y and Moon J 2012 *Energy Environ. Sci.* **5** 5340–5
- [16] Kamoun N, Bouzouita H and Rezig B 2007 *Thin Solid Films* **515** 5949
- [17] Kishore Kumar Y B, Suresh Babu G, Uday Bhaskar P and Sundara Raja V 2009 *Sol. Energy Mater. Sol. Cells* **93** 1230
- [18] Daranfed W, Aida M S, Attaf N, Bougdira J and Rinnert H 2012 *J. Alloys Compd.* **542** 2227
- [19] Bhosale S M, Suryawanshi M P, Kim J H and Moholkar A V 2015 *Ceram. Intern.* **41** 8299
- [20] Vigil-Galan O, Courel M, Espindola-Rodriguez M, Izquierdo-Roca V, Saucedo E and Fairbrother A 2013 *J. Renew. Sustain. Energy* **5** 053137
- [21] Barkhouse D A R, Gunawan O, Gokmen T, Todorov T K and Mitzi D B 2012 *Prog. Photovolt., Res. Appl.* **20** 6–11
- [22] Mitzi D and Guha S 2010 *Appl. Phys. Lett.* **97** 143508
- [23] Courel M, Andrade-Arvizu J A and Vigil-Galán O 2016 *Mater. Res. Express* **3** 095501
- [24] Siebentrit S 2013 *Thin Solid Films* **535** 1–4
- [25] Courel M, Valencia-Resendiz E, Andrade-Arvizu J A, Saucedo E and Vigil-Galán O 2017 *Sol. Energy Mater. Sol. Cells* **159** 151–8
- [26] Tanaka K, Moritake N and Uchiki H 2007 *Sol. Energy Mater. Sol. Cells* **91** 1199–201
- [27] Katagiri H, Sasaguchi N, Hando S, Hochino S, Ohashi J and Yokota T 1997 *Sol. Energy Mater. Sol. Cells* **49** 407–14
- [28] Tanaka K, Fukui Y and Uchiki H 2011 *Sol. Energy Mater. Sol. Cells* **95** 838–42
- [29] Araki H, Kubo Y, Aya K, Jimbo K, Shwe Maw W, Yamazaki M, Oishi K and Takeuchi A 2009 *Sol. Energy Mater. Sol. Cells* **93** 996–9
- [30] Katagiri H, Jimbo K, Kimura R, Kamimura T, Yamada S, Maw W S, Araki H and Oishi K 2007 *Thin Solid Films* **515** 5997
- [31] Yoo H and Kim J H 2010 *Thin Solid Films* **518** 6567
- [32] Diwatek K, Mohiteb K, Shinde M, Rondiya S, Pawbake A, Dated A, Pathane H and Jadhkar S 2017 *Energy Proc.* **110** 180–7
- [33] Zhou Y L, Zhou W H, Lei M, Du Y F and Wu S X 2011 *J. Phys. Chem. C* **115** 19632–9
- [34] Parkin I P, Price L S, Hibbert T G and Molloy K C 2001 *J. Mater. Chem.* **11** 1486–90
- [35] Munce C G, Parker G K, Holt S A and Hope A 2007 *Colloids Surf. A* **295** 152–8
- [36] Serrano J, Cantarero A, Cardona M, Garro N, Lauck R, Tallman R E, Ritter A and Weinstein B A 2004 *Phys. Rev. B* **69** 014301
- [37] Khalkar A, Lim K S, Yu S M, Shin D W, Oh T S and Yoo J B 2015 Effects of sulfurization pressure on the conversion efficiency of CO sputtered  $\text{Cu}_2\text{ZnSnS}_4$  thin film solar cells *Int. J. Photoenergy* **2015** 750846
- [38] Zhi J, Shurong W, Zhishan L, Min Y, Sijia L, Yilei L, Qichen Z and Ruiting H 2017 *Mater. Sci. Semicond. Process.* **57** 239–43
- [39] Li Y, Yuan T, Jiang L, Su Z and Liu F 2014 *J. Alloys Compd.* **610** 331–6
- [40] Zhou Z, Wang Y, Xu D and Zhang Y 2010 *Sol. Energy Mater. Sol. Cells* **94** 2025–42
- [41] Cui Y, Zuo S, Jiang J, Yuan S Z and Chu J 2011 *Sol. Energy Mater. Sol. Cells* **95** 2136–40
- [42] Goodman L A 1974 *RCA Rev.* **35** 613
- [43] Tang D D, Wang Q, Liu F, Zhao L, Han Z, Sun K, Lai Y, Li J and Liu Y 2013 *Surf. Coat. Technol.* **232** 53
- [44] Shavel A, Cadavid D, Ibáñez M, Carrete A and Cabot A 2012 *J. Am. Chem. Soc.* **134** 1438
- [45] Zhou M, Gong Y, Xu J, Fang G, Xu Q and Dong J 2013 *J. Alloy. Compd.* **574** 272–7
- [46] Xia Y, Cheng Z, Zhang Z, Fang X and Liang G 2014 *Nanoscale Res. Lett.* **9** 208–14
- [47] Zhai X, Jia H, Zhang Y, Lei Y, Wei J, Gao Y, Chu J, He W, Yin J and Zheng Z 2014 *CrystEngComm* **16** 6244–9
- [48] Xu J, Cao Z, Yang Y and Xie Z 2014 *J. Renew. Sustain. Energy* **6** 053110
- [49] Maeda K, Tanaka K, Fukui Y and Uchiki H 2011 *Japan. J. Appl. Phys.* **50** 01BE10
- [50] Majeed Khan M A, Kumar S, Alhoshan M and Dwayyan A S A 2013 *Opt. Laser Technol.* **49** 196
- [51] Rajeshmon V G, Kartha C S, Vijayakumar K P, Sanjeeviraja C, Abe T and Kashiwaba Y 2008 *Sol. Energy* **85** 249
- [52] Das S and Mandal K C 2012 Low-cost  $\text{Cu}_2\text{ZnSnS}_4$  thin films for large-area high-efficiency heterojunction solar cells *38th IEEE Photovoltaic Specialists Conf. (PVSC) (Austin, Texas)* p 2668
- [53] Kim D, Kwon Y, Lee D, Yoon S, Leed S and Yoo B 2015 *J. Electrochem. Soc.* **162** D36–41
- [54] Jamil Ikhmayies S and Ahmed Bitar R N 2013 *J. Mater. Res. Technol.* **2** 221–7
- [55] Gunawan O, Gokmen T and Mitzi D B 2014 *J. Appl. Phys.* **116** 1–9
- [56] Gonzalez J C, Ribeiro G M, Viana E R, Fernandes P A, Salome P M P, Gutierrez K, Abelenda A, Matinaga F M, Leit J P and da Cunha A F 2013 *J. Phys. D: Appl. Phys.* **46** 155107
- [57] Sze S M 1981 *Physics of Semiconductor Devices* (New York: Wiley)
- [58] Shah C T, Noyce R N and Shockley W 1957 *Proc. IRE* **45** 1228–43
- [59] Brotzmann M, Vetter U and Hofsass H J 2009 *Appl. Phys.* **106** 063704
- [60] Schenk A and Krumbein U J 1995 *Appl. Phys.* **78** 3185
- [61] Mali S, Shinde P S, Betty C A, Bhosale P N, Oh Y W and Patil P S 2012 *J. Phys. Chem. Solids* **73** 735–40
- [62] Boutebakh F Z, Lamri Zeggag M, Attaf N and Aida M S 2017 *Opt. Int. J. Light Electron Opt.* **144** 180–90
- [63] Patel M, Mukhopadhyay I and Ray A 2013 *Semicond. Sci. Technol.* **28** 055001
- [64] Emrani A, Vasekar P and Westgate C R 2013 *Sol. Energy* **98** 335–40
- [65] Luque A and Hegedus S 2011 *Handbook of Photovoltaic Science and Engineering* 3rd edn (New York: Wiley)
- [66] Altamura G 2014 Development of CZTSSe thin films based solar cells *PhD Thesis* Joseph-Fourier—Grenoble I, University
- [67] Li W, Chen J, Yan C and Hao X 2015 *J. Alloys Compd.* **632** 178–84
- [68] Bhosale S M, Suryawanshi M P, Gaikwad M A, Bhosale P N, Kim J H and Moholkar A V 2014 *Mater. Lett.* **129** 153–5
- [69] Li J, Mitzi D B and Shenoy V B 2011 *ACS Nano* **5** 8613–9
- [70] Kumar Y B K, Bhaskar P U, Babu G S and Raja V S 2010 *Phys. Status Solidi a* **207** 149–56
- [71] Rajeshmon V G, Kartha C S, Vijayakumar K P, Sanjeeviraja C, Abe T and Kashiwaba Y 2011 *Sol. Energy* **85** 249–55
- [72] Espindola-Rodríguez M, Placidi M, Vigil-Galán O, Izquierdo-Roca V, Fontané X, Fairbrother A, Sylla D, Saucedo E and Pérez-Rodríguez A 2013 *Thin Solid Films* **535** 67–72

- [73] Katagiri H 2005 *Thin Solid Films* **480–481** 426–32
- [74] Gershon T, Shin B, Bojarczuk N, Gokmen T, Lu S and Guha S 2013 *J. Appl. Phys.* **114** 154905
- [75] Biccari F, Chierchia R, Valentini M, Mangiapane P, Salza E, Malerba C, Azanza Ricardo CL, Mannarino L, Scardi P and Mittiga A 2011 *Energy Proc.* **10** 187–91
- [76] Ge J, Jiang J, Yang P, Peng C, Huang Z, Zuo S, Yang L and Chu J 2014 *Sol. Energy Mater. Sol. Cells* **125** 20–6
- [77] Tanaka K, Oonuki M, Moritake N and Uchiki H 2009 *Sol. Energy Mater. Sol. Cells* **93** 583–7
- [78] Suryawanshi M P, Shin S W, Ghorpade U V, Gurav K V, Agawane G L, Woo Hong C, Ho Yun J, Patil P S, Kim J H and Moholkar A V 2014 *Sol. Energy* **110** 221–30
- [79] Vigil-Galán O, Courel M, Espindola-Rodriguez M, Jiménez-Olarte D, Aguilar-Frutis M and Saucedo E 2015 *Sol. Energy Mater. Sol. Cells* **132** 557–62

# Réalisation et caractérisation électrique d' hétérojonctions en couches minces pour application photovoltaïque

## RESUME

L'objectif de ce travail porte sur la réalisation et caractérisation électrique des hétérojonctions en couche mince par une technique simple et bon marché en l'occurrence la méthode de dépôt par Spray pyrolyse (SP). Dans la première partie de ce travail nous avons élaboré des séries de films avec différentes conditions de déposition en vue d'une optimisation du procédé dans le but d'obtenir de films avec de bonnes propriétés optoélectroniques pour être appliqués en photovoltaïque. Les paramètres étudiés sont la température de la température du substrat, le temps de dépôt, la molarité de cuivre et de zinc. La caractérisation structurale des films a révélé que ces derniers ont une structure tétragonale (kesterite) avec une préférentielle orientation vers (112) qui est indépendant de condition étudié. La présence de phase secondaire et lié fortement à la composition de film et les concentrations des précurseurs dans la solution de départ. Les caractérisations optiques et électriques ont montré que les films CZTS déposés par spray ont de bonne propriétés optoélectroniques, une assez bonne absorbance dans le visible avec une conductivité élevée. les hétérojonctions fabriquer montrent un comportement redresseur, les caractérisation G-f révèlent la présence des états d'interface entre la couche absorbante (CZTS) et la couche tampon (ZnS) avec une densité d'ordre  $10^{10}$   $\text{ev}^{-1}\text{cm}^{-2}$ , avec l'amélioration des propriétés électriques avec l'addition de couche ZnO entre CZTS et ZnS. La cellule solaire CZTS/CdS trompé à 450 °C montres un rendement égale à 0.43 % et un courant de courte circuit égale a 9.8  $\text{mA}/\text{Cm}^2$ .

**Mots clés :** couches minces, CZTS, spray pyrolyse, hétérojonction, cellules solaire

## انجاز ودراسة الخصائص الكهربائية للوصلات غير المتجانسة انطلاقا من لأغشية الرقيقة لاستعمالها في التطبيقات الكهروضوئية

### ملخص

موضوع الرسالة يتناول تحضير,انجاز ودراسة الخصائص الكهربائية للوصلات الغيرمتجانسة و المكونة انطلاقا من اغشية رقيقة وذلك باستعمال تقنية سهلة و بسيطة و التى تتمثل فى تقنية الرش الحرارى (spray pyrolysis SP) . فى الجزء الاول من هذا العمل قمنا بتحضير سلسلة من العينات باستعمال مختلف شروط تجريبية من اجل ايجاد افضل الشروط للحصول على شرائح CZTS ذات خصائص كهروضوئية جيدة حيث يمكن استعمالها فى الخلايا شمسية. الوسائط التى قمنا بدراستها كانت على التولى : درجة حرارة المسند,مدة التحضير , تركيز ملح النحاس و الزنك. الدراسة البنيوية وضحت ان تركيب البلورى للشرائح كان ذو تركيبية Tetragonale بينما الاتجاه البلورى المفضل فى اتجاه المستوي (112).الدراسة الضوئية و الكهربائية وضحت ان شرائح CZTS المحضرة خلال هذا العمل تمتاز بخصائص جيدة و التى تتمثل فى امتصاص عال للضوء و ناقلية كهربائية جيدة مما يرشح هذه الشرائح للاستعمال فى التطبيقات الكهروضوئية.دراسة الخصائص الكهربائية باستعمال (I(V) للوصلات الغير المتجانسة المنجزة CZTS/ZnS و بينت ان الوصلات لها خاصية التقويم.دراسة العيوب بين البينيات بالاستعمال (G-f) اثبتت وجود كثافة عيوب فى السطح البيني CZTS / ZnS قيمتها فى حدود  $10^{10} \text{ cm}^{-1} \text{ ev}$  .كما بينت اضافة طبقة من ZnO تحسن فى الخصائص الكهربائية للبنية ,فى حين أن الخلايا الشمسية CZTS / CdS الملدنة عند 450 درجة مئوية تحت غاز  $\text{H}_2\text{S}$  اعطت افضل مردود للخلايا الشمسية المجزة حوالي 0.43 % و كثافة تيار تساوي 9.8 ملي أمبير / سم<sup>2</sup>

**الكلمات المفتاحية :** شرائح رقيقة, CZTS, الرش الحرارى,وصلة غير متجانسة, الخلايا الشمسية

## ABSTRACT

The present work deals with the deposition of CZTS thin films and related devices by a simple and cheap technique such as Spray Pyrolysis (SP). For this purpose, a set of CZTS thin film was prepared using various deposition conditions in order to optimize the deposition conditions allow us to prepare suitable films devoted to the photovoltaic applications. The studied deposition parameters were the substrate temperature, deposition time, and copper and zinc salt concentrations. The structural analysis shows that the obtained films are polycrystalline; they exhibit a tetragonal structure with a preferential orientation along (112). However, the structural properties and secondary phases were affected by the deposition conditions. From the optical and electrical characterization results, we inferred that the deposited films have suitable optoelectronic properties for the photovoltaic applications, since they present a good absorption in the visible range coupled with a higher conductivity. Finally; the fabricated CZTS heterojunction with various back contacts show a rectification behavior, the G-f characterization reveals the presence of interface state at CZTS/ZnS interface with a state density in the order of  $10^{10} \text{ eV}^{-1}\text{cm}^{-2}$ . The addition of ZnO intrinsic layer enhances the heterojunction device properties. Whereas, the solar cells based CZTS/CdS annealed at 450 °C under H<sub>2</sub>S gas show the best solar cell efficiency about 0.43 % and a current density equal 9.8 mA/cm<sup>2</sup>.

**Key Words:** *thin films; CZTS; spray pyrolysis; hetero-junction; solar cells.*